

**CUADERNOS  
de  
INVESTIGACIÓN GEOGRÁFICA**

---

***GEOGRAPHICAL RESEARCH LETTERS***



Tomo 51 (1)

2025

ISSN: 1697-9540

UNIVERSIDAD DE LA RIOJA  
LOGROÑO (ESPAÑA)

# CUADERNOS DE INVESTIGACIÓN GEOGRÁFICA

## GEOGRAPHICAL RESEARCH LETTERS

### Editor Principal / *Editor-in-Chief*

Noemí Lana-Renault Monreal (Universidad de La Rioja)

### Editores Adjuntos / *Associate Editors*

José Arnáez (Universidad de La Rioja)

Makki Korchaní (University of Nebraska, Estados Unidos)

Jorge Lorenzo-Lacruz (Universidad de La Rioja)

Raquel Montorio Lloveria (Universidad de Zaragoza)

Estela Nadal Romero (Instituto Pirenaico de Ecología, CSIC)

Purificación Ruiz-Flaño (Universidad de La Rioja)

### Consejo Editorial / *Editorial Board*

Santiago Beguería Portugués (Estación Experimental de Aula Dei, CSIC)

*Spatial analysis, Climate change, Water resources management, Environmental hydrology*

E. Cammeraat (Universiteit van Amsterdam, Holanda)

*Geomorphology, Soil Science, Soil Conservation*

S.R. Fassnacht (Colorado State University, EEUU)

*Environmental hydrology, Snow hydrology, Hydrological Modeling*

H. Holzmann (Universitat für Bodenkultur Wien, Austria)

*Hydrological modeling, Surface hydrology, Soil hydrology, Snow Hydrology, Climate change*

P. Hughes (University of Manchester, Reino Unido)

*Glacial and Periglacial Geomorphology, Climate change*

V. Jomelli (Université Paris I, Francia)

*Climate change, Climatology, Paleoclimatology, Glaciology, Periglacial Geomorphology*

J.J. Keizer (Universidade de Aveiro, Portugal)

*Ecological impact of wildfire, Soil erosion, Wind erosion*

M.A. Lenzi (Università di Padova, Italia)

*Fluvial geomorphology, Natural hazards, Sedimentology*

M. López-Vicente (Universidad de Jaén)

*Sustainability, Water Resources Management, Soils, Hydrological modelling*

Y. Onda (University of Tsukuba, Japón)

*Water Quality, Hydrology, Soil Science, Freshwater Ecology, Soil erosion, Geomorphology*

D. Palacios (Universidad Complutense de Madrid)

*Palaeoclimatology, Glaciology*

J.L. Peña (Universidad de Zaragoza)

*Geomorphology, Geoarchaeology, Natural hazards, Holocene*

J. Poesen (Katholieke Universiteit Leuven, Alemania)

*Geomorphology, Soil erosion, Badland geomorphology, Environmental change*

J.B. Ries (Universität Trier, Alemania)

*Water resources management, Soil erosion, Land degradation*

M.A. Romero Díaz (Universidad de Murcia)

*Soil erosion, Badland geomorphology, Reforestation, Piping geomorphology*

E. Serrano Cañadas (Universidad de Valladolid)

*Geomorphology, Glacial and periglacial environments, Quaternary*

M. Vanmaercke (Katholieke Universiteit Leuven, Alemania)

*Soil erosion, Sediment Transport, Geomorphology*

L. Vázquez Selem (Universidad Nacional Autónoma de México, México)

*Paleoclimatology, Glacial geomorphology, Volcanoes, Natural Hazards*

S. Vicente-Serrano (Instituto Pirenaico de Ecología, CSIC)

*Climatology, Droughts, Climate change, Environmental hydrology, Remote sensing*

G-L. Wu (Northwest Agriculture & Forestry University, Chinese Academy of Sciences, China)

*Soil and Water Conservation, Soil erosion, Land degradation, Desertification*

**Cuadernos de Investigación Geográfica = Geographical Research Letters (ISSN: 0211-6820)** is a scientific journal that publishes two issues per year. It includes papers on Physical Geography and other related environmental sciences (Hydrology, Ecology, Climatology). Interdisciplinary studies with Human Geography are also welcome. The peer review and publication of articles in *Cuadernos de Investigación Geográfica* is free of charge, in agreement with the policy of the journal of making accessible the advances in Physical Geography to the scientific community. All papers are subject to full peer review.

Since 2015 *Cuadernos de Investigación Geográfica = Geographical Research Letters* has been included in the Emerging Sources Citation Index (ESCI) of Clarivate Analytics, a new edition of the Web of Science, within the subject category of *Geography (Physical)*. The journal is also indexed in SCOPUS and SCIMAGO Journal & Country Rank within the subject categories of Geography, Planning and Development, Environmental Sciences, and Earth and Planetary Sciences.

**Fotografía de portada / Cover photo:** Paisaje invernal en el Puerto de Vegarada (León)/ Winter view of the Vegarada Pass (León). Autor / Author: Adrián Melón-Nava.

**CUADERNOS DE INVESTIGACIÓN GEOGRÁFICA**  
**GEOGRAPHICAL RESEARCH LETTERS**

ISSN 1697-9540

**Tomo 51 (1) 2025**

**CONTENIDO / CONTENT**

**José Arnáez, Noemí Lana-Renault, José María García-Ruiz, Isabel Terroba.** 50 years of Cuadernos de Investigación Geográfica

*50 años de Cuadernos de Investigación Geográfica*..... 3

**Adrián Melón-Nava, Amelia Gómez-Villar.** Snow Cover Variability in the Cantabrian Mountains (Spain): A Watershed-Level Study Using Satellite Records (2000–2024)

*Variabilidad de las cubiertas de nieve en la Cordillera Cantábrica (norte de España): un estudio a nivel de cuencas a partir de registros satelitales (2000-2024)*..... 7

**Ana Casado, Federico Javier Berón De La Puente, Verónica Gil.** Effects of DEM Resolution and Area Thresholds on Automated Fluvial Morphometry, Arroyo del Oro (Argentina)

*Efectos de la resolución del DEM y de los umbrales de área en la morfometría fluvial automatizada, Arroyo del Oro (Argentina)* ..... 33

**Andrea S. Brendel, Federico Ferrelli, Maximiliano Garay, Agustina Gutierrez, Vanesa Perillo, Maria Cintia Piccolo.** The Role of Green Roofs in Climate Change Mitigation and Adaptation: Analyzing Performance During Extreme Rainfall Events

*El papel de los techos verdes en la mitigación y adaptación al cambio climático: análisis de su efectividad durante eventos de lluvia extrema* ..... 51

**Marco Navarro, Melina Paredes, Miguel Pezo, Eduardo Oyague.** Assessing the Design and Management of Protected Areas: Landscape Geography in Lomas and Tillandsiales of Southwestern Peru

*Evaluación del diseño y gestión de áreas protegidas: Geografía del paisaje en Lomas y Tillandsiales del Suroeste Peruano* ..... 71

**Virginia Alberdi Nieves.** Analysis of Climate Change Impacts on Andean Forests Using Potential Distribution Models (2010-2069)

*Ánalisis de los impactos del cambio climático en los bosques andinos mediante modelos de distribución potencial (2010–2069)* ..... 89

<b>Dhais Peña-Angulo, Santiago Beguería, Víctor Trullenque-Blanco, José Carlos González-Hidalgo.</b> Variabilidad espacial y temporal de las precipitaciones extraordinarias en España (1916-2022)	105
<i>Spatial and Temporal Variability of Extraordinary Precipitations in Spain (1916-2022) .....</i>	
<b>Carolina Calvi, Edoardo Melendi, Eleonora Carol.</b> Análisis espectral espacio-temporal de humedales de alta montaña y su relación con la variabilidad climática	
<i>Spatio-Temporal Spectral Analysis of High Mountains Wetlands and Their Relationship to Climate Variability .....</i>	127
<b>Christoph Correia, Jesús Ortúño Castillo, Marta Toro Bermejo, Patricia Pérez Ramírez.</b> Advancements in High-Resolution Land Use Mapping: Methodologies and Insights from the Rethinkaction H2020 Project	
<i>Avances en la cartografía de alta resolución de usos del suelo: metodologías y aprendizajes del proyecto H2020 RethinkAction .....</i>	145



## 50 YEARS OF CUADERNOS DE INVESTIGACIÓN GEOGRÁFICA

JOSÉ ARNÁEZ<sup>1</sup>, NOEMÍ LANA-RENAULT<sup>2</sup>,  
JOSÉ MARÍA GARCIA-RUIZ<sup>3</sup>, ISABEL TERROBA<sup>4</sup>

<sup>1</sup>*Editor-in-Chief of Cuadernos de Investigación Geográfica 1988-2024*  
*Universidad de La Rioja.*

<sup>2</sup>*Editor-in-Chief of Cuadernos de Investigación Geográfica 2025*  
*Universidad de La Rioja.*

<sup>3</sup>*Editor-in-Chief of Cuadernos de Investigación Geográfica 1975-1987*  
*Instituto Pirenaico de Ecología (CSIC Alumni).*

<sup>4</sup>*Servicio de Publicaciones, Universidad de la Rioja.*

In 2024, *Cuadernos de Investigación Geográfica* celebrated its 50th anniversary. The journal began as a multidisciplinary publication, featuring both geographical and historically oriented articles. In fact, during its initial issues (numbers 1 to 5), the title was *Cuadernos de Investigación (Geografía e Historia)*. This editorial initiative emerged from the academic ambitions of a small group of young university professors who were teaching at the Colegio Universitario de La Rioja, an institution that was also in its early stages of development at the time. The journal was initially conceived as a platform to disseminate the research activities carried out in this institution. Additionally, it welcomed contributions from scholars affiliated with nearby universities, particularly the University of Zaragoza. *Cuadernos de Investigación (Geografía e Historia)* also disseminated the findings of undergraduate dissertations and doctoral theses that were stated to be supervised at the Colegio Universitario de La Rioja. As such, the journal could be characterized as departmental in nature, driven by local and regional scholarly output. This profile was consistent with that of many Geography and History journals published by Spanish universities during that period: departmental publications created by and for departmental scholars.

In 1980, with issue number 6, *Cuadernos de Investigación (Geografía e Historia)* gave way to the current *Cuadernos de Investigación Geográfica*, reflecting the need to provide to geographical research its own distinct space. At that time, the journal's editorial line focused on publications dedicated to physical geography and environmental sciences, while also accepting contributions from human geography and social sciences, where human–environment interactions give rise to dynamic and evolving landscapes and spaces. Topics such as spatial planning and the application of advanced geographic methods and techniques also found a place within the journal's scope.

The early issues of *Cuadernos de Investigación Geográfica* were not significantly different from those of its predecessor. They included contributions from the professors of Geography at the Colegio Universitario de La Rioja, researchers from the Instituto Pirenaico de Ecología (CSIC), and scholars from the University of Zaragoza and the University of the Basque Country. The journal also facilitated the publication of initial research by a group of young geographers who were at the time developing their doctoral theses and beginning their careers in geographic science. The journal soon attracted attention among Spanish geographers, leading to the publication of articles by authors from a wide range of academic institutions.

In 1992, the University of La Rioja was created, and from that point onward, it assumed the responsibility for the funding and publication of *Cuadernos de Investigación Geográfica*. The editorial team began to consider the idea that the journal needed to make a qualitative leap in order to broaden its reach beyond national boundaries and attract international contributors. This objective is illustrated in Figure 1, which shows that while over more than 90% of first authors were affiliated with Spanish institutions between 1975 and 1984, international participation rose to nearly 50% during the period 2015–2024. The journal's internationalization strategy was further supported by the addition of the English-language title *Geographical Research Letters* in 2018, as well as by the publication of articles in English. These initiatives aimed to expand readership and enhance the journal's global impact. This trend is illustrated in Figure 2. Whereas 100% of the articles were originally published in Spanish at the journal's inception, this figure has declined to barely 20%, with the majority of articles now being published in English.

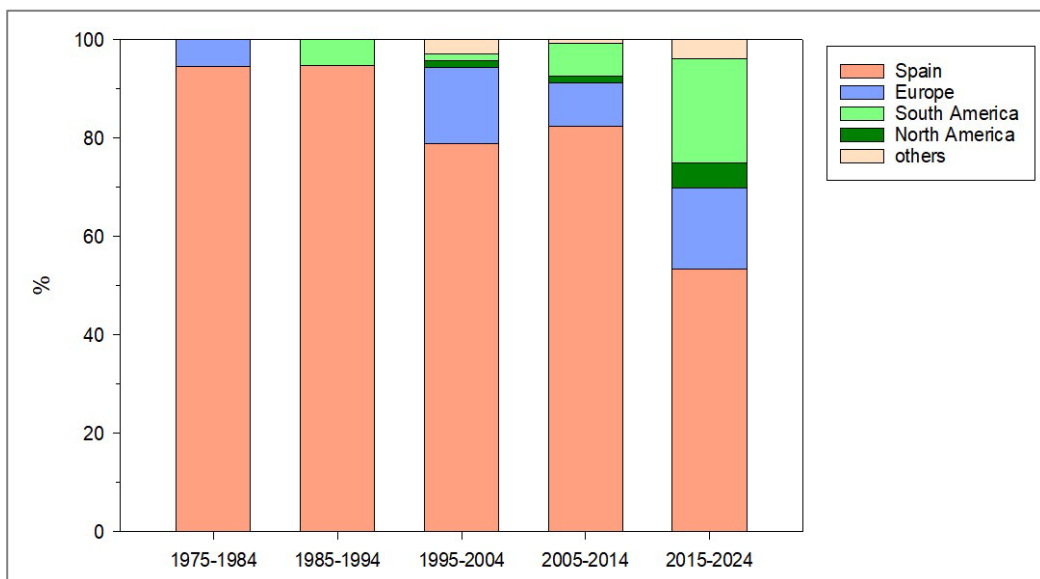


Figure 1. Geographical origin of the first author.

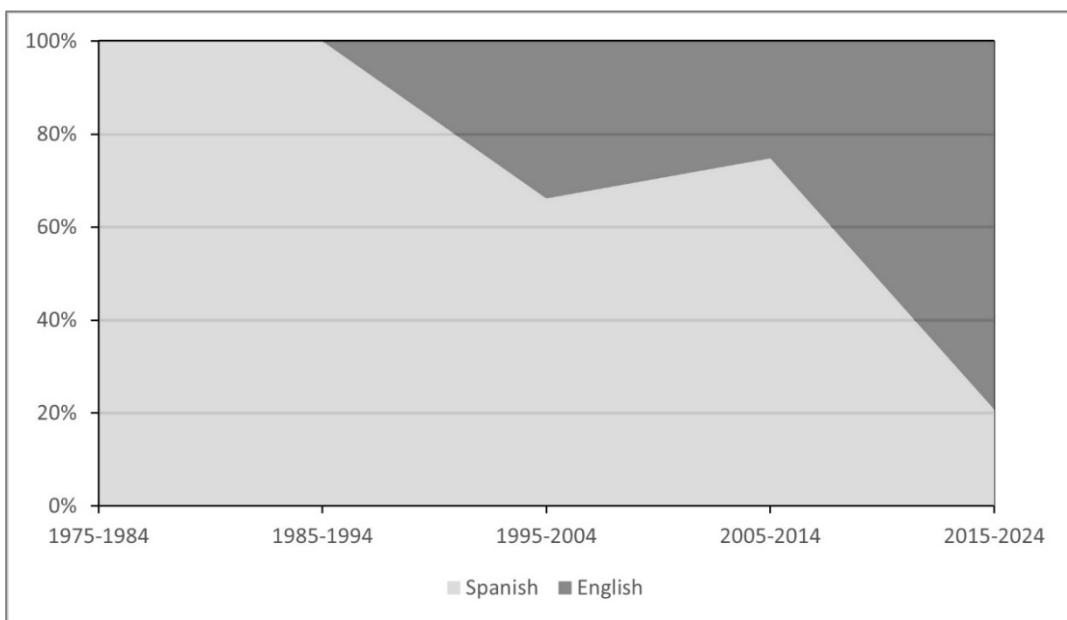


Figure 2. Contribution of articles written in English.

A further development in the journal's history was the increase in the number of annual issues. Until 2009, only one issue was published per year. From that year onward, the annual volume was divided into two issues, thereby enabling the publication of special thematic issues on topics of particular relevance.

As previously noted, since the journal's beginning, the journal's successive editorial teams have consistently shown a strong commitment to ensuring the widest possible dissemination of the work published in its pages. This requires undertaking the challenge of establishing the conditions for the journal to be included in the leading scientific databases —a goal that has been achieved progressively, though with steady determination. *Cuadernos de Investigación Geográfica* was indexed in the Scimago Journal & Country Rank (SJR) (<https://www.scimagojr.com>) in 2009, reaching the first-quartile in the categories of Earth and Planetary Sciences, Environmental Science, and Geography, Planning and Development in 2017 and 2018, and consistently maintaining a second-quartile position across most of the database's annual series. Another significant milestone in the journal's trajectory was the awarding of the Sello de Calidad de Revistas Científicas Españolas in 2016, a distinction granted by FECYT (Spanish Foundation for Science and Technology), which certifies those Spanish journals that meet the highest editorial and scientific quality standards. In *Cuadernos de Investigación Geográfica* was additionally indexed in Scopus (Elsevier) ([www.scopus.com](http://www.scopus.com)), achieving first-quartile rankings in the category of Geography, Planning and Development between 2016 and 2022, and in Environmental Science between 2017 and 2021. Since 2020, the journal has also been indexed in the Web of Science (Clarivate Analytics) ([www.webofscience.com](http://www.webofscience.com)), where it is evaluated within the Physical Geography category of the Journal Citation Reports (JCR).

An analysis of the more than 500 articles published throughout the journal's history reveals that 48% are devoted to topics related to geomorphology, with particular emphasis on glacial processes and soil erosion. Climatology and climate change account for 11%, while studies on climate-related hazards—especially floods and wildfires—represent 10%. Less frequent topics include biogeography (4.5%) and hydrology (4.5%). Contributions within the field of Human Geography constitute 5.8% of the total, with rural spaces being the most commonly addressed.

Over the past 50 years, *Cuadernos de Investigación Geográfica* has both reflected and contributed to the evolution of Geography, particularly within the Spanish context. Certain topics have been progressively abandoned, as researchers have shifted their focus toward more multidisciplinary subjects or those more closely aligned with prevailing social and scientific concerns: environmental impacts, natural hazards, and climate change (Figure 3). On the other hand, no editor overlooks that the present and future of scientific journals in the field of Geography necessarily depend on maximizing their international presence, reinforced by strategic positioning in key databases and an increase in the number of citations of their articles. Undoubtedly, in the short term, these requirements will be highly selective concerning Spanish Geography journals, and the authors of this Editorial Note hope and wish that *Cuadernos de Investigación Geográfica* continues to be among the most highly considered in the field.

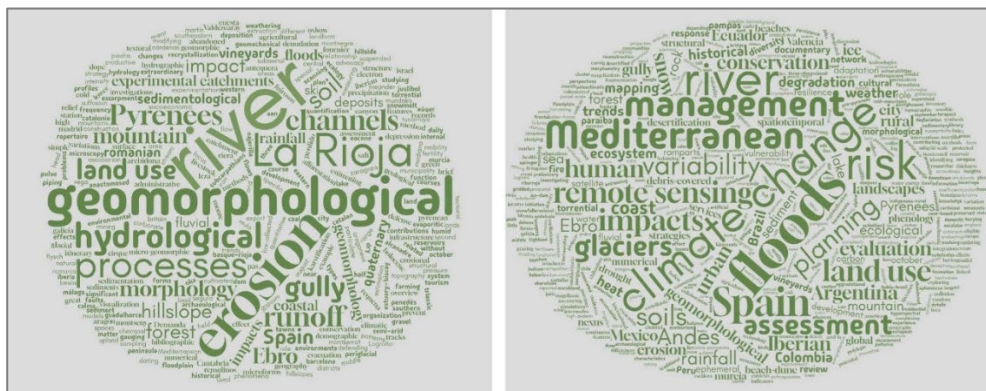


*Figure 3. Word cloud of article titles between 1980 and 1984 (left), and 2020 and 2024 (right).*

We cannot conclude this text without expressing our sincere acknowledgement to all those who have contributed—and continue to contribute—to the progress of the journal. This gratitude extends to the authors who have placed their trust in our editorial product, to the reviewers who ensure the journal's quality by providing expert guidance, and to the various editorial teams, including both the editors and the members of the editorial board. Without their dedication, this project would not have reached its 50th anniversary.



# SNOW COVER VARIABILITY IN THE CANTABRIAN MOUNTAINS (SPAIN): A WATERSHED-LEVEL STUDY USING SATELLITE RECORDS (2000–2024)

ADRIÁN MELÓN-NAVA\* , AMELIA GÓMEZ-VILLAR

<sup>1</sup>*Departamento de Geografía y Geología, Universidad de León,  
Campus de Vegazana, s/n, 24071 León, Spain.*

**ABSTRACT.** This study presents an analysis of the main snow cover dynamics in the Cantabrian Mountains (northern Spain) using satellite imagery, examining the snow cover dates of appearance and melting, extent, duration and persistence. The study area comprises 36 hydrographic watersheds. Using Google Earth Engine (GEE), 14,082 satellite images (2000–2024) from MODIS-Terra, Landsat 5–8, and Sentinel-2 were analysed to create daily snow cover classifications. Seasonal series of Snow Cover Fraction (SCF) were extracted by 500-meter elevation intervals in each watershed and analyzed to extract indicators and trends.

Results reveal reductions in snow cover extent. In autumn, it is reduced at ~2%/decade above 1,500 m. Notable and significant negative trends (~10% and up to -16%/decade in some basins) were detected in winter, particularly on the southern slopes of the Cantabrian Mountains. In spring, most basins show negligible and homogeneous trends among watersheds, except above 2,000 m, where pronounced reductions in extent (2.5% per decade) are observed. A shortening snow season is detected, caused by earlier occurrences of the Last Ephemeral Snow Day (LESD), occurring 2.7 days by decade earlier vs 0.4 days by decade earlier in case of the First Ephemeral Snow Day (FESD). The duration of the first snow cover of the season decreased noticeably above 1,500 m (9 days/decade). Peak seasonal snow cover extent tends to occur slightly later, and above 2,000 m. These events are markedly shorter due to a delay in the Snow Onset Day (SOD) and earlier Snow Melt Out Day (SMOD). The maximum SCF occurs between January 22nd and February 5th, depending on altitude, and is shifting earlier, especially at lower elevations. The mean snow cover duration is 16.4 days, with notable altitudinal variability (6.6 days at 500–1000 m and 38.5 days above 2,000 m), decreasing by 1 day/decade, with reductions up to 5.8 days/decade above 2,000 m, where the duration of the longest snow cover has decreased 8 days/decade. Snow cover persistence has declined by 1.2%/decade, with sharper reductions (3.4%) above 1,500 m.

Despite biases from prolonged periods of cloud cover, dense canopy cover in some watersheds or the occurrence of rapid snow accumulation and melting events undetected by the satellites, findings ultimately reveal decreases in the duration, extent and persistence of snow cover since the early 21st century, although some of these are not statistically significant. These results highlight shifts in seasonal snow cycles, emphasizing the need for further research with longer time series and alternative observational datasets.

## *Variabilidad de las cubiertas de nieve en la Cordillera Cantábrica (norte de España): un estudio a nivel de cuencas a partir de registros satelitales (2000–2024)*

**RESUMEN.** Este estudio analiza la dinámica de la cubierta de nieve en la Cordillera Cantábrica (norte de España), mediante imágenes satelitales, evaluando las fechas de aparición y fusión, extensión, duración y permanencia del manto nival. El área de estudio comprende 36 cuencas hidrográficas. Utilizando *Google Earth Engine*, se analizaron 14.082 imágenes satelitales (2000–2024) de MODIS-Terra, Landsat 5–8 y Sentinel-2 para crear clasificaciones diarias de la cubierta de nieve. Se extrajeron series temporales de la Fracción de Cubierta Nival (SCF) en intervalos de 500 metros de altitud en cada cuenca y se analizaron indicadores y tendencias.

Los resultados revelan reducciones en la extensión de la cubierta de nieve. En otoño, la extensión se reduce un 2%/década por encima de los 1.500 m. Se detectaron tendencias negativas notables, de hasta 16%/década en algunas cuencas en invierno, particularmente en la vertiente sur. En primavera, la tendencia es homogénea y estable (con algunas excepciones), aunque por encima de los 2.000 m, la extensión disminuye un 2,5%/década. La temporada de

nieve se acorta por la ocurrencia más temprana de la Fecha de Última Fusión de Nieve Efímera (LESD), que avanza a 2,7 días/década frente al adelanto de 0,4 días/década de la Fecha de Primera Cubierta Nival Efímera (FESD). La duración de la primera cubierta de nieve de la temporada disminuyó por encima de los 1.500 m (9 días/década). El máximo estacional de la extensión de cubiertas de nieve tiende a ocurrir más tarde, y por encima de los 2.000 m es de menor duración debido a un retraso en el día de inicio de la cubierta de nieve más larga (SOD) y a una fusión más temprana de la cubierta de nieve más larga (SMOD). La máxima SCF ocurre entre el 22 de enero y el 5 de febrero, dependiendo de la altitud, y tiende a adelantarse, especialmente en altitudes más bajas. La duración media de las cubiertas de nieve es de 16,4 días, con gran variabilidad altitudinal (6,6 días en 500–1.000 m y 38,5 días por encima de 2.000 m), disminuyendo 1 día/década, con reducciones de hasta 5,8 días/década por encima de los 2.000 m, donde la duración de la cobertura nival más larga ha disminuido 8 días/década. La permanencia de la cubierta de nieve ha disminuido un 1,2%/década (un 3,4% por encima de los 1.500 m).

Aunque existen algunos sesgos, como períodos prolongados de nubosidad, alta cobertura forestal en algunas cuencas o la ocurrencia de eventos rápidos de acumulación y derretimiento de nieve no detectados por los satélites, los resultados revelan disminuciones en la duración, extensión y permanencia de la cubierta de nieve desde principios del s. XXI (aunque algunas no son estadísticamente significativas), particularmente por encima de los 1.500 m. Los cambios en los ciclos estacionales de la nieve en la Cordillera Cantábrica subrayan la necesidad de realizar investigaciones adicionales utilizando series temporales más largas u otros datos observacionales.

**Keywords:** Snow, Snow Variability, Trend, Cantabrian Mountains, Watershed.

**Palabras clave:** nieve, variabilidad de la nieve, tendencia, Cordillera Cantábrica, cuencas hidrográficas.

**\*Corresponding author:** Adrián Melón-Nava, Departamento de Geografía y Geología, Universidad de León, Campus de Vegazana s/n, 24071, León (Spain). E-mail address: amelon@unileon.es

Received: 10/02/2025

Accepted: 10/07/2025

## 1. Introduction

Snow cover plays a crucial role in the Earth's energy balance due to its high reflectivity (albedo) (Meng, 2017). It also plays a key role in the hydrological cycle of mountain regions, as it leads to the accumulation of snowpacks that function as natural reservoirs, regulating water availability for human consumption, agriculture, and hydroelectric power generation (Bormann *et al.*, 2018; Gascoin *et al.*, 2015). Snow can also pose significant natural hazards, such as avalanches or landslides (Beato Bergua *et al.*, 2019; García-Hernández and López-Moreno, 2024; Santos González *et al.*, 2010) and rain-on-snow flooding events (Corripio and López-Moreno, 2017; Morán-Tejeda *et al.*, 2019). The study of snow cover variability is essential for understanding climatic patterns and their implications on ecosystems, water resources, and socio-economic activities (Notarnicola, 2020; Zhong *et al.*, 2021).

Snow cover variability refers to the seasonal cycle of snow presence on the surface, including key metrics such as the timing of the first snowfall, duration of snow cover, peak snow accumulation, and the final melt-out date (Zhong *et al.*, 2021). It is influenced by multiple climatic and environmental factors, including temperature fluctuations, precipitation regimes, topographic characteristics, and vegetation cover (Notarnicola, 2020). These effects are particularly relevant in mid-latitude mountain ranges such as the Cantabrian Mountains, where interannual variability in snowfall directly influences water availability, vegetation dynamics, and geomorphological processes (López-Moreno *et al.*, 2020). Changes in snow persistence and seasonality affect plant phenology in alpine ecosystems in the Cantabrian Mountains (Espinosa del Alba *et al.*, 2025; Illa *et al.*, 2022) and impact winter tourism and ski resorts (Pisabarro, 2020). Given the increasing vulnerability of mountain environments to climate change, it is crucial to quantify changes in snow cover trends and their underlying drivers (Notarnicola, 2020; Ye *et al.*, 2015).

The Cantabrian Mountains, located in northern Spain, exhibit a transitional climate between oceanic and Mediterranean influences, leading to high interannual variability in snow cover duration and extent (Ortega Villazán and Morales Rodríguez, 2015). Recent satellite observations indicate significant reductions in snow cover extent and duration (Melón-Nava, 2024). Similar trends have been reported in other European mountain ranges, such as the Pyrenees, where winter snowfall are expected to decrease by up to 29% at lower elevations under Representative Concentration Pathway (RCP) 8.5 scenarios (Bonsoms *et al.*, 2025), and the Alps, where snow cover duration has shortened by 5–7 days per decade since the 1960s (Monteiro and Morin, 2023). On a global scale, satellite records have identified a 5.12% reduction in snow cover (Young, 2023) and decreases of the snow cover extent in all seasons in the Northern Hemisphere since 1975 (Hori *et al.*, 2017). These trends highlight the widespread impact of climate change on mountain cryosphere (Notarnicola, 2024).

Remote sensing is a useful technique in snow cover monitoring, allowing for large-scale analysis with high temporal and spatial resolution. The Normalized Difference Snow Index (NDSI) is widely used to differentiate snow from other land covers (Hall *et al.*, 1995), despite limitations related to cloud cover (Gascoin *et al.*, 2015; Tiede *et al.*, 2021) and forested areas (Gascoin *et al.*, 2024). The MODIS instrument, operational since 2000, provides daily observations with a 500-meter spatial resolution, enabling long-term monitoring of snow variability (Notarnicola, 2024). Additionally, the integration of Landsat and Sentinel-2 imagery has allowed for higher spatial resolution assessments (Zhang and Jiang, 2022). These methodologies have been applied in mountainous regions worldwide such as the Pyrenees (Barrou Dumont *et al.*, 2024; Gascoin *et al.*, 2015) the Alps (Orusa *et al.*, 2023) and the Himalayas (Sasaki *et al.*, 2024).

Cloud-based geospatial analysis platforms, such as GEE, have further enhanced snow studies by facilitating rapid processing of extensive datasets (Gorelick *et al.*, 2017). Several studies have employed Google Earth Engine to analyze snow cover variability across different mountain regions, revealing significant trends in snow variability. Notarnicola (2020) documented hotspots of declining snow persistence in the European Alps, attributing these changes to increasing winter temperatures. In the Himalayas, Sasaki *et al.* (2024) applied machine learning techniques within GEE to map snowline altitudes, observing a general upward shift due to climate warming. Tang *et al.* (2022) assessed snow variability in high mountains in Asia, highlighting regional differences in snow seasonality driven by synoptic weather patterns. Gascoin *et al.* (2015) studied the Pyrenees and confirmed a steady decrease in snow cover extent using MODIS and Landsat imagery. López-Moreno *et al.* (2020) focused on the Iberian Peninsula, where they detected significant reductions in snow duration above 2,000 m. Malnes *et al.* (2016) examined snow season variability in boreal-Arctic transition areas, revealing strong latitudinal gradients in snow persistence. Finally, Ye *et al.* (2015) analyzed interdecadal changes in Eurasia, concluding that atmospheric circulation shifts were a major driver of snow cover trends.

This study is the first to analyse seasonal snow cover dynamics in the Cantabrian Mountains at the scale of hydrographic watersheds. Using MODIS, Landsat 5–8, and Sentinel-2 data (2000–2024), it examines trends in snow cover extent, duration and persistence across 36 hydrographic watersheds, assess variations in key snow variability indicators, and identify differences between elevation bands. By leveraging satellite-based analyses and cloud-computing tools, this research provides a detailed evaluation of snow cover metrics and changes in the Cantabrian Mountains watersheds.

## 2. Study area

The Cantabrian Mountains are located in the north of Iberian Peninsula, in southwestern Europe (Fig.1). Its highest peak is Torre Cerredo, located in the Picos de Europa National Park, at 2,650 m. The range extends longitudinally, with its ridges reaching approximately 2,000 m in the main massifs, which stretch over 300 km, from the Sierra de Ancares (in the provinces of Lugo and León), with Alto de Cuiña (1,992 m) standing out, to the sector of the Sierra de Peña Labra Massif, where Pico Valdecebollas

reaches 2,143 m in the province of Palencia, near the border with Cantabria. A few dozen kilometers further east, the Montes de Valnera (1,717 m) is located, straddling Burgos and Cantabria. Although at a lower altitude, this area receives important snowfall and it marks the easternmost extent of the study. The study area covers 16,263 km<sup>2</sup>, divided into 36 hydrographic watersheds, covering four water agencies (C.H. in Spanish): C.H. Cantábrico (northern part of the study area), C.H. Duero (southern part), C.H. Ebro (eastern part), C.H. Miño-Sil (western part).

Snow cover distribution in the Cantabrian Mountains is highly variable, particularly during melting periods, due to the region's transitional climate between oceanic and Mediterranean climate influences, with a continentalized nuance. A distinct contrast exists between the northern and southern slopes (Ortega Villazán and Morales Rodríguez, 2015), where watershed divides act as both a natural barrier and a transitional zone. The northern slopes, under a strong oceanic influence, experience milder annual average temperatures (7.5°C to 12°C), consistent precipitation (up to 1,800 mm annually), and frequent cloud cover. In contrast, the southern slopes exhibit greater thermal variability, with larger daily and seasonal temperature oscillations, resulting in colder winters and hotter summers, lower annual precipitation (around 800 mm) and annual average temperatures ranging from 2.5°C to 10°C (Aemet, 2018).

Although snowfall events generally bring lower snow levels to the northern slopes, with a decreasing trend toward the east, snow persistence is shaped by multiple factors, including altitude, humidity, temperature, wind-driven accumulation, and solar radiation. The Cantabrian Mountains receive the highest winter precipitation in the Iberian Peninsula, averaging 506 mm (Hidalgo-Hidalgo *et al.*, 2024). Above 1,500 m, winters are harsh throughout the region, with frequent frosts and snowfall, often intensified by strong windstorms. Notably, occasional southerly wind events can cause sudden temperature spikes above 20°C in northern valleys due to a pronounced Foehn effect.

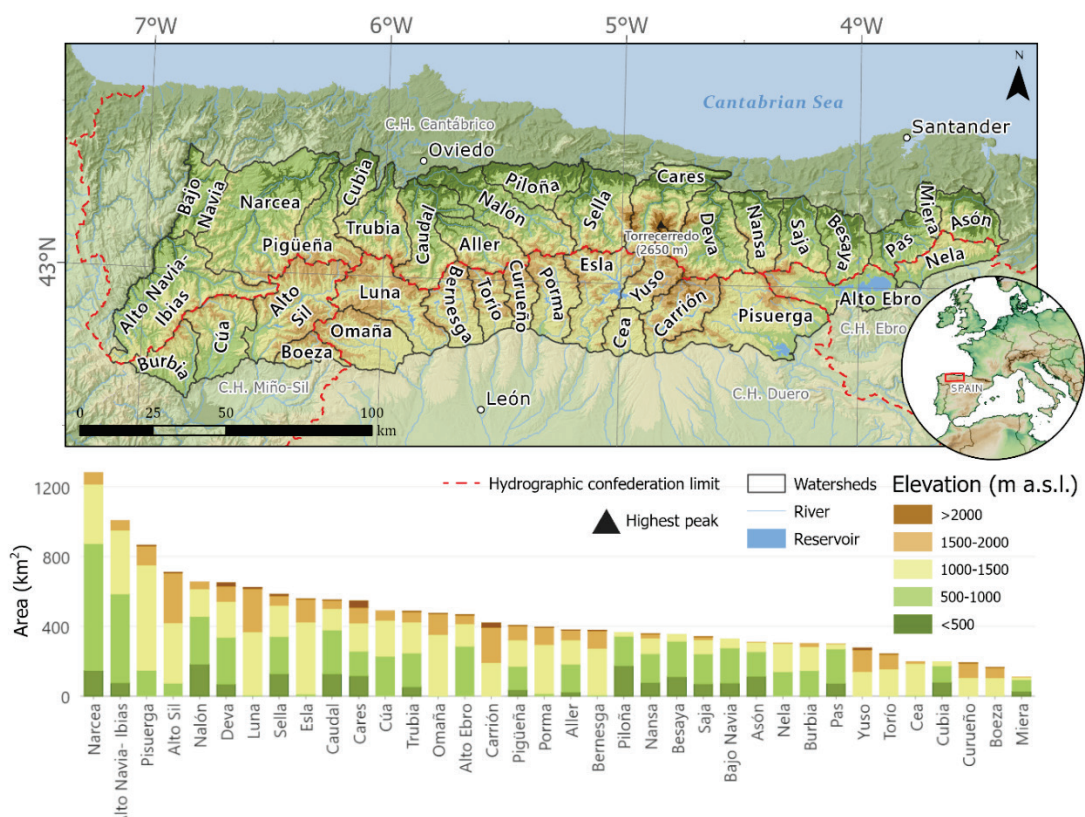


*Figure 1. Cantabrian Mountains watersheds map and hypsometric distribution of the 36 watersheds in 500 m interval elevation bands.*

### 3. Data and methodology

#### 3.1. Data

A multi-sensor daily snow cover dataset was generated to analyse snow dynamics in the Cantabrian Mountains. Satellite images from MODIS-Terra, Landsat 5–8, and Sentinel-2 were processed using Google Earth Engine to generate daily time series of snow cover for the period 2000–2024. This was achieved through the methodology detailed in Melón-Nava (2024). MODIS imagery provides continuous daily observations, ensuring baseline temporal coverage throughout the study period. Landsat 5–8 and Sentinel-2 offer higher spatial detail, but with longer revisit intervals. To maximise spatial detail while maintaining temporal continuity, the highest-resolution image available was selected for each day when possible. The Normalized Difference Snow Index (NDSI),  $NDSI = \frac{Green\ band - SWIR\ band}{Green\ band + SWIR\ band}$ , effectively distinguishes snow from other surfaces like vegetation, soil, and water due to this spectral contrast. It also separates snow from clouds, as clouds exhibit high reflectance in both the visible and SWIR ranges, unlike snow. NDSI values range from -1 to 1, with values greater than 0.4 typically indicating snow, providing a robust threshold for classification according to Hall *et al.* (1995) and Hall and Riggs (2010). For snow-cover classification using MODIS, the ‘NDSI\_Snow\_cover’ band was converted to Fractional Snow Cover (FSC) following the approach of Rittger *et al.* (2013) and Salomonson and Appel (2004).

$$FSC = -0.01 + 1.45 \times NDSI$$

Pixels with  $FSC > 0.15$  were classified as snow-covered, representing both partially and fully snow-covered areas, based on the threshold estimations in the Picos de Europa region by Revuelto *et al.* (2021).

The spatial resolution varies depending on the band resolution of each satellite, ranging from 500 m for the MODIS sensor on the Terra satellite, to 30 meters with Landsat, or 20 meters with Sentinel-2. The main limitations include cloud presence, topographic shadows, and underestimation of snow cover in forested areas where snow remains on the ground but not on the top of tree canopies or shrubs. To ensure data quality, the presence of clouds was assessed independently for each satellite image and at the watershed level. For each image and date, the proportion of cloud-covered area was calculated for each watershed based on the available cloud information for each sensor. Watersheds with more than 50% cloud cover on a given date were excluded from the analysis for that date. This procedure ensured that the snow cover time series was based only on valid and reliable observations for each watershed. This approach prevents the total cloud cover filtering of the image, as it was found that, on many occasions, some watersheds were entirely covered by clouds while others had very low cloud cover, allowing for the use of information from the latter. Overestimations of snow cover extent were found in cases where fog coincided with areas not covered by snow, leading to high SCF values. These days have been manually evaluated to determine whether they truly represent the actual snow extent situation. Masking is applied to pixels occupied by clouds, water bodies (rivers and reservoirs) and topographical shadows. In all images, areas corresponding to the main watersheds of the study area, as well as cloud cover and topographic shadows were masked.

The hydrographic watersheds of the Cantabrian Mountains were delineated, resulting in a division into 36 basins. This delineation was based on cartographic data of hydrographic watersheds boundaries. The delineation process was guided by the *Atlas of Spanish Landscapes* (Mata Olmo and Sanz Herráiz, 2003). For the western limit, in the Navia River watershed, the Navia river was used as the boundary, considering only its right side.

An ImageCollection was created in Google Earth Engine to aggregate 24 seasons, from 2000–2001 to 2023–2024. Each season begins on September 1<sup>st</sup> and ends on August 31<sup>st</sup> of the following year. This was accomplished using a hierarchical method for each day (Fig.2), prioritising satellite images with the highest spatial resolution (Sentinel-2 > Landsat 5–8 > MODIS).

A total of 14,082 images were used since 2000 September 1<sup>st</sup> to 2024 August 31<sup>st</sup>, with 5,193 images from MODIS (daily images from 2000-2024), 520 images from Landsat-5 images (2000-2012), 1,194 images from Landsat-8 images (2013-2024) and 7,175 images from Sentinel-2 (2015-2024). On average, 216 days per year (59.1%) were valid for the study, as they had cloud cover below 80% (Image filtering).

The following stage focuses on filling data gaps at the pixel level, caused by consecutive days of cloud cover obscuring satellite observations. To mitigate this, a temporal gap-filling algorithm is applied, using linear interpolation of snow cover (or absence) between the last valid observation before the cloud period and the first after it. This method, based on Sproles *et al.* (2018) and adapted to the Cantabrian Mountains' conditions, is constrained to a maximum gap of 5 consecutive days, which helps reduce missing values in areas with ephemeral cloud cover. This threshold is consistent with the average cloud persistence in the region (3.3 days on average) (Melón-Nava, 2024). Gap-filling is performed under specific rules: if both pre- and post-cloud observations indicate snow cover or snow-free conditions, the missing days are classified accordingly. For transitions, linear interpolation of NDSI values determines the presence or absence of snow. Therefore, only snow covers recorded during cloud-free periods are analyzed. Rapid snow accumulation and melting events under cloudy conditions are undetected by the satellites, so are not recorded.

The following phase involves creating a daily mosaic that prioritizes the available satellite image for that day with the highest spatial resolution, so Sentinel-2 images are prioritized over Landsat, and both are prioritized over MODIS-Terra. In this way, the snow cover classification with the highest possible resolution is obtained for each day. Following this, the Snow Cover Fraction is calculated, which will serve as the basis for calculating the other snow variability indicators.

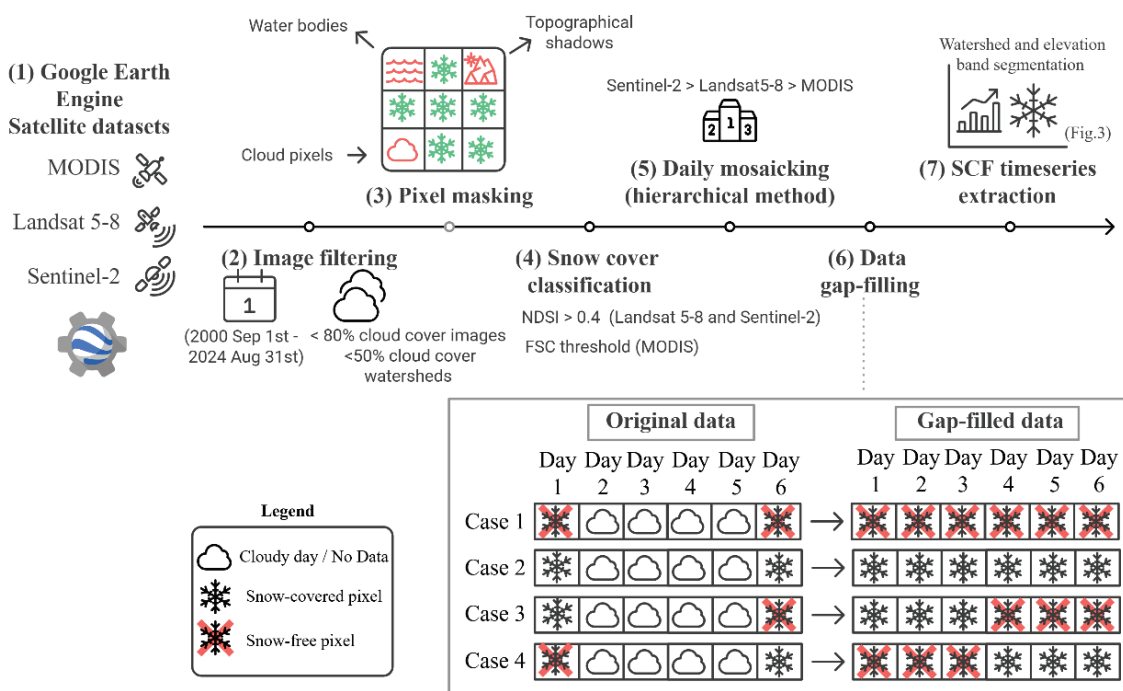


Figure 2. Workflow for obtaining time series of SCF in Google Earth Engine from satellite images. The gap-filling example shows a data gap of 4 days.

### 3.2. Methodology: Extraction of metrics to assess the seasonal variability of snow cover

Once the daily snow cover image collection is created from the available satellite images, the next step involves generating time series of Snow Cover Fraction (SCF) (Fig. 3), which quantifies the proportion of an area covered by snow in comparison to the total visible area (cloud-free) for a given day. Seasons are defined from September 1<sup>st</sup> to August 31<sup>st</sup> across the 36 delineated hydrographic watersheds, segmented into 500-meter elevation bands (<500 m, 500–1000 m, 1000–1500 m, 1500–2000 m, >2000 m). These thresholds were chosen following previous studies in the region (Melón-Nava, 2024) to enable consistent comparisons. SCF is calculated for the whole perimeter of the Cantabrian Mountains, for the watersheds and for all the elevation bands.

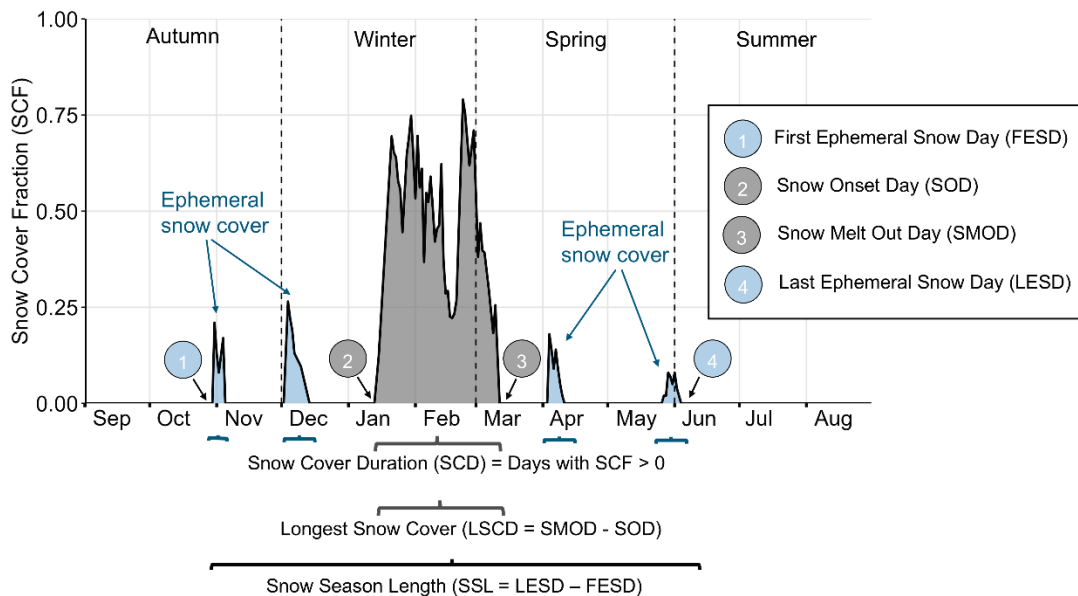


Figure 3. Example of the calculation of snow cover variability metrics for a fictional SCF season.

This process theoretically yields 4,320 time series (24 years × 36 basins × 5 altitudinal ranges), representing the maximum number of possible combinations if all basins included all five altitudinal ranges. However, not all basins cover every altitudinal range due to the watersheds' topographical characteristics. Thus, a total of 3,432 time series have been analysed (24 years × 143 unique altitudinal ranges across the 36 basins). These allow for comparisons between basins, altitudes, and seasons, as well as the extraction of trends using the Sen's slope over the 24-year satellite image record. To assess the statistical significance of these trends, we also applied the Mann-Kendall test. Trends with  $p$ -values below 0.05 were considered statistically significant. All analyses were conducted independently for each combination of watershed and altitudinal range.

The analysis was structured into four groups of variables, based on their typology. Firstly, the extent of snow cover was calculated by season of the year: autumn (September-October-November, or S-O-N), winter (December-January-February, or D-J-F) and spring (March-April-May, or M-A-M). Subsequently, an analysis was conducted on the dates of the first (FESD) and last ephemeral snow cover (LESD), as well as the duration of the first snow cover throughout the seasons (Mean FESD Duration). These variables represent the temporal extremes of each season and help define the potential snow cover period in each area. (Table 1).

Then, variables related to the longest-lasting snow cover of each season were examined. This includes measuring the date when the longest snow cover appears (SOD) and melts (SMOD), as well as the date of the most extensive snow cover (Max SCF Day). These variables provide an indication of the most stable and notable snow covers occurring each season in each location.

*Table 1. Description of the variables extracted from SCF time series to define the variability of each snow cover season.*

ACRONYM	SNOW METRIC	DESCRIPTION
<b>SCF</b>	Snow Cover Fraction	Fraction of the study area covered by snow: 1 represents total snow cover, and 0 means no snow cover.
<b>SCD</b>	Snow Cover Duration	Sum of the days with snow cover greater than 0.05*. Indicates snow frequency throughout the season.
<b>FESD</b>	First Ephemeral Snow Day	First day of the water year (starting from September 1) with detected snow cover ( $SCF > 0.05^*$ ). Calculated by pixel.
<b>LESD</b>	Last Ephemeral Snow Day	Last day of the year (starting from September 1) with detected snow cover ( $SCF > 0.05^*$ ) before total melting. Calculated by pixel.
<b>MEAN FESD DURATION</b>	Mean FESD duration	Duration (in days) of the first ephemeral snow cover detected in the season.
<b>SSL</b>	Snow Season Length	Number of days between the first ephemeral snow day (FESD) and the last ephemeral snow day (LESD). Indicates the absolute dates of the season's first and last snowfall, even if minimal.
<b>SOD</b>	Snow Onset Day	First day (starting from September 1) of the season's Longest Snow Cover Duration (LSCD).
<b>SMOD</b>	Snow Melt Out Day	First snow-free day following the end of the Longest Snow Cover Duration (LSCD) period, starting from September 1.
<b>LSCD</b>	Longest Snow Cover Duration	Longest duration of snow cover during the season. It is calculated as the difference between SMOD and SOD.
<b>RDL (ZHONG ET AL., 2021)</b>	Ratio Duration - Length	Measures the intra-seasonal persistence of snow cover. It is calculated as the ratio of Snow Cover Duration (SCD) to Snow Season Length (SSL). Values close to 1 indicate continuous snow cover during the snow season, whereas lower values indicate intermittent or variable snow cover.
<b>MAX SCF DAY</b>	Day with maximum SCF	Day when the maximum SCF value occurs. If multiple equal maximum values occur (for example, several days with $SCF = 1$ ), the average date is taken.

\*For the study of snow presence in the SCF time series, values greater than 0.05 were used as the error threshold to prevent a single misclassified pixel as snow from producing an erroneous result. Thus, at least 5% of the area (e.g., a watershed elevation band) must be covered by snow to be considered a snow-covered day.

Finally, the last group of variables refers to the duration and persistence of snow cover. This includes measuring the maximum duration of the most persistent snow cover each season (LSCD), calculated from the previously mentioned SOD and SMOD variables. The mean duration of snow covers was also measured, considering each cover as the period of snow presence between two complete melt events. Additionally, the RDL factor (unitless) was calculated as the ratio between Duration and Length, providing an indication of snow cover stability in each location.

## 4. Results

### 4.1. Extent of Snow Cover

The mean SCF values show an uneven distribution throughout the season (Fig. 4). During autumn, snowfall can occur over extensive areas, but snow cover usually persists for only a few days. The mean snow cover extent in autumn is only notable in some years above 1500 m, and even then, the mean snow cover extent in autumn rarely exceeds 25% of the area above 2000 m (Fig. 4). During winter, there is marked interannual variability above 1500 m, with some seasons reaching SCF values close to 1, while others, such as the 2023–2024 season, show mean values near 0.25. In spring, differences

between altitudes above 1500 m and lower elevation bands stand out, with a marked altitudinal gradient. The Yuso (0.17) and Carrión (0.15) watersheds exhibit the highest mean SCF throughout the season, in contrast to the low mean values recorded in the Piloña (0.02) and Cubia (0.02). Moreover, substantial differences are observed across the seasons, with the highest mean SCF values occurring in winter, reaching 0.34 for the Yuso watershed. Noticeable variations are also found between altitudinal bands, with the highest mean SCF values occurring at the uppermost elevations. The >2,000 m bands show consistent values across all watersheds, ranging from 0.08 to 0.15 in autumn, 0.73 to 0.82 in winter, and 0.39 to 0.66 in spring. In spring, larger differences between watersheds emerge, with higher values recorded in the Sella watershed (0.66) (see Appendix 1).

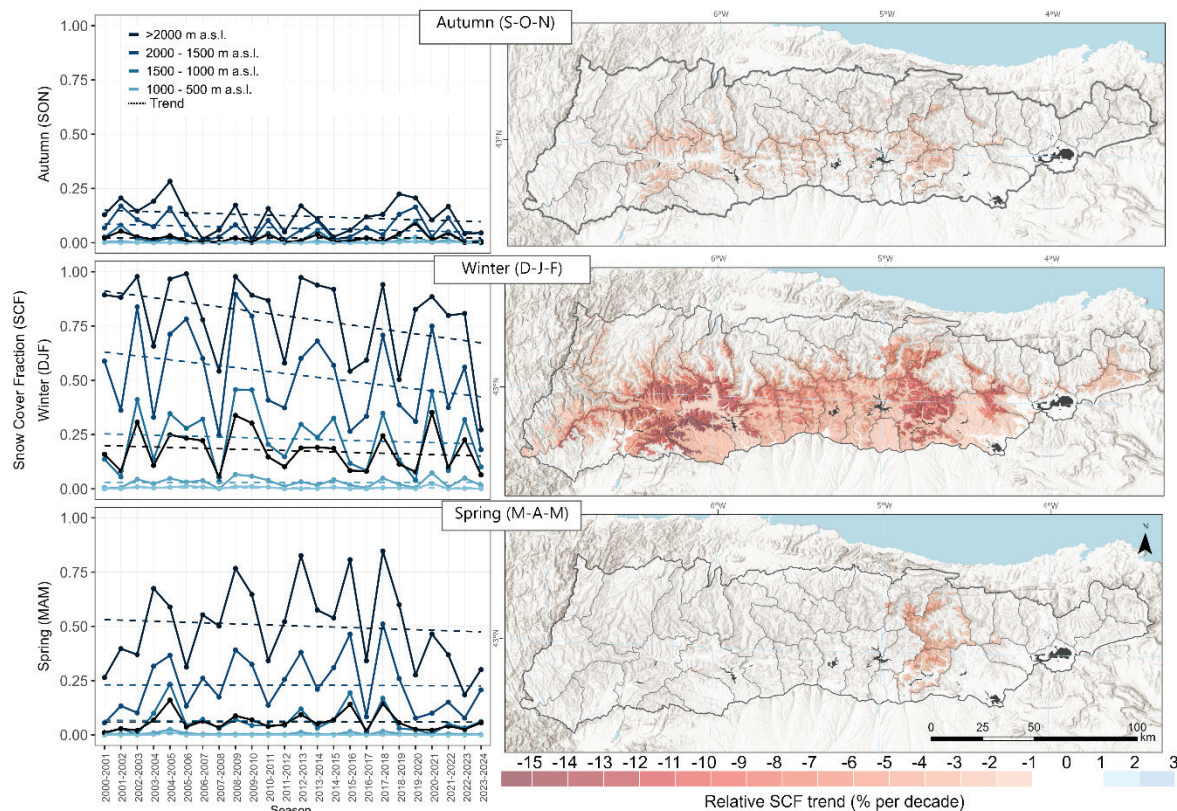


*Figure 4. Timeseries of Snow Cover Fraction evolution (2000-2024) and relative SCF trend map (by watersheds) by season of the year (Autumn, Winter and Spring). Black lines in timeseries represent the whole study area values and trendline.*

The trend of the SCF in autumn (Table 2) is homogeneous at elevations above 1,500 m, with a decrease of around 2% per decade. However, it is during winter, the period of maximum snow accumulation, that the most marked (and statistically significant) reductions in snow cover extent have occurred during the 2000–2024 period. For the entire Cantabrian Mountains, the decrease is 2.08% per decade, but the most substantial declines are observed in areas with higher snow accumulation (>1500 m). These include an 8.95% per decade reduction in the 1500–2000 m range and a 10.4% per decade decrease above 2,000 m. In the 1000–1500 m range, the decline is more moderated at 2% per decade (Table 2). Due to the asymmetry in altitudes between the northern and southern slopes of the range, declines are more pronounced on the southern slope, which has a higher mean elevation. Above 1,500 m, two key areas stand out (Fig. 4): the southwestern region of the study area, particularly Omaña (-16%/decade), Alto Sil (-13.3%/decade) and Luna (-12.6%/decade) watersheds and the eastern massifs, as the Carrión (-12%/decade), Deva (-10.3%/decade) and Saja (-12.3%/decade) watersheds. In spring,

the overall trend for the Cantabrian Mountains remains stable (Table 2), with some exceptions in the Carrión, Deva and Cares watersheds (around -1% to -2% per decade). In areas above 2,000 m, losses exceed 2.4% per decade. In this elevational band, some areas record greater losses, as in the case of Nansa watershed (-7.9% per decade).

*Table 2. SCF mean results and trends by season of the year and elevation bands.*

	Autumn (S-O-N)		Winter (D-J-F)		Spring (M-A-M)	
	Mean SCF	Relative trend (%/decade)	Mean SCF	Relative trend (%/decade)	Mean SCF	Relative trend (%/decade)
<b>Cantabrian Mountains (all altitude ranges)</b>	0.02	0.03	0.18	-2.08*	0.06	-0.01
<b>&gt;2000 m</b>	0.12	-2.32*	0.79	-10.40*	0.50	-2.45
<b>2000 - 1500 m</b>	0.07	-1.63*	0.53	-8.95*	0.23	-0.18
<b>1500 - 1000 m</b>	0.02	0.09	0.23	-2.04*	0.06	-0.37
<b>1000 - 500 m</b>	0.00	-	0.03	0.08	0.01	-0.07

\* Trends statistically significant at the 95% confidence level ( $p < 0.05$ ).

#### 4.2. Snow cover temporal patterns

The temporal pattern of snow cover varies each year depending on when the first snow cover is detected, its duration, the date of final snowmelt and when the longest-lasting snow cover occurs each season. These factors have been measured using several parameters, as detailed in Table 1.

Regarding the temporal extremes of snow seasons, the FESD indicates the timing of the first snow cover each season, as long as it is subsequently detected by satellites. In some years, the FESD date is nearly identical or the same across most elevation bands, particularly if the first snowfall event results in widespread snow across all altitudes. In general, FESD occurs earlier in the western part of the Cantabrian Mountains compared to the eastern region (Fig. 5). Above 1,500 m, FESD tends to occur during the first half of November (November 3rd above 2,000 m and November 10th between 2,000 and 1,500 m). In these higher elevation bands, the first snow cover has occasionally occurred as early as mid-October, as observed during the 2008–2009 season. In the 1,500–1,000 m range, it occurs in the second half of November (November 23rd), while below 1,000 m, it occurs, on average, during the first half of December (December 11th). However, over the 24 years analysed, it has been recorded as early as late November and as late as mid-January (2003–2004 season), reflecting marked interannual variability, particularly in these lower altitudinal bands. FESD tend to occur earlier (-1.66 days/decade above 2,000 m), but later (-6.4 days/decade) below 1,000 m. This indicates that at lower altitudes, the occurrence of the first snowfall events becomes more concentrated, reducing differences between altitudes. However, notable interannual variability prevents these trends from being considered statistically significant at this stage. The earliest FESD are recorded in Cares (>2000 m, October 23rd) and Deva watersheds (>2000 m, October 20th), indicating the first snow occurrence in these high-elevation regions.

The LESD, which marks the last snowmelt date, is heavily influenced by altitude, as well as by other factors such as temperature, solar radiation, topography or presence of liquid precipitation following snowfall events in each watershed. Moreover, LESD values can vary by several weeks each year depending on the persistence of snow cover or the occurrence of an exceptionally early or late final snowfall event of the season. Snowmelt generally follows a gradual progression across elevation bands over time (Fig. 5). LESD first occurs at the lowest elevations, around late February or early March in the 500–1000 m range. It then progresses with a gradual gradient, occurring in late March for the 1000–1500 m range, late April for the 1500–2000 m range, and mid-May for elevations above 2000 m. It is

important to note that these are mean values for altitudinal bands, and at the highest elevations, local topography plays a significant role in the persistence of small snow patches in favourable areas. Therefore, in these specific areas, snow cover duration can extend on average until July (Fig. 5).

Trends for LESD show an earlier melt date in the highest elevation bands (-2.9 days/decade above 2,000 m and 4.4 days/decade between 2000 – 1500 m), while elevations below 1500 m display stable or slightly (~1 day/decade) delayed trends, although with high interannual variability. It is important to note that these parameters do not fully define the overall snow season, as early snowfall or late snowmelt may occur even in seasons with limited snow accumulation.

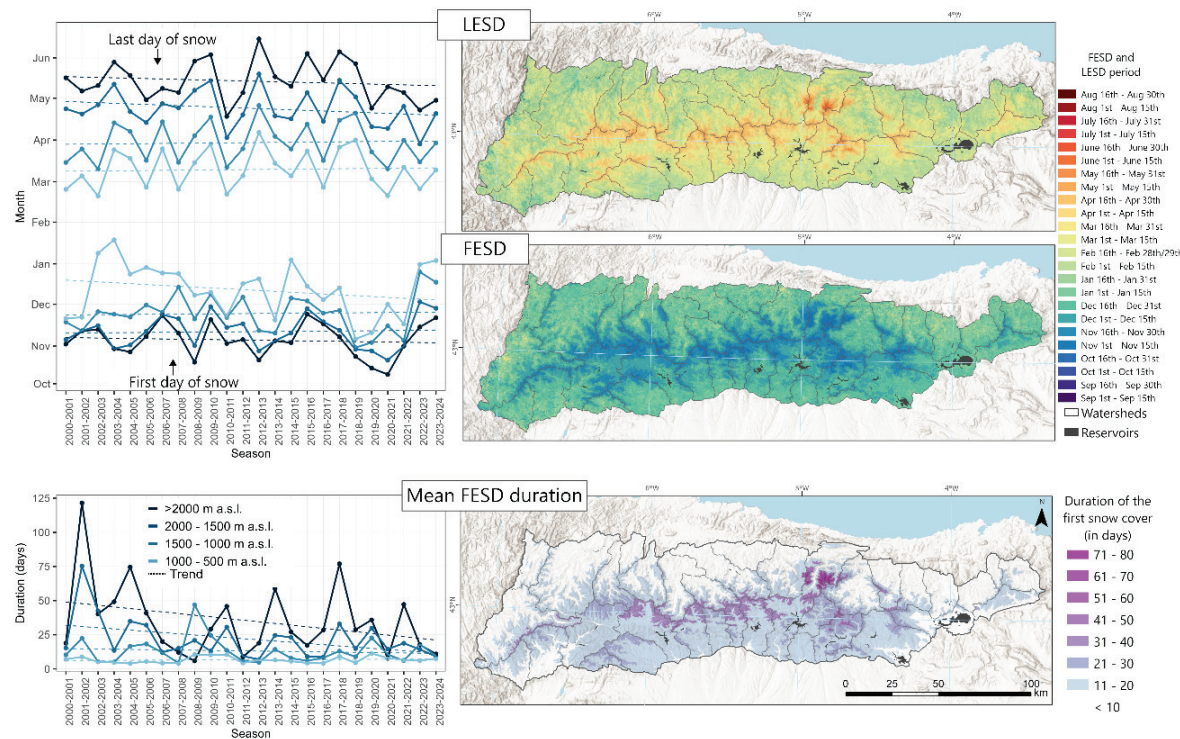


*Figure 5. Timeseries of seasonal FESD, LESD and mean FESD duration (2000-2024) and mean values maps by watersheds.*

Examining the duration of the first snow cover event detected (FESD), there is high variability, with some long-lasting first snow covers and others where it is ephemeral, lasting only a few days, particularly in low-altitude areas (Fig. 5). Mean FESD duration value of 12.8 days is recorded for the whole study area (Table 3), with a progressive increase from 6.7 days in areas below 1,000 m to an average of 35.1 days above 2,000 m. The average durations vary noticeably among watersheds in the different elevation bands, especially above 1,500 meters, where, for example, the Cares records an average of 42.6 days compared to 10.5 days in the Pas watershed in the 1,500-2000 m band (Table 3). Particularly noteworthy is the persistence of the first snow cover in the Picos de Europa (the longest durations are recorded in Cares (>2000 m, 74.8 days) and Deva (>2000 m, 54.2 days). Conversely, the shortest mean durations occur in Bernesga (500-1000 m, 3.5 days) and Luna watersheds (500-1000 m, 4.5 days), reflecting transient snow cover at lower elevations (Appendix 2). Notably, the snowfall of 9–10 November 2001 (Fig. 5) was exceptional for its intensity and extent, covering almost the entire Cantabrian Mountains. That year, FESD values were very similar across all altitudes, and at elevations above 1500 m, this first snow cover turned out to be the most persistent of the season, lasting over 120 days (four months) above 2000 m, despite its early occurrence.

Table 3. Mean FESD, LESD and FESD duration values and trends by altitudinal ranges.

	FESD		LESD		Mean FESD Duration	
	Mean DOY	Trend (days/decade)	Mean DOY	Trend (days/decade)	Duration (in days)	Trend (days/decade)
<b>Cantabrian Mountains (all altitude ranges)</b>	Nov 21 <sup>st</sup>	-0.40	Apr 4 <sup>th</sup>	-2.68	12.80	-3.22
<b>&gt;2000 m</b>	Nov 3 <sup>rd</sup>	-1.66	May 15 <sup>th</sup>	-2.92	35.10	-12.10*
<b>2000 - 1500 m</b>	Nov 10 <sup>th</sup>	0.93	Apr 25 <sup>th</sup>	-4.44	21.70	-8.88*
<b>1500 - 1000 m</b>	Nov 23 <sup>rd</sup>	0.90	Mar 30 <sup>th</sup>	1.10	13.10	-1.54
<b>1000 - 500 m</b>	Dec 11 <sup>th</sup>	-6.41	Mar 10 <sup>th</sup>	1.10	6.94	0.46

\* Trends statistically significant at the 95% confidence level ( $p < 0.05$ ).

There has been a notable decline in the duration of the first snow cover during the 2000–2024 period, with reductions of -12.1 days/decade above 2,000 m and -8.9 days/decade in the 2000 – 1500 m band (statistically significant reductions) and more stable durations below 1500 m ( $\pm 1$  day/decade).

#### 4.3. Longest snow cover of each season

The dominant snow cover episodes of each season (those with the longest duration) has been analysed using the Snow Onset Day (SOD) and Snow Melt Out Day (SMOD) variables. Like LESD and FESD, there is a greater temporal concentration in SOD dates than SMOD dates, as major snowfall events often affect all catchments and elevations, resulting in the longest-lasting snow cover of the season.

The SOD indicates the date when the first day of the longest-lasting snow cover is detected. This tends to occur earlier at higher elevations (Fig. 6), typically around late December for elevations above 1500 m and mid-January for elevations below 1500 m. Earliest SOD are recorded above 2,000 m in Cares and Deva (Nov 25<sup>th</sup>), indicating that the most lasting snow covers of the season result from early snowfall events. While marked altitudinal variability was observed during the 2002–2006 period, from 2006 onwards, there is a noticeable trend towards the concentration of SOD dates across all elevation bands, suggesting that a single important snowfall event often covers all altitudes. However, trends show a delay in SOD (Table 4) at elevations above 1000 m (4.8 days/decade above 2,000 m and 7.2 days/decade between 2,000 – 1,500 m) and an advancement below 1000 m (8.5 days/decade). Interannual variability remains high, depending on when the first major snowfall events occur, with SOD dates ranging from November to February across seasons.

The SMOD date, marking the end of the melt of the longest-lasting snow cover, is also strongly influenced by altitude (Fig. 6), which significantly affects snow cover durability. At lower elevations (below 1500 m), SMOD typically occurs in late January to mid-February (Table 4). For the 1500–2000 m band, it occurs in mid-March, while at elevations above 2000 m, it occurs in early April. Latest SMOD are recorded in Sella (>2,000 m, Apr 30<sup>th</sup>) and Cares (Apr 28<sup>th</sup>), indicating a later snow persistence. Earliest SMOD occur in Bajo Navia (500–1000 m, Jan 9<sup>th</sup>) and Trubia (Jan 12<sup>th</sup>), referring to the fact that the most significant snow covers tend to melt earlier in these areas of the northern slope of the mountain range. Trends reveal earlier occurrence of SMOD dates for the 500–1000 m (7.3 days/decade) and >2000 m bands (3.1 days/decade), whereas a later occurrence is observed between 2000–1500 m (5.2 days/decade) and 1500–1000 m (3 days/decade).

The Max SCF Day shows a strong altitudinal concentration, as it is closely linked to the most significant snowfall event of the season. Max SCF Day typically occurs in late January for elevations below 1500 m and early February for elevations above 2000 m. In this case, the differences between watersheds are not very significant, as the snow cover date tends to be driven by a major snowfall event

affecting all or most of the watersheds. Therefore, little spatial variability is found (Fig. 6), with the earliest values in the 500-1000 m elevation zones of the western watersheds, such as Cúa (Jan 2<sup>nd</sup>), Burbia (Jan 3<sup>rd</sup>), or Alto Navia-Ibias (Jan 5<sup>th</sup>). The latest values occur, on average, only a month later above 2,000 m in some watersheds (Appendix 3). Trends indicate an earlier occurrence of Max SCF Day in all elevation bands, especially in lower altitudes: 3.5 days per decade in 1,500 – 1000 m and 8.2 days per decade below 1000 m (Table 4).

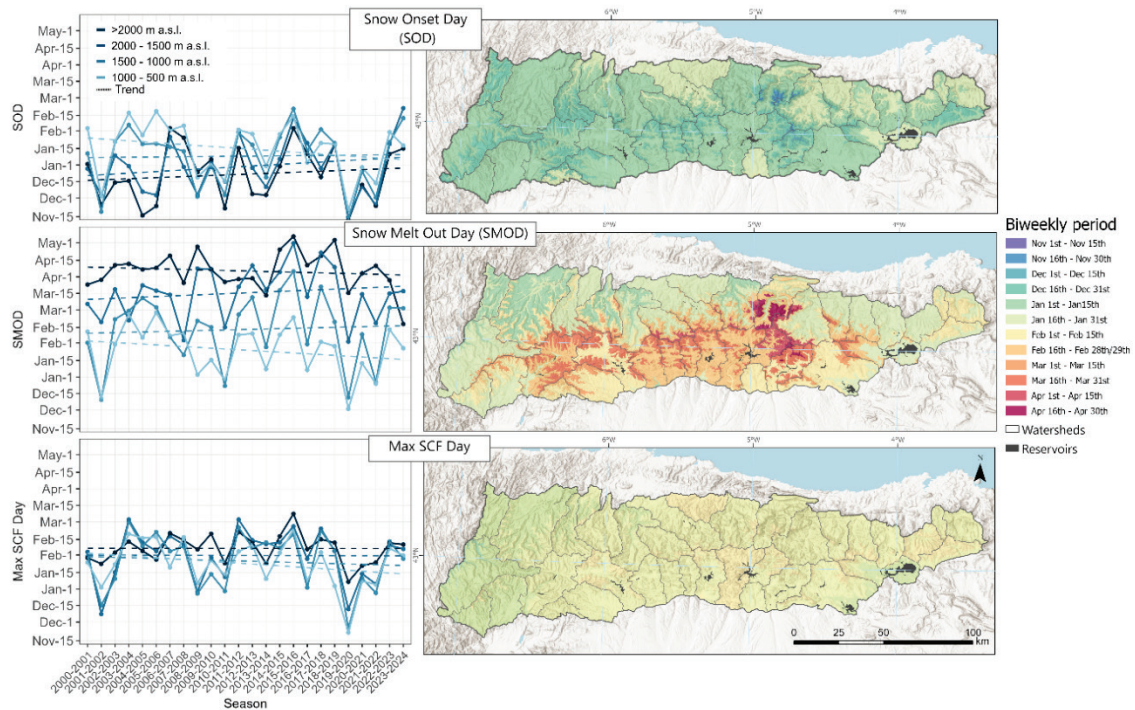


Figure 6. Timeseries of seasonal SOD, SMOD and max. SCF Day (2000-2024) and mean values maps by watersheds.

Table 4. Mean SOD, SMOD and Max SCF Day values and trends by altitudinal ranges.

	SOD		SMOD		Max SCF Day	
	Mean DOY	Trend (days/decade)	Mean DOY	Trend (days/decade)	Mean DOY	Trend (days/decade)
<b>Cantabrian Mountains (all altitude ranges)</b>	Jan 7 <sup>th</sup>	0.87	Feb 17 <sup>th</sup>	2.00	Jan 24 <sup>th</sup>	-3.89
<b>&gt;2000 m</b>	Dec 22 <sup>nd</sup>	4.83	Apr 5 <sup>th</sup>	-3.12	Feb 5 <sup>th</sup>	-0.10
<b>2000 - 1500 m</b>	Dec 29 <sup>th</sup>	7.22	Mar 16 <sup>th</sup>	5.19	Jan 29 <sup>th</sup>	-0.27
<b>1500 - 1000 m</b>	Jan 7 <sup>th</sup>	1.17	Feb 11 <sup>th</sup>	3.03	Jan 24 <sup>th</sup>	-3.54
<b>1000 - 500 m</b>	Jan 14 <sup>th</sup>	-8.58	Jan 23 <sup>rd</sup>	-7.31	Jan 22 <sup>nd</sup>	-8.18

\* Trends statistically significant at the 95% confidence level ( $p < 0.05$ ).

#### 4.4. Snow cover durability and persistence

Several variables are analyzed to define the durability and persistence of snow, as the longest snow cover duration, (LSCD, resulting from the difference between SMOD and SOD), the average duration of snow covers throughout the season (MED) and the Ratio of Duration/Length (RDL), which highlights areas where snow cover is more persistent (Fig 7).

The duration of the most important snow cover of the season (LSCD) varies considerably across altitudinal ranges (Table 5), being 13 days in the 500–1000 m range, 36.1 days for the 1000–1500 m range, 78.7 days for 1500–2000 m, and 106 days above 2000 m. The watersheds with the longest durations are Cares and Deva (above 2000 m), corresponding to the Picos de Europa massif, and Carrión (Fuentes Carrionas massif), where both exceed 140 days (155, 143.6 and 142.8, respectively, found in Appendix 4). These are the highest-altitude sectors of the Cantabrian Mountains. The shortest durations are found below 1,000 m in the Caudal watershed (8.8 days). In these lower elevation zones (500-1,000 m), the durations in the eastern part of the study area are higher than in the rest of the watersheds, as seen in the Miera watershed (20.2 days). Decreasing trends in duration are observed above 1500 m, with a -8 days per decade reduction above 2000 m and -2 days per decade between 1500–2000 m. Slight increases are observed below 1500 m (~1.5 days per decade).

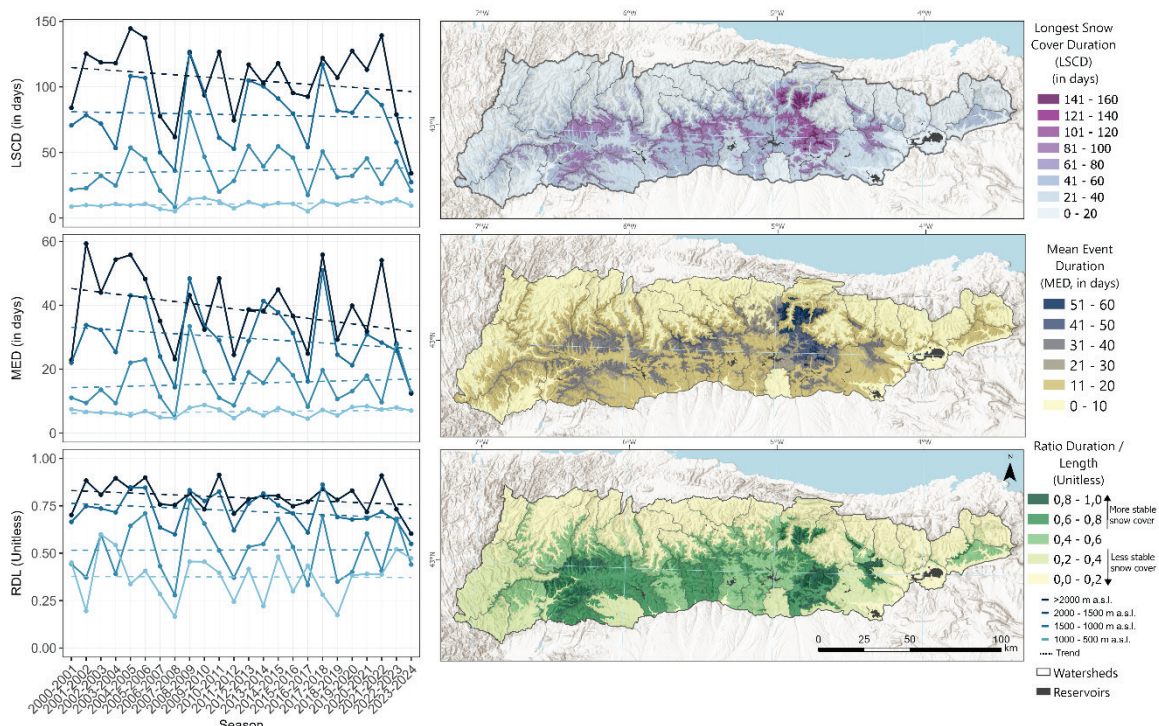


*Figure 7. Timeseries of seasonal LSCD, MED and RDL values (2000-2024) and mean value maps by watersheds.*

*Table 5. Mean LSCD, MED and RDL values and trends by altitudinal ranges.*

	LSCD		MED		RDL	
	Mean value (in days)	Trend (days/decade)	Mean value (in days)	Trend (days/decade)	Mean value (Unitless)	Trend (%/decade)
<b>Cantabrian Mountains (all altitude ranges)</b>	42.1	1.1	16.4	-0.9	0.56	-1.2
<b>&gt;2000 m</b>	106	-8	38.5	-5.8	0.79	-3.3
<b>2000 - 1500 m</b>	78.7	-2	29.8	-2.9	0.72	-3.5
<b>1500 - 1000 m</b>	36.1	1.9	15.5	1.2	0.52	0.1
<b>1000 - 500 m</b>	13	1.3	6.67	0.4	0.19	-0.2

\* Trends statistically significant at the 95% confidence level ( $p < 0.05$ ).

The average duration of snow covers (MED) follows the same trend as LSCD, although with lower absolute values, as ephemeral snowfalls are also considered here. The areas with the highest average snow cover persistence are found above 2,000 m in the Cares (55.9 days), Sella (55.5 days), Deva (52 days), Carrión (51.7 days) and Yuso (51.2 days) watersheds, all of them above 50 days of MED (Appendix 4). The MED shows a decreasing trend above 1500 m (-5.8 days/decade above 2,000 m and -2.9 days/decade between 2,000-1,500 m) and persistence under 1,500 m.

Regarding the RDL (Ratio duration-length), this variable considers both the frequency of snow cover detection (SCD) and the Snow Season Length (SSL), which is useful for assessing the persistence of snow cover. Higher RDL values are observed at higher elevations (0.79 above 2,000 m) and lower values at lower elevations (0.38 below 500 m). The watersheds with the most stable snow cover are the high-altitude areas (>2,000 m) of the Cares, Deva, Sella, Alto Sil, Carrión, Curueño, Porma, Pisueña, and Yuso watersheds, all of them with RDL values above 0.8. Low values, below 0.4, are common in low-altitude areas (<1,000 m) of the watersheds on the northern slopes, where snowfall can occur over several months during the season but lasts only a few days. RDL trends remain stable at lower elevations, but above 1,500 m, there is a decrease in snow persistence at a rate of approximately ~-3.4% per decade.

## 5. Discussion

The results show that snow cover in the Cantabrian Mountains experiences high interannual variability across all analysed variables, with pronounced altitudinal gradients. Since 1940, the succession of snowy and less snowy years has been observed in the Cantabrian Mountains, with a trend towards a decrease in snowfall days and an increase in interannual variability (Ortega Villazán and Morales Rodríguez, 2015). The most extensive, durable, and stable snow covers are found in areas above 1,500 m, which also show the most regressive trends for these parameters. It should be noted that the area above 2000 m is limited in many catchments, particularly when working at a spatial resolution of 500 m (MODIS). While trends were still computed for this elevation band for completeness, results at this altitude should be interpreted with caution in basins where the available surface is minimal. This limitation is inherent to the hypsometry of the Cantabrian Mountains, where the distribution of surface area across elevation bands is highly uneven, with a sharp decrease in extent above 2000 m.

The extent of snow cover has significantly decreased (Table 2) during the winter months (DJF), particularly on the southern slope of the Cantabrian Mountains and in areas above 1,500 m, with reductions of up to 16% per decade in some watersheds in the southwestern study area and other areas south of the watershed divide. This reduction aligns with previous studies that have observed a general decrease in SCF and SCD in these areas (Melón-Navarrete, 2024) and allows us to identify that this decline occurs particularly in the winter months, as reported by Hidalgo-Hidalgo *et al.* (2024). They indicate that the greatest reductions in snow cover in the Cantabrian Mountains occur in December (4.3% per five-year period) and January (6.3% per five-year period), with an average decline of 3.5% when considering the entire winter season, based on optical and radar sensor data for the same study period, starting in the year 2000. These rates of decline are slightly higher than those generally recorded in this study, which are around 2% per decade across all elevations during the same period (Table 2). However, the study areas are not exactly the same, as that study also includes the Montes de León and some foothill areas. In the same regions, declines of approximately 2% per decade are observed in autumn, with some areas also experiencing reductions in spring, which aligns with the low rates of change in snow cover extent detected by Hidalgo-Hidalgo *et al.* (2024) during the spring and autumn months.

These changes are likely driven by increasing temperatures and alterations in precipitation patterns, influenced by large-scale atmospheric variability such as the North Atlantic Oscillation (NAO) (Merino *et al.*, 2014). The most negative trends occur in the western (Alto Sil, Boeza, Omaña, Luna) and south slope watersheds (Yuso, Carrión, Pisueña), where precipitation is mainly associated with westerly and south-westerly weather types, which have decreased in frequency since the mid-20th

century in favour of anticyclonic patterns during winter months, significantly reducing precipitation (Fernández-González *et al.*, 2012). This is consistent with other studies, highlighting the southern slope of the Cantabrian Mountains as having a strong negative correlation between the NAO index and winter precipitation, as well as snowpack duration (Alonso-González *et al.*, 2020). These regions also exhibit higher (more irregular distribution) snowfall concentration indices (CI) compared to the northern slope (Lemus-Canovas *et al.*, 2024), making them more sensitive to synoptic pattern changes and resulting in significant reductions in snow extent, duration, and persistence. It is estimated that 85% of snowfall events originate from low-level flow from the N or NE in northern Spain (de Pablo Dávila *et al.*, 2021).

The date of the FESD shows a later occurrence at lower altitudes, while the first ephemeral snow cover duration has decreased notably, with reductions of more than 8.8 days per decade above 1,500 m and 12 days per decade above 2,000 m. Similarly, LESD shows an earlier melting date at higher altitudes (3 days/decade above 2,000 m and 4.4 days/decade between 1,500 and 2,000 m). These changes indicate a slight shift towards earlier and shorter snow seasons above 1,500 m. It should be noted that the FESD in this study refers to the first snow cover detected in cloud-free satellite images, which generally occurs one or more days before the actual event, introducing greater uncertainty compared to LESD. Early snowfall at lower elevations, such as the exceptional event (Gallinar Cañedo *et al.*, 2022) in late October 2018 (2018–2019 season, Fig. 5), can have negative environmental and economic effects. This event, which accumulated 50 cm of snow at 1,000 m in Asturias on the northern slope of the Cantabrian Mountains and covered areas below 500 m, caused road disruptions and power outages due to fallen branches and trees still retaining foliage.

SOD and SMOD tend to occur later, with SMOD occurring up to 2 days later per decade. At higher altitudes, above 2,000 m, there is a notable shortening of snow cover duration due to delayed SOD and earlier SMOD. The values of SMOD and FESD can be highly dependent on both the overall snow accumulation throughout the season and the presence of late snowfall events, which can influence the season's variability. Broader studies (Peng *et al.*, 2013) warn of a high sensitivity due to the correlation between the melting date and the presence of positive temperature anomalies during the melt months. The mean of the maximum SCF date is occurring earlier, particularly at lower altitudes, ranging between January 22<sup>nd</sup> and February 5<sup>th</sup>, depending on elevation. February, followed by January, was identified as the month with the highest number of snowfall events on the northern slope of the Cantabrian Mountains during the period from 1988 to 2018 (de Pablo Dávila *et al.*, 2021). The duration of the longest snow cover (SMOD – SOD) has decreased by up to 2 days per decade above 1,500 m and 8 days per decade above 2,000 m, where the five ski resorts in the Cantabrian Mountains are located. These resorts have faced challenges due to notable declines in snow cover duration in the last decades, directly impacting the socio-economic activity of nearby areas by reducing visitor numbers. In nearby mountains, evident reductions in snow availability for these infrastructures are observed, with warnings that even the effectiveness of snowmaking for their maintenance may be compromised if temperature increases are very high (Pons *et al.*, 2015). Below 1,500 m, the duration of the longest snow covers has slightly increased, by up to 1.9% per decade.

Average snow cover duration also shows slight positive trends below 1,500 m, while above this elevation, significant declines are observed, with reductions of -2.9 days per decade between 1,500–2,000 m and up to 5.8 days per decade above 2,000 m. These values are comparable to those detected in other studies, such as declines of 5–7 days per decade in the Alps during the 1968–2017 winter period (Monteiro and Morin, 2023) or significant declines in the Pyrenees above 2,100 m, with non-significant trends at 1,500 m due to high interannual variability (López-Moreno *et al.*, 2020). Snow cover persistence, as quantified by the RDL index, shows a non-significant decreasing trend (3.4% per decade) above 1,500 m. This indicates that snow cover is becoming increasingly intermittent within the snow season at these elevations. Southern slope basins experiencing the greatest reductions in snow extent and duration also exhibit high RDL values, exceeding 0.8 in some cases. This suggests that these reductions are not due to rapid melting or unstable snow covers but are likely driven by decreases in snowfall events, as explained earlier due to changes in synoptic patterns.

These findings are consistent with broader regional analyses. Alonso-González *et al.* (2020), using MODIS data and physically-based snow modelling, demonstrated that the Cantabrian Mountains, together with the Pyrenees, exhibit the deepest and most persistent snowpacks in the Iberian Peninsula at similar elevations. Despite this, the high interannual variability in snowpack parameters observed in the Cantabrian Mountains suggests a strong sensitivity to climatic factors.

The different temporal coverage of satellite sensors represents a key limitation when assessing long-term trends in snow cover duration. While MODIS provides a continuous record since 2000, the Landsat archive includes earlier data but with lower temporal frequency and less consistent availability. In this study, Landsat data were used only from 2000 onwards to align with the start of the MODIS time series and ensure consistency when comparing trends across sensors. Sentinel-2, meanwhile, covers only the most recent years, albeit with higher spatial resolution. These differences in temporal coverage affect the length of the available time series and must be considered when interpreting trend results. We addressed this by aggregating data at the scale of watersheds and altitudinal bands, which helps reduce local variability and improve robustness. Additionally, although MODIS offers a longer time series, its coarse resolution makes it particularly sensitive to spatial heterogeneity in mountainous terrain. In steep areas, where snow distribution changes rapidly over short distances, this may introduce uncertainty in the classification. This is consistent with recent findings (Bayle *et al.*, 2024), which highlight how changes in observation availability and environmental complexity can lead to artificial trends in satellite-based time series. A further limitation concerns the length of the time series. Our dataset covers 24 years (2000–2024), which is shorter than the 30-year period typically recommended as a standard climatological baseline. Caution is required when interpreting trends, and future work should aim to integrate longer and more homogeneous time series, as well as complementary observational sources (e.g., time-lapse cameras), to validate and refine satellite-derived trends.

The implications of these trends extend beyond snow dynamics, affecting hydrological systems, socio-economic activities (Beniston *et al.*, 2018) and alpine ecosystems (Espinosa del Alba *et al.*, 2025). The earlier snowmelt and shorter snow season could reduce spring and summer water availability, impacting river discharge and water resources for agriculture, hydroelectric power, and human consumption. Alpine vegetation and fauna adapted to stable snow conditions may also experience disruptions in their life cycles. Furthermore, the declining snow cover duration above 1,500 m presents a challenge for winter tourism, particularly for ski resorts, which are already facing operational difficulties due to unreliable snow conditions.

## 6. Conclusions

This study provides a detailed analysis of snow cover variability in the Cantabrian Mountains based on satellite imagery from 2000 to 2024. The results indicate a significant reduction in snow cover extent, particularly during the winter months, with declines of up to 16% per decade in some watersheds. These reductions are more pronounced above 1,500 m and on the southern slopes of the mountain range. Snow cover duration is also decreasing, especially at higher altitudes, where the longest snow cover events have shortened by 8 days per decade above 2,000 m. The timing of key snow seasonal indicators has shifted, with the LESD occurring earlier (2.7 days/decade), while the FESD remains relatively stable. Additionally, the date of maximum snow cover is shifting earlier, particularly at lower elevations.

The results suggest a growing trend toward shorter and less stable snow seasons in the region. These changes are likely linked to rising temperatures and modifications in precipitation patterns, which influence the interannual variability of snow accumulation and persistence. Although some biases exist due to cloud cover, forested areas, and rapid snowmelt events undetected by satellites, the findings highlight a decreasing trend of snow cover extent, duration, and stability over the past two decades, with implications for ecosystems and human activities, particularly in high-altitude areas and regions reliant on snow for tourism and water supply.

Future work will involve analysing longer satellite data series, comparing them with other observational data sources such as webcam images and manual records, and relating current temperature and precipitation trends to changes in snow variability. Further monitoring and analysis are essential to better understand and predict these changes.

## Acknowledgements

Adrián Melón-Nava was supported by the FPU program of the Spanish Ministerio de Universidades (FPU20/01220).

Landsat-8 data (USGS Landsat 8 Level 2, Collection 2, Tier 1) courtesy of the U.S. Geological Survey ([https://developers.google.com/earth-engine/datasets/catalog/LANDSAT\\_LC08\\_C02\\_T1\\_L2](https://developers.google.com/earth-engine/datasets/catalog/LANDSAT_LC08_C02_T1_L2), accessed on 10 January 2025).

Landsat-5 data (USGS Landsat 5 Level 2, Collection 2, Tier 1) courtesy of the U.S. Geological Survey ([https://developers.google.com/earth-engine/datasets/catalog/LANDSAT\\_LT05\\_C02\\_T1\\_L2](https://developers.google.com/earth-engine/datasets/catalog/LANDSAT_LT05_C02_T1_L2), accessed on 10 January 2025).

Imagery from the NASA MODIS instrument (MOD10A1.061 Terra Snow Cover Daily Global 500m), courtesy NASA NSIDC DAAC ([https://developers.google.com/earth-engine/datasets/catalog/MODIS\\_061\\_MOD10A1#description](https://developers.google.com/earth-engine/datasets/catalog/MODIS_061_MOD10A1#description), accessed on 10 January 2025).

Imagery from Sentinel-2 ([https://developers.google.com/earth-engine/datasets/catalog/COPERNICUS\\_S2\\_SR\\_HARMONIZED](https://developers.google.com/earth-engine/datasets/catalog/COPERNICUS_S2_SR_HARMONIZED), accessed on 10 January 2025) courtesy of Copernicus Services (<https://dataspace.copernicus.eu/explore-data/data-collections/sentinel-data/sentinel-2>, accessed on 10 January 2025).

Image processing was carried out thanks to the Google Earth Engine platform (<https://earthengine.google.com/>, accessed on 10 January 2025).

## References

- AEMET, 2018. Mapas climáticos de España (1981-2010) Y ETo (1996-2016). <https://doi.org/10.31978/014-18-004-2>
- Alonso-González, E., López-Moreno, J.I., Navarro-Serrano, F.M., Revuelto, J. 2020. Impact of North Atlantic Oscillation on the Snowpack in Iberian Peninsula Mountains. *Water* 12, 105. <https://doi.org/10.3390/W12010105>
- Barrou Dumont, Z., Gascoin, S., Inglada, J., Dietz, A., Köhler, J., Lafaysse, M., Monteiro, D., Carmagnola, C., Bayle, A., Dedieu, J.-P., Hagolle, O., Choler, P. 2024. Trends in the annual snow melt-out day over the French Alps and the Pyrenees from 38 years of high resolution satellite data (1986-2023), EGUSphere [preprint], <https://doi.org/10.5194/EGUSPHERE-2024-3505>
- Beato Bergua, S., Poblete Piedrabuena, M.Á., Marino Alfonso, J.L. 2019. Snow avalanches, land use changes, and atmospheric warming in landscape dynamics of the Atlantic mid-mountains (Cantabrian Range, NW Spain). *Applied Geography* 107, 38-50. <https://doi.org/10.1016/J.APGEOG.2019.04.007>
- Beniston, M., Farinotti, D., Stoffel, M., Andreassen, L.M., Coppola, E., Eckert, N., Fantini, A., Giacoma, F., Hauck, C., Huss, M., Huwald, H., Lehning, M., López-Moreno, J.I., Magnusson, J., Marty, C., Morán-Tejeda, E., Morin, S., Naaim, M., Provenzale, A., Rabatel, A., Six, D., Stötter, J., Strasser, U., Terzaghi, S., Vincent, C. 2018. The European mountain cryosphere: A review of its current state, trends, and future challenges. *The Cryosphere* 12, 759-794. <https://doi.org/10.5194/TC-12-759-2018>
- Bonsoms, J., López-Moreno, J.I., Lemus-Cánovas, M., Oliva, M. 2025. Future winter snowfall and extreme snow events in the Pyrenees. *Atmospheric Research* 315, 107912. <https://doi.org/10.1016/J.ATMOSRES.2025.107912>

- Bormann, K.J., Brown, R.D., Derksen, C., Painter, T.H. 2018. Estimating snow-cover trends from space. *Nature Climate Change* 8, 924-928. <https://doi.org/10.1038/s41558-018-0318-3>
- Corripio, J.G., López-Moreno, J.I. 2017. Analysis and Predictability of the Hydrological Response of Mountain Catchments to Heavy Rain on Snow Events: A Case Study in the Spanish Pyrenees. *Hydrology* 4(2), 20. <https://doi.org/10.3390/HYDROLOGY4020020>
- de Pablo Dávila, F., Rivas Soriano, L.J., Mora García, M., González-Zamora, Á. 2021. Characterization of snowfall events in the northern Iberian Peninsula and the synoptic classification of heavy episodes (1988–2018). *International Journal of Climatology* 41(1), 699-713. <https://doi.org/10.1002/JOC.6646>
- Espinosa del Alba, C., Fernández-Pascual, E., Jiménez-Alfaro, B. 2025. Microclimatic variation regulates seed germination phenology in alpine plant communities. *Journal of Ecology* 113(1), 249-262. <https://doi.org/10.1111/1365-2745.14461>
- Fernández-González, S., Del Río, S., Castro, A., Penas, A., Fernández-Raga, M., Calvo, A.I., Fraile, R., 2012. Connection between NAO, weather types and precipitation in León, Spain (1948-2008). *International Journal of Climatology* 32(14), 2181-2196. <https://doi.org/10.1002/JOC.2431>
- García-Hernández, C., López-Moreno, J.I. 2024. Extreme snowfalls and atmospheric circulation patterns in the Cantabrian Mountains (NW Spain). *Cold Regions Science and Technology* 221, 104170. <https://doi.org/10.1016/J.COLDREGIONS.2024.104170>
- Gascoin, S., Hagolle, O., Huc, M., Jarlan, L., Dejoux, J.F., Szczypta, C., Martí, R., Sánchez, R. 2015. A snow cover climatology for the Pyrenees from MODIS snow products. *Hydrology and Earth System Sciences* 19, 2337-2351. <https://doi.org/10.5194/HESS-19-2337-2015>
- Gascoin, S., Luoju, K., Nagler, T., Lievens, H., Masiokas, M., Jonas, T., Zheng, Z., De Rosnay, P., 2024. Remote sensing of mountain snow from space: status and recommendations. *Frontiers in Earth Science* 12, 1381323. <https://doi.org/10.3389/FEART.2024.1381323>
- Gorelick, N., Hancher, M., Dixon, M., Ilyushchenko, S., Thau, D., Moore, R. 2017. Google Earth Engine: Planetary-scale geospatial analysis for everyone. *Remote Sensing of Environment* 202, 18-27. <https://doi.org/10.1016/J.RSE.2017.06.031>
- Hall, D.K., Riggs, G.A. 2010. Normalized-Difference Snow Index (NDSI). Encyclopedia of Snow, Ice and Glaciers.
- Hall, D.K., Riggs, G.A., Salomonson, V.V. 1995. Development of methods for mapping global snow cover using moderate resolution imaging spectroradiometer data. *Remote Sensing of Environment* 54(2), 127-140. [https://doi.org/10.1016/0034-4257\(95\)00137-P](https://doi.org/10.1016/0034-4257(95)00137-P)
- Hidalgo-Hidalgo, J.D., Collados-Lara, A.J., Pulido-Velazquez, D., Fassnacht, S.R., Husillos, C. 2024. Synergistic Potential of Optical and Radar Remote Sensing for Snow Cover Monitoring. *Remote Sensing* 16(19), 3705. <https://doi.org/10.3390/RS16193705>
- Hori, M., Sugiura, K., Kobayashi, K., Aoki, T., Tanikawa, T., Kuchiki, K., Niwano, M., Enomoto, H. 2017. A 38-year (1978–2015) Northern Hemisphere daily snow cover extent product derived using consistent objective criteria from satellite-borne optical sensors. *Remote Sensing of Environment* 191, 402-418. <https://doi.org/10.1016/J.RSE.2017.01.023>
- Illa, E., Pérez-Haase, A., Brufau, R., Font, X. 2022. Living on the edge: Plant diversity in the Iberian chionophilous vegetation. *Applied Vegetation Science* 25, e12701. <https://doi.org/10.1111/AVSC.12701>
- Lemus-Canovas, M., Alonso-González, E., Bonsoms, J., López-Moreno, J.I., 2024. Daily concentration of snowfalls in the mountains of the Iberian Peninsula. *International Journal of Climatology* 44, 485-500. <https://doi.org/10.1002/JOC.8338>
- López-Moreno, J.I., Soubeyroux, J.M., Gascoin, S., Alonso-Gonzalez, E., Durán-Gómez, N., Lafaysse, M., Vernay, M., Carmagnola, C., Morin, S. 2020. Long-term trends (1958–2017) in snow cover duration and depth in the Pyrenees. *International Journal of Climatology* 40(14), 6122-6136. <https://doi.org/10.1002/JOC.6571>

- Malnes, E., Karlsen, S.R., Johansen, B., Bjerke, J.W., TØmmervik, H. 2016. Snow season variability in a boreal-Arctic transition area monitored by MODIS data. *Environmental Research Letters* 11(12), 125005. <https://doi.org/10.1088/1748-9326/11/12/125005>
- Mata Olmo, R., Sanz Herráiz, C. 2003. Atlas de los paisajes de España. Ministerio de Medio Ambiente.
- Melón-Nava, A. 2024. Recent Patterns and Trends of Snow Cover (2000–2023) in the Cantabrian Mountains (Spain) from Satellite Imagery Using Google Earth Engine. *Remote Sensing* 16(19), 3592. <https://doi.org/10.3390/RS16193592>
- Meng, C. 2017. Quantifying the impacts of snow on surface energy balance through assimilating snow cover fraction and snow depth. *Meteorology and Atmospheric Physics* 129, 529-538. <https://doi.org/10.1007/S00703-016-0486-5>
- Merino, A., Fernández, S., Hermida, L., López, L., Sánchez, J.L., García-Ortega, E., Gascón, E. 2014. Snowfall in the Northwest Iberian Peninsula: Synoptic Circulation Patterns and Their Influence on Snow Day Trends. *The Scientific World Journal* 2014, 480275. <https://doi.org/10.1155/2014/480275>
- Monteiro, D., Morin, S. 2023. Multi-decadal analysis of past winter temperature, precipitation and snow cover data in the European Alps from reanalyses, climate models and observational datasets. *The Cryosphere* 17(8), 3617-3660. <https://doi.org/10.5194/TC-17-3617-2023>
- Morán-Tejeda, E., Fassnacht, S.R., Lorenzo-Lacruz, J., López-Moreno, J.I., García, C., Alonso-González, E., Collados-Lara, A.J. 2019. Hydro-Meteorological Characterization of Major Floods in Spanish Mountain Rivers. *Water* 11, 2641. <https://doi.org/10.3390/W11122641>
- Notarnicola, C. 2024. Snow cover phenology dataset over global mountain regions from 2000 to 2023. *Data Brief* 56, 110860. <https://doi.org/10.1016/J.DIB.2024.110860>
- Notarnicola, C. 2020. Hotspots of snow cover changes in global mountain regions over 2000–2018. *Remote Sensing of Environment* 243, 111781. <https://doi.org/10.1016/J.RSE.2020.111781>
- Ortega Villazán, M.T., Morales Rodríguez, C.G. 2015. El clima de la Cordillera Cantábrica castellano-leonesa: diversidad, contrastes y cambios. *Investigaciones geográficas* 63, 45-67. <http://doi.org/10.14198/INGEO2015.63.04>
- Orusa, T., Viani, A., Cammareri, D., Borgogno Mondino, E. 2023. A Google Earth Engine Algorithm to Map Phenological Metrics in Mountain Areas Worldwide with Landsat Collection and Sentinel-2. *Geomatics* 3(1), 221-238. <https://doi.org/10.3390/GEOMATICS3010012>
- Peng, S., Piao, S., Ciais, P., Friedlingstein, P., Zhou, L., Wang, T. 2013. Change in snow phenology and its potential feedback to temperature in the Northern Hemisphere over the last three decades. *Environmental Research Letters* 8(1), 014008. <https://doi.org/10.1088/1748-9326/8/1/014008>
- Pisabarro, A. 2020. Snow cover as a morphogenic agent determining ground climate, landforms and runoff in the Valdecebollas massif, Cantabrian Mountains. *Cuadernos de Investigación Geográfica* 46, 81-102. <https://doi.org/10.18172/cig.3823>
- Pons, M., López-Moreno, J.I., Rosas-Casals, M., Jover, E. 2015. The vulnerability of Pyrenean ski resorts to climate-induced changes in the snowpack. *Clim Change* 131, 591-605. <https://doi.org/10.1007/S10584-015-1400-8>
- Revuelto, J., Alonso-González, E., Gascoin, S., Rodríguez-López, G., López-Moreno, J.I. 2021. Spatial Downscaling of MODIS Snow Cover Observations Using Sentinel-2 Snow Products. *Remote Sens* 13(22), 4513. <https://doi.org/10.3390/RS13224513>
- Rittger, K., Painter, T.H., Dozier, J. 2013. Assessment of methods for mapping snow cover from MODIS. *Advances in Water Resources* 51, 367-380. <https://doi.org/10.1016/J.ADVWATRES.2012.03.002>
- Salomonson, V. V., Appel, I. 2004. Estimating fractional snow cover from MODIS using the normalized difference snow index. *Remote Sensing of Environment* 89(3), 351-360. <https://doi.org/10.1016/J.RSE.2003.10.016>
- Santos González, J., Redondo Vega, J.M., Gómez Villar, A., González Gutiérrez, R.B. 2010. Avalanches in the Alto Sil (Western Cantabrian Mountain, spain). *Cuadernos de Investigación Geográfica* 36, 7-26. <https://doi.org/10.18172/cig.1224>

- Sasaki, O., Miles, E.S., Pellicciotti, F., Sakai, A., Fujita, K. 2024. Contrasting patterns of change in snowline altitude across five Himalayan catchments. *EGUsphere* [preprint]. <https://doi.org/10.5194/EGUSPHERE-2024-2026>
- Tang, Z., Deng, G., Hu, G., Zhang, H., Pan, H., Sang, G. 2022. Satellite observed spatiotemporal variability of snow cover and snow phenology over high mountain Asia from 2002 to 2021. *Journal of Hydrology* 613(8), 128438. <https://doi.org/10.1016/J.JHYDROL.2022.128438>
- Tiede, D., Sudmanns, M., Augustin, H., Baraldi, A. 2021. Investigating ESA Sentinel-2 products' systematic cloud cover overestimation in very high altitude areas. *Remote Sensing of Environment* 252, 112163. <https://doi.org/10.1016/J.RSE.2020.112163>
- Ye, K., Wu, R., Liu, Y. 2015. Interdecadal change of Eurasian snow, surface temperature, and atmospheric circulation in the late 1980s. *Journal of Geophysical Research: Journal of Geophysical Research: Atmospheres* 120(7), 2595-3005. <https://doi.org/10.1002/2015JD023148>
- Young, S.S. 2023. Global and Regional Snow Cover Decline: 2000-2022. *Climate* 11(8), 162. <https://doi.org/10.3390/CLI11080162>
- Zhang, C., Jiang, L. 2022. Fractional Snow Cover Mapping with High Spatiotemporal Resolution based on Landsat, Sentinel-2 And Modis Observation. *International Geoscience and Remote Sensing Symposium (IGARSS) 2022*, 3935-3938. <https://doi.org/10.1109/IGARSS46834.2022.9884171>
- Zhong, X., Zhang, T., Kang, S., Wang, J. 2021. Spatiotemporal variability of snow cover timing and duration over the Eurasian continent during 1966–2012. *Science of The Total Environment* 750, 141670. <https://doi.org/10.1016/J.SCITOTENV.2020.141670>

**Appendix 1. SCF mean values (2000-2024) by watersheds and seasons**

	SCF Autumn (S-O-N)				SCF Winter (D-J-F)				SCF Spring (M-A-D)				Watershed mean
	500-1000 m	1000-1500 m	1500-2000 m	>2000 m	Watershed mean	500-1000 m	1000-1500 m	>2000 m	Watershed mean	500-1000 m	1000-1500 m	>2000 m	
Aller	0.00	0.03	0.09	0.14	0.03	0.03	0.26	0.60	0.82	0.19	0.01	0.31	0.54
Alto Ebro	0.01	0.03	0.08	0.13	0.02	0.04	0.26	0.61	0.80	0.19	0.01	0.06	0.44
Alto Navia - Ibias	0.00	0.02	0.05	0.07	0.11	0.01	0.03	0.17	0.43	0.10	0.04	0.18	0.44
Alto Sil	0.00	0.03	0.07	0.11	0.04	0.03	0.21	0.49	0.73	0.26	0.00	0.06	0.43
Ason	0.00	0.02	0.04	0.08	0.00	0.04	0.31	0.57	0.10	0.01	0.08	0.24	0.02
Bajo Navia	0.01	0.02	0.07	0.13	0.01	0.03	0.15	0.03	0.07	0.01	0.03	0.20	0.01
Bernesga	0.00	0.02	0.07	0.13	0.03	0.01	0.18	0.50	0.78	0.24	0.00	0.05	0.48
Besaya	0.01	0.02	0.04	0.05	0.01	0.04	0.22	0.22	0.07	0.01	0.06	0.20	0.02
Boza	0.00	0.01	0.04	0.05	0.02	0.02	0.12	0.31	0.66	0.15	0.00	0.03	0.39
Burbia	0.00	0.02	0.04	0.08	0.01	0.02	0.12	0.39	0.09	0.00	0.02	0.16	0.02
Cares	0.01	0.03	0.09	0.15	0.04	0.05	0.32	0.63	0.80	0.27	0.01	0.10	0.33
Carrión	0.03	0.06	0.13	0.13	0.04	0.03	0.23	0.47	0.78	0.30	0.05	0.19	0.51
Caudal	0.00	0.02	0.07	0.11	0.01	0.02	0.22	0.56	0.77	0.12	0.01	0.06	0.22
Cea	0.00	0.01	0.03	0.03	0.01	0.01	0.07	0.21	0.21	0.07	0.00	0.02	0.06
Cúa	0.00	0.02	0.06	0.06	0.02	0.02	0.16	0.43	0.12	0.00	0.04	0.18	0.03
Cubia	0.00	0.02	0.07	0.13	0.04	0.03	0.24	0.54	0.80	0.29	0.06	0.25	0.53
Curueño	0.02	0.09	0.15	0.15	0.03	0.03	0.22	0.60	0.82	0.19	0.01	0.06	0.59
Devra	0.00	0.02	0.09	0.15	0.03	0.03	0.22	0.49	0.78	0.25	0.00	0.07	0.46
Esla	0.00	0.02	0.06	0.12	0.03	0.02	0.19	0.48	0.73	0.27	0.00	0.05	0.42
Luna	0.00	0.02	0.07	0.11	0.03	0.01	0.19	0.48	0.73	0.27	0.00	0.05	0.42
Miera	0.00	0.02	0.03	0.08	0.01	0.03	0.29	0.57	0.12	0.01	0.09	0.28	0.04
Nalón	0.00	0.03	0.08	0.08	0.01	0.03	0.26	0.51	0.79	0.15	0.01	0.10	0.51
Nansa	0.00	0.03	0.09	0.13	0.02	0.04	0.31	0.62	0.79	0.15	0.01	0.10	0.51
Narcea	0.00	0.02	0.07	0.11	0.03	0.01	0.04	0.19	0.47	0.10	0.00	0.05	0.35
Nela	0.01	0.03	0.07	0.11	0.02	0.04	0.31	0.56	0.18	0.01	0.10	0.25	0.05
Omaña	0.00	0.01	0.05	0.08	0.02	0.02	0.11	0.35	0.71	0.14	0.00	0.02	0.39
Pas	0.00	0.02	0.05	0.05	0.01	0.03	0.24	0.51	0.70	0.07	0.01	0.07	0.19
Pigüeña	0.00	0.03	0.09	0.13	0.03	0.02	0.23	0.58	0.82	0.20	0.00	0.06	0.26
Piloña	0.00	0.01	0.06	0.11	0.02	0.02	0.17	0.42	0.78	0.16	0.01	0.06	0.40
Pistierga	0.00	0.02	0.07	0.11	0.03	0.01	0.17	0.53	0.75	0.23	0.00	0.05	0.44
Porma	0.00	0.02	0.08	0.08	0.01	0.04	0.30	0.61	0.13	0.01	0.09	0.28	0.05
Saja	0.00	0.03	0.09	0.15	0.02	0.03	0.27	0.57	0.81	0.16	0.01	0.09	0.66
Sella	0.00	0.02	0.07	0.14	0.03	0.01	0.19	0.51	0.79	0.26	0.00	0.05	0.52
Torío	0.00	0.02	0.07	0.11	0.02	0.02	0.21	0.51	0.74	0.15	0.01	0.06	0.21
Trubia	0.00	0.02	0.07	0.11	0.02	0.05	0.28	0.57	0.82	0.34	0.01	0.08	0.55
Yuso	0.03	0.08	0.14	0.12	0.02	0.03	0.21	0.50	0.77	0.16	0.01	0.06	0.48
Mean	0.00	0.02	0.07	0.12	0.02	0.03	0.21	0.50	0.77	0.16	0.01	0.06	0.48

**Appendix 2. Mean FESD, LESD and Mean FESD duration values (2000-2024) by watersheds and seasons**

	FESD 500-1000 m	1000-1500 m	1500-2000 m	>2000 m	Watershed mean	LESF 500-1000 m	1000-1500 m	1500-2000 m	>2000 m	Mean FESD duration (in days)				Watershed mean
										500-1000 m	1000-1500 m	1500-2000 m	>2000 m	
Aller	Nov 29th	Nov 19th	Nov 05th	Nov 09th	Nov 12th	Nov 12th	Nov 21st	Apr 14th	May 05th	May 09th	May 09th	May 09th	May 09th	45.7
Alto Ebro	Dec 18th	Nov 19th	Nov 07th	Nov 03rd	Nov 17th	Nov 17th	Mar 03rd	Apr 04th	Apr 27th	May 11th	Apr 10th	Apr 10th	Apr 10th	45.7
Alto Navia -Tobias	Nov 28th	Nov 23rd	Nov 12th	Nov 21st	Nov 21st	Nov 21st	Jan 23rd	Mar 25th	Apr 23rd	Mar 23rd	Mar 23rd	Mar 23rd	Mar 23rd	35.0
Alto Sil	Dec 01st	Nov 22nd	Nov 06th	Nov 01st	Nov 11th	Nov 11th	Feb 04th	Mar 29th	Apr 19th	May 11th	Apr 19th	Apr 19th	Apr 19th	35.0
Azón	Dec 13th	Nov 26th	Nov 29th	Nov 29th	Dec 07th	Dec 07th	Feb 25th	Apr 01th	Apr 03rd	Apr 03rd	Apr 03rd	Apr 03rd	Apr 03rd	11.7
Bajío Navia	Nov 27th	Nov 23rd	Nov 07th	Nov 06th	Nov 10th	Nov 10th	Dec 17th	Apr 06th	Apr 30th	May 12th	Apr 14th	Apr 14th	Apr 14th	9.7
Bemasega	Nov 18th	Nov 23rd	Nov 23rd	Nov 17th	Dec 17th	Dec 17th	Mar 03th	Mar 21st	Mar 21st	Mar 08th	Mar 08th	Mar 08th	Mar 08th	9.7
Besaya	Dec 15th	Dec 06th	Dec 02nd	Nov 23rd	Nov 09th	Nov 20th	Jan 13th	Mar 06th	Apr 13th	Apr 15th	Apr 15th	Apr 15th	Apr 15th	9.5
Boeza	Nov 24th	Nov 22nd	Nov 13th	Nov 22nd	Nov 27th	Nov 27th	Dec 26th	Mar 10th	Apr 18th	Apr 18th	Apr 18th	Apr 18th	Apr 18th	14.3
Cares	Nov 30th	Nov 02nd	Oct 23rd	Nov 05th	Nov 05th	Nov 05th	Mar 06th	Apr 09th	May 06th	Jun 07th	May 04th	May 04th	May 04th	11.9
Carrión	Nov 17th	Nov 08th	Oct 27th	Nov 07th	Nov 07th	Nov 09th	Feb 01st	Mar 27th	Apr 25th	May 2nd	Apr 27th	Apr 27th	Apr 27th	7.8
Caudal	Nov 28th	Nov 20th	Nov 08th	Nov 09th	Nov 19th	Nov 19th	Dec 07th	Mar 08th	Apr 04th	Apr 29th	Apr 03rd	Apr 03rd	Apr 03rd	14.3
Cea	Nov 18th	Dec 07th	Nov 29th	Nov 29th	Dec 07th	Dec 07th	Jan 19th	Mar 19th	Apr 09th	Apr 09th	Mar 09th	Mar 09th	Mar 09th	10.2
Chía	Dec 04th	Nov 13th	Nov 13th	Nov 13th	Nov 19th	Nov 19th	Jan 26th	Mar 26th	Apr 18th	Apr 18th	Mar 28th	Mar 28th	Mar 28th	10.2
Cubilla	Dec 02nd	Nov 28th	Nov 28th	Nov 28th	Nov 21st	Nov 21st	Jan 21st	Mar 19th	Apr 09th	Apr 09th	Feb 29th	Feb 29th	Feb 29th	9.3
Curniño	Dec 04th	Nov 06th	Nov 04th	Nov 04th	Nov 06th	Nov 06th	Nov 06th	Mar 29th	Apr 29th	May 15th	May 15th	May 15th	May 15th	8.2
Dava	Nov 26th	Nov 18th	Nov 03rd	Oct 20th	Nov 11th	Nov 11th	Feb 15th	Apr 03rd	May 04th	Jun 08th	Apr 03rd	Apr 03rd	Apr 03rd	12.3
Esla	Nov 26th	Nov 17th	Nov 05th	Nov 04th	Nov 10th	Nov 10th	Jan 07th	Apr 09th	Apr 22nd	May 08th	Apr 13th	Apr 13th	Apr 13th	17.7
Luna	Nov 20th	Nov 22nd	Nov 07th	Oct 31st	Nov 14th	Nov 14th	Dec 18th	Mar 27th	Apr 19th	May 05th	Apr 03rd	Apr 03rd	Apr 03rd	12.3
Miera	Dec 23rd	Nov 28th	Nov 15th	Nov 07th	Nov 05th	Nov 05th	Nov 05th	Dec 08th	Mar 12th	Apr 05th	Mar 23rd	Apr 29th	Apr 29th	24.4
Nalon	Dec 06th	Nov 18th	Nov 18th	Nov 05th	Nov 05th	Nov 05th	Nov 11th	Mar 21st	Apr 08th	May 04th	May 04th	May 04th	May 04th	7.3
Nansa	Dec 08th	Nov 23rd	Nov 23rd	Nov 05th	Nov 10th	Nov 10th	Nov 22nd	Mar 02nd	Apr 06th	May 04th	Apr 09th	Apr 09th	Apr 09th	11.6
Narea	Dec 01st	Nov 25th	Nov 25th	Nov 19th	Nov 19th	Nov 19th	Nov 24th	Feb 05th	Mar 24th	Apr 16th	Apr 16th	Apr 16th	Apr 16th	13.3
Nela	Dec 12th	Nov 21st	Nov 19th	Nov 19th	Nov 13th	Nov 13th	Nov 23rd	Mar 17th	Apr 03rd	Apr 19th	Mar 31st	Mar 31st	Mar 31st	10.6
Onísana	Dec 17th	Nov 25th	Nov 25th	Nov 10th	Nov 10th	Nov 10th	Nov 17th	Feb 01st	Mar 01st	Apr 14th	Apr 26th	Apr 26th	Apr 26th	14.2
Pas	Dec 18th	Nov 30th	Nov 23rd	Nov 05th	Nov 04th	Nov 04th	Nov 12th	Feb 02nd	Apr 04th	May 02nd	May 02nd	May 02nd	May 02nd	11.9
Pigüeña	Nov 27th	Nov 23rd	Nov 23rd	Nov 05th	Nov 04th	Nov 04th	Nov 12th	Dec 09th	Feb 10th	Mar 29th	Apr 12th	Apr 12th	Apr 12th	10.5
Pilonia	Dec 05th	Nov 28th	Nov 28th	Nov 21st	Nov 06th	Nov 06th	Nov 21st	Feb 13th	Mar 17th	Apr 19th	Apr 29th	Apr 29th	Apr 29th	11.3
Pisueña	Dec 12th	Nov 21st	Nov 21st	Nov 18th	Nov 04th	Nov 05th	Nov 10th	Nov 17th	Dec 21st	Apr 06th	Apr 18th	Apr 18th	Apr 18th	14.7
Porma	Nov 22nd	Nov 22nd	Nov 23rd	Nov 06th	Nov 06th	Nov 06th	Nov 05th	Nov 05th	Nov 17th	Mar 02nd	Apr 04th	Apr 04th	Apr 04th	14.7
Saja	Dec 10th	Nov 25th	Nov 15th	Nov 05th	Oct 31st	Nov 13th	Nov 13th	Nov 13th	Feb 21st	Apr 07th	Jun 05th	Apr 12th	Apr 12th	11.5
Sella	Nov 30th	Nov 24th	Nov 25th	Nov 06th	Nov 06th	Nov 06th	Nov 09th	Dec 14th	Mar 31st	Apr 26th	May 10th	May 10th	May 10th	16.8
Torio	Dec 03rd	Nov 22nd	Nov 22nd	Nov 08th	Nov 06th	Nov 06th	Nov 07th	Feb 17th	Apr 01st	Apr 22nd	May 23rd	May 23rd	May 23rd	12.6
Trubia	Nov 20th	Nov 04th	Nov 27th	Nov 07th	Nov 07th	Nov 07th	Nov 07th	Mar 28th	Apr 24th	May 18th	Apr 23rd	Apr 23rd	Apr 23rd	13.4
Yuso	Dec 11th	Nov 23rd	Nov 10th	Nov 03rd	Nov 21st	Nov 21st	Nov 21st	Mar 10th	Mar 30th	May 15th	Apr 4th	Apr 4th	Apr 4th	22.7
Mean														22.7

**Appendix 3. Mean SOD, SMOD and Max SCF Day (2000-2024) by watersheds and seasons**

	SOD			SMOD			Max SCF day		
	500-1000 m	1000-1500 m	1500-2000 m	>2000 m	Watershed mean	500-1000 m	1000-1500 m	1500-2000 m	>2000 m
Aller	Jan 11th	Jan 3rd	Dec 18th	Dec 24th	Jan 3rd	Feb 15th	Apr 6th	Mar 26th	Jan 17th
Alto Ebro		Jan 10th	Dec 23rd	Dec 29th	Mar 20th	Mar 20th	Mar 20th	Mar 19th	Jan 26th
Alto Navia - Irias	Jan 5th	Dec 25th	Dec 29th	Jan 1st	Jan 15th	Jan 22nd	Mar 2nd	Jan 12th	Jan 11th
Alto Sil	Jan 6th	Jan 7th	Dec 19th	Dec 23rd	Dec 29th	Jan 16th	Mar 16th	Mar 16th	Jan 13th
Asón	Jan 20th	Jan 8th	Jan 7th	Jan 12th	Jan 12th	Feb 1st	Feb 17th	Feb 17th	Jan 25th
Bajío Navia	Dec 30th	Dec 31st	Jan 5th	Dec 23rd	Dec 22nd	Jan 9th	Jan 1st	Jan 1st	Jan 30th
Bernesga	Jan 9th	Jan 5th	Jan 14th	Jan 14th	Jan 14th	Jan 13th	Feb 15th	Jan 27th	Jan 07th
Beasaya	Jan 15th	Jan 16th	Dec 29th	Jan 9th	Jan 14th	Jan 26th	Feb 10th	Jan 25th	Jan 22nd
Boenza	Burbia	Jan 10th	Jan 13th	Jan 4th	Jan 9th	Jan 24th	Feb 9th	Feb 27th	Jan 17th
Cares	Jan 5th	Jan 6th	Dec 26th	Nov 25th	Dec 29th	Jan 18th	Feb 6th	Feb 24th	Jan 04th
Carrión	Jan 9th	Dec 23rd	Dec 5th	Dec 23rd	Dec 23rd	Jan 19th	Feb 14th	Apr 18th	Mar 7th
Caudal	Jan 7th	Jan 2nd	Dec 23rd	Dec 26th	Jan 1st	Jan 15th	Feb 4th	Mar 2nd	Mar 22nd
Cea	Feb 4th	Jan 14th	Jan 20th	Jan 6th	Jan 23rd	Feb 11th	Feb 11th	Feb 12th	Jan 21st
Cia	Jan 8th	Jan 5th	Jan 7th	Jan 6th	Jan 7th	Jan 17th	Feb 4th	Feb 13th	Jan 14th
Cubia	Curueño	Dec 19th	Dec 25th	Dec 25th	Dec 22nd	Jan 10th	Jan 16th	Jan 28th	Jan 03rd
Devra	Jan 18th	Jan 7th	Dec 19th	Nov 25th	Dec 29th	Jan 29th	Feb 13th	Feb 23rd	Mar 26th
Esla	Jan 17th	Jan 6th	Jan 4th	Jan 3rd	Jan 10th	Feb 4th	Feb 20th	Mar 23rd	Jan 24th
Luna	Jan 10th	Jan 1st	Dec 18th	Dec 18th	Dec 30th	Jan 16th	Mar 21st	Mar 25th	Mar 28th
Miera	Jan 4th	Dec 22nd	Dec 27th	Dec 21st	Dec 21st	Dec 31st	Jan 11th	Jan 29th	Jan 21st
Nalón	Jan 19th	Jan 9th	Dec 31st	Dec 26th	Dec 21st	Jan 1st	Jan 10th	Feb 17th	Feb 17th
Nansa	Jan 5th	Jan 7th	Jan 8th	Jan 7th	Jan 8th	Jan 14th	Feb 4th	Feb 17th	Feb 17th
Nercea	Nela	Dec 26th	Dec 26th	Jan 7th	Jan 7th	Jan 1st	Jan 11th	Jan 26th	Jan 19th
Omaría	Jan 17th	Jan 11th	Dec 24th	Dec 26th	Dec 24th	Dec 31st	Jan 4th	Jan 28th	Jan 21st
Pas		Jan 7th	Dec 7th	Dec 27th	Dec 27th	Jan 11th	Jan 11th	Jan 26th	Jan 22nd
Pigüeña	Piloña	Dec 28th	Dec 27th	Jan 5th	Jan 5th	Jan 8th	Jan 17th	Mar 25th	Jan 31st
Pisterra	Jan 19th	Jan 18th	Jan 2nd	Jan 2nd	Dec 17th	Jan 29th	Feb 10th	Feb 19th	Feb 03rd
Portmá	Jan 14th	Jan 13th	Dec 25th	Jan 5th	Jan 2nd	Jan 26th	Feb 4th	Feb 17th	Jan 21st
Saja	Jan 15th	Jan 2nd	Dec 19th	Dec 15th	Dec 10th	Jan 27th	Feb 16th	Mar 12th	Feb 01st
Salla	Jan 6th	Jan 5th	Dec 28th	Dec 31st	Jan 19th	Feb 19th	Apr 1st	Feb 27th	Jan 23rd
Torío	Jan 17th	Jan 4th	Dec 28th	Dec 28th	Jan 3rd	Jan 26th	Feb 4th	Mar 13th	Jan 28th
Trubia	Jan 2nd	Dec 23rd	Dec 10th	Dec 22nd	Dec 22nd	Jan 7th	Feb 18th	Apr 3rd	Jan 24th
Yuso	Jan 14th	Jan 7th	Dec 22nd	Dec 29th	Jan 7th	Jan 23rd	Feb 11th	Mar 16th	Feb 07th
Mean									Jan 24th

**Appendix 4. Mean SCD, MED and RDL values (2000-2024) by watersheds and seasons**

	LSCD	MED						RDL						Watershed				
		500-1000 m	1000 - 1500 m	1500 - 2000 m	>2000 m	Watershed mean	500-1000 m	1000 - 1500 m	>2000 m	Watershed mean	500-1000 m	1000 - 1500 m	>2000 m	Watershed mean	500-1000 m	1000 - 1500 m	>2000 m	Watershed mean
Aller	12.2	44.0	89.8	93.0	52.9	6.7	17.4	45.9	34.2	21.7	0.05	0.53	0.73	0.79	0.43	0.25	0.46	0.40
Alto Ebro		37.3	88.3	87.4	71.0		14.3	35.3	35.5	28.4	0.35	0.29	0.55	0.65	0.46	0.23	0.52	0.40
Alto Navia - Ibias	11.2	29.0	63.4	27.4	7.5		13.6	25.1	12.8	0.32	0.37	0.72	0.72	0.59	0.78	0.70	0.53	0.18
Alto Sil	11.0	40.7	88.7	105.9	61.6	7.9	18.0	34.0	34.6	23.6	0.30	0.74	0.81	0.91	0.69	0.25	0.53	0.25
Ason	14.0	38.0	42.3	24.8	7.8		14.7	21.3	21.3	12.2	0.21	0.35	0.38	0.38	0.23	0.45	0.61	0.45
Bajo Navia	11.3	21.8			13.1	6.8	10.9		7.4	0.18	0.32	0.32	0.32	0.26	0.42	0.61	0.92	0.45
Bernesga	15.5	41.2	92.6	99.9	59.8	5.9	17.3	30.2	33.0	21.1	0.05	0.59	0.78	0.70	0.53	0.72	0.81	0.82
Besaya	13.3	28.0			15.4	8.0	14.2		8.8	0.20	0.29	0.29	0.29	0.20	0.29	0.29	0.29	0.18
Boza	10.4	25.3	61.2	67.2	38.5	7.4	12.5	23.2	24.4	16.9	0.19	0.73	0.76	0.87	0.64	0.45	0.53	0.34
Burbia	12.0	25.0	52.8	22.6	6.8		12.1	20.1	20.1	10.6	0.35	0.45	0.53	0.53	0.45	0.42	0.61	0.92
Cares	15.2	49.6	114.3	155.0	68.7	7.9	18.5	50.5	55.9	27.7	0.26	0.42	0.61	0.92	0.45	0.22	0.54	0.82
Carrión		37.2	91.3	142.8	90.4		16.9	35.0	51.7	34.5	0.05	0.72	0.81	0.92	0.82	0.22	0.54	0.82
Caudal	8.8	34.0	74.8	93.3	42.9	5.4	14.7	25.7	34.1	16.6	0.05	0.49	0.53	0.59	0.34	0.22	0.54	0.45
Cea	10.0	31.0	68.3	35.8	5.4		9.4	13.0	9.2	0.05	0.42	0.80	0.80	0.42	0.42	0.42	0.42	0.42
Cúa	10.0	31.5	65.0	35.5	6.4		15.7	23.5	15.2	0.28	0.47	0.64	0.64	0.46	0.46	0.46	0.46	0.46
Cubia	9.1	22.7			12.5	6.1	11.8		7.5	0.20	0.28	0.28	0.28	0.20	0.28	0.28	0.28	0.18
Curueño		52.1	98.0	115.6	106.8		17.8	33.5	44.5	39.0	0.05	0.71	0.69	0.88	0.76	0.31	0.54	0.45
Deva	13.9	38.0	107.4	143.6	61.2	7.0	14.8	45.4	52.0	24.7	0.26	0.30	0.69	0.93	0.45	0.22	0.55	0.45
Esla	18.4	46.3	80.3	83.2	54.8	6.1	18.4	27.2	30.3	20.5	0.20	0.52	0.69	0.79	0.55	0.22	0.54	0.46
Luna	16.3	43.1	80.0	112.5	66.3	6.8	17.6	30.4	38.4	24.5	0.05	0.61	0.65	0.86	0.54	0.22	0.54	0.46
Miera	20.2	38.4			14.8	7.4	15.5	32.2	6.8	0.26	0.28	0.31	0.31	0.22	0.28	0.28	0.28	0.22
Nalón	12.6	49.7	92.2		40.1	6.4	18.9	32.5	32.5	15.9	0.05	0.50	0.70	0.70	0.32	0.32	0.32	0.32
Nansa	48.9	89.1	90.3	57.9	4.8		19.8	33.1	35.8	23.0	0.30	0.47	0.56	0.70	0.42	0.22	0.55	0.45
Narcea	11.5	28.2	59.8	26.9	6.7		12.9	23.3	12.4	0.30	0.53	0.57	0.57	0.36	0.36	0.36	0.36	0.36
Nela		48.3	50.8	49.5			19.9	20.4		20.2	0.05	0.53	0.72	0.72	0.62	0.62	0.62	0.62
Omaña	9.9	24.7	64.5	81.8	45.2	7.0	11.7	24.2	29.6	18.1	0.44	0.45	0.56	0.67	0.53	0.31	0.54	0.45
Pas	19.2	32.8	43.0	27.2	6.2		15.6	16.8	12.4	0.26	0.71	0.57	0.57	0.40	0.40	0.40	0.40	0.40
Pigueña	12.4	33.8	89.2	94.7	55.8	6.4	14.8	33.8	38.3	22.8	0.20	0.46	0.61	0.68	0.40	0.22	0.55	0.40
Piloña	11.2	23.9			13.1	6.2	10.8		6.8	0.05	0.21	0.21	0.21	0.10	0.10	0.10	0.10	0.10
Pisuerga		31.3	65.5	94.3	63.7		13.0	23.5	35.3	23.9	0.35	0.40	0.65	0.78	0.55	0.31	0.54	0.45
Porma	14.9	39.7	94.2	92.0	59.5	8.8	16.1	32.8	29.9	21.9	0.05	0.49	0.56	0.82	0.48	0.22	0.54	0.48
Saja	14.9	46.1	83.9	0.0	29.6	7.4	19.5	32.2	0.0	12.8	0.05	0.41	0.59	0.89	0.40	0.22	0.54	0.40
Sella	14.3	45.8	95.2	136.9	59.6	7.5	20.6	33.2	55.5	24.2	0.05	0.49	0.62	0.81	0.40	0.22	0.54	0.40
Torío	17.5	50.1	94.2	106.4	69.4	5.2	18.8	33.8	41.9	27.0	0.05	0.60	0.71	0.71	0.52	0.22	0.52	0.40
Trubia	9.4	33.8	72.7	97.3	43.9	5.2	13.6	25.9	24.5	14.9	0.05	0.42	0.64	0.83	0.40	0.22	0.52	0.40
Yuso	47.7	102.5	135.3	95.2	21.6	40.1	51.2	37.6	37.6	37.6	0.05	0.59	0.75	0.89	0.74	0.22	0.54	0.40
Mean	13	36.1	78.4	106	42.1	6.7	15.5	29.8	38.5	16.4	0.19	0.52	0.72	0.79	0.56	0.22	0.54	0.40





## EFFECTS OF DEM RESOLUTION AND AREA THRESHOLDS ON AUTOMATED FLUVIAL MORPHOMETRY, ARROYO DEL ORO (ARGENTINA)

ANA CASADO<sup>1\*</sup>,  
FEDERICO JAVIER BERÓN DE LA PUENTE<sup>2</sup>,  
VERÓNICA GIL<sup>2</sup>

<sup>1</sup>*Consejo Nacional de Investigaciones Científicas y Técnicas (CONICET), Centro de Emprendedorismo y Desarrollo Territorial Sostenible, Universidad Provincial del Sudoste, Argentina.*

<sup>2</sup>*Consejo Nacional de Investigaciones Científicas y Técnicas (CONICET, Dpto. de Geografía y Turismo, Universidad Nacional del Sur, Argentina.*

**ABSTRACT.** The resolution of Digital Elevation Models (DEM) as well as the area threshold to define streams and catchments are important sources of uncertainty in automated fluvial morphometry. This study examines the applicability of three global surface models, produced with resolutions of 12.5 (ALOS), 30 and 90 m (SRTM), along with five area thresholds ranging from 0.15 to 10%. It aims at evaluating the effects of varying resolution-threshold combinations on the extraction of morphometric parameters and indices (PIm) in the Arroyo del Oro, a mountain basin located in south-western Buenos Aires (Argentina). The analysis considers the accuracy of drainage definitions, the variability of resulting PIm, and its implications for flood and water erosion assessments. Results show that the higher thresholds affect the PIm that depend on the complexity of the drainage network. Coarser resolutions impact on relief, slope and length parameters, but yield small discrepancies for the remaining PIm. For the 0.15% threshold, SRTM30 provides good fit of drainage composition parameters, and it is therefore suitable to assess the efficiency and capacity of the basin to evacuate floods. However, the use of higher resolution (ALOS12) is most suitable to assess erosion potential, due to better fit of slope-dependent PIm. Applications based on the global characteristics of middle to large-sized basins rely on a more flexible choice, as geometry parameters are unaffected by resolution and threshold.

### *Efectos de la resolución del DEM y de los umbrales de área en la morfometría fluvial automatizada, Arroyo del Oro (Argentina)*

**RESUMEN.** La resolución de los Modelos Digitales de Elevación (DEM), así como el umbral de área utilizado para definir la red de drenaje, son fuentes importantes de incertidumbre en morfometría fluvial automatizada. Este estudio examina la aplicabilidad de tres modelos globales, producidos con resoluciones de 12,5 (ALOS PALSAR RTC), 30 y 90 m (SRTM), junto con cinco umbrales de área entre 0,15 y 10%. El objetivo es evaluar los efectos de las diferentes combinaciones resolución-umbral en la extracción de parámetros e índices morfométricos (PIm) en la cuenca del Arroyo del Oro, una cuenca serrana localizada en el Sudoeste Bonaerense (Argentina). El análisis considera la precisión en la definición del drenaje y los parámetros asociados, la variabilidad de los PIm resultantes y sus implicaciones para la evaluación del peligro de crecidas y erosión hídrica. Los resultados indican que los mayores umbrales afectan los PIm que dependen de la complejidad de la red de drenaje. Las resoluciones más gruesas afectan los parámetros de relieve, pendiente y longitud, pero producen pequeñas discrepancias para los PIm remanentes. El umbral de 0,15 % y la resolución de 30 m proporcionan un buen ajuste de la composición del drenaje, resultando adecuados para evaluar la eficiencia y la capacidad de la cuenca para evacuar las crecidas. Sin embargo, el uso de una resolución más alta (12,5 m) es más adecuado para evaluar el potencial de erosión, debido a un mejor ajuste de los PIm que dependen de la pendiente. Para aplicaciones basadas en las características globales

de cuencas de tamaño mediano a grande, la elección es más flexible, debido a que los parámetros de geometría no se ven afectados por resolución o umbral.

**Keywords:** DEM resolution, area thresholds, morphometric parameters and indices, Arroyo del Oro.

**Palabras clave:** resolución, umbrales de área, parámetros e índices morfométricos, arroyo del Oro.

Received: 1 September 2024

Accepted: 24 January 2025

**\*Corresponding author:** Ana Casado. Consejo Nacional de Investigaciones Científicas y Técnicas (CONICET), Centro de Emprendedorismo y Desarrollo Territorial Sostenible, Universidad Provincial del Sudoreste, Argentina. Email: ana.casado@uns.edu.ar

## 1. Introduction

The automated extraction of morphometric information from Digital Elevation Models (DEM) is a common task in fluvial assessment and modelling. While a range of hydro-processing tools are available, few studies evaluate the effectiveness of such tools or the quality of the results for morphometric assessment (Dávila Hernández *et al.*, 2022; Shekar and Mathew, 2024). There are some issues that remain to be addressed for successful extraction of morphometric information from DEMs. These are mainly linked to the DEM source and resolution, but also to the parameters used in automated hydro-processing.

The growing diversity of data sources challenges the choice of DEMs meeting optimal scale-related quality and resolution, while balancing the costs for acquisition and processing (Boulton and Stokes, 2018; Dávila Hernández *et al.*, 2022). Current trends are evolving to high-resolution terrain models obtained from photogrammetry and LiDAR techniques. However, the spatial coverage of such products is limited compared to global, space-borne elevation data, and their high cost prevents their widespread use in many countries (Boulton and Stokes, 2018; Courty *et al.*, 2019). In this context, the middle-resolution surface models derived from the Shuttle Radar Topography Mission (SRTM, NASA) have become the most globally used for hydrological modelling. Even if they contain altimetry bias due to buildings, vegetation and other elements on the terrain surface (Gallant and Read., 2016; O'Loughlin *et al.*, 2016), the popularity of SRTM DEMs relies on their free access and wide availability, along with their acceptable quality (Boulton and Stokes, 2018; Courty *et al.*, 2019; Dávila Hernández *et al.*, 2022). More recently, global surface models of higher resolution, such as ALOS PALSAR with Radiometric Terrain Correction (NASA-JAXA and ASF), among others, permitted to improve automated extraction of morphometric parameters due to their greater topographic detail (Niipele and Chen, 2019). The effects of DEM resolution on fluvial morphometry have received early attention (Hancock, 2005; Thompson *et al.*, 2001), and remain of current interest (Buakhao and Kangrang, 2016; Datta *et al.*, 2022; Nourani *et al.*, 2013; Wu *et al.*, 2017). Most studies report that the effects of resolution are not linear, as they depend on the size and the terrain complexity of the study basin. Furthermore, it has been observed that DEMs from different sources may produce greater variability than resolution for the same source. These findings highlight the diversity of sources of uncertainty in the analysis and interpretation of basin properties extracted from DEMs.

While the DEM affect the quality of the morphometric parameters being extracted, the complexity of parameters involved in runoff dynamics challenges determining the accuracy of such parameters (Shekar and Mathew, 2024). Most GIS-based hydro-processing tools available today build on the D8 algorithm (O'Callaghan and Mark, 1984), which assumes that runoff follows the direction of the terrain

gradient once it exceeds a minimum accumulation area for the conformation of a channel unit. This area threshold ( $A_s$ ) constitutes the most important parameter in stream definition. In practice,  $A_s$  is defined using a standard value which is assumed as constant throughout the basin. Most GIS-based hydro-processing tools propose using 1% of maximum flow accumulation by default (Ozulu and Gökgöz, 2018). Yet a number of methods to define  $A_s$  have been early developed. These are based, among others, on stream drop and slope-area relationships (Tarboton *et al.*, 1991), on the scaling properties of stream fractal geometry (da Ros and Borga, 1997), and on variable morphologic and geologic influence within the study basin (Lopez García and Camarasa Belmonte, 1999; Montgomery and Foufoula Georgiou, 1993). Despite the value of these approaches, so far there is no global consensus on this issue (Datta *et al.*, 2022; Niipele and Chen, 2019; Ozulu and Gökgöz, 2018; Wu *et al.*, 2017). Moreover, the range of variability in morphometric extractions and its implications for the understanding of basin dynamics still represents an important research gap for many regions (Shekar and Mathew, 2024).

From the above, it follows that automated fluvial morphometry face two important challenges. The first is linked to the choice of an input DEM that ensures the most suitable relationship between resolution, basin size and terrain topography. The second involves the definition of an area threshold allowing for a suitable definition of the basin drainage complexity. More importantly, there are no optimal, generalized resolution-threshold combinations, as a given resolution or threshold may yield more or less suitable results depending on the context of the study and its applications in fluvial morphometry.

This paper aims at determining the effects of DEM resolution and area thresholds for automated extraction of morphometric parameters within the Arroyo del Oro (Argentina), a mountain basin that conforms the headwaters of the Sauce Grande River. It compares the applicability of popular global surface models, available with resolutions of 12.5 (ALOS), 30 and 90 m (SRTM), along with five area thresholds ranging from 0.15 to 10%. This yields fifteen possible resolution-threshold combinations. The validation of the results considers three criteria. These include the accuracy in drainage definitions and computed parameters, the variability of the resulting morphometric indices, and its implications for flood and water erosion assessment. Although the potential for transferability of the results to other regional basins remains to be evaluated, findings from this investigation provide valuable insights for making informed resolution and area threshold selection in watershed modelling, having wider testing applicability for water resources managing for a variety of spatial scales.

## **2. Study area**

The Arroyo del Oro drains the north-eastern slopes of the Sierra de la Ventana range and flows down into the Sauce Grande River (Fig. 1). The drainage network develops over metamorphic rock in the headwaters, and excavates quaternary fluvial and wind deposits in the lower section (Gil, 2012). Headwater slopes are steep (20%, on average), while the foothills and the alluvial plain exhibit undulating to gentle topography (Volonté and Gil, 2023). Bare rock soils cover 60% of the basin. Land use is predominantly agricultural, and limited to moderately deep soils over the foothills. Except for the town of Villa Ventana, which is home to 952 people (INDEC, 2022), population density is low (0.27 hab./km<sup>2</sup>).

The regional climate is dry subhumid (Casado, 2021). Mean annual temperature is 14.2 °C and mean annual rainfall is 725 mm (1981-2020). Rainfall variability is marked, and responds to regional circulation features (Gil *et al.*, 2008; Zapperi *et al.*, 2006; Zapperi *et al.*, 2007) as well as to global climate anomalies such as El Niño-Southern Oscillation (Scian, 2000). The stream flow regime is flashy and driven by torrential storms. Long periods of little or no flow are interspersed with floods of high relative magnitude (Casado *et al.*, 2016). Although excess water is evacuated quickly, storms and floods are frequent, and constitute a major threat to urban population and infrastructures (Gil *et al.*, 2016). In addition, soil water erosion is the main constraint to the agricultural aptitude of basin soils (INTA, 2018).

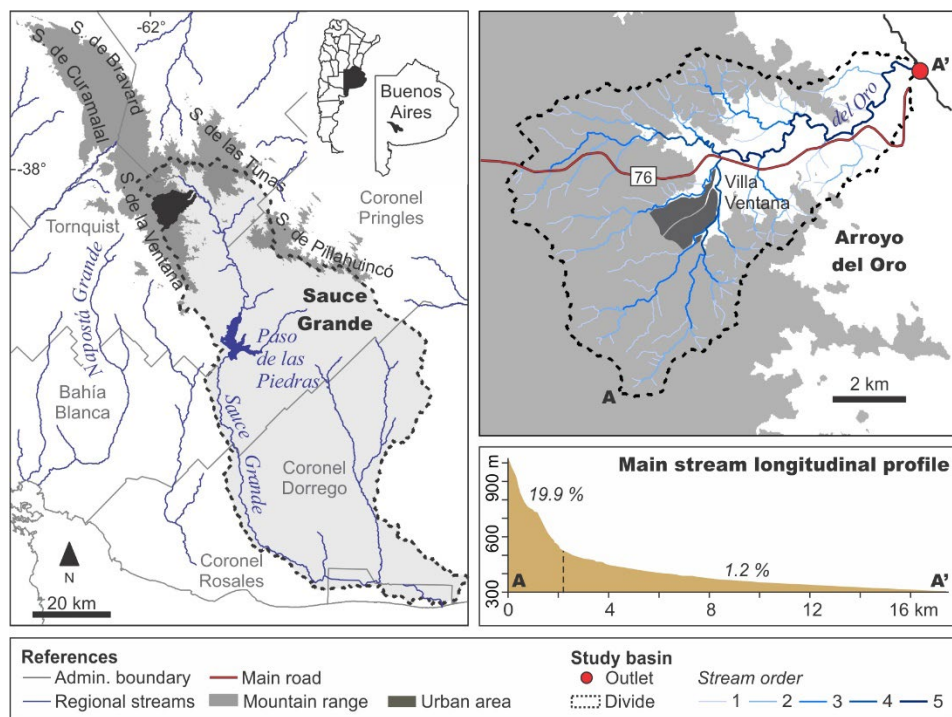


Figure 1. Map of the Arroyo del Oro basin showing main regional features.

### 3. Materials and methods

This study evaluates the influence of varying DEM resolution and area thresholds for automated morphometric analysis in the Arroyo del Oro basin. The analysis builds on a four-step procedure which involves (1) catchment and stream definition, (2) extraction of morphometric parameters, (3) computation of morphometric indices, and (4) validation of the results relative to the reference basin (Fig. 2).

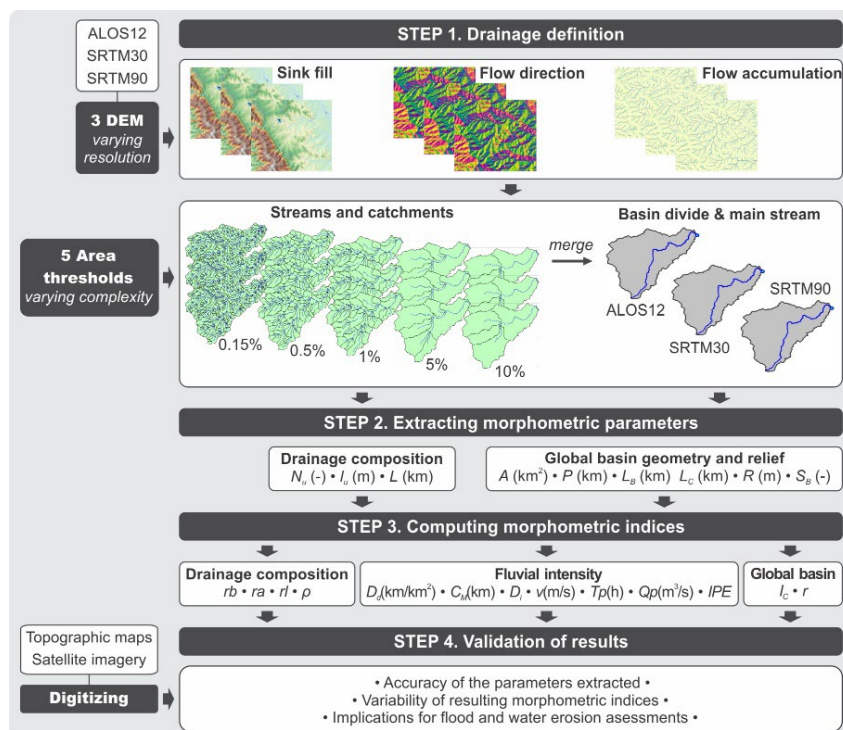


Figure 2. Methodological scheme for morphometric analysis.

### 3.1. DEM quality assessment

This paper uses three different DEMs with resolutions of 12.5, 30 and 90 m. All three are global surface models produced by space-borne SAR missions, SRTM (NASA) and ALOS (NASA-JAXA & ASF). Hereafter, these models are referred to as ALOS12, SRTM30 and SRTM90, respectively. Table 1 summarizes DEM metadata. Although an updated version of SRTM30 has been released in 2021 (NASADEM), it relies on an array of terrain products and auxiliary data that were not available during the original processing of SRTM (NASA JPL, 2021). The version released in 2014 (SRTMGL1) has been void filled like SRTM90, and underpins radiometric terrain correction of ALOS12. Comparatively, SRTMGL1 allows minimizing the effects of the DEM source on the resulting data, and is likely more suitable for the purpose of the study.

The ability of the models to reproduce terrain elevation and forms was evaluated in terms of accuracy and reliability. Vertical errors were determined relative to known orthometric heights, extracted from the national levelling network (RN-Ar, IGN, Argentina) for the upper Sauce Grande basin. Orthometric heights were converted to ellipsoid heights (WGS84) using two online tools, GeoidEval v2.4 (for EGM96) and GEOIDE-Ar 16 (IGN, Argentina). Errors were reported as the mean error (ME) and the root mean square error (RMSE), as indicators of bias and statistical distribution of error, respectively (Fisher and Tate 2006). Since errors are likely to vary spatially, we inspected for artefacts (padi terraces) and outliers using GIS-based neighbourhood analysis within focal windows of 3x3 cells (Hengl *et al.* 2004). Artefacts were detected using metrics of variety, where 1 indicates that all nine cells have the same elevation value, and 9 indicates the opposite. Outliers were detected using the statistical approach of Felicísimo (1994), which builds on extreme deviations of normalized residuals using a Student's *t* test. For a confidence level of 95%, the value of *t* is 1.96. The spatial offset of extracted streams relative to reference was used as a simple, additional measure of DEM reliability. Offset analysis used the longest flow path instead of the entire stream network to ensure that the results were unaffected by drainage complexity.

Table 1. Metadata of the DEMs used in the study.

Metadata	ALOS12	SRTM30	SRTM90
Model ID	ALPSRP240256410	SRTM1S39W062V3	SRTM3S39W062V2
Acquisition date	29/07/2010	11/02/2000	11/02/2000
Version	Radiometric Terrain Corrected (RT1) based on SRTMGL1 (05/05/2015)	SRTMGL1 - 1 Arc-Second Global Void filled (23/09/2014)	SRTMGL3 - 3 Arc-Second Global Void Filled (17/04/2013)
Projection	WGS84 UTM20S		WGS84
Horizontal datum		WGS84	
Vertical datum		Earth Gravitational Model 1996 (EGM96)	
Height	Ellipsoid (WGS 84)	Geoid (EGM96)	Geoid (EGM96)
Spatial resolution	12.5 m	1 arc-second (~30 meters)	3 arc-seconds (~90 meters)
Raster size	~0.5° lat / ~1° lon	1 degree tiles	1 degree tiles
Centre coord.	-38.0 / -62.1		-38.5 / -61.5

### 3.2. Drainage definition

Streams and catchments were defined from each DEM using HEC-HMS GIS module (v4.11, U.S. Army Corps of Engineers). For each model, we computed flow direction and flow accumulation layers using standard sink and drainage pre-processing parameters (Fig. 2). This yielded three sets of drainage data from which to define the streams and their catchments.

In practice, the minimum drainage area to define a stream is 1% of the basin surface (USACE, 2023). This is the default for most GIS-based hydro-processing tools (Ozulu and Gökgöz, 2018), and

thus represents a standard area threshold. However, the lower (or higher) the area threshold ( $A_s$ ), the greater (or smaller) the complexity of the stream network being extracted. Even though many morphometric parameters depend on the drainage complexity, some others do not. Thus, a given  $A_s$  may be more or less suitable relative to varying applications in fluvial morphometry. Moreover, the lower the  $A_s$ , the greater the processing requirements relative to the basin size. In this regard,  $A_s$  should also provide a reasonable balance between topographic detail and processing capacities for a given study basin. In this paper, we tested four additional area thresholds below and above the standard 1% (Table 2). These take arbitrary values of 0.15%, a low threshold involving reasonable processing times, and of 10%, a high threshold allowing detecting a bound depicting main streams and catchments; the values of 0.5 and 5% were used to inspect for potential intermediate breaks.

The combination of three DEMs and five area thresholds yielded fifteen sets of drainage elements. All layers were exported to a Geographical Information System (GIS). Area, length, and other basic statistics were obtained from the attribute tables.

*Table 2. Contributing area thresholds used in the study and number of equivalent grid cells by DEM.*

$A_s$ (%)	Area (km <sup>2</sup> )	Grid cell number		
		ALOS12	SRTM30	SRTM90
0.15	0.1	595	121	13
0.5	0.3	1984	404	45
1	0.6	3968	809	90
5	3.1	19840	4043	449
10	6.2	39680	8086	898

### 3.3. Morphometric parameters and indices

We considered a range of morphometric parameters and indices (PIm) popularly used for flood and water erosion assessments (Table 3). Following Romero Díaz and López Bermúdez (1987), parameters are different from indices in that the latter result from a relationship between two or more parameters. To ensure the readability of the results, PIms were assembled into three groups. These account for (i) global basin characteristics, (ii) drainage composition, and (iii) a set of indices designating the intensity of fluvial processes.

*Table 3. Morphometric parameters and indices used in the study.*

#### (i) Global basin characteristics: geometry and relief

PIm	Equation	Application	Reference
<i>Area</i>	$A$ (km <sup>2</sup> )	Input parameter for basin shape and fluvial intensity indices	-
<i>Perimeter</i>	$P$ (km)	Input parameter for basin shape indices	-
<i>Basin length</i>	$L_B$ (km)	Input parameter for basin shape indices	
<i>Longest flow path</i>	$L_C$	Input parameter for velocity and flood hydrograph parameters: Qp & Tp	
<i>Mean basin slope</i>	$S_B$ (%)	Input parameter for velocity and erosion potential indices	
<i>Basin relief</i>	$R(m) = \max\Delta Z$ (1)	Maximum gradient of the basin	Schumm (1956)
<i>Relief ratio</i>	$r = R/L_B$ (2)	Indicates the geomorphic evolution of basins	Schumm (1956)
<i>Compactness coefficient</i>	$m = 0.282P/\sqrt{A}$ (3)	Basin shape index designating both the intensity and erosive capacity of floods	Gravelius (1914)

(ii) Drainage composition			
PIHm	Equation	Description	Reference
Stream number	$N_u$	Input parameter for drainage composition and fluvial intensity indices.	Horton (1945)
Average stream length	$l_u$ (km)	Input parameter for drainage composition and fluvial intensity indices	Horton (1945)
Total length	$L$ (km)	Input parameter for drainage density index	Horton (1945)
Bifurcation ratio	$rb = N_u/N_{u+1}$ (4)	Indicates how water flows and branches within a basin (drainage composition)	Horton (1945)
Length ratio	$rl = l_u/l_{u-1}$ (5)	Indicates the hierarchical structure and connectivity of stream networks within a basin (drainage development)	Horton (1945)
Rho coefficient	$\rho = rl/rb$ (6)	Indicates channel storage capacity to evacuate floods.	Horton (1945)
(iii) Fluvial intensity			
PIHm	Equation	Description	Reference
Drainage density	$D_d$ (km/km <sup>2</sup> ) = $L/A$ (7)	Measures the stream distribution by basin area. High drainage density indicates higher and faster floods	Horton (1945)
Constant of channel maintenance	$C_M$ (km) = $1/D_d$ (8)	The inverse of Dd indicates sediment transport capacity and erosion potential of drainage networks	Schumm (1956)
Drainage intensity	$D_i = D_d(N_1/A)$ (9)	Indicates both efficiency and capacity of drainage networks to evacuate torrential rainfall	Romero Díaz and López Bermúdez (1987)
Flow velocity	$v$ (m/s) = $0.278(L_c/T_c)$ (10)	Input parameter for Qp and Tp ( $T_c$ computed with CN = 73)	NRCS (2010)
Peak discharge	$Qp$ (m <sup>3</sup> /s) = $0.278A qp$ $qp = (1.31/L_c)rl^{0.43}v$ (11)	Maximum instantaneous discharge during a high-rainfall event (dynamics of flood events)	Rodríguez Iturbe and Valdés (1979)
Time to peak	$Tp$ (h) = $\frac{0.44L_crb^{0.55}ra^{-0.55}rl^{-0.38}}{v}$ (12)	Time interval between the beginning of effective rainfall and the peak discharge (dynamics of flood events)	Rodríguez Iturbe and Valdés (1979)
Potential erosion index	$IPE = (D_iS_B)/m$ (13)	Integrates the three erosion enhancing factors: drainage intensity, average slope and shape	Ferrando (1994)

### 3.4. Validation of results

The quality of the results obtained for each resolution-threshold combination was determined relative to the basin of reference (Fig. 2). Validation involved inspecting for the accuracy in drainage definitions and computed parameters, the variability of resulting morphometric indices, and the implications for flood and water erosion assessments. The stream network was digitized from an Ikonos satellite image captured in 2003 (Google Earth historical archive; © 2022 Maxar Technologies). In addition to exhibiting good quality and resolution, the year of capture falls within the radar missions from which the MDE were derived (2000 and 2010). This permitted to reduce potential shifts resulting from the natural evolution of vegetation and landforms. The basin divide was digitized from a topographic map following the inflections of contour lines (3763-36-3, 1:50,000; IGN, Argentina). The map was projected using the spatial reference transformations defined by the IGN (Campo Inschaupe to POSGAR94, and POSGAR94 to WGS84) to ensure the spatial integrity of the analysis. Relief parameters were also obtained from the topographic map. In this case, however, vertical adjustment was considered unnecessary because basin relief and slope depend on relative elevation differences. Reference PIms were computed from attribute tables and 3D analysis in GIS.

## 4. Results and discussion

### 4.1. DEM accuracy and reliability

Known elevations available from the RN-Ar levelling network range from 199 to 441 m (23 points). Coefficients of determination of equivalent DEM elevation values were close to unity for all three models (0.99), suggesting a very good fit (Fig. 3). Mean errors increased with lower resolution from 3.9 to 4.1 m; this was between 1.4 and 1.5% of known elevations. The error dispersion (RMSE) increased with lower resolution as well from 7.6 to 8.1 m. Accuracy loss with lowering resolution is closely related to complex terrain (Fisher and Tate, 2006), and results from a systematic attenuation of the relief as the DEM resolution becomes coarser (Buakhao and Kangrang, 2016; Datta *et al.*, 2022). Major errors were between 11 and 25°m, and responded mainly to vegetation bias irrespective of resolution. Certainly, SRTM and ALOS DEMs are surface models, and therefore contain vertical noise due to buildings, vegetation and other elements on the terrain surface (Gallant and Read, 2016; Nourani *et al.*, 2013; O'Loughlin *et al.*, 2016).

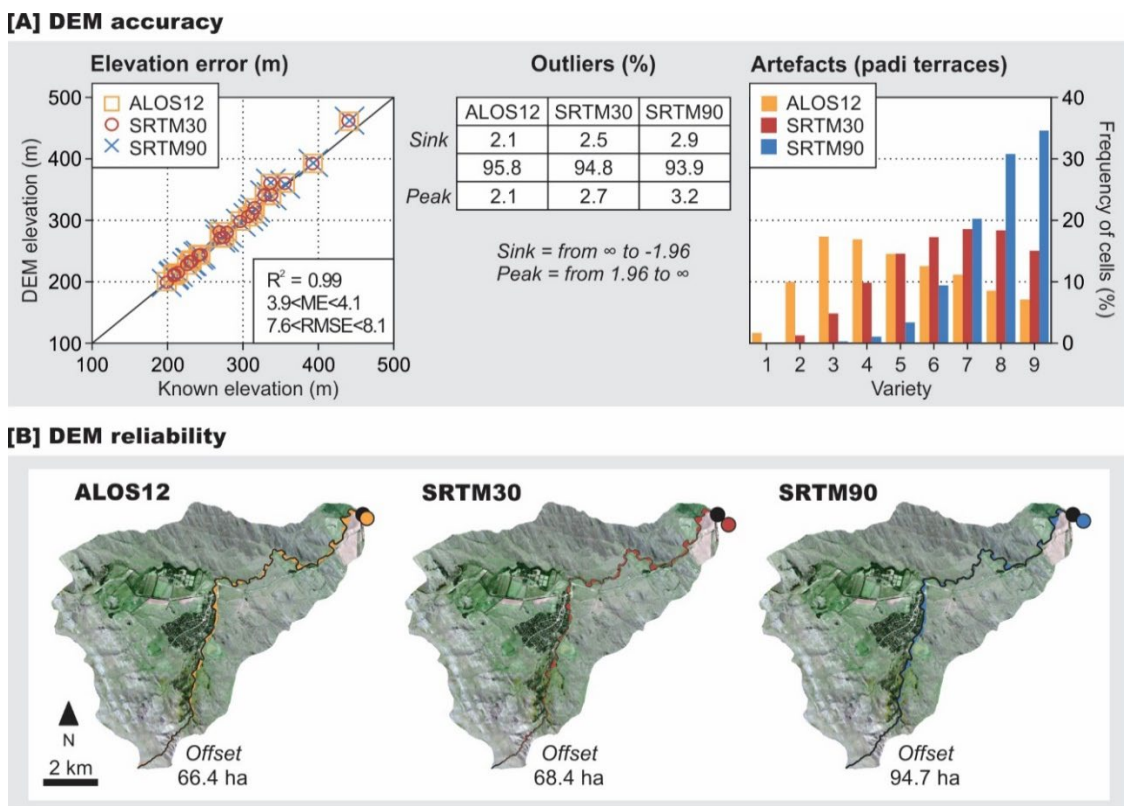


Figure 3. Quality of the input DEMs.

Relative error assessment suggested acceptable DEM quality as well. Outliers were between 4.2 and 6.1%, and at least one cell value was different from the remaining eight neighbouring cell values for 98% of the study basin or more (Fig. 3). Interestingly, the frequency of cells for increasing levels of elevation variety describes contrasting distributions among DEMs. While ALOS12 exhibits a right-skewed distribution (greater proportion of artefacts), SRTM30 distribution is skewed to the left (lesser proportion of artefacts), and SRTM90 is exponentially artefact-free. This responds to the artefact dependence on the spatial and vertical resolution of the source data relative to the terrain forms (Hengl *et al.*, 2004). All three DEMs are integer rasters. This implies that any elevation difference between adjacent grid cells is at least 1 m, and corresponding slopes are 1% (SRTM90), 3% (SRTM30), and 8% (ALOS12). In this regard, artefacts are expected to increase with increasing resolution along with flat terrain.

The spatial offset of DEM-extracted main streams relative to reference was less than 1.5% of the basin surface, suggesting that all three models are reliable to reproduce flow patterns (Fig. 3). However, some stream sections revealed important shifts. This responds to complex relationships between resolution and topography (Buakhao and Kangrang, 2016; Thompson *et al.*, 2001; Wu *et al.*, 2008), along with morphological variations for the same resolution (Boulton and Stokes, 2018), and vegetation noise (Nourani *et al.*, 2013). In the upper basin ( $S_B = 40\%$ ), the fluvial network integrates a branch of v-shaped streams excavated on bedrock with little or no vegetation (Volonté and Gil, 2023). Here, the algorithm is not affected by aggregated elevation values nor vegetation inducing false reliefs, and stream definitions are acceptable for all three models. In the middle and lower sections ( $S_B = 14\%$ ), the main stream excavates quaternary deposits forming a wider channel. The influence of resolution is here apparent yet not widespread, and depends on both stream morphology and vegetation cover. In sections lacking riparian vegetation, lower resolution DEMs smooth channel landforms, and therefore fail to define streams in dynamic sections. This was observed for SRTM90 throughout the entire stream. On the other hand, vegetation bias results in false positive reliefs that shift the stream towards adjacent, lower terrain. In these cases, the higher the resolution, the greater the noise and the greater the probability of computing vegetation as a topographic feature. At the basin scale, however, the advantages (topographic detail) and disadvantages (noise) of higher resolution compensate and, in terms of shift, the quality of the streams extracted from SRTM30 and ALOS12 is higher than that extracted from SRTM90.

#### 4.2. Global basin morphometric parameters

Global basin parameters are affected by DEM resolution only. Basin area and length fit well to reference for all three DEMs (Fig. 4). Notable differences are found for the basin perimeter though, with overestimations ranging from 34% (SRTM90) to 47% (ALOS12) of the reference value. This behaviour may obey to the gridded structure of the models (Wu *et al.*, 2008). Since  $P$  represents the sum of the sides of the grid cells along the basin divide, the greater the number of cells with increasing resolution, the larger the resulting length. We computed a correction factor (FC) to account for the number of cells along the divide for a given resolution ( $p$ ). The expression to obtain a corrected value of  $P$  is as follows:  $P_C = [P / (\text{FC } p)] (p^{2^{0.5}})$ . Given  $\text{FC} \approx 2$ , the  $P_C$  was 36.6 (SRTM90), 36.8 (SRTM30) and 37.0 (ALOS12). Hereafter, any PIm involving the basin perimeter will use  $P_C$  values instead of original  $P$ .

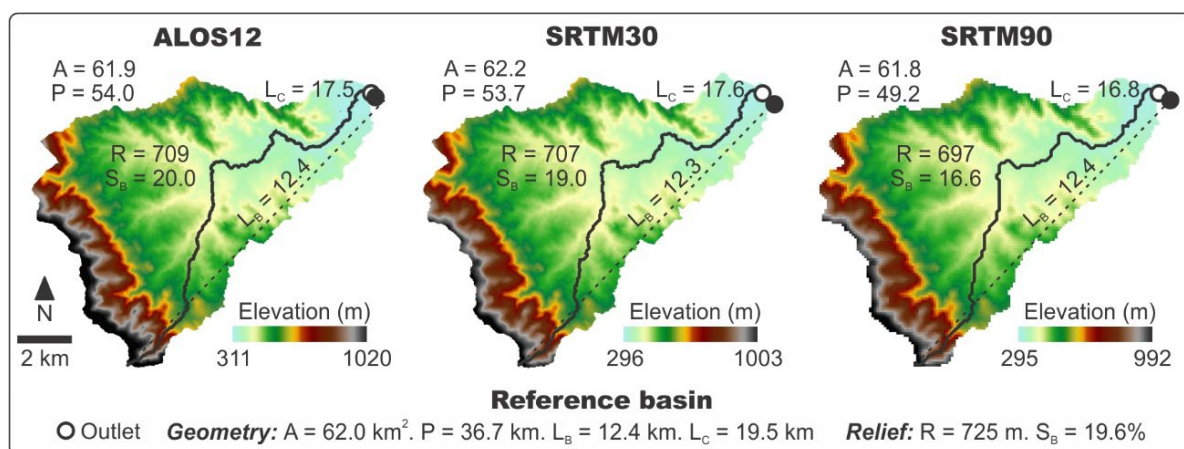


Figure 4. Global basin morphometric parameters for the Arroyo del Oro by DEM resolution.

The effects of the gridded structure of DEMs impact on the longest flow path length as well ( $L_c$ ; Fig. 4). However, in opposition to  $P$ ,  $L_c$  is underestimated in all cases, and remains up to 2 km below the reference length for the best fit (ALOS12). This is a consequence of the way streams are defined. As the algorithm links cell centroids in the flow direction (Wu *et al.*, 2008), one may expect that the

larger the cell size, the larger the length. However, if the channel width is close to (or less than) the grid cell size, then the streams will be defined by straight lines irrespective of their sinuosity, which ultimately affects their total length (Boulton and Stokes, 2018). The ratio of  $L_C$  to  $L_B$  (Schumm, 1956) represents a straightforward index to determine whether the reduced length is due to the DEM structure, to the DEM resolution, or to a combination of both. For the Arroyo del Oro, this ratio ranges from 1.36 (SRTM90) to 1.43 (ALOS12), remaining between 14 and 10% below reference, respectively. Considering that  $L_B$  fits very well for all three models, this suggests that even the smaller cell size used in analysis (12.5 m) is insufficient to capture the sinuosity of the main stream channel.

The effects of DEM resolution are more evident when global relief parameters are considered (Fig. 4). The greater the grid cell size, the greater the terrain smoothing (Buakha and Kangrang, 2016; Wu *et al.*, 2017), and so the basin relief and slope decrease along with decreasing resolution. In addition, the literature reports that terrain smoothing is greater for steep slopes than for flat reliefs. This is of particular interest within mountain basins, where steep and rolling lands dominate over flatlands. For the Arroyo del Oro, the average basin slope was affected by resolution up to 15% below reference (SRTM90), remaining 2% below reference for the model of highest resolution (ALOS12).

#### 4.3. Parameters of drainage composition

Automated stream definition typically differs from reference drainage networks (Niipele and Chen, 2019). In some cases, this is due to scale issues concerning the document used as a base for reference (Gil *et al.*, 2019). On most cases, however, this results from inadequate estimations of the minimum area required to define a stream. Figure 5 illustrates the effects of varying area thresholds ( $A_s$ ) along with varying DEM resolution for stream definition in the Arroyo del Oro basin. Since higher thresholds imply higher minimum areas for a stream channel to initiate (O'Callaghan and Mark, 1984), the larger the area threshold, the greater the impact on the definition of first-order streams. Increasing thresholds result into a progressive simplification of the drainage complexity, and consequently impact on the indices involving Horton's ratios. The best fit was found for the smaller threshold for all parameters and across all three models (Fig. 5).

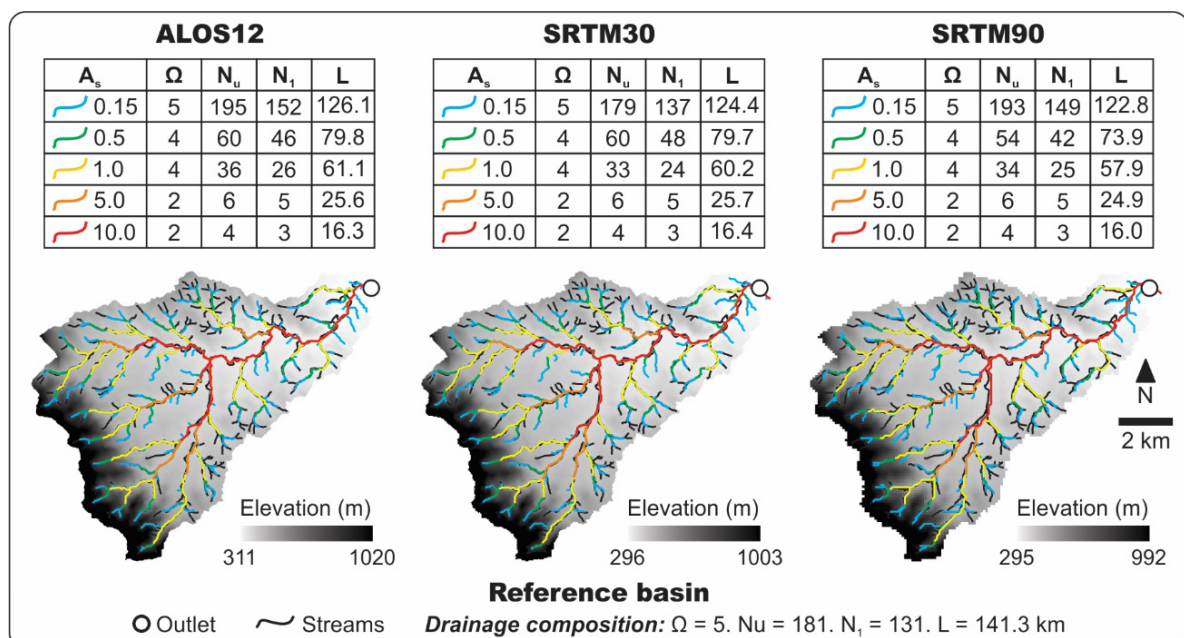


Figure 5. Drainage composition of the Arroyo del Oro by area threshold and DEM resolution.

The effects of resolution on drainage composition are more apparent for the stream length than for the number of streams (Fig. 5). While  $L$  increases with resolution like  $L_C$ ,  $N_u$  and  $N_l$  vary among the models with unclear relationships. Visual comparison to reference shows that all DEMs provide fairly accurate delineations of higher order streams, but not accurate enough for the lowest orders. Major shifts concern first-order streams. Many collectors in the headwaters are omitted, whereas many false segments are depicted along the main streams. However, omissions and additions compensate for the entire basin, with SRTM30 providing the best fit. Similar results were found by Li and Wong (2010), who suggested that an optimal threshold may not exist for the entire basin due to local variations in topography. This was reported by early studies (Lopez García and Camarasa Belmonte, 1999; Montgomery and Foufoula Georgiou, 1993), by Lee and Kim (2011), and more recently by Wu *et al.* (2017). Another possible source for this problem was more recently proposed by Dávila Hernández *et al.* (2022), who found that fill sink and flow routing algorithms, relative to the DEM resolution, may affect the definition of pits governing the water movement through the model. Similarly, Wang *et al.* (2019) reviewed existing sink-processing algorithms, and discussed existing ways of improving their computation efficiency to provide a satisfactory solution to this issue.

#### 4.4. Morphometric indices

Table 4 summarizes the indices that depend on global characteristics of the drainage basin, and so are unaffected by the area threshold. The compactness coefficient ( $m$ ) is within the limits of variation for slightly rectangular basins (Zavoianu, 1985), with very good fit and small differences among the three models. This occurs because basin area and perimeter (corrected) adjust well for all DEMs, and are therefore suitable for basin shape-derived indices. The relief ratio exhibits good fit as well, and therefore indicates that terrain smoothing with increasing grid cell size has no major implications relative to the basin length. The effects of DEM resolution emerge for flow velocity, and respond to both reduced  $L_C$  and  $S_B$  for all models, with maximum difference for SRTM90.

Table 4. Basin geometry- and relief-derived morphometric indices for the Arroyo del Oro by DEM resolution.

Morphometric Index	Reference basin	ALOS12	SRTM30	SRTM90	Best fit (%)	Max. difference (%)
Compactness coeff. (m)	1.31	1.31	1.31	1.31	--	--
Relief ratio (r)	0.06	0.06	0.06	0.06	--	--
Flow velocity (v, m/s)	4.43	4.36	4.28	4.02	-1.7 (ALOS12)	-9.3 (SRTM90)

The remaining indices depend on the drainage composition to a greater or lesser extent, and are therefore affected by both DEM resolution and area threshold. Errors in index estimations were computed as residuals between extracted and reference PIM for each resolution-threshold combination. To ensure readability of the results, errors are expressed as deviations relative to reference values (Fig. 6). Since the best fit for drainage parameters was found for the lowest area threshold, all indices exhibit the smaller deviations for  $As = 0.15\%$ . In terms of resolution, however, no generalizations can be made through the indices. This is due to compensation and/or accumulation of errors resulting from computation of the parameters involved in each case. Resolution-related deviations behave differently among the indices, and will have different implications for flood and water erosion assessment.

Bifurcation and length ratios ( $rb$ ,  $rl$ ) provide information on the basin efficiency and capacity to evacuate flows (Zavoianu, 1985), and remain of current interest for flood assessment (Shekar and Mathew, 2024). For  $As = 0.15\%$ ,  $rb$  and  $rl$  exhibit good fit for the three models (Fig. 5), and remain within the normal range for mountain basins with good drainage capacity (Horton, 1945). Deviations of the bifurcation ratio are positive and greater in magnitude than for the length ratio. This is due to overestimation of first-order streams, and concerns the three DEMS. Shorter stream lengths, as provided

by all models, do not necessarily affect  $rl$  because such reduction remains constant among orders. Thus,  $rl$  deviations remain below 2% of the reference value, and compensate the deviations of  $rb$  for computation of the rho coefficient. Note that the perfect fit of  $\rho$  for  $As = 1\%$  is specious, and results from  $rb$  and  $rl$  deviations of similar magnitude and direction. For  $As > 1\%$ ,  $rb$  and  $rl$  deviations result in values of  $\rho$  greater than 82% of reference values, denoting drainage basins with greater attenuation of flows and erosion (Horton, 1945).

The peak discharge ( $Q_p$ ) and the time to peak ( $T_p$ ) are the basic parameters of the direct runoff hydrograph. In this study,  $Q_p$  and  $T_p$  were computed based on the Geomorphological Instantaneous Unit Hydrograph (GIUH) developed by Rodríguez Iturbe and Valdés (1979), which links the unit hydrograph with Horton's laws. The best fit for  $Q_p$  is found for area thresholds below the standard (Fig. 5), with deviations between 3% (SRTM90) and 8% (ALOS12) for  $As = 0.15\%$ . Considering that  $Q_p$  is a product of velocity, and that velocity is underestimated for the three resolutions (Table 4), it follows that positive deviations of  $Q_p$  respond to lower drainage capacity due to shorter main stream length,  $L_C$ . This ultimately leads to greater water accumulation, and so  $Q_p$  values are higher than reference. The time to peak exhibited very good fit for the three DEMs, with differences between 1% (ALOS12) and 9% (SRTM90). Here, shorter  $L_C$  values compensate with higher  $rb$ , while  $rl$  values remain close to reference in all three cases. The best fit is obtained for ALOS12, as it yields the smallest deviations for the majority of the PIm involved in computation of both  $Q_p$  and  $T_p$ .

Deviations of the remaining indices are linked to the area threshold more than to the DEM resolution (Fig. 6). Increasing  $As$  leads to reduced total length, with deviations up to -89% (SRTM90) for the highest threshold ( $As = 10\%$ ). This consequently affects drainage density ( $D_d$ ) and the constant for channel maintenance ( $C_M$ ). Best fits are found for  $As = 0.15\%$ , although shorter stream lengths lead to  $D_d$  deviations between -11% (ALOS12) and -13% (SRTM90) relative to the reference basin. Because all three models provide a greater number of first-order streams,  $N_1$  compensates for reduced total length, and the drainage intensity  $D_i$  shows better fit than the drainage density. Yet  $D_i$  deviations increase notably with increasing thresholds due to progressive simplification of the stream network, and have greatest influence on the erosion potential index.

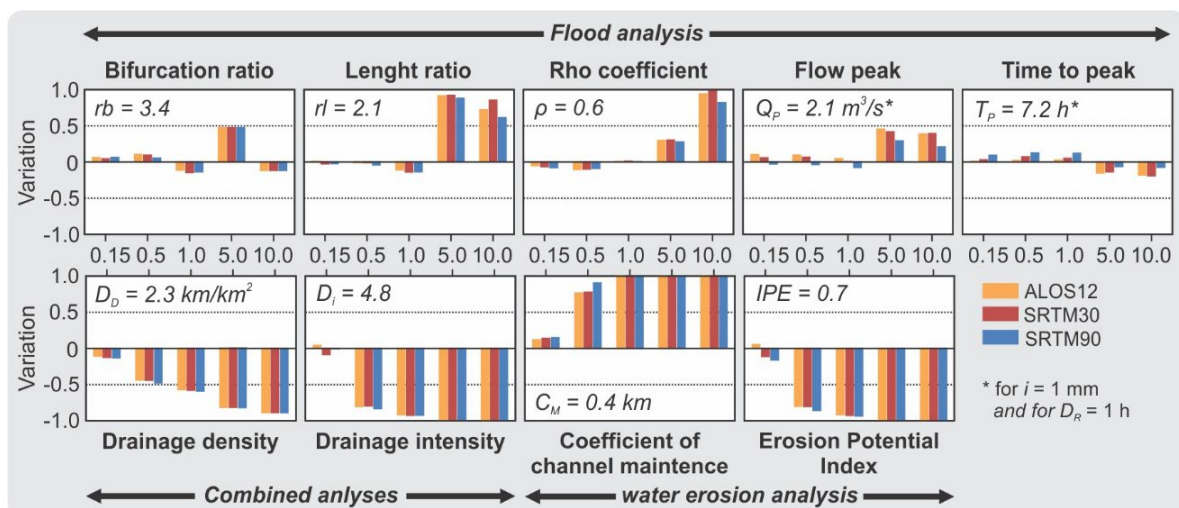


Figure 6. Deviation of morphometric indices relative to reference values by DEM resolution and area threshold. Arroyo del Oro basin.

#### 4.5. What resolution and what threshold for what application?

The accuracy of global basin parameters will depend primarily on the choice of the input DEM, as these properties do not depend on the definition of streams. Within the Arroyo del Oro basin, all three DEMs yielded acceptable results for area, perimeter (corrected), basin length, and shape-related indices (Fig. 7). This is an interesting outcome, suggesting that studies based on applications other than terrain description may rely on middle- to low-resolution DEMs without significant performance loss. On the other hand, slope was clearly affected by resolution, with the best fit for ALOS12. Yet SRTM models yielded acceptable results as well, and thus may provide important processing benefits in cases where the basin size represents a computational challenge (Boulton and Stokes, 2018; Buakhao and Kangrang, 2016; Courty *et al.*, 2019). In addition, results showed that area thresholds greater than standard may notably contribute to reduce the number of basins units to merge for global geometry and relief analysis. While the 10% threshold ( $6.2 \text{ km}^2$ ) allowed detecting the main subbasins identified for the study area, trial and error analysis revealed that thresholds of 25% ( $15.5 \text{ km}^2$ ) or greater may be used to obtain a single basin unit along with its corresponding longest flow path, which ultimately allows avoiding subbasin merging.

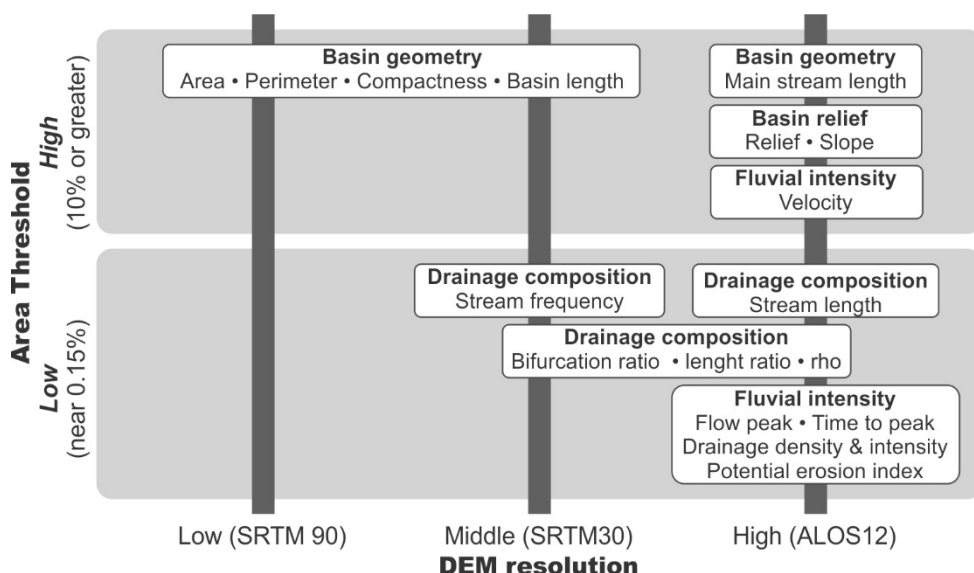


Figure 7. Synthesis of the results.

PIm relying on the accuracy of the drainage network exhibited strong dependence on the area threshold, with 0.15% providing the best results (Fig. 7). Trial and error revealed that thresholds greater than  $0.1 \text{ km}^2$  ( $\sim 0.17\%$ ) resulted on stream frequency and length reductions of up to 6 and 15%, respectively, affecting all composition and intensity indices. Results for thresholds below  $0.09 \text{ km}^2$  ( $\sim 0.14\%$ ) showed improvements of the stream length, but overestimation of the stream frequency. This resulted in better adjustment of drainage density and  $Dd$ -derived indices, but yielded greater shifts for the indices depending on the number of streams. Accordingly, the best match is near  $0.1 \text{ km}^2$ , and it is therefore close to the threshold tested here. Even though the potential for transferability of such threshold to other regional basins remains to be evaluated, these results highlight the potential risks of the systematic use of most popular hydro-processing tools. Indeed, the 1% threshold resulted in the omission of first-order streams by 82%, and reduced the total stream length by 57%.

The relationship between accuracy and resolution for the same threshold was comparatively less clear, due to the compensation (or accumulation) of errors in the extraction of morphometric parameters. For drainage composition PIm, resolution-related differences were not much important and, for  $As = 0.15\%$ , results were within the range of variability of the reference basin. Comparatively, SRTM30

yielded the best balance between accuracy and processing demand, being particularly suitable for flood-related studies building on Horton ratios, while ALOS12 provided better slope and length adjustment, being best suited to flood and water erosion applications using indices of fluvial intensity.

#### 4.6. Further research perspectives

Regardless of the acceptable quality of the results, we identified some issues in the definition of the streams that merit further investigation. First, all three DEMs failed to define first-order streams, omitting collectors in the headwaters and depicting false segments in the middle and lower sections. This may be related to the effects of local topography and geology on the definition of an optimal area threshold for the entire basin (Lee and Kim, 2011; Li and Wong, 2010; Wu *et al.*, 2017), as well as to the use of standard algorithms for fill sink and flow routing (Dávila Hernández *et al.*, 2022; Wang *et al.*, 2019), depicting two important issues that need to be addressed before extracting topographic attributes and terrain features from DEMs. Second, input DEMs used in this study are global surface models, and therefore contain vegetation bias that result in greater noise as the model resolution becomes finer (Nourani *et al.*, 2013). In this regard, further research should evaluate the potential accuracy benefits of using bare-earth models (Gallant and Read, 2016; O'Loughlin *et al.*, 2016), as well as the newer version of the SRTM30 (NASADEM), offering updated and refined elevation data. Furthermore, elevation data used in the study is 24 year-old (SRTM) and 14 year-old (ALOS). Thus, exploring for evolving links between fluvial forms and processes along with land use change, by means of automated morphometry, would strengthen the temporal validity of the results. Although these approaches exceed the scope of the present study, they inform of the complexity of parameters involved in extracting reliable drainage networks from DEMs. Therefore, they open to an array of further research perspectives that need to be addressed prior to evaluating the potential of transferability of the present results to other regional basins.

### 5. Conclusions

Automated morphometric analysis deals with two important challenges. These are linked to the choice of a suitable DEM resolution, and to the definition of an area threshold that holds for reference Horton's ratios. This study examined and compared the applicability of three global DEMs of different resolution (ALOS12, SRTM30 and SRTM90 m) and five area thresholds (0.15 to 10%) for the extraction of morphometric parameters and indices (PIm) within a mountain basin with varying topography. The results indicated that neither optimal nor generalized resolution-threshold combinations may be derived among PIm. In applications that depend on drainage composition, the definition of an appropriate threshold is more important than the resolution of the input model. The best fit was found for  $As = 0.15\%$  for all three DEMs, with differences that remained within the range of variability of the reference basin in all cases. Comparatively, SRTM30 provided the best balance between accuracy and time processing, being particularly suitable for applications linked to flood assessment. In the case of studies focusing on the erosion potential of basins, however, ALOS12 may yield better results as it fits better for slope-dependent parameters and indices. In the context of applications based on global basin parameters, the use of lower resolution and higher area thresholds may contribute to reduce processing times without significant performance loss. Despite the analysis focused on a 62 km<sup>2</sup> pilot basin, findings from this investigation inform on the regular issues linked to data and parameter selection decisions in watershed modelling, having wider testing applicability to other regional basins along with varying spatial scales.

### Acknowledgements

The authors duly thank the international space agencies, the National Aeronautics and Space Administration of the USA (NASA) and the Japan Aerospace Exploration Agency (JAXA), as well as the Alaska Satellite Facility (ASF) and the Instituto Geográfico Nacional (IGN Argentina) for providing

open access to terrain data. Funding was provided by the National Council of Scientific and Technical Research (CONICET) through the Multi-year Research Project (PIP, for its Spanish acronym) with code number 2022/24 0358, and by the Secretaría de Ciencia y Tecnología de la Universidad Nacional del Sur through the Research Group Project (PGI, for its Spanish acronym) with code number 24/G092.

## References

- Boulton, S.J., Stokes, M., 2018. Which DEM is best for analyzing fluvial landscape development in mountainous terrains? *Geomorphology* 310, 168-187. <https://doi.org/10.1016/j.geomorph.2018.03.002>
- Buakhao, W., Kangrang, A., 2016. DEM resolution impact on the estimation of the physical characteristics of watersheds by using SWAT. *Advances in Civil Engineering* 2016, e8180158. <https://doi.org/10.1155/2016/8180158>
- Casado, A., 2021. Rainfall-runoff modelling in dryland catchments, Sauce Grande, Argentina. *Tecnología y ciencias del agua* 12, 254-303. <https://doi.org/10.24850/j-tyca-2021-05-06>
- Casado, A., Peiry, J.-L., Campo, A.M., 2016. Geomorphic and vegetation changes in a meandering dryland river regulated by a large dam, Sauce Grande River, Argentina. *Geomorphology* 268, 21-34. <https://doi.org/10.1016/j.geomorph.2016.05.036>
- Courty, L.G., Soriano Monzalvo, J.C., Pedrozo Acuña, A., 2019. Evaluation of open-access global digital elevation models (AW3D30, SRTM, and ASTER) for flood modelling purposes. *Journal of Flood Risk Management* 12, e12550. <https://doi.org/10.1111/jfr3.12550>
- da Ros, D., Borga, M., 1997. Use of digital elevation model data for the derivation of the geomorphological instantaneous unit hydrograph. *Hydrological processes* 11, 13-33. [https://doi.org/10.1002/\(SICI\)1099-1085\(199701\)11:1<13::AID-HYP13>3.0.CO;2-1](https://doi.org/10.1002/(SICI)1099-1085(199701)11:1<13::AID-HYP13>3.0.CO;2-1)
- Dávila Hernández, S., González Trinidad, J., Júnez Ferreira, H.E., Bautista Capetillo, C.F., Morales de Ávila, H., Cázares Escareño, J., Ortiz Letechipia, J., Robles Rovelo, C.O., López Baltazar, E.A., 2022. Effects of the Digital Elevation Model and hydrological processing algorithms on the geomorphological parameterization. *Water* 14, 2363. <https://doi.org/10.3390/w14152363>
- Datta, S., Karmakar, S., Mezbahuddin, S., Hossain, M.M., Chaudhary, B.S., Hoque, M.E., Abdullah Al Mamun, M.M., Baul, T.K., 2022. The limits of watershed delineation: implications of different DEMs, DEM resolutions, and area threshold values. *Hydrology Research* 53, 1047-1062. <https://doi.org/10.2166/nh.2022.126>
- Felicísimo, A.M., 1994. Parametric statistical method for error detection in digital elevation models. *ISPRS Journal of Photogrammetry and Remote Sensing* 49, 29-33. [https://doi.org/10.1016/0924-2716\(94\)90044-2](https://doi.org/10.1016/0924-2716(94)90044-2)
- Ferrando, F.J., 1994. Métodos hidromorfométricos para determinar la erosividad en cuencas hidrográficas. *Tecnología y ciencias del agua* 9, 5-14.
- Fisher, P.F., Tate, N.J., 2006. Causes and consequences of error in digital elevation models. *Progress in Physical Geography* 30, 467-489. <https://doi.org/10.1191/030913306pp492ra>
- Gallant, J., Read, A., 2016. A near-global bare-Earth DEM from SRTM. The International Archives of the Photogrammetry, Remote Sensing and Spatial Information Sciences 41, 137-141. <https://doi.org/10.5194/isprs-archives-XLI-B4-137-2016>
- Gil, V., 2012. Geomorfología y procesos de vertiente. Cuenca alta del río Sauce Grande (Buenos Aires, Argentina). *Cuaternario y Geomorfología* 26, 133-150.
- Gil, V., Gentili, J., Campo, A.M., Jelinski, G., Crisafulli, M., 2016. Evaluación del peligro potencial de crecidas en cuencas serranas. Sistema de Ventania, provincia de Buenos Aires. *III Encuentro de Investigadores en Formación en Recursos Hídricos*, Ezeiza, Argentina.

- Gil, V., Volonte, A., Campo, A.M., 2019. Índices morfométricos a diferentes escalas aplicados al peligro de crecidas en cuencas pequeñas. Cuenca del arroyo San Bernardo, Argentina. *Revista Brasileira de Geomorfología* 20, 811-824. <https://dx.doi.org/10.20502/www.ugb.org.br>
- Gil, V., Zapperi, P., Campo, A.M., Iuorno, M.V., Ramborger, M.A., 2008. Análisis de las precipitaciones de otoño y primavera en el Suroeste bonaerense. *VII Jornadas de Geografía Física*, Jujuy, Argentina.
- Gravelius, H., 1914. *Grundriß der gesamten Gewässerkunde. Band I: Flußkunde (Compendium of Hydrology. Volume I: Rivers)*. Göschen, Berlin, Germany.
- Hancock, G.R., 2005. The use of digital elevation models in the identification and characterization of catchments over different grid scales. *Hydrological Processes* 19, 1727-1749. <https://doi.org/10.1002/hyp.5632>
- Hengl, T., Gruber, S., Shrestha, D., 2004. Reduction of errors in digital terrain parameters used in soil-landscape modelling. *International Journal of Applied Earth Observation* 5, 97-112. <https://doi.org/10.1016/j.jag.2004.01.006>
- Horton, R.E., 1945. Erosional development of streams and their drainage basins: hydrophysical approach to quantitative morphology. *Bulletin of the Geological Society of America* 56, 275-370.
- INDEC, 2022. Censo Nacional de Población, Hogares y Viviendas 2022. Bases de datos REDATAM. Available at: <https://redatam.indec.gob.ar/> (last access: 23/12/2024).
- INTA, 2018. Carta de suelos de la República Argentina. 3963-5 TORNQUIST Available at: <https://zenodo.org/records/7837681> (last access: 23/12/2024).
- Lee, G., Kim, J.C., 2011. Comparative analysis of geomorphologic characteristics of DEM-based drainage networks. *Journal of Hydrologic Engineering* 16, 137-147. [https://doi.org/10.1061/\(ASCE\)HE.1943-5584.0000295](https://doi.org/10.1061/(ASCE)HE.1943-5584.0000295)
- Li, J., Wong, D., 2010. Effects of DEM sources on hydrologic applications. *Computers, Environment and Urban Systems* 34, 251-261. <https://doi.org/10.1016/j.compenvurbsys.2009.11.002>
- Lopez García, M.J., Camarasa Belmonte, A.M., 1999. Use of geomorphological units to improve drainage network extraction from a DEM: Comparison between automated extraction and photointerpretation methods in the Carraixet catchment (Valencia, Spain). *International Journal of Applied Earth Observation and Geoinformation* 1, 187-195. [https://doi.org/10.1016/S0303-2434\(99\)85012-0](https://doi.org/10.1016/S0303-2434(99)85012-0)
- Montgomery, D.R., Foufoula Georgiou, E., 1993. Channel network source representation using digital elevation models. *Water Resources Research* 29, 3925-3934. <https://doi.org/10.1029/93WR02463>
- NASA JPL., 2021. *NASADEM Merged DEM Global 1 arc second V001*. Distributed by OpenTopography. <https://doi.org/10.5069/G93T9FD9>. Accessed: 2024-12-16
- Niipele, J.N., Chen, J., 2019. The usefulness of alos-palsar dem data for drainage extraction in semi-arid environments in The Iishana sub-basin. *Journal of Hydrology: Regional Studies* 21, 57-67. <https://doi.org/10.1016/j.ejrh.2018.11.003>
- Nourani, V., Mokhtarian-Asl, S., Khosravi-Sorkhkolaee, M., Sharghi, E., 2013. Effect of DEM type and resolution in extraction of hydro-geomorphologic parameters. In: V. Mladenov (Ed.), *Recent Advances in Continuum Mechanics, Hydrology and Ecology*. WSEAS, Rhodes Island, Greece, pp. 98-103.
- NRCS, 2010, *Part 630: Hydrology, Chapter 15: Time of concentration*. Natural Resources Conservation Service, USDA, Washington DC, USA, 29 pp.
- O'Callaghan, J.F., Mark, D.M., 1984. The extraction of drainage networks from digital elevation data. *Computer vision, graphics, and image processing* 28, 323-344. [https://doi.org/10.1016/S0734-189X\(84\)80011-0](https://doi.org/10.1016/S0734-189X(84)80011-0)
- O'Loughlin, F.E., Paiva, R.C., Durand, M., Alsdorf, D., Bates, P., 2016. A multi-sensor approach towards a global vegetation corrected SRTM DEM product. *Remote Sensing of Environment* 182, 49-59. <https://doi.org/10.1016/j.rse.2016.04.018>
- Ozulu, I.M., Gökgöz, T., 2018. Examining the stream threshold approaches used in hydrologic analysis. *ISPRS International Journal of Geo-Information* 7, 201. <https://doi.org/doi:10.3390/ijgi7060201>

- Rodríguez Iturbe, I., Valdés, J.B., 1979. The geomorphologic structure of hydrologic response. *Water resources research* 15, 1409-1420. <https://doi.org/10.1029/WR015i006p01409>
- Romero Díaz, M.A., López Bermúdez, F., 1987. Morfometría de redes fluviales: revisión crítica de los parámetros más utilizados y aplicación al Alto Guadalquivir. *Papeles de Geografía* 12, 47-62.
- Scian, B., 2000. Episodios ENSO y su relación con las anomalías de precipitación en la pradera pampeana. *Geoacta* 25, 23-40.
- Schumm, S.A., 1956. Evolution of drainage systems and slopes in badlands at Perth Amboy, New Jersey. *Geological society of America bulletin* 67, 597-646. [https://doi.org/10.1130/0016-7606\(1956\)67\[597:EODSAS\]2.0.CO;2](https://doi.org/10.1130/0016-7606(1956)67[597:EODSAS]2.0.CO;2)
- Shekar, P.R., Mathew, A., 2024. Morphometric analysis of watersheds: a comprehensive review of data sources, quality, and geospatial techniques. *Watershed Ecology and the Environment* 6, 13-25. <https://doi.org/10.1016/j.wsee.2023.12.001>
- Tarboton, D.G., Bras, R.L., Rodriguez Iturbe, I., 1991. On the extraction of channel networks from digital elevation data. *Hydrological Processes* 5, 81-100. <https://doi.org/10.1002/hyp.3360050107>
- Thompson, J.A., Bell, J.C., Butler, C.A., 2001. Digital elevation model resolution: effects on terrain attribute calculation and quantitative soil-landscape modeling. *Geoderma* 100, 67-89. [https://doi.org/10.1016/S0016-7061\(00\)00081-1](https://doi.org/10.1016/S0016-7061(00)00081-1)
- USACE, 2023, *Hydrologic Modeling System HEC-HMS User's Manual* Hydrologic Engineering Center, U.S. Army Corps of Engineers, Davis, CA, USA.
- Volonté, A., Gil, V., 2023. Diagnóstico y monitoreo de ambientes fluviales a partir de geoindicadores. Cuenca del Oro (Argentina). *Cuadernos Geográficos* 62, 130-149. <https://doi.org/10.30827/cuadgeo.v62i1.25343>
- Wang, Y.-J., Qin, C.-Z., Zhu, A.-X., 2019. Review on algorithms of dealing with depressions in grid DEM. *Annals of GIS* 25, 83-97. <https://doi.org/10.1080/19475683.2019.1604571>
- Wu, M., Shi, P., Chen, A., Shen, C., Wang, P., 2017. Impacts of DEM resolution and area threshold value uncertainty on the drainage network derived using SWAT. *Water SA* 43, 450-462. <https://doi.org/10.4314/wsa.v43i3.10>
- Wu, S., Li, J., Huang, G.H., 2008. A study on DEM-derived primary topographic attributes for hydrologic applications: Sensitivity to elevation data resolution. *Applied Geography* 28, 210-223. <https://doi.org/10.1016/j.apgeog.2008.02.006>
- Zapperi, P., Casado, A., Gil, V., Campo, A.M., 2006. Caracterización de las precipitaciones invernales en el Suroeste bonaerense. In: N. Cazzaniga, M. Vaquero (Eds.), *Ambiente natural, campo y ciudad: Estrategias de uso y conservación en el Sudoeste Bonaerense*. Ediciones UNS, Bahía Blanca, pp. 63-68.
- Zapperi, P., Ramos, B., Gil, V., Campo, A.M., 2007. Caracterización de las precipitaciones estivales en el Suroeste bonaerense. In: *Contribuciones Científicas*. GAEA, Posadas, pp. 483-491.
- Zavoianu, I., 1985. *Morphometry of drainage basins. Serie 20: developments in water science*. Elsevier, Amsterdam, Nederlands.





# THE ROLE OF GREEN ROOFS IN CLIMATE CHANGE MITIGATION AND ADAPTATION: ANALYZING PERFORMANCE DURING EXTREME RAINFALL EVENTS

ANDREA S. BREND<sup>1,2\*</sup> , FEDERICO FERRELLI<sup>1,3</sup> ,  
MAXIMILIANO GARAY<sup>2</sup> , AGUSTINA GUTIERREZ<sup>4,5</sup>,  
VANESA PERILLO<sup>1,4</sup> , MARIA CINTIA PICCOLO<sup>1,3</sup>

<sup>1</sup>*Instituto Argentino de Oceanografía (IADO, CONICET/UNS), Camino La Carrindanga Km 7 E1,  
Bahía Blanca B8000CPB, Buenos Aires, Argentina.*

<sup>2</sup>*Departamento de Agronomía, Universidad Nacional del Sur,  
San Andrés 612, Bahía Blanca B8001, Buenos Aires, Argentina.*

<sup>3</sup>*Departamento de Geografía y Turismo, Universidad Nacional del Sur, 12 de Octubre  
1098 Cuarto Piso, Bahía Blanca B8000CTX, Buenos Aires, Argentina.*

<sup>4</sup>*Departamento de Biología, Bioquímica y Farmacia, Universidad Nacional del Sur,  
San Juan 670 Piso 1, Bahía Blanca B8000ICN, Buenos Aires, Argentina.*

<sup>5</sup>*Centro de Recursos Naturales Renovables de la Zona Semiárida (CERZOS, CONICET/UNS),  
Camino La Carrindanga Km 7 E1, Bahía Blanca B8000CPB, Buenos Aires, Argentina.*

**ABSTRACT.** This study evaluated the water storage and runoff capacities of an extensive green roof simulator in Bahía Blanca, Argentina, during the region's most extreme precipitation event in 47 years. The analysis involved a time series of daily precipitation from 1961 to 2022. A Green Roof model was applied using daily precipitation data, potential evapotranspiration, and field-measured water storage capacity data from 2022. The model was based on a 1 m<sup>2</sup> green roof simulator, with 50 % of its surface covered by native species. The substrate depth was set at 15 cm, with a soil water storage capacity of 58.7 mm. Precipitation in Bahía Blanca showed considerable variability across temporal scales. The most frequent events (89 %) involved less than 20 mm of rainfall, followed by events between 20.1 mm and 40 mm (8 %). Eight events with precipitation between 80.1 mm and 100 mm were recorded, with March 24, 2022, marking the highest daily rainfall in 15 years (90.3 mm). However, when examining three-day accumulated rainfall, the period from March 23 to 25, 2022, accumulated 150.3 mm, making it the most extreme event in the last 47 years and the second highest in the 62 years analyzed. During this event, total runoff amounted to 83.4 mm, indicating a substantial water storage of 44.6 % by the green roof simulator. Given the projected increase in the frequency and intensity of extreme rainfall events, green roofs offer a sustainable and innovative solution for mitigating and adapting to climate change impacts. Additionally, they serve as crucial urban green infrastructures for managing runoff, particularly in regions prone to intense precipitation events like Bahía Blanca.

***El papel de los techos verdes en la mitigación y adaptación al cambio climático: análisis de su efectividad durante eventos de lluvia extrema***

**RESUMEN.** En este estudio se evaluó la capacidad de almacenamiento de agua y escorrentía de un simulador de techo verde extensivo en la ciudad de Bahía Blanca (Argentina), durante el evento de precipitación más extremo de los últimos 47 años. Para ello, se analizó la serie temporal de precipitación diaria del período 1961-2022. Se utilizó el modelo Green Roof con datos de precipitación y evapotranspiración potencial diaria y de capacidad de campo medidas *in situ* durante el año 2022 y se seleccionó el período más extremo en términos de precipitación. El modelo se aplicó considerando un simulador de techo verde con una superficie de 1 m<sup>2</sup>, cubierto al 50 % por

especies nativas. La profundidad del sustrato fue 15 cm y la capacidad máxima de almacenamiento de agua del suelo fue 58,7 mm. Bahía Blanca presentó una marcada variabilidad de las precipitaciones a diferentes escalas temporales. Las precipitaciones más frecuentes fueron las menores de 20 mm (89 %), seguidas de las de entre 20,1 y 40 mm (8 %). Se detectaron ocho eventos entre 80,1 mm y 100 mm, entre los que destaca el de 24 de marzo de 2022 por ser el evento de mayor precipitación diaria de los últimos 15 años (90,3 mm). Sin embargo, al analizar las precipitaciones acumuladas en tres días consecutivos, se observó que la cantidad registrada durante el período 23-25 de marzo (150,3 mm) fue la más extremo de los últimos 47 años y la segunda más importante de los 62 años analizados. Durante este evento se generó una escorrentía total de 83,4 mm, lo que indica que el simulador de techo verde tuvo una buena capacidad de almacenamiento de agua, alcanzando un 44,6 %. Considerando que se prevé un aumento en la frecuencia e intensidad de eventos pluviométricos extremos, los techos verdes representan una alternativa innovadora y sostenible para mitigar y adaptarse a los efectos del cambio climático, permitiendo además gestionar la escorrentía en entornos urbanos, particularmente en regiones con eventos pluviométricos extremos frecuentes, como Bahía Blanca.

**Keywords:** Green roof, water balance model, runoff, extreme precipitation events, native species, sustainable cities.

**Palabras clave:** techo verde, modelo de balance hídrico, escorrentía, eventos extremos de precipitación, especies nativas, ciudades sostenibles.

Received: 15 October 2024

Accepted: 13 May 2025

**\*Corresponding author:** Andrea Brendel, Instituto Argentino de Oceanografía (IADO, CONICET/UNS), Camino La Carrindanga Km 7 E1, Bahía Blanca B8000CPB, Buenos Aires, Argentina. E-mail: asbrendel@iado-conicet-gob.ar; andreabrendeluns@gmail.com

## 1. Introduction

Urban expansion has transformed natural areas into impermeable surfaces, altering their hydrological patterns and flow regimes (Zhang *et al.*, 2018). Among the most significant changes resulting from this process are the increase in peak flows, the reduction in water concentration times, the modification of the water balance, and the increase in surface runoff volume (Li *et al.*, 2018; Paule-Mercado *et al.*, 2017). Additionally, climate change has caused a significant increase in the frequency and intensity of extreme precipitation events, directly affecting the recurrence and magnitude of flooding in numerous cities (Berggren *et al.*, 2012; Pour *et al.*, 2020). Therefore, rapid urbanization and climate change are expected further to increase the risk of flooding in the near future (Yin *et al.*, 2015; Zhou *et al.*, 2019). Among the mitigation measures implemented worldwide, green roofs are one of the most adopted, as they can be easily installed on existing buildings without requiring additional land space (Carter and Jackson, 2007). Moreover, these green infrastructures provide multiple environmental benefits, such as water quality purification (Rowe, 2011), reduction of building temperatures and the urban heat island effect (He *et al.*, 2020), as well as contributing to the decrease of air pollution (Speak *et al.*, 2012). Furthermore, they mitigate greenhouse gas emissions by promoting carbon absorption and retention, which aids in reducing CO<sub>2</sub> levels in the atmosphere (Perillo *et al.*, 2023).

Green roofs can mitigate stormwater runoff by collecting and retaining precipitation, reducing the flow volume to conventional stormwater infrastructure (Driscoll *et al.*, 2015). The water storage capacity depends on several factors, including the construction conditions of the green roof, such as substrate type and vegetation, slope, and drainage system, among others. Studies on the capacity of these infrastructures to store precipitation and manage urban runoff are becoming increasingly common worldwide, but in Argentine cities, they remain scarce. Mentens *et al.* (2006) analyzed 18 extensive

green roofs with different growing media and vegetation coverage in Central Europe and found an average runoff reduction of 50 %. In New York, it was demonstrated that a green roof on a commercial building retains 89 % of water during intense rains (> 25 mm/event) (Todorov *et al.*, 2018), while in a semi-arid region of China with an annual precipitation of 425 mm/year, green roofs showed water storage ranging from 34.7 % to 48.5 %, depending on the substrate moisture level before the precipitation event (Liu *et al.*, 2020). A study in Lisboa (Portugal), which shares a climate comparable to the study area, revealed a 73 % rainwater storage capacity rate in green roofs (Brandão *et al.*, 2017). Despite this, studies on how green roofs manage water storage and runoff during extreme precipitation events have not yet been conducted in Bahía Blanca, Argentina.

This study investigates the hydrological dynamics of a green roof system in Bahía Blanca city, Argentina, by applying a water balance model to a green roof simulator (Figs. 1 and 2). The approach combines physical measurements from the simulator with hydrological modeling to evaluate performance during extreme precipitation events. While the simulator provided essential data on substrate and vegetation characteristics, the model enabled the assessment of water storage and runoff dynamics under various precipitation conditions. The green roof simulator is located in Bahía Blanca city (Argentina) (Fig. 1), in the lower basin of the Napostá Grande stream, whose course crosses the city and originates from the Ventania mountain system (Fig. 1). This lower basin location makes the city vulnerable to accumulated upstream runoff, increasing flood risk during intense precipitation events (Mastrandrea and Pérez, 2022). The region has a sub-humid climate, with average annual precipitation and temperature of 627.4 mm and 15.6 °C, respectively (1961-2022). The area is characterized by the most severe extreme precipitation events in the Pampas Region (Aliaga *et al.*, 2017). These phenomena are considered the most representative and have the most significant adverse effects, mainly due to the alteration of socioeconomic activities in rural areas and the emergence of socio-environmental problems in urban settings (Bohn *et al.*, 2011). The city is situated in a flat environment, with different terrace levels in the north and northeast and low, flood-prone lands in the south, influencing normal runoff conditions. As a consequence, during extreme precipitation, flooding occurs, especially in neighborhoods located in the southern sector and over the floodplain of the Napostá stream toward the north of the city (Mastrandrea and Pérez, 2022). Given that precipitation events in the region are expected to become more frequent and intense in the near future (Brendel, 2023), it is essential to understand the capacity of green roofs to reduce runoff during precipitation of varying magnitudes.

This study evaluated the water storage and runoff capacities of an extensive green roof simulator in Bahía Blanca, Argentina, during the region's most extreme precipitation event in 47 years. The specific objectives were to:

- Analyze precipitation patterns and identify extreme events in Bahía Blanca from 1961-2022,
- Evaluate the hydrological performance of a green roof simulator during the most extreme precipitation event of the last 47 years using the Green Roof Water Balance Model,
- Compare the model results with international literature and discuss their implications for urban planning in Bahía Blanca.

The relevance of these results is reflected in providing specific and applicable data to the climatic and geographical conditions of Bahía Blanca, which will serve as a basis for designing green infrastructure strategies adapted to the region. It is expected that the results will not only improve water management in the city but also serve as a model for implementing nature-based solutions in other urban areas with similar characteristics worldwide.

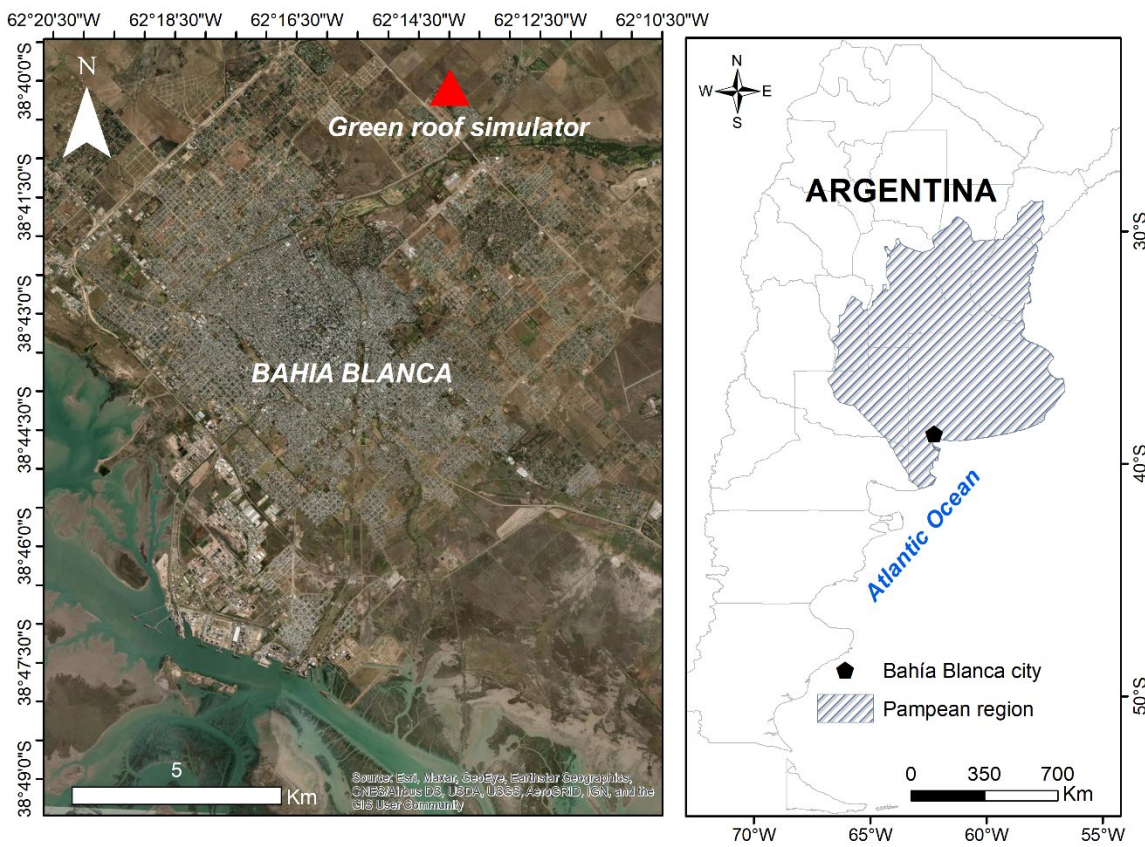


*Figure 1. Location of the green roof simulator in Bahía Blanca city (Argentina).*

## 2. Material and methods

### 2.1. Structure and characteristic of green roof simulator

This study analyzed one extensive green roof simulator ( $1 \text{ m}^2$ ) vegetated with native species selected from an experimental setup of eight simulators installed in April 2021 at the Argentine Institute of Oceanography (IADO, CONICET-UNS) experimental site (Fig. 2a). This simulator was chosen because it was designed explicitly with drought-resistant native species and a substrate composition optimized for local climatic conditions. In contrast, the other seven simulators tested different combinations of exotic species and substrate compositions for other research purposes. The selected simulator was specifically designed to evaluate the performance of locally-adapted species under extreme precipitation conditions. It was divided into nine cells following a completely randomized design, with three replicates of each native species distributed randomly (Fig. 3). The green roof simulator was constructed following the guidelines of Barbaro *et al.* (2017), as follows: a waterproof membrane to prevent moisture penetration; a drainage layer to facilitate the flow of excess water toward the drains, avoiding waterlogging and oxygen deficiency in the soil; a geotextile filter layer to contain the plant roots, protect the drainage layer, and prevent the leaching of organic matter; and finally, the substrate layer composed of 80 % inorganic material (70 % pumice and 10 % perlite) and 20 % organic matter (15 % peat and 5 % compost) with a height of 15 cm (Fig. 3). The planted species were herbaceous and native (*Sphaeralcea bonariensis*, *Aloysia gratissima*, *Atriplex undulata*, *Senecio pampeanus*), as they utilize water more efficiently and exhibit greater drought tolerance than their non-native counterparts (Butler *et al.*, 2012; Paço *et al.*, 2019), thereby ensuring better vegetation survival rates and overall green roof performance under the region's semi-arid conditions (Figs. 2 and 3).

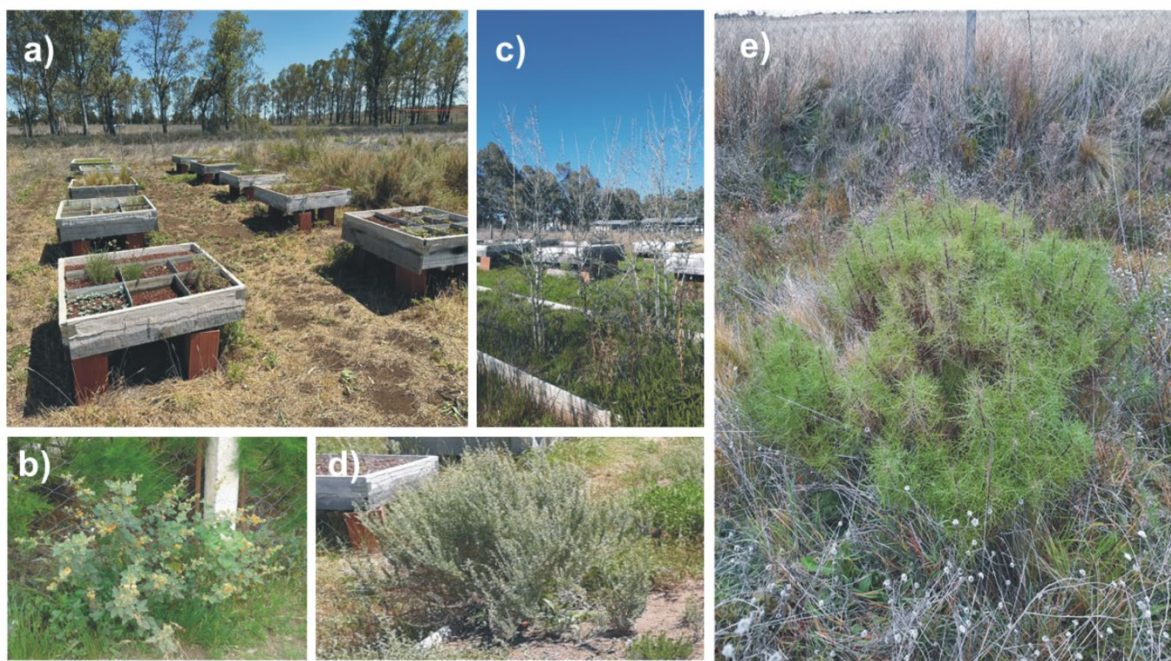


*Figure 2. Experimental setup of green roof simulators at IADO experimental site and species used in this study. a) General view of simulator setup showing the eight 1m<sup>2</sup> simulators with different substrate and vegetation treatments, b) *Sphaeralcea bonariensis*, c) *Aloysia gratissima*, d) *Atriplex undulata*, and e) *Senecio pampeanus*.*

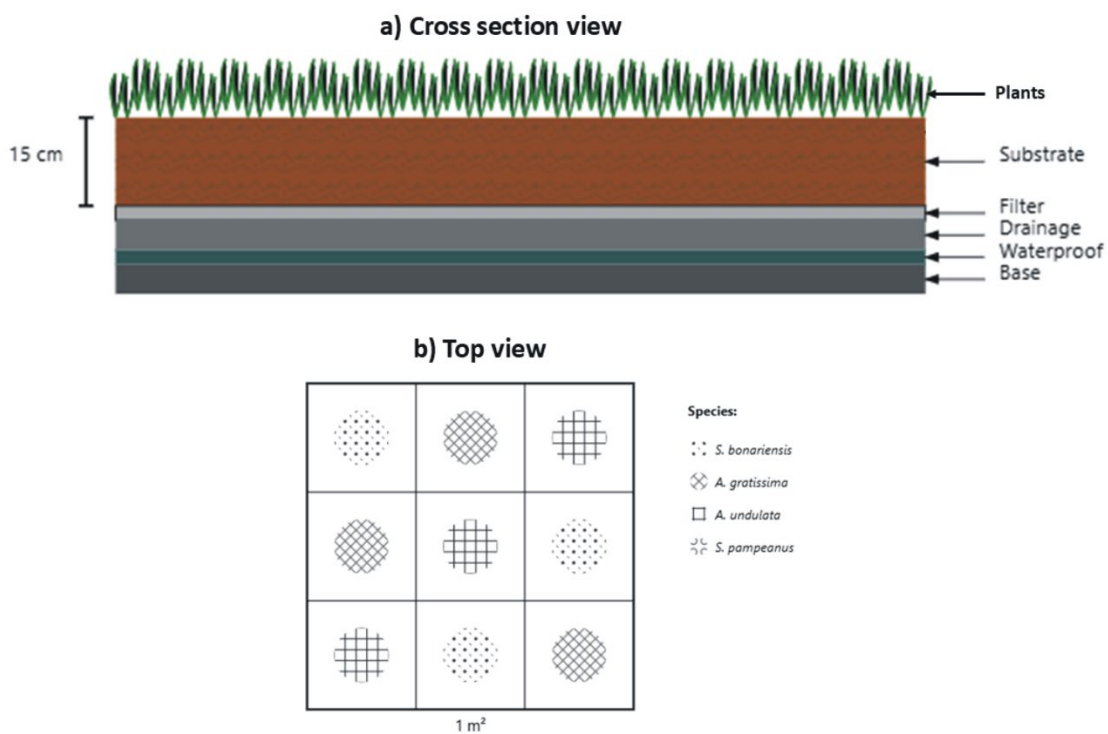


*Figure 3. Schematic representation of the green roof simulator design. a) Cross section view showing the different layers, b) top view illustrating the randomized distribution of native species.*

## 2.2. Green roof model

### 2.2.1. Model Overview

In this study, the GreenRoof Water Balance Model (Raes *et al.*, 2006) was applied to a green roof simulator (see section 2.1.) located in Bahía Blanca city (Figs. 1 and 2). This model has been widely used in numerous urban green roofs around the world, such as in Belgium (Vanuytrecht *et al.*, 2014), Poland (Burszta-Adamiak and Mrowiec, 2013), and Maryland (Starry *et al.*, 2016), but it has not yet been explored in Argentina, characterized by significant climate variability and increasing extreme precipitation events in urban areas (Pérez *et al.*, 2015; Ferrelli *et al.*, 2019; Brendel *et al.*, 2021).

The model calculates the water retained in a green roof and the amount discharged as runoff, based on precipitation and potential or reference evapotranspiration (ET<sub>0</sub>). Calculations can be performed for user-specified roofs, with or without vegetation cover. Additionally, factors affecting the balance between runoff, evaporation, and water storage can be specified: (i) roof characterization (type, area, orientation, slope, from completely protected from wind and sun to extremely windy and sun-exposed) and (ii) vegetation characterization (type of vegetation, degree of vegetation cover, substrate depth, presence of a drainage or reservoir layer) (Table 1).

The model parameters (Table 1) were based on the physical characteristics of the previously described simulator, incorporating its dimensions, vegetation coverage, orientation, slope, and field-measured water storage capacity. While direct runoff measurements were not performed, the model provides reliable estimates of hydrological performance when incorporating high-quality local measurements. Therefore, the runoff values presented in this study represent model outputs based on field-measured substrate properties and local meteorological data during the extreme precipitation event of March 23-25, 2022.

*Table 1. Green roof simulator parameters and characteristics included in the model. W<sub>max</sub> represents the maximum water storage capacity (mm); a<sub>rain</sub> is a dimensionless program parameter related to rainfall interception based on roof orientation; Kc is the crop coefficient that accounts for vegetation characteristics; p is the threshold fraction of maximum water storage capacity below which vegetation experiences water stress.*

	Parameters	Characteristics
<b>Field-measured parameters</b>	Vegetation	Herbaceous. Species: <i>Sphaeralcea bonariensis</i> , <i>Aloysia gratissima</i> , <i>Atriplex undulata</i> , <i>Senecio pampeanus</i> .
	Coverage (%)	75 %
	Area (m <sup>2</sup> )	1 m <sup>2</sup>
	Substrate Depth (cm)	15 cm
<b>Model input parameters</b>	W <sub>smax</sub>	58.7 mm
	a <sub>rain</sub>	0.0003
	Slope (°)	5°
	Orientation	North
	Kc	1.0
	p	0.5

### 2.2.2. Maximum water storage capacity (W<sub>smax</sub>)

To determine W<sub>smax</sub> (maximum water storage capacity), the substrate's field capacity (FC) and bulk density were measured *in situ*. Following the method of Cassel and Nielsen (1986), three undisturbed substrate samples were collected from the green roof simulator using metal cylinders. These samples were saturated with water and allowed to drain gravitationally until reaching field capacity. Subsequently, bulk density and volumetric water content at field capacity were determined for each sample. The obtained W<sub>smax</sub> value was 58.7 mm.

### 2.2.3. Daily water balance components

#### Incoming Water

The model determines the daily water balance, considering incoming ( $W_{in}$ ) and outgoing water flows ( $W_{ro}$  and  $W_{ET}$ ). Where  $W_{in}$  is the daily precipitation (mm), modified by the cosine of the slope and orientation of the roof to correct for the effect of wind on rain capture:

$$W_{in} = R_{obs} \times \Omega \times \cos\left(\frac{X \times \pi}{180}\right) \times (1 + a_{rain} \times X) \quad (1)$$

where  $R_{obs}$  is the daily precipitation (mm),  $\Omega$  is the area of the green roof ( $m^2$ ),  $a_{rain}$  is a dimensionless program parameter, and  $X$  is the slope of the roof (in degrees). The value of  $a_{rain}$  depends on the orientation of the roof, the local wind and rainfall characteristics, as roofs oriented towards a dominant wind direction receive more precipitation than flat roofs or those oriented in other directions (Raes *et al.*, 2006). For this study, since our green roof is north-oriented, we used  $a_{rain} = 0.0003$ , which accounts for the influence of dominant northern winds on rainfall capture, indicating a slight increase in capture with slope for this orientation. This value was obtained from the Green Roof Water Balance Model standard correction factors for different roof orientations.

#### Water Storage Update

$W_{sact}$  (actual water storage) is calculated using a daily water balance.  $W_{sact}$  is initialized at 0 or at a measured initial value for the first day. For each subsequent day,  $W_{sact}$  is updated using the following equation:

$$W_{sact} = W_{sact(t-1)} + W_{in} - W_{ET} - W_{ro} \quad (2)$$

where  $W_{sact(t-1)}$  is the water stored from the previous day,  $W_{in}$  is the incoming rainfall,  $W_{ET}$  is the water lost through evapotranspiration, and  $W_{ro}$  is water lost as runoff. The daily calculation follows this sequence: first, incoming rainfall ( $W_{in}$ ) is added to the previous day's storage; if this sum exceeds  $W_{smax}$  (here, 58.7 mm), the excess water becomes runoff ( $W_{ro}$ ); finally, evapotranspiration losses ( $W_{ET}$ ) are subtracted.  $W_{sact}$  is constrained between 0 (completely dry roof) and  $W_{smax}$  (saturated roof).

#### Evapotranspiration

$W_{ET}$  is the amount of water lost from the green roof through evapotranspiration (ET, mm), which depends on the atmospheric evaporative demand (ETo) and the characteristics of the roof.

$$W_{ET} = \Omega \times K_s \times K_c \times ET_{o^*} \quad (3)$$

Where  $\Omega$  is the roof area ( $m^2$ ),  $K_s$  is the water stress coefficient,  $K_c$  is the crop coefficient, and  $ET_{o^*}$  is the adjusted ETo (mm/day).  $ET_{o^*}$  is the ETo adjusted for slope, orientation, and position. The slope and orientation of the roof determine the amount of radiation received and, consequently, the ETo. Additionally, the ETo is influenced by the position of the roof to prevailing winds.  $K_s$  is a water stress coefficient that modifies evapotranspiration from the roof ( $K_c \times ET_{o^*}$ ) and varies linearly between 0 (complete stress) when  $W_{sact}$  is equal to zero (empty root reservoir) and 1 (no stress) above a threshold value when the vegetation on the green roof does not experience water stress. The threshold, which depends on the characteristics of the roof or vegetation, is specified as the fraction  $p$  of  $W_{smax}$ .

The Green Roof Water Balance Model provides standard crop coefficient ( $K_c$ ) values for different roof surface conditions and vegetation types (Allen *et al.*, 1998).  $K_c$  is set to 1.10 for a bare substrate layer, reflecting the high initial evaporation rate from exposed substrate surfaces. When considering vegetation,  $K_c$  values vary according to plant type: succulent-mosses have the lowest value ( $K_c = 0.40$ ) due to their water-conservative nature and reduced transpiration rates; both mosses-

succulents and succulent-grasses combinations show intermediate values ( $K_c = 0.70$ ), while grass-herb combinations exhibit the highest coefficient ( $K_c = 1.00$ ) due to their greater transpiration rates.

In our study, we selected  $K_c = 1.0$  following these guidelines for grass-herb combinations, despite using drought-tolerant native species. This value was chosen because: (i) our green roof simulator contained a diverse mix of herbaceous species rather than solely succulents; (ii) the vegetation coverage was relatively high (75%), resulting in greater total transpiration surface area; and (iii) while these native species are efficient in water use during drought conditions, they can exhibit opportunistic water consumption during wet periods, a common adaptation in semi-arid environments with irregular precipitation patterns. This approach also allowed us to avoid underestimating potential evapotranspiration during periods when water was abundantly available, such as during the extreme rainfall event analyzed. The  $K_c$  value is then used to estimate the actual evapotranspiration rate of the green roof by multiplying it by the reference evapotranspiration ( $ETo$ ).

### *Runoff generation*

When the sum of incoming rainfall and existing stored water exceeds  $W_{Smax}$ , runoff occurs:

$$W_{ro} = W_{in} - (W_{Smax} - W_{Sact}) \quad (4)$$

where  $W_{ro}$  is the amount of water lost due to runoff (mm) when  $W_{in}$  exceeds the roof's storage capacity.  $W_{Sact}$  is the water effectively retained on the roof (mm).  $W_{Smax}$  depends on the type of roof and surface, while  $W_{Sact}$  depends on precipitation and evapotranspiration from the green roof and is updated daily.  $W_{Sact}$  varies from zero when the roof is completely dry to  $W_{Smax}$  when the roof is saturated with rain.

### *Vegetation Water Stress*

When the water content stored in the substrate drops below the threshold fraction  $p$  of  $W_{Smax}$ , the stress level ( $S$  in %) for the green roof vegetation is calculated using:

$$S = 100 \times \left(1 - \frac{W_{Sact}}{p \times W_{Smax}}\right) \quad (5)$$

where  $p$  is the threshold for vegetation water stress,  $W_{Smax}$  is the maximum and  $W_{Sact}$  is the actual amount of water retained on the roof (mm). The threshold for vegetation water stress ( $p$ ) was set to 0.5, indicating that plants experience water stress when water storage drops below 50 % of maximum capacity ( $W_{Smax}$ ). This value was selected based on the drought-tolerant characteristics of our native species, consistent with validated green roof models (Vanuytrecht *et al.*, 2014; Starry *et al.*, 2016; Liu *et al.*, 2021; Zhang *et al.*, 2021) and particularly suitable for extensive green roofs in regions with frequent water deficits.

#### *2.2.4. Model Application and Data Input*

Users can customize the roofs simulated by the Green Roof Model to site-specific conditions by adjusting the program parameters that describe the processes mentioned above. In this case, the model parameters were applied to a green roof simulator in Bahía Blanca (Fig. 2a). The values of the parameters used to apply the model are shown in Table 1. The effect of orientation, slope, and position on precipitation interception and evapotranspiration from the roof was modeled using empirical equations based on observations from the calibration site. Daily data on precipitation and potential evapotranspiration were obtained for the year 2022 from a weather station of the National Meteorological Service (SMN, Argentina), located in the peripheral area of the city. The behavior of daily precipitation was analyzed as suggested by the Expert Group on Climate Change Detection and Indices (ETCCDI; <http://etccdi.pacificclimate.org>). Therefore, daily precipitation exceeding 50 mm was considered extreme (Brendel *et al.*, 2021).

### 3. Results

#### 3.1. Annual and Monthly Characterization of Precipitation from 1961 to 2022

Bahía Blanca has an average annual precipitation of 627.4 mm ( $\pm 145.4$  mm) (Fig. 4). Additionally, it shows notable interannual variability, with a minimum of 306 mm in 2019 and a maximum of 1,086 mm in 1976 (Fig. 4a). Summer is the season with the highest precipitation (192 mm), followed by autumn and spring, which have similar values (175 mm and 173 mm, respectively) (Fig. 4b). On the other hand, winter is the season with the lowest precipitation, with an average total of 86 mm. March is the wettest month, 78.3 mm, while June has the lowest recorded precipitation levels (26.2 mm) (Fig. 4b).

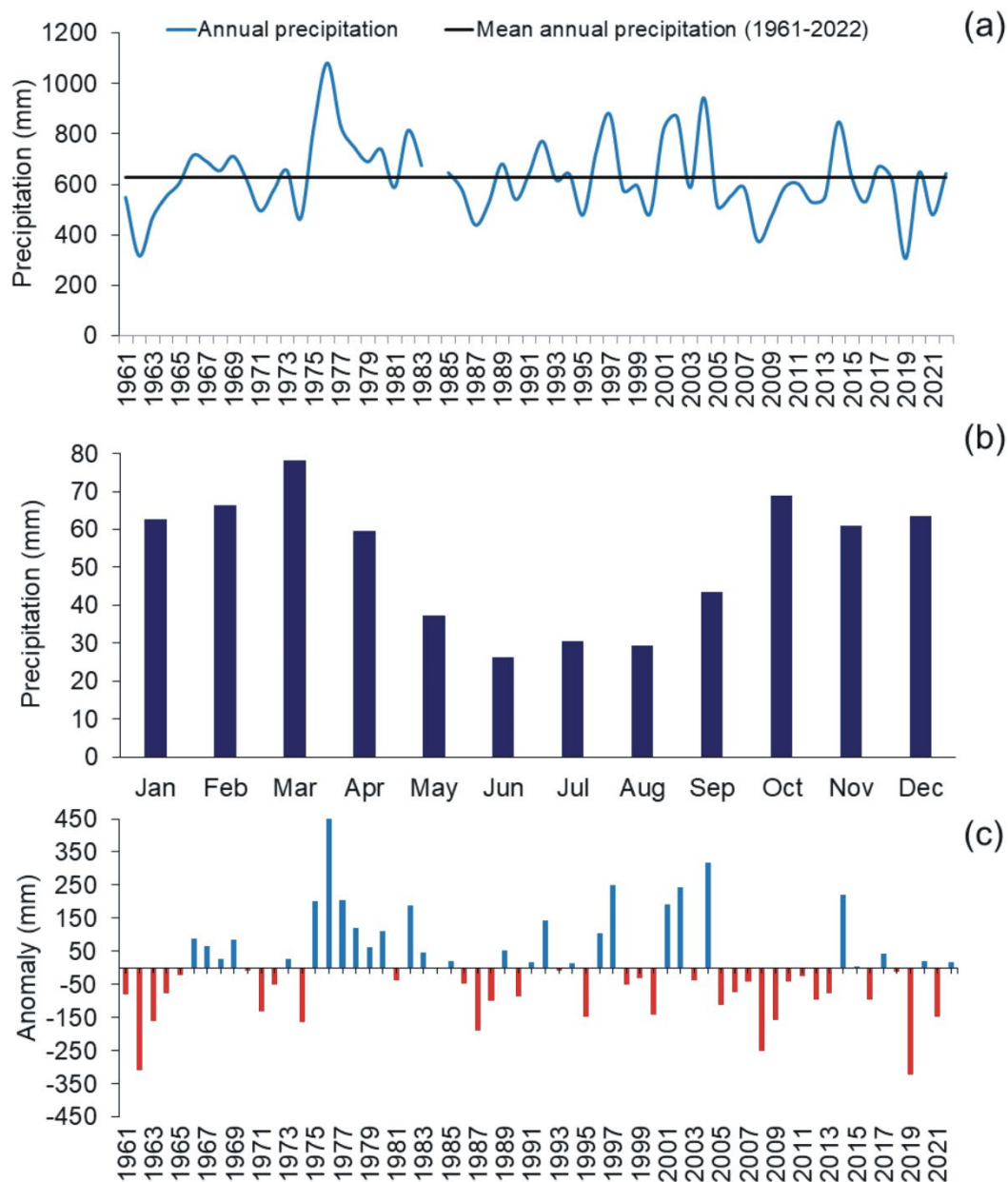


Figure 4. a) annual precipitation, b) monthly precipitation, and c) interannual precipitation anomalies in Bahía Blanca, Argentina (1961-2022).

Four well-defined periods of positive and negative anomalies were observed in the rainfall time series, demonstrating the significant interannual precipitation variability. The first period, characterized by a higher percentage of negative anomalies, extended from 1961 to 1974 (-10.1 to -310 mm), while the second occurred between 1975 and 1985, exhibiting positive anomalies (47.6 to 454.8 mm) (Fig. 4c). During this interval, six consecutive years with positive anomalies were recorded, including the year with the highest recorded precipitation (1082.2 mm, anomaly = 454.8 mm) (Fig. 4c). The third and most prolonged period was characterized by alternating positive and negative anomalies from 1986 to 2004. The fourth period (2005 to 2022) predominantly featured dry conditions (-5.4 to -286.5 mm), with the exceptions of 2014 (220 mm), 2017 (25 mm), and 2020 and 2021, which had positive anomalies of approximately 20 mm. It is noteworthy that during this period, negative anomalies were more significant than positive ones (-321 mm and 220.7 mm, respectively), and the most extreme negative anomaly over the 61 years studied was recorded (-321 mm in 2019) (Fig. 4c).

### 3.2. Characterization of Daily Precipitation from 1961 to 2022

Daily precipitation from 1961 to 2022 is shown in Figure 5. The most frequent occurrences are those less than 20 mm (89 %), while those between 20.1 and 40 mm represent 8 %. Precipitation events between 40.1 and 60 mm account for 2 %, and those between 60.1 and 80 mm comprise 0.5 % (Fig. 5a). Events exceeding 80.1 mm occurred only 11 times in the 62 years analyzed, with a total of eight events between 80.1 mm and 100 mm, highlighting the event on March 24, 2022, as the highest daily precipitation in the last 15 years (90.3 mm) (Fig. 5b). However, when analyzing the accumulated precipitation over three consecutive days, it was observed that the amount recorded from March 23 to 25 was the most extreme rainfall event in the last 47 years and the second most significant in the 62 years analyzed (Fig. 6). This event was characterized by a total precipitation of 150.3 mm, of which 51 mm occurred on March 23, 90.3 mm on March 24, and 9 mm on March 25 (Fig. 6).

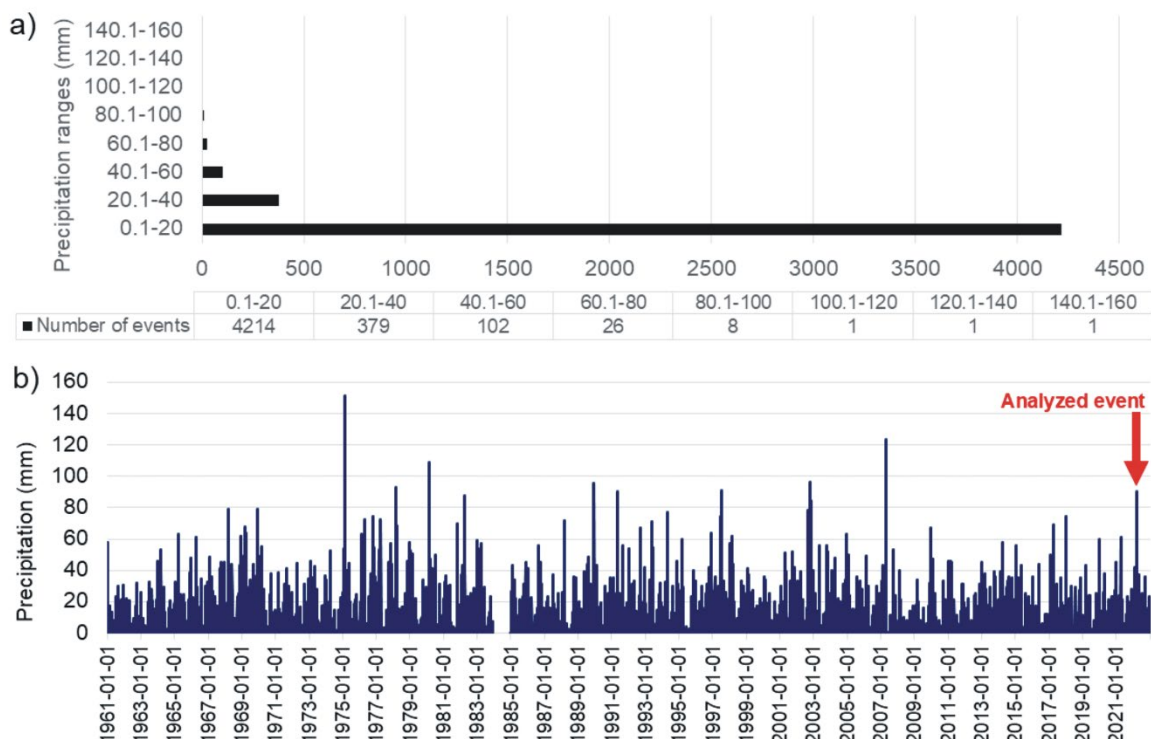


Figure 5. a) Number of events by precipitation ranges and b) daily precipitation during 1961-2022 period.

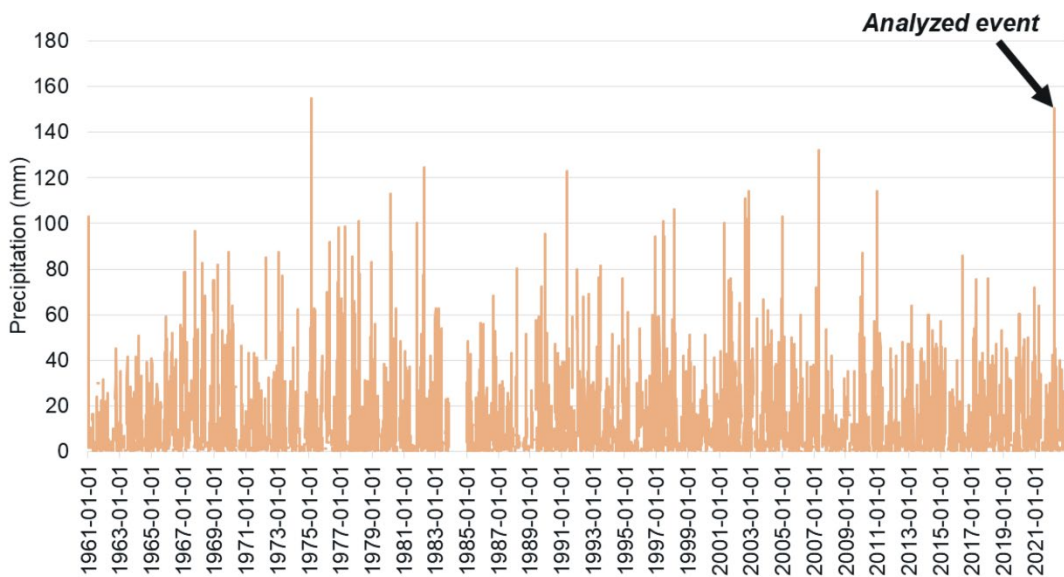
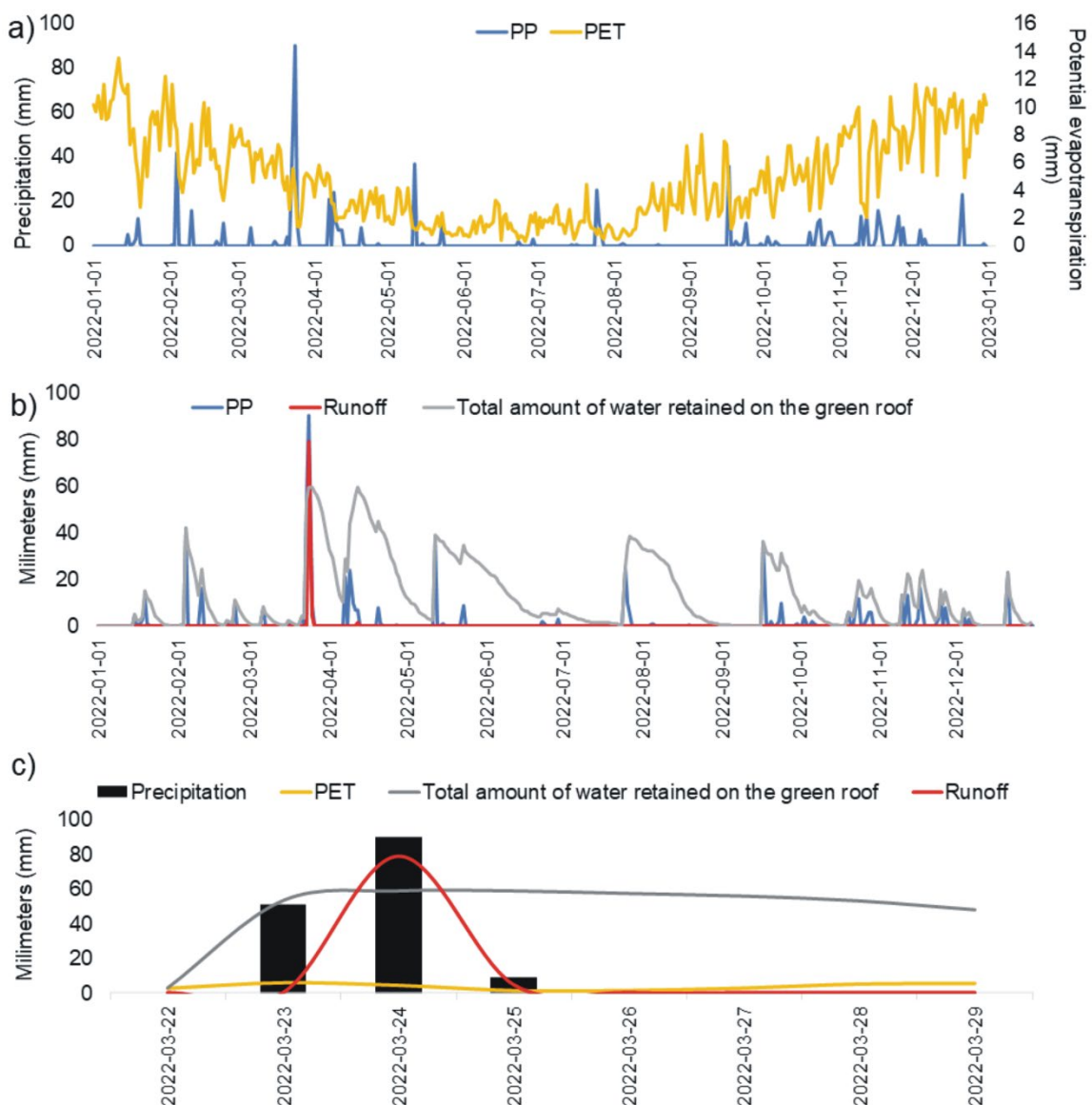


Figure 6. Accumulated precipitation over three consecutive days during 1961-2022 period.

### 3.3. Hydrological Response of the Green Roof to Precipitation in 2022 and During March 23 to 25

In 2022, Bahía Blanca recorded 74 precipitation events (days with precipitation  $> 0.1$  mm), with most events (54 events, 73 %) involving less than 5 mm of rainfall, 13 events (18 %) between 5-20 mm, 4 events (5 %) between 20-40 mm, and only 3 events (4 %) exceeding 40 mm (Fig. 7a). Several periods exhibited precipitation values exceeding PET, suggesting elevated water availability, specifically during March 23-25, April 7-12, and October 23-24, 2022 (Fig. 7a). Among all precipitation events, only two generated runoffs when  $W_{Smax}$  (58.7 mm) was exceeded, representing less than 3 % of the total events (Fig. 7b). It is essential to highlight that during precipitation episodes, part of the water is retained in the soil matrix, while vegetation reduces water outflow through both canopy interception (water caught on leaves and stems) and transpiration processes, and the rest is lost through surface and subsurface runoff. A clear relationship between precipitation and evapotranspiration (PET) was observed throughout 2022 (Fig. 7a). PET, representing atmospheric water demand, exceeded precipitation for most of the year, which indicates the high annual water deficit characteristic of the regional climate (643 mm of rainfall versus 1740 mm of PET) (Fig. 7a).

The most significant runoff generation was estimated by the model during March 23-25, 2022 (Fig. 7c). Despite receiving 51 mm of precipitation on March 23, no runoff was generated during this event. Subsequently, on March 24, with rainfall of 90.3 mm,  $W_{Sact}$  reached 11.5 mm, while  $W_{Ro}$  amounted to 78.8 mm, indicating that the green roof stored 12.7 % of the incoming rain, with the remaining 87.3 % lost as runoff. This lower storage value can be attributed to elevated soil moisture content from the previous day's precipitation, which reduced the available storage capacity. On March 25, of the 9 mm of rainfall received, 4.6 mm resulted in runoff, corresponding to a storage of 48.9 %. Therefore, during the three-day event (total precipitation 150.3 mm), the green roof generated a total runoff of 83.4 mm, resulting in a cumulative storage of 44.6 % (Fig. 7c).



*Figure 7. Hydrological dynamics of the green roof simulator. a) Daily precipitation (PP) and potential evapotranspiration (PET) during 2022; b) precipitation, runoff, and the amount of water stored in the roof in 2022 and c) precipitation, potential evapotranspiration, runoff and the amount of water stored in the roof during 22-29 March 2022*

#### 4. Discussion

The study of precipitation, particularly during extreme events, is a fundamental element in understanding climate due to the various environmental and social consequences they generate, such as flooding, soil erosion, and biodiversity loss (Brendel *et al.*, 2017). Precipitation is a highly variable parameter across different temporal scales: annual, seasonal, and daily (Bekele *et al.*, 2017; Ferrelli *et al.*, 2019). In Bahía Blanca, significant variability in precipitation has been observed over the last 62 years due to its location in a transitional zone between temperate and arid climates (Aliaga *et al.*, 2017). This variability significantly influences plant species' survival and performance on green roofs, particularly in climates with high water deficit and irregular precipitation patterns, such as Bahía Blanca (Perillo *et al.*, 2023). The high variability necessitates substrate compositions and native plant selections that can rapidly adapt to sudden changes between prolonged dry periods and intense precipitation events. This ensures water storage capacity and runoff management even under extreme climatic conditions (Perillo *et al.*, 2023).

The analyzed precipitation event was the most extreme in the last 47 years and the second most significant from 1960 to 2022. This situation is associated with global warming, the main cause of climate change (Padhiary *et al.*, 2018). According to the Sixth Assessment Report of the Intergovernmental Panel on Climate Change (IPCC, 2021), the last four decades have been successively warmer than any other since 1850. The average air temperature in the previous two decades of the 21st century (2000-2020) was 1°C higher than in the 1850-1900 period and 1.1°C higher in 2011-2020 compared to 1850-1900. This temperature increase has primarily been driven by greenhouse gas emissions from human activities, especially CO<sub>2</sub> (Padhiary *et al.*, 2018), whose concentration reached peak levels in at least two million years in 2019 (IPCC, 2021). Consequently, the increase in atmospheric water vapor has modified precipitation patterns worldwide (Bekele *et al.*, 2017; Muthuwatta *et al.*, 2018), manifesting in Bahía Blanca with an increase in precipitation intensity over the last six decades (Ferrelli *et al.*, 2021). Looking forward, precipitation variability and extremes are projected to intensify globally (IPCC, 2021), with regional variations depending on local conditions and emission scenarios. For Bahía Blanca specifically, projections indicate increased precipitation toward the end of the 21st century, particularly under high emission scenarios (RCP 8.5) (Brendel, 2023). This trend is particularly concerning as climate change exacerbates flooding risks through increased frequency and intensity of extreme events (Avashia and Garg, 2020; Leandro *et al.*, 2020). The city's vulnerability is further heightened by its location in the lower basin of the Napostá Grande stream and urban infrastructure limitations (Zapperi, 2014; Mastrandrea and Pérez, 2022), making the implementation of green infrastructure solutions increasingly critical. Given these local challenges and future climate projections, it is essential to evaluate green roof performance through reliable methodologies. Model simulations have emerged as a valuable tool to assess the hydrological performance of green roofs (Busker *et al.*, 2022). Several models have been developed for this purpose, each addressing different aspects of green roof hydrology. Liu *et al.* (2021) used HYDRUS-1D to simulate runoff response under different substrate designs, while Zhang *et al.* (2021) employed a physically based model to evaluate stormwater storage during intense rainfall events. Hamouz *et al.* (2020) analyzed single events runoff from extensive green roofs in cold climates, and Shafique *et al.* (2018) proposed a comprehensive model considering different substrate compositions and rainfall intensities. In Bahía Blanca, our application of the Green Roof Water Balance Model represents the first attempt to evaluate extensive green roof performance during extreme precipitation events in this region. While the model has not undergone formal validation locally, its implementation provides valuable insights due to the incorporation of high-quality local measurements, including daily precipitation, potential evapotranspiration, and field-measured water storage capacity obtained through rigorous soil sampling and laboratory analysis.

The water storage capacity of green roofs fundamentally depends on substrate properties, vegetation types, and local climatic conditions (Akther *et al.*, 2018; Peng *et al.*, 2019). Studies have shown that climatic factors such as rainfall intensity, antecedent dry period, solar radiation, air temperature, relative humidity, and evapotranspiration rate significantly influence the hydrological performance of green roofs (Wong and Jim, 2015; Zhang *et al.*, 2021). However, in climates with significant water deficits, runoff variability is primarily attributed to precipitation, evapotranspiration, substrate water storage capacity, and initial water content before a rain event (Liu *et al.*, 2021; Todorov *et al.*, 2018). In this context, and considering the climate of Bahía Blanca, the daily variability of runoff analyzed and water storage could be linked to these factors. The variation in water storage capacity observed during the three-day extreme event (March 23-25, 2022) clearly demonstrates the influence of antecedent moisture conditions on the green roof's hydrological performance. On March 23, the green roof showed maximum storage capacity with no runoff generation despite receiving 51 mm of precipitation. This optimal performance can be attributed to initially dry substrate conditions, resulting from the characteristic high evapotranspiration rates of the warm season (PET values around 4-5 mm/day in March). However, this precipitation event significantly increased the substrate moisture content, thereby reducing its storage capacity for subsequent rainfall. Consequently, on March 24, when 90.3 mm of rain fell on the already moistened substrate, the storage capacity decreased substantially to 12.7 %, with most of the precipitation (87.3 %) converting to runoff. This behavior aligns with findings

from Liu *et al.* (2021), who reported that water storage capacity in green roofs varies from 34.7 % to 48.5 % depending on initial moisture conditions, with dry substrates showing significantly higher storage capacities. While direct measurements of initial substrate moisture were not available in our study, the daily water balance calculations through the model provide valuable insights into the substrate's moisture status and its influence on storage performance. This moisture-dependent behavior is particularly relevant in Bahía Blanca's climate, where the typically dry substrate conditions favor high initial storage capacities, but consecutive rain events can rapidly reduce this effectiveness.

The green roof simulator analyzed showed optimal performance in retaining precipitation and reducing runoff generated during the most extreme precipitation event in the last 47 years, with an average water storage capacity of 44.6 % and 55.5 % runoff. These values align with those reported in numerous experimental green roof plots worldwide using validated models (Gong *et al.*, 2019; Harper *et al.*, 2015; Lee *et al.*, 2015; Liu *et al.*, 2019; Stovin *et al.*, 2012; Zhang *et al.*, 2021). For example, Palla *et al.* (2009) using SWMS\_2D found water storage of 51.5 % during a 153.2 mm event, remarkably similar to our water storage of 44.6% during a 150.3 mm event. Similarly, Villarreal and Bengtsson (2005) reported values of 20-40 % during intense short-duration events. More recent studies have further validated these water storage ranges under various conditions. Zhang *et al.* (2021) documented values of 42.8-56.7 % during extreme events exceeding 100 mm in China, while Liu *et al.* (2021) found comparable results (34.7-48.5 %) in semi-arid conditions, emphasizing the critical role of initial substrate moisture in determining storage capacity. These findings align closely with our results, particularly considering our use of field-measured water storage capacity and local meteorological data. Additionally, Hamouz *et al.* (2020) reported similar ranges (30-45 %) during extreme events, noting decreased efficiency near substrate saturation, while Shafique *et al.* (2018) found values of 40-60 % during intense rainfall events, emphasizing substrate characteristics' importance. The consistency between our model's predictions and these validated studies, especially those conducted under similar rainfall intensities or climatic conditions, suggests that despite lacking formal validation, the Green Roof model provides reliable estimates of hydrological performance under local conditions. This alignment with international findings strengthens confidence in the model's utility for urban planning in Bahía Blanca, though future local validation would further enhance its applicability.

The hydrological performance of green roofs varies according to local climate. For instance, in a dry climate in southern Australia, water storage capacity was observed to range from 51 % to 96 % (Beecham and Razzaghmanesh, 2015), while in a humid tropical climate in Hong Kong, it varied between 24.3 % and 36.3 % (Wong and Jim, 2014). Additionally, average runoff retention is significantly higher in extensive green roofs in dry subhumid climates (75.2 %) compared to maritime climates (43.4 %) (Sims *et al.*, 2019). This corroborates that the use of green roofs in Bahía Blanca, a city with significant water deficits but intense and frequent wet events, is crucial for controlling urban runoff. On the other hand, substrate selection is fundamental as it can affect both the hydrological performance of the system and the quality of the drained water (Shafique *et al.*, 2018). The substrate significantly influences water storage capacity more than vegetation type and cover (Berndtsson, 2010; Liu *et al.*, 2019; Stovin *et al.*, 2012; Zhang *et al.*, 2019).

In this study, the substrate used is lightweight with high porosity, composed of 80% inorganic material (70 % pumice and 10 % perlite) and 20 % organic matter (15 % peat and 5 % compost), which provides high water storage capacity and good drainage properties, essential for the hydraulic dynamics of a green roof (Hachoumi *et al.*, 2021). Furthermore, the local climate, characterized by significant annual water deficits and high evapotranspiration rates in the warm season, produces a substrate with low moisture content. This characteristic is important, as studies have shown that dry substrates can store more water due to a larger water storage volume during precipitation events (Liu *et al.*, 2020). Regarding the appropriate vegetation type for extensive green roofs, the selection of species with short roots that exhibit rapid growth, low maintenance, and high tolerance to extreme climatic conditions, especially to water deficits, is suggested (Shafique *et al.*, 2018). Thus, native species selected for their drought tolerance were used in the green roof simulator (Perillo *et al.*, 2023). Furthermore, it has been

shown that these species possess a remarkable ability to retain precipitation, especially during intense rainfall events (Todorov *et al.*, 2018). Therefore, considering that the study area projects an increase in the severity of rainfall in the near future, using native species is essential to mitigate the effects of climate change (Brendel, 2023).

Finally, the simulation provides robust evidence of green roof hydrological performance during extreme events, strengthened by integrating locally-adapted native vegetation and optimally selected substrate composition. This comprehensive approach generates valuable data precisely calibrated for Bahía Blanca's context, establishing a strong foundation for green infrastructure implementation in the region. Future research on full-scale installations will build upon these findings by incorporating continuous runoff monitoring systems and examining additional aspects such as edge effects, root development dynamics, and long-term maintenance. Direct runoff measurements in future studies will complement our modeling approach, providing additional insights into the temporal dynamics of water movement through the green roof system during extreme events. This combination of modeling and empirical measurements will further advance our understanding of green roof behavior in the region, ultimately enhancing their effectiveness as a climate change adaptation strategy.

## 5. Conclusion

This study represents the first assessment of green roof performance in Bahía Blanca. It demonstrates their effectiveness as an innovative and sustainable solution for mitigating the effects of climate change and managing urban runoff, particularly in regions experiencing frequent extreme rainfall events. The results showed that during the most extreme precipitation event recorded in the last 47 years, the green roof successfully retained an average of 44.6 % of the rainfall, significantly reducing surface runoff volume and mitigating the risk of flooding within the city.

In the context of climate change, where an increase in the frequency and intensity of extreme rainfall events is expected, adopting green infrastructure is not only a mitigation measure but also an essential strategy for urban adaptation. The information generated by this study is crucial for developing policies and strategies for green infrastructure development in Bahía Blanca and other regions with similar climatic conditions. Integrating green roofs into urban planning can significantly enhance the sustainability and resilience of cities in the face of future climate challenges.

## Acknowledgements

The authors would like to thank CONICET and the National University of South (UNS) for supporting and funding this study (project ANPCYT-PICT 2021-832). We also thank the National Meteorological Service (SMN) for providing the data.

## References

- Akther, M., He, J., Chu, A., Huang, J., Van Duin, B. 2018. A review of green roof applications for managing urban stormwater in different climatic zones. *Sustainability*, 10(8), 2864. <https://doi.org/10.3390/su10082864>
- Aliaga, V. S., Ferrelli, F., Piccolo, M. C. 2017. Regionalization of climate over the Argentine Pampas. *International Journal of Climatology*, 37(S1), 1237-1247. <https://doi.org/10.1002/joc.4765>
- Allen, R.G., Pereira, L. S., Raes, D., Smith, M. 1998. Crop evapotranspiration-Guidelines for computing crop water requirements. *FAO Irrigation and Drainage Paper*, 56, FAO Rome, 300(9), D05109.
- Avashia, V., Garg, A. 2020. Implications of land use transitions and climate change on local flooding in urban areas: An assessment of 42 Indian cities. *Land Use Policy*, 95, 104571. <https://doi.org/10.1016/j.landusepol.2020.104571>

- Barbaro, L.A., Soto, M.S., Sisaro, D., Karlanian, M., Stanganelli, S. 2017. Sustratos para techos verdes sustentables (extensivos). *Ediciones INTA*.
- Bekele, F., Mosisa, N., Terefe, D. 2017. Analysis of current rainfall variability and trends over Bale-Zone SouthEastern highland of Ethiopia. *Climate Change*, 3(12), 889-902. <https://doi.org/10.4172/2157-7617.1000417>
- Beecham, S., Razzaghmanesh, M. 2015. Water quality and quantity investigation of green roofs in a dry climate. *Water Research*, 70, 370-384. <https://doi.org/10.1016/j.watres.2014.12.015>
- Berggren, K., Olofsson, M., Viklander, M., Svensson, G., Gustafsson, A.M. 2012. Hydraulic impacts on urban drainage systems due to changes in rainfall caused by climatic change. *Journal of Hydrologic Engineering*, 17(1), 92-98. [https://doi.org/10.1061/\(ASCE\)HE.1943-5584.0000406](https://doi.org/10.1061/(ASCE)HE.1943-5584.0000406)
- Berndtsson, J.C. 2010. Green roof performance towards management of runoff water quantity and quality: A review. *Ecological Engineering*, 36(4), 351-360. <https://doi.org/10.1016/j.ecoleng.2009.12.014>
- Bohn, V.Y., Piccolo, M.C., Perillo, G.M.E. 2011. Análisis de los períodos secos y húmedos en el sudoeste de la provincia de Buenos Aires (Argentina). *Revista de Climatología*, 11, 31-44.
- Brandão, C., do Rosário Cameira, M., Valente, F., de Carvalho, R.C., Paço, T.A. 2017. Wet season hydrological performance of green roofs using native species under Mediterranean climate. *Ecological Engineering*, 102, 596-611. <https://doi.org/10.1016/j.ecoleng.2017.02.025>
- Brendel, A.S., Bohn, V.Y., Piccolo, M.C. 2017. Variabilidad de la precipitación y su relación con los rendimientos agrícolas en una región semiárida de la llanura pampeana (Argentina). *Estudios Geográficos*, 78(282), 7-29. <https://doi.org/10.3989/estgeogr.201723>
- Brendel, A., Ferrelli, F., Piccolo, M.C., Perillo, G.M.E. 2021. Impacto de eventos pluviométricos sobre el caudal diario de un río de la región Pampeana (Argentina). *Interespaço: Revista de Geografía e Interdisciplinaridade*, 7(e202112), 1-22. <http://doi.org/10.18764/2446-6549.e202112>
- Brendel, A.S. 2023. Impacto del cambio climático: Un análisis espacial del riesgo futuro al cambio climático en el sur de la Región Pampeana (Argentina). *Papeles de Geografía*, 69, 155-168. <https://doi.org/10.6018/geografia.563951>
- Burszta-Adamiak, E., Mrowiec, M. 2013. Modelling of green roofs' hydrologic performance using EPA's SWMM. *Water Science and Technology*, 68(1), 36-42. <https://doi.org/10.2166/wst.2013.238>
- Busker, T., de Moel, H., Haer, T., Schmeits, M., van den Hurk, B., Myers, K., ... & Aerts, J. 2022. Blue-green roofs with forecast-based operation to reduce the impact of weather extremes. *Journal of Environmental Management*, 301, 113750. <https://doi.org/10.1016/j.jenvman.2021.113750>
- Butler, C., Butler, E., Orians, C. M. 2012. Native plant enthusiasm reaches new heights: Perceptions, evidence, and the future of green roofs. *Urban forestry & urban greening*, 11(1), 1-10. <https://doi.org/10.1016/j.ufug.2011.11.002>
- Carter, T., Jackson, C.R. 2007. Vegetated roofs for stormwater management at multiple spatial scales. *Landscape and Urban Planning*, 80(1-2), 84-94. <https://doi.org/10.1016/j.landurbplan.2006.06.005>
- Cassel, D.K., Nielsen, D.R. 1986. Chapter 36: Field Capacity and Available Water Capacity. In *Methods of Soil Analysis, Part 1. Physical and Mineralogical Methods*. Soil Science Society of America. Madison, WI, USA. 2nd edition.
- Driscoll, C.T., Eger, C.G., Chandler, D.G., Davidson, C.I., Roodsari, B.K., Flynn, C.D., ... & Groffman, P.M. 2015. Green infrastructure: Lessons from science and practice. A publication of the *Science Policy Exchange*, 32.
- Ferrelli, F., Brendel, A.S., Aliaga, V.S., Piccolo, M.C., Perillo, G.M.E. 2019. Climate regionalization and trends based on daily temperature and precipitation extremes in the south of the Pampas (Argentina). *Cuadernos de Investigación Geográfica: Geographical Research Letters*, 45(1), 393-416. <https://doi.org/10.18172/cig.3622>

- Ferrelli, F., Brendel, A.S., Piccolo, M.C., Perillo, G.M.E. 2021. Evaluación de la tendencia de la precipitación en la región Pampeana (Argentina) durante el período 1960-2018. *Raega-O Espaço Geográfico em Análise*, 51, 41-57. <http://dx.doi.org/10.5380/raega.v51i0.69962>
- Gong, Y., Yin, D., Li, J., Zhang, X., Wang, W., Fang, X., Wang, Q. 2019. Performance assessment of extensive green roof runoff flow and quality control capacity based on pilot experiments. *Science of the Total Environment*, 687, 505-515. <https://doi.org/10.1016/j.scitotenv.2019.06.063>
- Hachoumi, I., Pucher, B., Vito-Francesco, D., Prenner, F., Ertl, T., Langergraber, G., Allabashi, R. 2021. Impact of green roofs and vertical greenery systems on surface runoff quality. *Water*, 13(19), 2609. <https://doi.org/10.3390/w13192609>
- Hamouz, V., Pons, V., Sivertsen, E., Raspati, G.S., Bertrand-Krajewski, J.L., Muthanna, T.M. 2020. Detention-based green roofs for stormwater management under extreme precipitation due to climate change. *Blue-Green Systems*, 2(1), 250-266. <https://doi.org/10.2166/bgs.2020.101>
- Harper, G.E., Limmer, M.A., Showalter, W.E., Burken, J.G. 2015. Nine-month evaluation of runoff quality and quantity from an experiential green roof in Missouri, USA. *Ecological Engineering*, 78, 127-133. <https://doi.org/10.1016/j.ecoleng.2014.06.013>
- He, Y., Yu, H., Ozaki, A., Dong, N. 2020. Thermal and energy performance of green roof and cool roof: A comparison study in Shanghai area. *Journal of Cleaner Production*, 267, 122205. <https://doi.org/10.1016/j.jclepro.2020.122205>
- Intergovernmental Panel on Climate Change (IPCC). 2021. Climate Change 2021: The Physical Science Basis. Contribution of Working Group I to the Sixth Assessment Report of the Intergovernmental Panel on Climate Change (V. Masson-Delmotte, P. Zhai, A. Pirani, S. L. Connors, C. Péan, S. Berger, N. Caud, et al., Eds.). Cambridge University Press. <https://doi.org/10.1017/9781009157896>
- Leandro, J., Chen, K.F., Wood, R.R., Ludwig, R. 2020. A scalable flood-resilience-index for measuring climate change adaptation: Munich city. *Water Research*, 173, 115502. <https://doi.org/10.1016/j.watres.2020.115502>
- Lee, J. Y., Lee, M. J., Han, M. 2015. A pilot study to evaluate runoff quantity from green roofs. *Journal of Environmental Management*, 152, 171-176. <https://doi.org/10.1016/j.jenvman.2015.01.049>
- Li, C., Liu, M., Hu, Y., Shi, T., Qu, X. 2018. Effects of urbanization on direct runoff characteristics in urban functional zones. *Science of the Total Environment*, 643, 301-311. <https://doi.org/10.1016/j.scitotenv.2018.06.211>
- Liu, W., Feng, Q., Chen, W., Wei, W., Deo, R.C. 2019. The influence of structural factors on stormwater runoff retention of extensive green roofs: New evidence from scale-based models and real experiments. *Journal of Hydrology*, 569, 230-238. <https://doi.org/10.1016/j.jhydrol.2018.12.037>
- Liu, W., Feng, Q., Deo, R.C., Yao, L., Wei, W. 2020. Experimental study on the rainfall-runoff responses of typical urban surfaces and two green infrastructures using scale-based models. *Environmental Management*, 66(4), 683-693. <https://doi.org/10.1007/s00267-020-01339-9>
- Liu, W., Engel, B. A., Feng, Q. 2021. Modelling the hydrological responses of green roofs under different substrate designs and rainfall characteristics using a simple water balance model. *Journal of Hydrology*, 602, 126786. <https://doi.org/10.1016/j.jhydrol.2021.126786>
- Mastrandrea, A., Pérez, M.I. 2022. Representaciones sociales del riesgo hídrico: Análisis crítico del discurso periodístico en la cuenca del arroyo Napostá Grande (Bahía Blanca, Argentina). *Revista Universitaria de Geografía*, 31(1), 19-22. <https://doi.org/10.52292/j.rug.2022.31.1.0039>
- Mentens, J., Raes, D., Hermy, M. 2006. Green roofs as a tool for solving the rainwater runoff problem in the urbanized 21st century? *Landscape and Urban Planning*, 77(3), 217-226. <https://doi.org/10.1016/j.landurbplan.2005.02.010>
- Muthuwatta, L., Sood, A., McCartney, M., Silva, N.S., Opere, A. 2018. Understanding the impacts of climate change in the Tana River Basin, Kenya. *Proceedings of the International Association of Hydrological Sciences*, 379, 37-42. <https://doi.org/10.5194/piahs-379-37-2018>
- Paço, T.A., Cruz de Carvalho, R., Arsénio, P., Martins, D. 2019. Green roof design techniques to improve water use under Mediterranean conditions. *Urban science*, 3(1), 14. <https://doi.org/10.3390/urbansci3010014>

- Padhiary, J., Patra, K.C., Das, D.M., Sahoo, B.C., Singh, K.K. 2018. Prediction of climate change impact on streamflow and evapotranspiration in Baitarani basin using SWAT model. *Journal of Agrometeorology*, 20(4), 325-328. <https://doi.org/10.54386/jam.v20i4.576>
- Palla, A., Gnecco, I., Laurenti, A. 2009. Hydrologic restoration in the urban environment using green roofs. *Water and Environmental Journal*, 23(3), 209-220. <https://doi.org/10.1111/j.1747-6593.2008.00133.x>
- Paule-Mercado, M.A., Lee, B.Y., Memon, S.A., Umer, S.R., Salim, I., Lee, C.H. 2017. Influence of land development on stormwater runoff from a mixed land use and land cover catchment. *Science of the Total Environment*, 599, 2142-2155. <https://doi.org/10.1016/j.scitotenv.2017.05.081>
- Peng, Z., Smith, C., Stovin, V. 2019. Internal fluctuations in green roof substrate moisture content during storm events: Monitored data and model simulations. *Journal of Hydrology*, 573, 872-884. <https://doi.org/10.1016/j.jhydrol.2019.03.051>
- Pérez, S., Sierra, E., Momo, F., Massobrio, M. 2015. Changes in average annual precipitation in Argentina's Pampa region and their possible causes. *Climate*, 3(1), 150-167. <https://doi.org/10.3390/cli3010150>
- Perillo, V.L., Brendel, A.S., Ferrelli, F., Gutiérrez, A., Vitale, A.J., Marinangeli, P., Piccolo, M.C. 2023. CO<sub>2</sub> flux dynamics of exotic and native species in an extensive green roof simulator with hydric deficit. *Urban Climate*, 49, 101567. <https://doi.org/10.1016/j.uclim.2023.101567>
- Pour, S.H., Abd Wahab, A.K., Shahid, S., Asaduzzaman, M., Dewan, A. 2020. Low impact development techniques to mitigate the impacts of climate-change-induced urban floods: Current trends, issues and challenges. *Sustainable Cities and Society*, 62, 102373. <https://doi.org/10.1016/j.scs.2020.102373>
- Raes, D., Timmerman, A., Hermy, M., Mentens, J. 2006. GreenRoof – water balance model. *K.U.Leuven University Faculty of Bioscience Engineering Division of Soil and Water Management*, Leuven, Belgium.
- Rowe, D.B. 2011. Green roofs as a means of pollution abatement. *Environmental Pollution*, 159(8-9), 2100-2110. <https://doi.org/10.1016/j.envpol.2010.10.029>
- Shafique, M., Kim, R., Rafiq, M. 2018. Green roof benefits, opportunities, and challenges–A review. *Renewable and Sustainable Energy Reviews*, 90, 757-773. <https://doi.org/10.1016/j.rser.2018.03.060>
- Sims, A.W., Robinson, C.E., Smart, C.C., O'Carroll, D.M. 2019. Mechanisms controlling green roof peak flow rate attenuation. *Journal of Hydrology*, 577, 123972. <https://doi.org/10.1016/j.jhydrol.2019.123972>
- Speak, A.F., Rothwell, J.J., Lindley, S.J., Smith, C.L. 2012. Urban particulate pollution reduction by four species of green roof vegetation in a UK city. *Atmospheric Environment*, 61, 283-293. <https://doi.org/10.1016/j.atmosenv.2012.07.043>
- Starry, O., Lea-Cox, J., Ristvey, A., Cohan, S. 2016. Parameterizing a water-balance model for predicting stormwater runoff from green roofs. *Journal of Hydrologic Engineering*, 21(12), 04016046. [https://doi.org/10.1061/\(ASCE\)HE.1943-5584.0001451](https://doi.org/10.1061/(ASCE)HE.1943-5584.0001451)
- Stovin, V., Vesuviano, G., Kasmin, H. 2012. The hydrological performance of a green roof test bed under UK climatic conditions. *Journal of Hydrology*, 414, 148-161. <https://doi.org/10.1016/j.jhydrol.2011.10.022>
- Todorov, D., Driscoll, C.T., Todorova, S. 2018. Long-term and seasonal hydrologic performance of an extensive green roof. *Hydrological Processes*, 32(16), 2471-2482. <https://doi.org/10.1002/hyp.13155>
- Vanuytrecht, E., Van Mechelen, C., Van Meerbeek, K., Willems, P., Hermy, M., Raes, D. 2014. Runoff and vegetation stress of green roofs under different climate change scenarios. *Landscape and Urban Planning*, 122, 68-77. <https://doi.org/10.1016/j.landurbplan.2013.11.001>
- Villarreal, E.L., Bengtsson, L. 2005. Response of a Sedum green-roof to individual rain events. *Ecological Engineering*, 25(1), 1-7. <https://doi.org/10.1016/j.ecoleng.2004.11.008>
- Wong, G.K., Jim, C.Y. 2015. Identifying keystone meteorological factors of green-roof stormwater retention to inform design and planning. *Landscape and Urban Planning*, 143, 173-182. <https://doi.org/10.1016/j.landurbplan.2015.07.010>
- Yin, J., Ye, M., Yin, Z., Xu, S. 2015. A review of advances in urban flood risk analysis over China. *Stochastic Environmental Research and Risk Assessment*, 29(3), 1063-1070. <https://doi.org/10.1007/s00477-014-0939-7>

- Zapperi, P.A. (2014). Caracterización del escurrimiento urbano en la ciudad de Bahía Blanca. *Revista Universitaria de Geografía*, 23(2), 125-150.
- Zhang, Y., Xia, J., Yu, J., Randall, M., Zhang, Y., Zhao, T., Shao, Q. 2018. Simulation and assessment of urbanization impacts on runoff metrics: Insights from land use changes. *Journal of Hydrology*, 560, 247-258. <https://doi.org/10.1016/j.jhydrol.2018.03.031>
- Zhang, Z., Szota, C., Fletcher, T.D., Williams, N.S., Farrell, C. 2019. Green roof storage capacity can be more important than evapotranspiration for retention performance. *Journal of Environmental Management*, 232, 404-412. <https://doi.org/10.1016/j.jenvman.2018.11.077>
- Zhang, S., Lin, Z., Zhang, S., Ge, D. 2021. Stormwater retention and detention performance of green roofs with different substrates: Observational data and hydrological simulations. *Journal of Environmental Management*, 291, 112682. <https://doi.org/10.1016/j.jenvman.2021.112682>
- Zhou, Q., Leng, G., Su, J., Ren, Y. 2019. Comparison of urbanization and climate change impacts on urban flood volumes: Importance of urban planning and drainage adaptation. *Science of the Total Environment*, 658, 24-33. <https://doi.org/10.1016/j.scitotenv.2018.12.184>





## ASSESSING THE DESIGN AND MANAGEMENT OF PROTECTED AREAS: LANDSCAPE GEOGRAPHY IN LOMAS AND TILLANDSIALES OF SOUTHWESTERN PERU

MARCO NAVARRO<sup>1,2\*</sup> , MELINA PAREDES<sup>2</sup> ,  
MIGUEL PEZO<sup>3</sup> , EDUARDO OYAGUE<sup>4</sup>

<sup>1</sup>*Instituto de Investigación de Energías Renovables Aplicadas, Universidad Privada de Tacna,  
Av. Jorge Basadre Grohmann Sur, Sector Capanique, Distrito de Pocollay,  
Provincia Tacna, Departamento de Tacna, 23003 Perú.*

<sup>2</sup>*Grupo de investigación Interdisciplinario de los Recursos Naturales, Ciencias Ambientales y  
de la Tierra (GIIRENCIAT). Facultad de Ingeniería de la Universidad Privada de Tacna.  
Av. Jorge Basadre Grohmann Sur, Sector Capanique, Distrito de Pocollay,  
Provincia Tacna, Departamento de Tacna, 23003 Perú.*

<sup>3</sup>*Universidad Nacional Jorge Basadre Grohmann de Tacna. Av. Miraflores s/n, Distrito,  
Provincia y Departamento de Tacna, 23000, Perú.*

<sup>4</sup>*Observatorio Ecohidrológico de la Selva Central, Universidad Nacional  
Intercultural de la Selva Central Juan Santos Atahualpa, Perú.*

**ABSTRACT.** Coastal desert ecosystems, such as the Lomas and Tillandsiales, are essential for the well-being of local populations, providing vital ecosystem goods and services, including climate regulation and water supply. These ecosystems are nationally recognized as important conservation targets. However, the Lomas and Tillandsiales in Tacna have been adversely affected and ecologically degraded due to uncontrolled population growth and inadequate regulation of human activities, such as agriculture, mining, and livestock grazing. Therefore, it is crucial to implement effective conservation strategies. Despite this need, when governmental entities delineate territories for potential protected areas, existing land use is often prioritized, leading to the exclusion of areas under current use rather than considering geographical criteria or ecological attributes of these vital ecosystems. This practice raises questions about the effectiveness of conservation efforts. To assess the proposed polygons for new protected areas by regional authorities, we compared these with natural ecosystem boundaries using various geographical tools. This comparison revealed substantial differences in geographical, ecological, and landscape metrics, indicating a decrease in ecological similarity and potentially lower effectiveness for conservation. We identified variations in geomorphological and morphometric diversity, with extreme cases showing coefficients of variability of 56% for the Gravelius index, 52% for the altitude index, and 43% for the morphometric protection index. These factors are critical as they strongly correlate with biodiversity, ecological processes, and the provision of ecosystem services, which are the main goals of conservation. Given these discrepancies, the newly proposed conservation area may inadequately fulfill its objectives. Once designated, the authorities should design and implement a management model that prioritizes expanding the protected areas to their natural limits, promoting restoration, and conducting ongoing monitoring of the metrics outlined in this research. Conservation should not merely involve declaring a spatial area as a reserve; it also requires defining these spaces based on tools and geographical knowledge to ensure the adequate protection and conservation of the Lomas and Tillandsiales ecosystems.

## **Evaluación del diseño y gestión de áreas protegidas: Geografía del paisaje en Lomas y Tillandsiales del Suroeste Peruano**

**RESUMEN.** Los ecosistemas del desierto costero como las Lomas y Tillandsiales son fundamentales para el bienestar de las poblaciones locales, ya que proporcionan bienes y servicios ecosistémicos importantes, como la regulación climática o el suministro de agua entre otros, siendo considerados como importantes objetos de conservación a nivel nacional. A pesar de esto, en Tacna, estos ecosistemas vienen siendo impactados y degradados ecológicamente por el desordenado crecimiento poblacional y la poca regulación de actividades humanas, como la agricultura, minería y uso pecuario, por lo que es necesario implementar estrategias de conservación. Sin embargo, cuando las entidades del estado realizan la delimitación de territorios para futuras áreas protegidas, se prioriza el uso actual, se excluyen los derechos de aprovechamiento otorgados, y no se consideran los criterios geográficos o los atributos ecológicos de estos importantes ecosistemas, lo que pone en discusión su efectividad. Por ello, utilizando diversas herramientas geográficas, se evaluaron los polígonos propuestos por las autoridades regionales como nueva área protegida comparándolos con los del ecosistema natural, demostrándose diferencias entre los índices geográficos, ecológicos y las métricas del paisaje, evidenciándose una cada vez menor similitud ecológica y posiblemente una menor efectividad para su conservación. Se observó que existen variaciones entre sus rangos de diversidad geomorfológica y morfométrica que llegan en casos extremos hasta un 56% de coeficiente de variabilidad para el índice de Gravelius, 52% para el de altitud y el 43% para el del índice de protección morfométrica. Éstos son factores muy importantes que tienen una alta correlación con la biodiversidad, los procesos ecológicos y la provisión de servicios ecosistémicos, objetivos principales para la conservación. A partir de estas diferencias planteamos que esta nueva área de conservación sería deficiente en el cumplimiento de sus objetivos. Sin embargo, proponemos que, una vez declarada como tal, la entidad administradora deberá diseñar e implementar un modelo de gestión que contemple prioritariamente la ampliación hacia límites naturales, la implementación de medidas de restauración y el monitoreo permanente de las métricas presentadas en la presente investigación, bajo el principio de que la conservación no solo es la declaración de un ámbito espacial en la categoría de reserva, sino en la necesidad de definir dichos espacios en base a herramientas y conocimientos geográficos que garanticen la efectiva protección y conservación de los ecosistemas de Lomas y Tillandsiales.

**Keywords:** Ecology, conservation, fog oases, morphometry, geomorphology.

**Palabras clave:** Ecología, conservación, oasis de neblina, morfometría, geomorfología.

Received: 13 December 2024

Accepted: 12 June 2025

**\*Corresponding author:** Marco Navarro, Grupo de Investigación Interdisciplinario de los Recursos Naturales, Ciencias Ambientales y de la Tierra (GIIRENCIAT), Facultad de Ingeniería de la Universidad Privada de Tacna, Perú. Email: marnavarro@upt.pe

### **1. Introduction**

The Peruvian coast features a desert strip interrupted by valleys that rely on river flow from the Andean foothills, as well as patches of vegetation found in foothills and flat areas that depend on fog. Coastal Lomas represent a unique ecosystem type known as fog oases (Moat *et al.*, 2021; Tovar *et al.*, 2018). These ecosystems develop due to the capture of water droplets by shrub and tree vegetation situated between 100 and 1,000 meters above sea level. They typically arise in areas with complex topography where atmospheric humidity is driven by advection and meets steep slopes (Beresford-Jones *et al.*, 2015). The Lomas are characterized by a permanent formation of structure consisting of shrub and tree species that are well-adapted to arid conditions. During the foggy season (from August to September on the southern Peruvian coast), plant diversity increases significantly due to the emergence of various herbaceous species, which typically have seeds in diapause during the dry season (MINAM, 2019). Due to their association with specific topographic features, the Lomas exhibit a discontinuous

distribution throughout the Sechura and Atacama Deserts, leading to a rich diversity of endemic species (Flores and Van Meerbeek, 2024). In flat or slightly sloping areas between 100 and 800 meters in altitude, where humidity meets the surface due to daily air mass movements caused by thermal variations and changes in density and pressure, Tillandsiales develop (Hesse, 2012). The Tillandsiales along the Peruvian coast comprise approximately five species of the genus *Tillandsia*, a group of Bromeliaceae that possess various physiological and anatomical adaptations, enabling them to absorb water and micronutrients from both soil (when available) and air (Rundel *et al.*, 1997; Belmonte *et al.*, 2022). Generally, each *Tillandsia* is dominated by one or a few species from the genus, resulting in lower specific and functional diversity compared to coastal Lomas (Stein *et al.*, 2023).

Currently, both formal and informal, as well as legal and illegal economic activities, threaten the conservation status of these ecosystems (Miyashiro and Ortiz, 2016). Activities such as mining and urban expansion can lead to direct ecosystem loss, replacing natural areas with land devoid of vegetation and generating permanent changes to the territorial landscape. Conversely, traditional practices such as camelid grazing have been conducted in the coastal Lomas since pre-Hispanic times without significant alteration (Baitzel and Rivera, 2019; Corcoran-Tadd, 2021). However, the introduction of more active species that consume plant material, including goats, since the colonial period has made the impacts of grazing activities much more harmful (Camel *et al.*, 2024). These direct human activities may interact with climate change, exacerbating their effects and diminishing the resilience of these ecosystems (Rau *et al.*, 2017; Tovar *et al.*, 2018). Evidence currently suggests a decline in the capacity of these ecosystems to provide essential services, such as habitat for important biodiversity and water resource capture (Ceballos, 2015; Madariaga, 2017).

Given the social and environmental risks, conservation proposals for the Lomas and Tillandsiales ecosystems in the Peruvian coastal desert are urgently needed, especially in areas facing rapid human pressures (Tovar *et al.*, 2018). However, it is crucial to have territorial planning documents that support this need, such as the Territorial Planning Plan of the Tacna Region (Gobierno Regional de Tacna, 2024). Upon the publication of the proposed polygon shapes for Regional Conservation Areas (RCAs) in El Peruano (2024), it has been noted that these boundaries are drawn on government-owned territories, excluding lands with preexisting rights. That evidence raises the question of whether these boundaries will effectively conserve such vital ecosystems and their biodiversity (Andrade, 2007). If the geographical landscape indices (topography, complexity, geomorphology, and surface) that underpin the ecological functioning of these ecosystems have been significantly altered from their natural state, ecological limitations for conservation are likely to arise (Olaya, 2009; Toivonen *et al.*, 2017).

This paper analyzes the differences in geomorphological and morphometric variability, as well as various landscape characterization indices, between the proposed polygons for regional conservation areas and the natural boundaries of the ecosystems intended for protection. The objective is to assess the extent to which the proposed areas preserve the ecosystem's spatial attributes, which are crucial for its sustainability. The questions we aim to address in this study are: (i) How does the geomorphological and morphometric variability of the ecosystem in the proposed areas for RCAs compare to the extent of the proposed protected ecosystem within their natural boundaries? (ii) What geographical tools can be used to measure the variation in landscape metrics between the compared polygons? (iii) Can the conservation of Lomas and *Tillandsia* ecosystems be effective without ensuring the preservation of their most significant geographical attributes?

## 2. Materials and methods

### 2.1. Study area

The study area is the coastal desert of the Tacna Region in southern Peru, from sea level to 2,000 meters above sea level. In this area, the Regional Government of Tacna has delimited five zones, proposing them as future conservation areas (Fig. 1), whose polygons were downloaded from the official statement

(RCA, El Peruano, 2024). These zones combine areas of seven large ecosystems characteristic of the coastal desert, including four Lomas: Chapolla, Tacahuay, Sama Grande, and Morro Sama. These Lomas represent a type of fog oasis formed by the interaction of masses of humidity from the Pacific Ocean carried eastward and intercepted by the coastal foothills. The three Tillandsiales, Intiorko, Yeseras, and Gallinazos, are large flat expanses covered by one of the most representative fog-dependent plant formations of the coastal desert, dominated by bromeliads of the genus *Tillandsia*. The total area of natural ecosystems is 619 km<sup>2</sup>, and the space proposed for conservation only reaches 235 km<sup>2</sup> (Table 1).

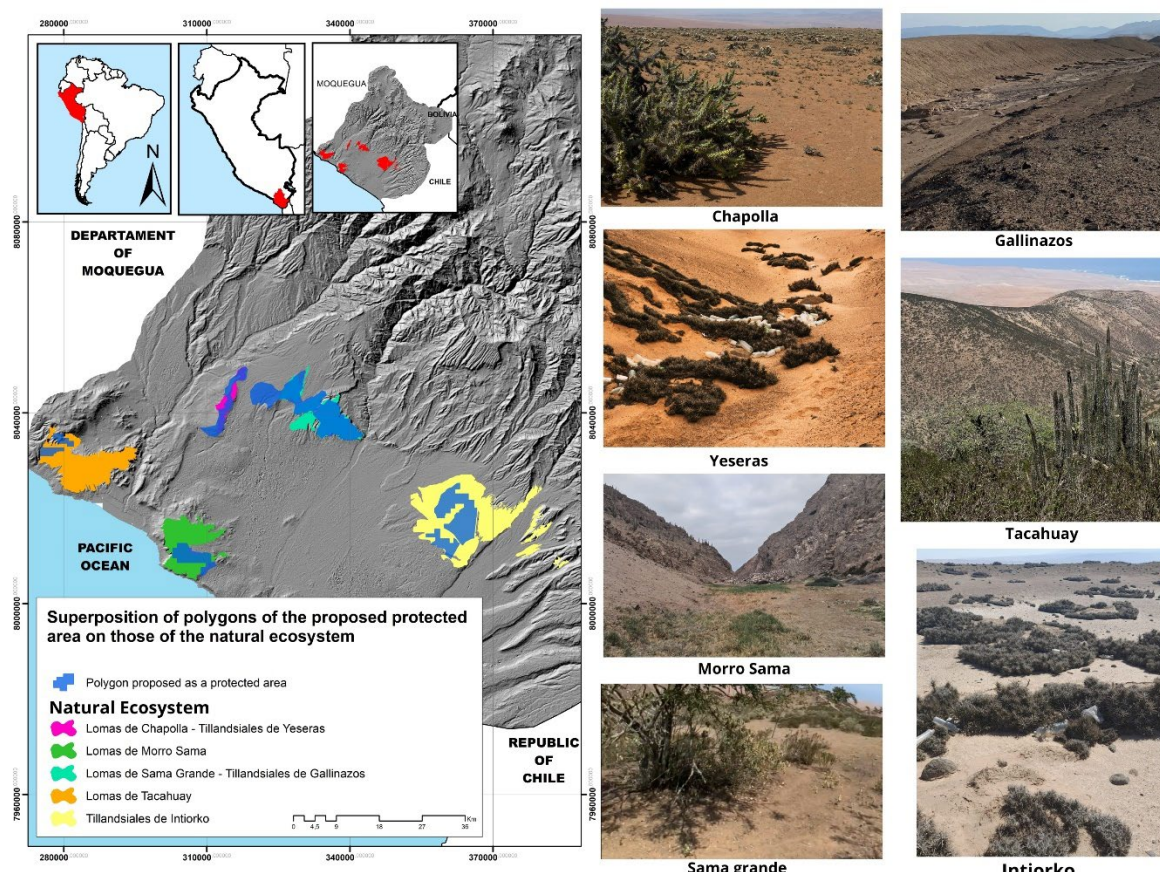


*Figure 1. Geographical location of the study area, the coast of the department of Tacna, where the five zones that occupy the seven ecosystems of hills and coastal desert evaluated are presented in a color palette, together with the blue polygons that the Regional Government proposes as conservation areas, together with their respective panoramic photographs.*

*Table 1. Description of the hilly and coastal desert ecosystems of the department of Tacna*

Ecosystem	Ecosystem area (km <sup>2</sup> )	Proposed area for RCA (km <sup>2</sup> )	Province
Lomas de Chapolla - Tillandsiales de Yeseras	22.1	24	Jorge Basadre
Lomas de Morro Sama	99.7	25	Tacna
Lomas de Sama Grande - Tillandsiales de Gallinazos	95.5	103.4	Tacna
Lomas de Tacahuay	128	11	Jorge Basadre
Tillandsiales de Intiorko	274	71.9	Tacna

The shapes representing the natural ecosystems were downloaded from the Peruvian Ecosystem Map (Ministerio del Ambiente, 2019), the National Vegetation Cover Map (Ministerio del Ambiente, 2015), and the Ecological and Economic Zonification of the Tacna Region (Gobierno Regional de Tacna, 2024). Subsequently, a manual correction of boundaries was made using high-resolution satellite images available on Google Earth (Google LLC, 2024) using QuickMapServices 0.19.36 in QGIS 3.40.0 (QGIS Development Team, 2024). Finally, the boundaries were adjusted based on primary information gathered during periodic field visits conducted between 2023 and 2024.

## 2.2. Geomorphologic, morphometric, and landscape analyses

To assess the geomorphological variability of natural Lomas and Tillandsiales ecosystems and the polygons proposed as new conservation areas, the Gravelius compactness index (Eq. 1) was used. This index measures the degree of compaction or geometric complexity of its territory, allowing the perimeter to be quantified per unit area and associated with edge effects, fragmentation, and connectivity.

$$K_g = \frac{P}{2\sqrt[2]{\pi \times A}} \quad (1)$$

where  $K_g$  is the Gravelius index,  $P$  is the polygon perimeter in km, and  $A$  is its area in  $\text{km}^2$ .

For the morphometric analysis, the available 12.5-meter resolution Alos-Palsar digital elevation models (Alaska Satellite Facility, 2024) were downloaded. Altitude values were extracted from these models, and the slope, morphometric protection index (MPI), topographic wetness index (TWI), and Aspect (Table 2) for the natural ecosystems and proposed protected areas were estimated. These morphometric indices are quantitative tools used in landscape analysis to understand the physical characteristics of the Earth's surface, such as watersheds, and their geomorphological processes (Toivonen *et al.*, 2018). They are used to describe the shape, size, and distribution of landscape elements, as well as to identify drainage and relief patterns (Olaya, 2009). All the factors evaluated influence species distribution and habitat suitability. The slope determines factors such as the depth of the soil or its stability, MPI measures how well a location is protected from exposure by the surrounding relief, the TWI assesses the spatial distribution of moisture, and the Aspect determines how much radiation receives the land (Mander *et al.*, 2017). Based on the morphometry rasters, the mean values and the coefficient of variability ( $CV = \text{sd}/\text{mean}$ ) were estimated for each study site, which helped compare vulnerability prioritize conservation that maximizes natural wetness and representativeness, as done by Doherty *et al.*, 2021, Harris and Baird 2019, Jeong *et al.*, 2024, Toivonen *et al.* 2018.

All the morphometric analyses were conducted using GIS packages such as spatialEco (Evans and Murphy, 2023), raster (Hijmans, 2024), and sp (Bivand *et al.*, 2013) in R 4.4.1 software (R Development Core Team, 2024). Like those done by Lipori and Martín (2022), Kondo *et al.* (2024), Faye and Ndiaye (2021), Bendjoudi and Hubert (2002).

To characterize each of the evaluated landscapes and compare the complexity and irregularity of the polygons proposed as future conservation areas about the boundaries of natural ecosystems, metrics or indices were calculated using Patch Analyst Tools v5.2 (Rempel *et al.*, 2012). Eight geographic indices were selected that represented the values of shape (3), edge (3), density-size (1), and area (1) (Table 3), in the same way as Ahmadzadeh *et al.*, 2023, Diktaş Bulut, 2023, Franco León *et al.*, 2024, Navarro *et al.*, 2021, Yu and Liu, 2025, developed in their respective investigations.

*Table 2. Geomorphological and morphometric variables calculated for the study areas.*

Variable	Description	Environmental importance
Gravelius compacity coefficient ( $K_g$ )	Relates the study site perimeter with the perimeter of a circumference with the same area	Includes of isolated habitats (headwaters, canyons) and corridor/connectivity attributes
Altitude	Obtained directly from the Digital Elevation Model, is the altitude (in meters above sea level) for each cell in the raster	Temperature, radiation, clouds interception
Slope	Slope Angle in Degrees ( $^{\circ}$ ) estimated for a raster cell as the average with respect to its eight neighboring cells	Solar radiation exposure, soil accumulation, terrain stability, soil moisture
Aspect	The circular values of orientation (0 - 360 $^{\circ}$ ) corresponding to the cell on the slope	Solar radiation, summer-winter effects, day-night effects
Morphometric protection index	It analyzes the immediate vicinity of each cell up to a user-defined boundary, to assess how the relief protects that point. Starting from a particular cell, the algorithm evaluates in the directions of the 8 neighboring cells to calculate the vertical angle between the point of interest and its immediate range. The vertical angle values are iterated until the evaluation distance limit is reached, and then the average value of all angles obtained is estimated as the MPI value.	Hydrological condition, solar radiation exposure
Topographic wetness index	It consists of two parts: the hydrological contribution area per unit contour length (m <sup>2</sup> /m) called the area of the specific basin and the local slope in radians. This index developed for hydrological modeling is used to locate saturated areas that can generate runoff and to estimate the average aquifer level.	Soil moisture, flow accumulation zones

*Table 3. Landscape metrics used to assess similarity between natural ecosystems and proposed polygons as RCAs.*

Metric	Name	Type	Description
<b>MSI</b>	Average Shape Index	Shape	Equal to 1 when the patches tend to AWMSI circularity, the value increases when they tend to be irregular.
<b>MPAR</b>	Perimeter-to-Area Ratio Average	Shape	Estimate the regularity or complexity of the shape of the geographic polygon.
<b>MPFD</b>	Average of the fractal dimension	Shape	Calculate the degree of complexity of each fragment based on the relationship between area and perimeter. The AWMPFD index has theoretical limits that are between 1 and 2; Higher values indicate greater complexity and values close to 1 indicate simpler geometric shapes.
<b>TE</b>	Total edge	Edge	Total patch perimeter.
<b>ED</b>	Edge density	Edge	Amount of perimeter with respect to the total area of the landscape. It is the sum total of all edge lengths of a class (TE), divided by the total area of the landscape.
<b>MPE</b>	Edge Perimeter Average	Edge	Express the average perimeter length (TE) of the spaces for each type of class. It is calculated by dividing the total value of the class perimeter (TE) by the total number of spots (NumP).
<b>MPS</b>	Average Patch Size	Density	It represents the average area of patches contained in a class. It should be analyzed in conjunction with the standard deviation of patch size (PSSD)
<b>CA</b>	Class Area	Area	Landscape composition measures are the area of each class.

### 2.3. Effectiveness assessment for the proposed conservation areas

Based on the data obtained, the variability ranges between the boundaries of the proposed polygons as new protected areas and those of the Lomas and Tillandsiales. To do this, the ratio of the area represented by the RCA polygon to the boundaries of the natural ecosystems was estimated. Regarding the Gravelius compactness coefficient, the ratio of the value in kg of each area proposed for RCA to the kg of the polygons comprising the entire natural ecosystems was estimated. The same ratio was then estimated based on the coefficients of variability (CV) of each of the calculated morphometric variables (Eq. 2).

$$R_{A/N} = \frac{Obs_A}{Obs_N} \quad (2)$$

where  $R_{A/N}$  is the ratio of values between the proposed RCA and the natural extent of each ecosystem,  $Obs_A$  is the value obtained for the RCA, and  $Obs_N$  is the value obtained for the Natural Extension of the ecosystem. The observed values can refer to the total surface area, Gravelius  $K_g$ , and coefficients of variation for altitude, slope, MPI, TWI, and Aspect.

Based on these ratios, nonlinear models were developed to evaluate the relationship between the proportion of area change versus the proportion of change in the geomorphological and morphometric parameters of the study polygons, similar to those carried out by El Jeitany *et al.* (2024), Lu *et al.* (2024), Macchioli *et al.* (2024), Speetjens *et al.* (2023), Wang *et al.* (2023), and Zhao *et al.* (2024) in their respective investigations.

Landscape parameters were analyzed by graphically representing positive or negative change by landscape metric, as well as by calculating a similarity index. Additionally, multivariate tests were conducted to assess the ecological similarity of the polygons based on landscape metrics for the extent of the natural ecosystem and the proposed RCA in each area of interest. For this, a principal components analysis (PCA) was applied, which allows for the reduction of the dimensionality of the data and shows how they are grouped according to the eight calculated variables (Warren *et al.*, 2008; Yu and Liu, 2025; Zhang *et al.*, 2025). All comparative analyses were conducted using R 4.4.1 (R Development Core Team, 2024).

## 3. Results

### 3.1. Geomorphological and morphometric differences

A comparison of the average data and the coefficient of variability (CV) for each geomorphological and morphometric parameter across five study areas reveals notable differences in their characteristic patterns (Table 4). Firstly, the most significant differences in the average CV between the RCA polygons and the natural ecosystems are observed in two variables: the Gravelius coefficient ( $K_g$ ), which has an average CV of -0.37, and the distribution of altitude values, with an average CV of -0.16. In contrast, for the other four variables, the average CV values exceed -0.09 units, indicating that the average variability for these parameters is quite similar. Secondly, there is a notable variation in the size of the proposed RCA polygons when comparing the average CV change values across the five sites. The most extreme case is found in the Tacahuay Lomas, where the proposed RCA polygon represents only 8.6% of the natural ecosystem area (0.086). The average reduction in variability for all other evaluated parameters in this case is 20%. In the Intiorko Tillandsial, where the RCA polygon covers 26.2% of the natural ecosystem (0.262), the average reduction in geomorphological and morphometric variability relative to the natural limits is 35%. The Morro Sama Hill has a proposed RCA area that is 25% of the ecosystem area (0.25), resulting in an average 8% reduction in variability. In contrast, the RCA proposals that encompass Loma Chapolla and Tillandsial Yeseras, as well as Loma Sama Grande with Tillandsial Gallinazos, which cover nearly all the ecosystems (with the RCA being 1.08 times the ecosystem area in both instances), show negligible changes in variability for these parameters (1% and 2%, respectively).

Table 4. Average and coefficient of variation for the geomorphological and morphometric indexes estimated for the study sites.

Proposed RCA / Natural Extent Ratio	Gravelius Kg			Altitude			Slope	
	Natural Extent	Proposed RCA	Natural Extent	Proposed RCA	Natural Extent	Proposed RCA	Natural Extent	Proposed RCA
Tacahuay	0.086	3.14	2.23	605 (0.41)	782 (0.36)	17.7 (0.47)	21.2 (0.38)	
Intiorko	0.262	5.94	2.63	963 (0.16)	914 (0.09)	6.32 (1.01)	4.14 (0.71)	
Morro Sama	0.250	3.16	1.79	655 (0.29)	543 (0.14)	14.4 (0.60)	9.49 (0.73)	
Chapoya - Yeseras	1.084	2.72	2.49	999 (0.07)	959 (0.10)	7.76 (0.63)	7.83 (0.61)	
Sama Grande - Gallinazos	1.083	4.43	2.37	1010 (0.13)	1011 (0.11)	14.7 (0.62)	12.9 (0.72)	
MPI								
Natural Extent	Proposed RCA	Natural Extent	Proposed RCA	Natural Extent	Proposed RCA	Natural Extent	Proposed RCA	Aspect
Tacahuay	0.17 (0.44)	0.19 (0.34)	(0.28)	6.81	6.49 (0.25)	189.7 (0.42)	191.1 (0.33)	
Intiorko	0.06 (0.81)	0.04 (0.46)	(0.26)	11.2	12.3 (0.18)	218.4 (0.36)	224.8 (0.34)	
Morro Sama	0.12 (0.51)	0.09 (0.61)	(0.30)	7.36	8.58 (0.30)	183.6 (0.51)	171.1 (0.57)	
Chapoya - Yeseras	0.06 (0.47)	0.06 (0.45)	(0.19)	8.77	8.68 (0.18)	171.1 (0.56)	182.1 (0.49)	
Sama Grande - Gallinazos	0.13 (0.57)	0.12 (0.66)	(0.33)	7.38	8.00 (0.35)	204.3 (0.41)	213.3 (0.40)	

Proposed RCA: proposed regional conservation area

Natural extent: natural extension of the ecosystem

Gravelius Kg: Gravelius compacity index

MPI: morphometric protection index

TWI: topographic wetness index

All values were represented as: average or average (coefficient of variation)

When correlating the Factor<sub>RCA</sub>/Factor<sub>Ecosystem</sub> ratios with the proportion of the natural ecosystem area expected to be conserved under the RCA proposals (illustrated in Fig. 2), it is evident that each geomorphological or morphometric factor exhibits distinct variations. The variation in altitude ranges, showing a coefficient of determination ( $R^2$ ) of 0.47, demonstrates the strongest correlation with spatial representativeness. The variations in the topographic humidity index and the morphometric protection index present moderate  $R^2$  values of 0.27 and 0.20, respectively. For the remaining parameters, the  $R^2$  values are all below 0.20, indicating that there is little significant difference in retaining the potential ranges of variability.

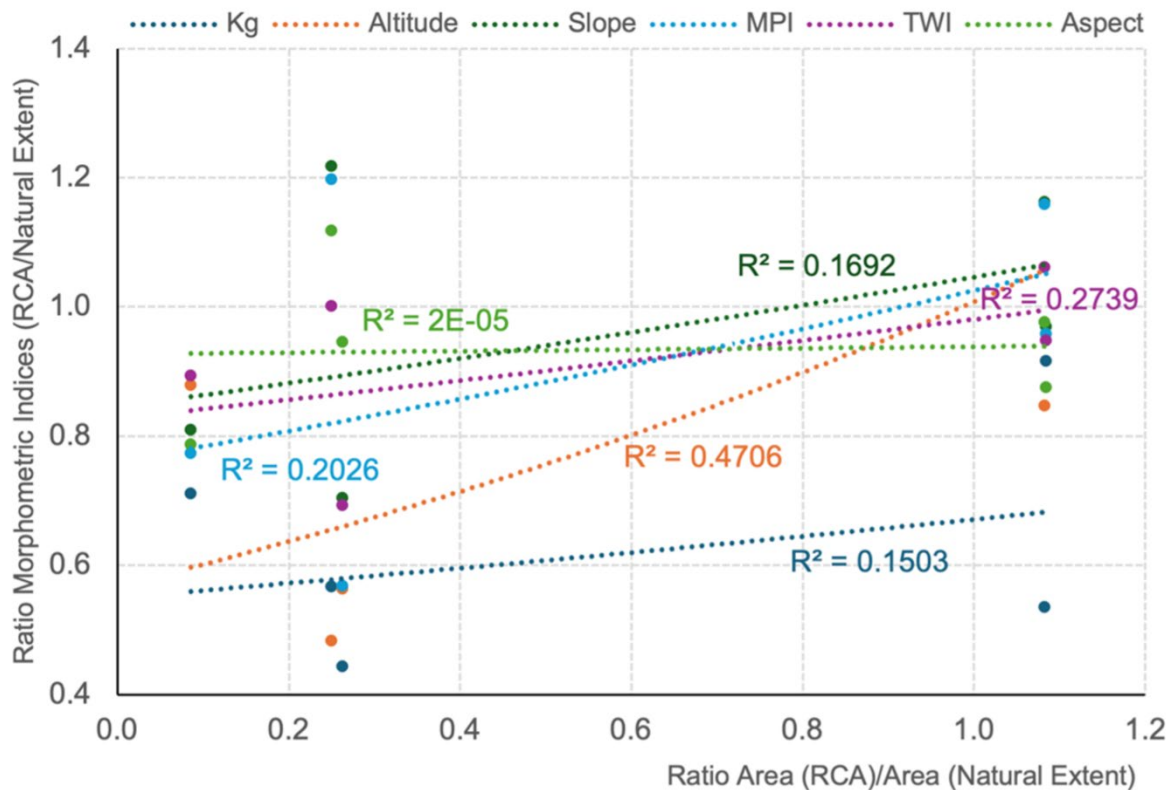


Figure 2. Nonlinear fit and coefficient of determination ( $R^2$ ) comparing the RCA/Natural surface area ratio (x – axis) versus the variability (CV) ratio of each geomorphological and morphometric variables (y -axis) estimated for the study areas.

### 3.2. Landscape metrics

By superimposing the polygons representing the natural boundaries of the ecosystem with those proposed for the new protected natural area (Fig. 1), significant geographical differences become apparent. These differences are evident not only in size but also in the linearity of their shapes, the reduction of their areas, and the increase in their edges. These factors are key indicators of ecological health, which are essential for conserving biodiversity.

A review of the landscape metrics for the eight indices used reveals significant variability in both landscapes (see Fig. 3a). This variability, both positive and negative, raises questions about the effectiveness of these metrics for conservation, given what each landscape metric represents (Table 3). Among the areas analyzed, the Lomas of Tacahuay, Morro Sama, and the Tillandsial of Intiorko exhibited the most significant variation, as indicated by the number of metrics that changed, influencing their ecological structure; these areas had seven, seven, and eight changing metrics, respectively (see Table 5).

Table 5. Landscape metrics calculated by polygon and study areas

Study area	Polygon	Shape			Edge		Density	Area	
		MSI	MPAR	MPFD	TE	ED	MPE	MPS	CA
Lomas de Chapolla - Tillandsiales de Yeseras	Natural Ecosistem	2.72	20.50	1.27	45369.03	0.73	45369.03	2208.07	2208.07
	RCA proposal	2.49	18.10	1.26	43240.53	1.84	43240.53	2393.49	2393.49
	% Change	-8.46	-11.71	-0.92	-4.69	151.06	-4.69	8.40	8.40
	Ecological condition	<i>Territory fragmentation leads to a loss of irregularity, with more regular shapes (squares, circles), severely impacting biodiversity by reducing ecosystem complexity and favoring generalist species. Additionally, environmental conditions at edges change, decreasing core areas, and the increased number of fragments reduces the average perimeter, affecting ecological functionality.</i>							
Lomas de Morro Sama	Natural Ecosistem	3.16	11.20	1.26	111993.53	1.81	111993.53	9971.68	9971.68
	RCA proposal	1.79	12.70	1.22	31589.50	1.34	31589.50	2491.59	2491.59
	% Change	-43.57	13.39	-3.63	-71.79	-25.70	-71.79	-75.01	-75.01
	Ecological condition	<i>The fragmentation of the territory leads to a loss of irregularity with more regular shapes (squares, circles), severely affecting biodiversity by reducing ecosystem complexity and favoring generalist species. Changes in edge conditions decrease core areas, reduce ecosystem connectivity, and increase the number of fragments with smaller perimeters. Fragment sizes shrink, offering fewer suitable conditions for species and ecological processes, along with lower resource availability due to area effects.</i>							
Lomas de Sama Grande - Tillandsiales de Gallinazos	Natural Ecosistem	4.43	16.10	1.30	153314.96	2.48	153314.96	9552.17	9552.17
	RCA proposal	2.37	8.20	1.23	85301.13	3.63	85301.13	10343.57	10343.57
	% Change	-46.53	-49.07	-5.32	-44.36	46.56	-44.36	8.28	8.28
	Ecological condition	<i>Territory fragmentation results in a loss of irregularity, forming more regular shapes (e.g., squares, circles), which severely impacts biodiversity. The ecosystem becomes less complex, favoring generalist species, while changes in edge conditions reduce core areas. Additionally, an increase in the number of fragments lowers the average perimeter of each fragment, further compromising ecological integrity.</i>							
Lomas de Tacahuay	Natural Ecosistem	3.14	9.80	1.26	125870.77	2.03	125870.77	12813.63	12813.63
	RCA proposal	2.23	23.90	1.26	26202.75	1.11	26202.75	1098.32	1098.32
	% Change	-28.90	143.88	-0.24	-79.18	-45.16	-79.18	-91.43	-91.43
	Ecological condition	<i>Territory fragmentation leads to a loss of irregularity, forming regular shapes (e.g., squares, circles), which severely affects biodiversity. Ecosystem complexity decreases, favoring generalist species, while changes at the edges reduce core areas. Connectivity between ecosystems is diminished, further harming biodiversity. An increase in the number of fragments reduces the average border perimeter, and smaller fragment sizes offer fewer suitable conditions for species and ecological processes, along with limited resource availability due to area effects.</i>							
Tillandsiales de Intiorko	Natural Ecosistem	5.92	12.70	1.31	347538.08	5.61	347538.08	27399.20	27399.20
	RCA proposal	2.63	11.00	1.25	78925.49	3.36	78925.49	7189.15	7189.15
	% Change	-55.67	-13.39	-5.08	-77.29	-40.18	-77.29	-73.76	-73.76
	Ecological condition	<i>Territorial fragmentation results in the loss of irregularity, forming regular shapes (e.g., squares, circles), which negatively impacts biodiversity. It reduces ecosystem complexity, favoring generalist species, while edge conditions diminish core areas. Ecosystem connectivity is weakened, increasing fragmentation with smaller fragments, lower perimeter-to-area ratios, and fewer suitable conditions for species and ecological processes. Resource availability also declines due to the area effect.</i>							

The ecological similarity index (Fig. 3b), based on inverse Euclidean distance, highlights the differences between the polygons representing natural ecosystems and those designated for conservation. This analysis highlights the importance of prioritizing effective conservation strategies. Notably, three proposed areas, the Morro Sama and Tacahuay Lomas and the Tillandsial Intiorko, exhibit significant deficiencies for conservation.

Additionally, the principal components analysis (PCA) produced two spatial dispersion graphs (see Fig. 4), illustrating how the polygons of the study areas cluster based on the eight evaluated variables. The upper graph reveals the ecological similarity of ecosystems within their natural boundaries, while the lower graph displays the proposed conservation polygons. This graph clearly shows a radical change between the areas, confirming the variability among the linear combinations of landscape metrics. In this PCA, the X-axis accounts for most of the data variance. At the same time, the Y-axis represents the second most significant portion of the variance, independent of the X-axis.

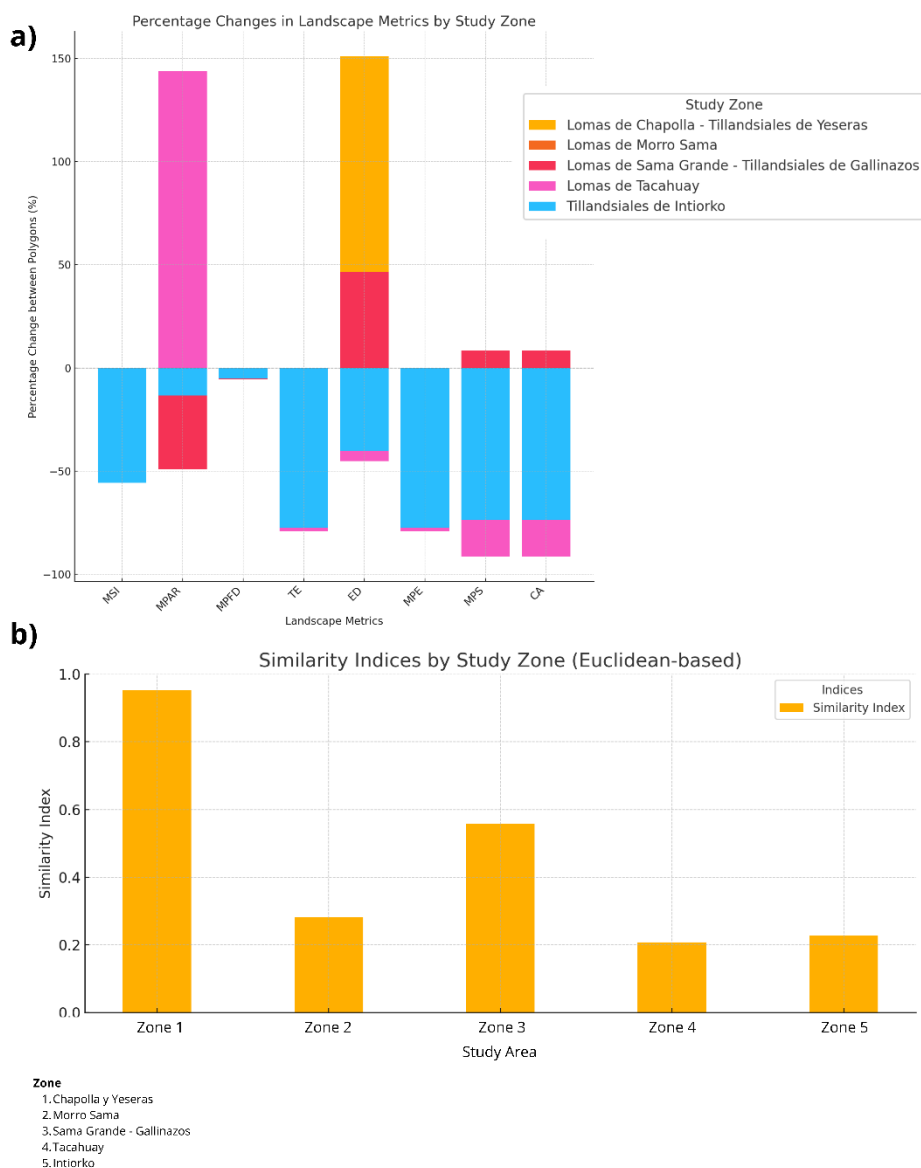
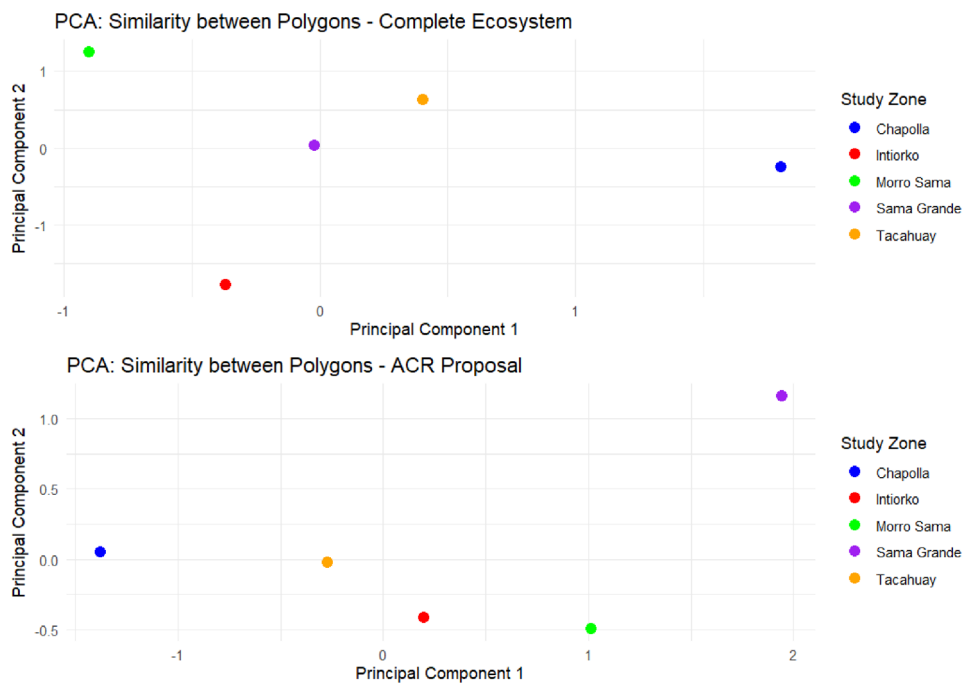


Figure 3. a) Efficiency graph according to the eight-landscape metrics evaluated, where positive and negative changes are observed. b) Bar graphs of the ecological similarity index by area of the polygons of the natural ecosystem and their proposed conservation area.



*Figure 4. Spatial dispersion graphs as a result of principal component analysis (PCA), in the upper part the dispersion of natural ecosystems and in the lower part it is observed how their dispersion and similarity change when their landscape metrics vary in the process of delimitation as a conservation area.*

#### 4. Discussion

The relationship between geography and landscape ecology, along with its practical applications, plays a crucial role in addressing new challenges in the conservation of natural heritage. Technological tools have been integrated to facilitate the accurate identification and delineation of ecosystems, as well as to analyze areas designated for conservation, community management, and sustainable use. For instance, the use of geographic tools has enabled us to identify the most representative areas of Lomas and Tillandsiales along the coast of Tacna. Our findings align with those of Moat *et al.* (2021), which highlight the occupancy areas of natural fog oases in the Tarapacá Desert and their underrepresentation in the protected areas system. These tools are not only essential for identification and delineation but also facilitate statistical calculations based on landscape metrics such as shape, area, size, and edge. It is vital to assess the quality of the polygons that represent ecosystems or delineate conservation areas (Vila Subirós *et al.*, 2006) to determine their effectiveness for conservation efforts.

Additionally, these tools enable us to test fundamental ecological theories on biodiversity distribution, including the biogeographic island theory proposed by MacArthur and Wilson (1963, 1967) and the theory by Gascon *et al.* (1999). Both models emphasize the importance of connectivity and patch size, suggesting that intense fragmentation can lead to an increase in generalist species at the expense of specialist species. This raises concerns about conserving small, isolated, or regular areas, as is the case with the proposed RCAs for Lomas and Tillandsiales in Tacna, which cover less than 50% of the natural limits of the targeted ecosystems (see Fig. 3a).

Landscape metrics are partially derived from geomorphological and morphometric factors, as analyzed in this paper. Morphometry includes elements such as orientation (or Aspect), exposure to direct sunlight (measured by the Mean Potential Index, MPI), and relative position concerning areas with closer proximity to groundwater (expressed by the Topographic Wetness Index, TWI). These factors play a fundamental role in the distribution, extent, and complexity of ecosystems (Olaya, 2009). This significance is especially pronounced in arid environments, where strategies to reduce water

consumption can be enhanced by terrain shapes that create optimal microclimates, thereby fostering extended periods of water availability (Elhag *et al.*, 2017). The ideal combination of these factors can promote greater species diversity, leading to the formation of areas that serve as biodiversity hotspots with high levels of complexity and richness, particularly in regions that are generally considered to be poor in biodiversity (Al-Rowaily *et al.*, 2012). In our observations, we find that specific parameters, such as the regularity of geographic polygons (kg) and the patterns of altitude distribution, demonstrate relatively high variability depending on the area in question. Other factors, such as topographic humidity and morphometric protection, which are closely associated with abrupt changes in altitude and slope, tend to exhibit medium variability. In contrast, slopes or aspects usually do not exhibit significant changes. Given the importance of factors that enhance water resource availability (or reduce water demand), it is crucial to consider these elements when delineating ecosystem protection areas, particularly in arid regions (Kadam *et al.*, 2017).

The results of the negative variation in landscape metrics indicate that those metrics related to the shape of polygons (see Fig. 3a), such as the Mean Shape Index (MSI) and the Perimeter-Area Ratio (PAR), reveal that the new conservation area for the Lomas and coastal desert in the Tacna Region, proposed by the government, has regular shapes. In contrast, the natural ecosystems exhibit more complex, fractal shapes. This difference is significant for conservation efforts because regular shapes can reduce species connectivity and increase the vulnerability of edges (With, 2019). More fractal shapes and complex geometries provide better conditions for biodiversity and enhance conservation opportunities, as evidenced by the decrease in the Mean Fractal Dimension (MPFD). Santos *et al.* (2006) highlight that if the edges of natural ecosystems are altered, perimeter bands with varying conditions for species will form. These modified edges often have lower ecological quality compared to the high-quality core areas.

Furthermore, greater total edge (TE) and average edge (MPE) measurements are associated with smaller core sizes due to variations in physical and biotic factors that can significantly impact population survival. In the proposed conservation area, the TE and MPE differ from the original ecosystem by approximately 70% in the Intiorko Tillandsia region. Therefore, it is crucial to protect core areas from surrounding zones.

Changes in landscape metrics have been shown to influence species distribution directly. In the Lomas and Tillandsiales, flora species such as *Tillandsia werdermanni* and *Carica candicans* are classified at various danger levels according to national and international standards (Decreto Supremo N° 043-2006-AG, 2006; Navarro *et al.*, 2020; IUCN, 2012). This necessitates an examination of the impacts that human activities have had over the years, as well as the changes in ecosystems related to shape, edge, size, and area. Verga *et al.* (2018) studied the relationship between fruit quality and seed abundance concerning area and edge, while Chacoff *et al.* (2006) observed a decrease in seed viability for *Acacia aroma* as fragment size diminished. Their findings also indicated lower predation indexes (less than 14%) in smaller fragments compared to larger ones, along with a 20% increase in the proportion of healthy seeds. These examples illustrate the consequences of fragmentation on the trophic chain, which likely affects all subsequent links. This phenomenon extends to other species in the community, which also experience population fluctuations based on the shapes, edges, areas, and sizes of the habitats they occupy. For instance, Tinajero and Rodríguez (2012) reported differences in bird records between fragmented and natural areas. This finding aligns with Wolff *et al.* (1997), who noted reduced movement in the grey-tailed field rodent. These dynamics suggest that the fauna of the Lomas and Tillandsiales regions will be adversely affected by changes in landscape metrics. For endangered lizard species, such as *Liolaemus poconchilensis* and *L. basadrei* (Valladares *et al.*, 2021), management strategies must account for their ecological niches and the landscape metrics that influence them. Studies conducted in nearby areas indicate that bird richness is significantly correlated with habitat area and size (Franco *et al.*, 2024).

Given the substantial scientific evidence showing little similarity between the landscape metrics—such as shape, edge, and area—of the natural ecosystem and the government's proposed conservation area, it is essential to provide comprehensive technical and scientific information regarding the limitations of

this new protected zone. Table 5 outlines the ecological conditions of the polygon for each study area, drawing parallels with analyses by Saura and Pascual-Hortal (2007). It can be concluded that the design of the conservation proposal has not been optimal and will present ecological limitations (Andrade, 2007).

This research aims to assist in the development of an effective management model for the new conservation area, highlighting the ecological challenges it will encounter from the outset. It emphasizes the importance of using geographical tools and principles of landscape ecology, suggesting that management based solely on political criteria or land-use rights is no longer sustainable. Instead, the focus should shift to the role of science and research. Political decisions alone cannot create protected areas across different government levels; these efforts must be supported by substantial technical expertise, which academia can uniquely provide, though it is often undervalued in conservation management processes. Moreover, this presents an opportunity to incorporate new methodologies into regional planning processes and strategies. An ecosystem approach, among others, can bolster regional efforts to combat climate change, conserve biodiversity, and address desertification and drought, thus significantly enhancing territorial management and development.

## 5. Conclusion

The deficiencies of the proposed new conservation area for conserving the Lomas and Tillandsial ecosystems in the Tacna Region have been demonstrated. The shape, border, size, and area of the area indicate that the methods used to delimit its polygons (technical land use criteria and consideration of the limits of preexisting rights) are inadequate and that conservation will not be effective. This highlights the need to develop a suite of geographic tools, which can also be used to evaluate design effectiveness.

Given these geographic limitations and the fact that the creation process is progressing slowly with the competent national authority, it is proposed that this protected area have a specific management model aimed at addressing the deficiencies identified. Its management must be regulated within the context of landscape ecology and its leading conservation indicators and objectives: restoring irregularity, complexity, and connectivity with the natural ecosystem. This is undoubtedly a complex task for its administrator and strategic partners and one in which technical considerations prevail over political criteria.

Research institutions, such as universities and specialized institutes, are excellent sources of scientific information. They can help ensure the conservation of the Lomas and Tillandsiales of the coastal desert. However, they must be articulated and considered in the management committees of protected areas or in the mechanisms of administration contracts. The results of their research must be increasingly linked to the decisions made by public entities.

## Acknowledgments

The authors would like to acknowledge the Programa Nacional de Investigación Científica y Estudios Avanzados – PROCIENCIA of the Consejo Nacional de Ciencia y Tecnología - CONCYTEC for funding the research project "Conservation status of Lomas and coastal desert ecosystems and their importance in contributing to the sustainable development of the Department of Tacna" under Contract No° PE51082394-2023-PROCIENCIA. The authors also acknowledge the Universidad Privada de Tacna for its technical and administrative implementation of the project through Rectoral Resolution No. 1517-2023-UPT-R.

Furthermore, the development of the fieldwork and data collection was made possible thanks to the Authorization for Scientific Research purposes issued by the Servicio Nacional Forestal y de Fauna Silvestre – SERFOR through the Resolution Directorate N° 147-2023-MIDAGRI-SERFOR-DGGSPFFS-DGSPF.

## References

- Ahmadvadeh, R., Dehdar Dargahi, M., Khorasani, N., Farsad, F., Rahimibashar, M. R., 2023. Assessment of wetland landscape changes based on landscape metrics and trophic state index (case study: Anzali International Wetland). *Environmental Monitoring and Assessment* 195(10), 1206. <https://doi.org/10.1007/s10661-023-11672-1>
- Alaska Satellite Facility, 2024. *About ASF*. <https://ASF.alaska.edu/about/>
- Andrade, A., 2007. *Aplicación del Enfoque Ecosistémico en Latinoamérica*. CEM-UICN. Bogotá, Colombia. <https://portals.iucn.org/library/sites/library/files/documents/CEM-007.pdf>
- Bendjoudi, H., Hubert, P., 2002. Le coefficient de compacité de Gravelius: analyse critique d'un indice de forme des bassins versants. *Hydrological Sciences Journal* 47(6), 921-930. <https://doi.org/10.1080/02626660209493000>
- Bivand, R., Pebesma, E., Gomez-Rubio, V., 2013. *Applied spatial data analysis with R*, Second edition. Springer, NY. <https://asdar-book.org/>
- Ceballos, A. M., 2015. Combinación de información Topográfica-Estructural Lidar y Teledetección hiperespectral para estimar la Diversidad Florística Vascular de un Bosque Mediterráneo Caducifolio en la Precordillera Andina del Maule, Chile. *Facultad de Ciencias Agronómicas*, Universidad de Chile.
- Chacoff, N., Morales, J., Vaquera, M., 2006. Efectos de la Fragmentación Sobre la Absorción y Depredación de Semillas en el Chaco Serrano. *Biotropica* 36, 109-117. <https://doi.org/10.1111/j.1744-7429.2004.tb00301.x>
- CMIP6, 2022. Coupled Model Intercomparison Project Phase 6. <https://pcmdi.llnl.gov/CMIP6/TermsOfUse/TermsOfUse6-1.html>
- Decreto Supremo N° 043-2006-AG. (13 de julio de 2006). (D. O. Peruano, Editor) *Aprueban categorización de especies amenazadas de flora silvestre*. SENACE <https://www.senace.gob.pe/wp-content/uploads/2016/10/NAT-3-3-03-DS-043-2006-AG.pdf>
- Diktaş Bulut, N., 2023. Human-Induced forest fragmentation in Trabzon, Eastern Black Sea Region, Türkiye: A case study. *Forest* 14(8), 1622. <https://doi.org/10.13140/RG.2.2.35869.36322>
- Doherty, K. D., Kuhlman, M. P., Durham, R. A., Ramsey, P. W., Mumme, D. L., 2021. Fine-grained topographic diversity data improve site prioritization outcomes for bees. *Ecological Indicators* 132, 108315. <https://doi.org/10.1016/j.ecolind.2021.108315>
- El Jeitany, J., Nussbaum, M., Pacetti, T., Schröder, B., Caporali, E., 2024. Landscape metrics as predictors of water-related ecosystem services: Insights from hydrological modeling and data-based approaches applied on the Arno River Basin, Italy. *Science of the Total Environment* 954, 176567. <https://doi.org/10.1016/j.scitotenv.2024.176567>
- El Peruano, 2024, (10 de 05 de 2024). *Boletín oficial: Comunicado del Gobierno Regional de Tacna*. <https://epdoc2.elperuano.pe/EPO/Descarga.asp?>
- Evans, J.S., Murphy, M.A., 2023. *spatialEco*. R package version 2.0-2, <https://github.com/jeffreyevans/spatialEco>
- Faye, C., Ndiaye, M., 2021. Use of geospatial tools in morphometric analysis and prioritisation of sub-catchments of the Soungrougrou (Casamance Basin). *Quaestiones Geographicae* 40(3), 65-84. <https://doi.org/10.2478/quageo-2021-0024>
- Franco León, P., Navarro Guzmán, M. A., Oyague Passuni, E. J., Ignacio Apaza, J. M., Jove C., 2024. Fragmentation, birds, and conservation of the Polylepis Forest in Southern Peru. *Cuadernos de Investigación Geográfica* 50(1), e5823. <https://doi.org/10.18172/cig.5823>
- Gascon C., Lovejoy, T.E., Bierregaard, R.O., Malcolm, J.R., Stouffer, P.C., Vasconcelos, H.L., Laurance, W.F., Zimmerman, B., Tocher, M., Borges, S., 1999. Matrix-habitat and species richness in tropical forest remnants. *Biological Conservation* 91(2-3), 223-229. [https://doi.org/10.1016/s0006-3207\(99\)00080-4](https://doi.org/10.1016/s0006-3207(99)00080-4)
- Gobierno Regional de Tacna, 2024. *Plataforma web para el servicio de información espacial del proceso de ordenamiento territorial del departamento de Tacna*. <https://geotacana.region tacna.gob.pe/>
- Google LLC., 2024. Google Earth Pro (version 7.3.6). <https://www.google.com/earth/>

- Harris, A., Baird, A. J., 2019. Microtopographic drivers of vegetation patterning in blanket peatlands recovering from erosion. *Ecosystems* 22, 1035-1054. <https://doi.org/10.1007/s10021-018-0321-6>
- Hijmans, R., 2024. Raster: Geographic Data Analysis and Modeling\_. R package version 3.6-30. <https://CRAN.R-project.org/package=raster>
- Jeong, A., Kim, M., Lee, S., 2024. Analysis of priority conservation areas using habitat quality models and MaxEnt models. *Animals* 14(11), 1680. <https://doi.org/10.3390/ani14111680>
- Kadam, A.K., Jaweed, T.H., Umrikar, B.N., 2017. Morphometric prioritization of semi-arid watershed for plant growth potential using GIS technique. *Model. Earth Syst. Environ.* 3, 1663–1673. <https://doi.org/10.1007/s40808-017-0386-9>
- Kondo, K. F., Tchakala, I., Dadja-Toyou, G. M., Sambienou, W. G., Adandedji, F., Boukari, O., Mama, D., 2024. Contribution to the sustainable management of water and soil resources in North-West Benin: Characterization of the watershed heads of the Ouémé and Pendjari rivers in the commune of Copargo. *European Scientific Journal* 20(33), 353-372. <https://doi.org/10.19044/esj.2024.v20n33p353>
- Lipori, M., Martín, G., 2022. Diseño, formas y modelos de las áreas destinadas a la conservación: Su incidencia sobre fragilidad individual y del sistema nacional de áreas protegidas de Argentina. *Revista del Departamento de Geografía* (UNC) 9(18), 109-136.
- Lu, Z., Zhuang, Y., Zhang, Y., Zhang, S., 2024. Evaluation of landscape sustainability of protected areas and identification of its correlation factors: A case study of Beijing, China. *Landscape Ecology* 39, 98. <https://doi.org/10.1007/s10980-024-01872-6>
- Macchioli Grande, M., Kaffas, K., Verdone, M., Borga, M., Cocozza, C., Dani, A., Errico, A., Fabiani, G., Gourdon, L., Klaus, J., Manca di Villahermosa, F.S., Massari, C., Murgia, I., Pfister, L., Preti, F., Segura, C., Tailliez, C., Trucchi, P., Zuecco, G., Penna, D., 2024. Seasonal meteorological forcing controls runoff generation at multiple scales in a Mediterranean forested mountain catchment. *Journal of Hydrology* 639, 131642. <https://doi.org/10.1016/j.jhydrol.2024.131642>
- Madariaga Olivares, I. P., 2017. *Evaluación del potencial de neblina mediante el sistema de atrapanieblas en las lomas de Ancón durante el evento del niño, en el distrito de Ancón, provincia de Lima periodo 2015-2016*. Repositorio Universidad Nacional de Moquegua.
- Mander, L., Dekker, S. C., Li, M., Mio, W., Punyasena, S. W., Lenton, T. M., 2017. A morphometric analysis of vegetation patterns in dryland ecosystems. *Royal Society Open Science* 4(2), 160443. <https://doi.org/10.1098/rsos.160443>
- MacArthur, A., Wilson, E. O., 1963. An equilibrium theory of insular zoogeography. *Evolution* 17(4), 373-387. <https://doi.org/10.2307/2407089>
- Ministerio del Ambiente, 2015. *Mapa Nacional de Cobertura Vegetal. (Memoria descriptiva)*. <https://www.gob.pe/institucion/minam/informes-publicaciones/2674-mapa-nacional-de-cobertura-vegetal-memoria-descriptiva>
- Ministerio del Ambiente, 2019. Mapa Nacional de Ecosistemas del Perú. <https://sinia.minam.gob.pe/mapas/mapa-nacional-ecosistemas-peru>
- Miyashiro, M., Ortiz, M., 2016. *Estimación mediante la teledetección de la variación de la cobertura vegetal en las lomas del distrito de Villa María del Triunfo por la expansión urbana y minera (1986-2014)*. Repositorio Universidad Mayor de San Marcos. <https://hdl.handle.net/20.500.12672/5281>
- Navarro Guzmán, M. A., Jove Chipana, C. A., Ignacio Apaza, J. M., 2020. Modelamiento de nichos ecológicos de flora amenazada para escenarios de cambio climático en el departamento de Tacna - Perú. *Colombia forestal*, 23 (1) <https://doi.org/10.14483/2256201X.14866>
- Navarro Guzmán, M. A., Pezo Sardon, M. A., Riveros Arteaga, G. C., Frisancho Soto, S. N., 2021. El planeamiento urbanístico contra el territorio: Fragmentación Antropogénica de los ecosistemas de Puna en el extremo sur del Perú. *Estudios Geográficos* 82 (390), e058. <https://doi.org/10.3989/estgeogr.202070.070>
- QGIS Development Team, 2023. *QGIS geographic information system*. <https://qgis.org>

- R Development Core Team, 2024. *A language and environment for statistical computing*. R Foundation for statistical computing, Vienna, Austria. <https://www.r-project.org/>
- Rempel, R., Kaukinen, D., Carr, A., 2012. *Patch Analyst and Patch Grid*. Ontario Ministry of Natural Resources. Centre for Northern Forest Ecosystem Research, Thunder Bay, Ontario. <https://learn.opengeoedu.de/en/monitoring/landschaftstrukturmasse/software/patch-analyst-arcmap-plugin>
- Santos, T., Tellería, J., 2006. Pérdida y fragmentación del hábitat: efecto sobre la conservación de las especies. *Ecosistemas* 15 (2). <https://www.revistaecosistemas.net/index.php/ecosistemas/article/view/180>
- Saura, S., Pascual-Hortal, L., 2007. A new habitat availability index to integrate connectivity in landscape conservation planning: Comparison with existing indices and application to a case study. *Landscape and Urban Planning* 83 (2-3), 91-103. <https://doi.org/10.1016/j.landurbplan.2007.03.005>
- Speetjens, N. J., Hugelius, G., Gumbrecht, T., 2023. The pan-Arctic catchment database (ARCADE). *Earth System Science Data* 15, 541–554. <https://doi.org/10.5194/essd-15-541-2023>
- Tinajero, R., Rodríguez, R., 2012. Efectos de la fragmentación del matorral desértico sobre poblaciones del aguililla cola-roja y el cernícalo americano en Baja California Sur, México. *Acta Zoológica Mexicana* 28 (2). <https://doi.org/10.21829/azm.2012.282844>
- Toivonen, J. M., Gonzales-Inca, C. A., Bader, M. Y., Ruokolainen, K., Kessler, M., 2018. Elevational shifts in the topographic position of Polylepis forest stands in the Andes of southern Peru. *Forests* 9(1), 7. <https://doi.org/10.3390/f9010007>
- IUCN, 2012. *Categorías y criterios de la lista roja de la UICN. Versión 3.1*. IUCN. Gland, Suiza y Cambridge, Reino Unido. <https://portals.iucn.org/library/sites/library/files/documents/RL-2001-001-2nd-Es.pdf>
- Valladares-Faúndez P, Franco-León P, Jove Chipana C, Navarro Guzmán M, Ignacio-Apaza J, Apaza JI, Cáceres Musaja C, Langstroth R, Aguilar-Kirigin A, Gutierrez, R.C., Abdala, C.S., 2021. A new lizard of the Liolaemus montanus group that inhabits the hyperarid desert of southern Peru. *Amphibian & Reptile Conservation* 15(2) [Taxonomy Section]: 10–22 (e278).
- Verga, E., Peluc, S., Landi, M., Galetto, L., 2018. Forest fragmentation effect on potential food sources for birds in Córdoba. *Ecología Austral*. <https://doi.org/10.25260/EA.18.28.2.0.429>
- Vila Subirós, J., Varga Linde, D., Llausàs Pascual, A., Ribas Palom, A., 2006. Conceptos y métodos fundamentales en ecología del paisaje (landscape ecology). Una interpretación desde la geografía. *Documents d'Anàlisi Geogràfica* 48, 151-166
- Wang, H., Wang, J., Ni, J., Cui, Y., Yan, S., 2023. Spatial scale effects of integrated landscape indicators on river water quality in Chaohu Lake basin, China. *Environmental Science and Pollution Research* 30(45), 100892–100906. <https://doi.org/10.1007/s11356-023-29482-w>
- Warren, D. L., Glor, R. E., Turelli, M., 2008. Environmental niche equivalency versus conservatism: Quantitative approaches to niche evolution. *Evolution. International Journal of Organic Evolution* 62 (11), 2868-2883. <https://doi.org/10.1111/j.1558-5646.2008.00482.x>
- With, K. A., 2019. Landscape effects on ecosystem structure and function. In *Essentials of Landscape Ecology* (Kimberley A. With, Ed). Oxford University Press. <https://doi.org/10.1093/oso/97801988388.003.0011>
- Wolff, J., Schauber, E., Edge, D., 1997. Effects of Habitat Loss and Fragmentation on the Behavior and Demography of Gray-Tailed Voles. *Conservation Biology* 11 (4), 945-956. <https://doi.org/10.1046/j.1523-1739.1997.96136.x>
- Yu, M., Liu, Y., 2025. Landscape ecological integrity assessment to improve protected-area management of forest ecosystem. *Ecologies* 6(2), 38. <https://doi.org/10.3390/ecologies6020038>
- Zhao, M., Zhou, Q., Luo, Y., Li, Y., Wang, Y., Yuan, E., 2024. Threshold effects between ecosystem services and natural and social drivers in karst landscapes. *Land* 13(5), 691. <https://doi.org/10.3390/land13050691>





# ANALYSIS OF CLIMATE CHANGE IMPACTS ON ANDEAN FORESTS USING POTENTIAL DISTRIBUTION MODELS (2010-2069)

VIRGINIA ALBERDI NIEVES

Facultad de Filosofía y Letras, Universidad de Extremadura, Spain.

**ABSTRACT.** In the 21st century, climate change has become the greatest global threat that affects different countries in different ways, affecting different areas, from the increased risk of desertification due to rising temperatures to areas at risk of flooding caused by increased rainfall. Combating climate change has therefore become a priority for many forests in the Andes. In this research, a study was carried out on the possible changes in the forests, as this is one of the regions with the greatest variety of ecosystems and forest formations in the world, analysing the current and future distribution of eight forest formations throughout the study area, by means of potential distribution models, using Maxent software, under three emission scenarios RCP 4.5, RCP 6.0 and RCP 8.5; with projections for the current period 2010-2039 and the future 2040-2069. The results show significant changes in the potential area of distribution of several forests across the different scenarios. Most of the analysed forests will suffer modifications in their current distribution, as is the case of the Lowland Forests and Highland Shrublands of the Humid Puna, which will decrease by more than 60% of their current extent in Bolivia. In the future distribution all the forests analysed will reduce their potential range, such as the Submontane and Dry Montane Forest of the Northern Yungas by 81.6% and the Low Andean Forest of the Western Xerophytic Puna (Peru) by 89.5% in the most restrictive scenario RCP 8.5, which may cause shifts to higher latitudes, with the loss of habitats.

## *Análisis de los impactos del cambio climático en los bosques andinos mediante modelos de distribución potencial (2010-2069)*

**RESUMEN.** El cambio climático se ha convertido en el siglo XXI en la mayor amenaza global que afecta a distintos países de una forma diferente, afectando a distintas zonas desde el aumento del riesgo de desertificación debido al aumento de las temperaturas hasta las zonas con riesgo de inundaciones provocadas por el aumento de las precipitaciones. Por ello la lucha contra el cambio climático se ha convertido en una prioridad para numerosos bosques de la Cordillera de los Andes. En esta investigación se realizó un estudio sobre los posibles cambios en los bosques, ya que se trata de una de las regiones con mayor variedad de ecosistemas y formaciones forestales del mundo, analizando su distribución actual y futura de ocho formaciones forestales a lo largo de la zona de estudio, mediante modelos de distribución potencial, utilizando el software Maxent, bajo tres escenarios de emisión RCP 4.5, RCP 6.0 y RCP 8.5; con proyecciones para el periodo actual 2010-2039 y el futuro 2040-2069. Los resultados nos indican que la mayor parte de los bosques analizados sufrirá modificaciones en su distribución actual, como es el caso de los Bosques Bajos y Arbustales Altimontanos de la Puna Húmeda que disminuye más del 60% su extensión actual en Bolivia. En la distribución futura todos los bosques analizados reducirán su área de distribución potencial, como el Bosque Submontano y Montano seco de Yungas del Norte el 81,6% y el Bosque Bajo Altoandino de Puna Xerofítica Occidental (Perú) el 89,5% en el escenario más restrictivo RCP 8.5, lo que puede provocar desplazamientos hacia latitudes más elevadas, con la pérdida de hábitats.

**Keywords:** Andes Mountain, climate change, forest, potential distribution models (PDM).

**Palabras clave:** Cordillera de los Andes, cambio climático, bosques, modelos de distribución potencial (MDP).

Received: 03 September 2024

Accepted: 25 April 2025

**Corresponding author:** Virginia Alberdi Nieves, Facultad de Filosofía y Letras, Universidad de Extremadura, Spain. Email address: virginiaan@unex.es

## 1. Introduction

The Andes Mountain region is the most biodiverse area in the world, where we can find the greatest variety of landscapes, ecosystems and climates, with more than 29,600 species of plants, 1990 species of birds, 700 species of mammals, 1140 species of amphibians, 70% of which are endemic, spread over 33 million hectares of forest (Navarro, 2014). These ecosystems have undergone changes and strong reductions caused by the pressure of human activity up to the present day (Báez *et al.*, 2016).

With regard to climate, various climate scenarios can be observed (Cuesta *et al.*, 2011). On the one hand, an increase of 2°C is possible, while in the Bolivian Altiplano there will be a decrease in precipitation of around 10%, and in areas such as Ecuador and Peru a decrease of 59%.

The impact of climate change on natural resources is very diverse, resulting in the disappearance of ecosystems, loss of resources and depletion of natural resources (Buytaert and Bievre, 2012). Biodiversity is characteristic of a variety of life forms (Báez *et al.*, 2016). Climate affects many aspects of ecosystems from nutrient circulation to productivity, and it is in forests that climate regulates their growth and determines their distribution limits in combination with climatic variables (Araújo and Peterson, 2012). It is estimated that the inhabitants of this area use around 25% of the species (De la Torre *et al.*, 2008). These mountain ecosystems are very vulnerable to climate change as they are topographically isolated where environmental conditions change considerably, the capacity to react to these perturbations has been studied by different methodologies. There are some studies that show an enormous loss of endemic species due to climate change in the northern Andes, a critical area of biodiversity loss (Malcolm, 2006). It is therefore important to know what will happen under the new climate scenarios. Another obvious example is the decline of trees in the Andes (Duque *et al.*, 2015), with enormous consequences for forest species (Gonzalez *et al.*, 2010), such as changes in distribution, changes in reproduction times, increased extinction rates, and changes in plant growth and development (Djoghlaf, 2007).

This situation is unprecedented, and to understand these processes it is necessary to take into account the orography that conditions and limits the use of large-scale climate models (Herzog *et al.*, 2012). It should also be taken into account that there is still some way to go in terms of species interactions and the evolution of ecosystems, and among the factors that determine their vulnerability could be related to (Pitman *et al.*, 2011) with the increase in temperatures and ecological and biological requirements. In this sense, there is an increasing need to confirm how such alterations may affect the spatial distribution of forests (Herzog *et al.*, 2012).

Among the studies related to the impacts that these alterations would have on the ecosystems of the Andes (Báez *et al.*, 2016; Terán-Valdez, 2019), in addition to those in which alterations in their habitats are verified (Ávila-Núñez and Otero 2019) and the possibility of new presences of plant species (Barrera *et al.*, 2020).

There is still a long way to go regarding the future of forest species in the Andes, for which there is not much work compared to other areas such as Central America and the Amazon (Pitman *et al.*, 2011). There are some studies with resolutions as low as 50km that have not been able to capture the enormous heterogeneity of the area (Gonzalez and Neilson 2010; Beaumont *et al.*, 2011), other works that focus on specific areas such as the Peruvian Andes (Cuentas, 2022) and the Ecuadorian Andes (Vistín *et al.*, 2022), but very few works as extensive as that of Villarreal-Veloz 2023.

At present, potential distribution models (PDM) are widely used tools to generate useful information to analyse and study forest species. Studies showing predictive modelling techniques use

the association of environmental values, in this case climatic variables and known presence in the area of interest, i.e. a statistical relationship between the occurrence and non-occurrence of species (Araujo and Peterson, 2012; Saupe *et al.*, 2012). It is proposed to target conservation action in areas with higher percentages of occurrence, as well as areas where species are expected to remain in the future. There are numerous methods to determine the distribution of species, including different techniques to generate each model and different biological data necessary for each model (Gutiérrez and Trejo 2023), of the most widely used are Generalised Linear Models (GLM) such as Maxent, which is a maximum entropy algorithm and works with both continuous and categorical variables, with a clear advantage over the rest (Felicísimo and Muñoz, 2011).

Therefore, the general objective of this research is to find out how climate change will influence the future distribution of forests in the Andes. To this end, an analysis of the current potential distribution and possible future projections was carried out using predictive models based on GLM such as MaxEnt (Maximum Entropy Modelling), for different emission scenarios RCP 4.5, RCP 6.0 and RCP 8.5, using the CCCma. The conclusions obtained showed the result of probable impacts on the future disposition of a series of forests in the Andes Mountains.

## **2. Methodology**

### **2.1 Study area**

The Andes occupy the coast of the Pacific Ocean from north to south with a length of 8,500 km (Fig. 1), and an average altitude of 4,000 m, covering an area of 2,870,596 km<sup>2</sup> (FAO, 2014) it is a mountain system located between 13°N and 48°S and crossing different countries, Colombia, Ecuador, Perú and Bolivia.

The Andes mountain range occupies a large territory and is characterised by its great environmental, geological and physiological variety. These characteristics are determined by several factors, among which are the relief and climatic variability, this great and diverse relief with river valleys, Andean plateaus, foothills, highlands and great altitudinal variation in which the Huascaran Peak (Peru) is located at 6,768 m. In addition to a great diversity of plant communities such as savannahs, scrublands, rainforests and coastal swamps (Alaggia *et al.*, 2022), the most geomorphologically diverse mountain range on the planet.

Temperature variability in the Andes depends mainly on two aspects: the altitudinal gradient and the time of year, so that the average temperature rate with respect to altitude is between 0.6°C and 0.7°C per 100 metres.

Precipitation in the Andes does not have a linear pattern but is determined by orography and wind influence, which characterises it by its high temporal and spatial variability (Mujica and Holle, 2002), with precipitation values ranging from areas of less than 200 mm per year to 3,000 mm.

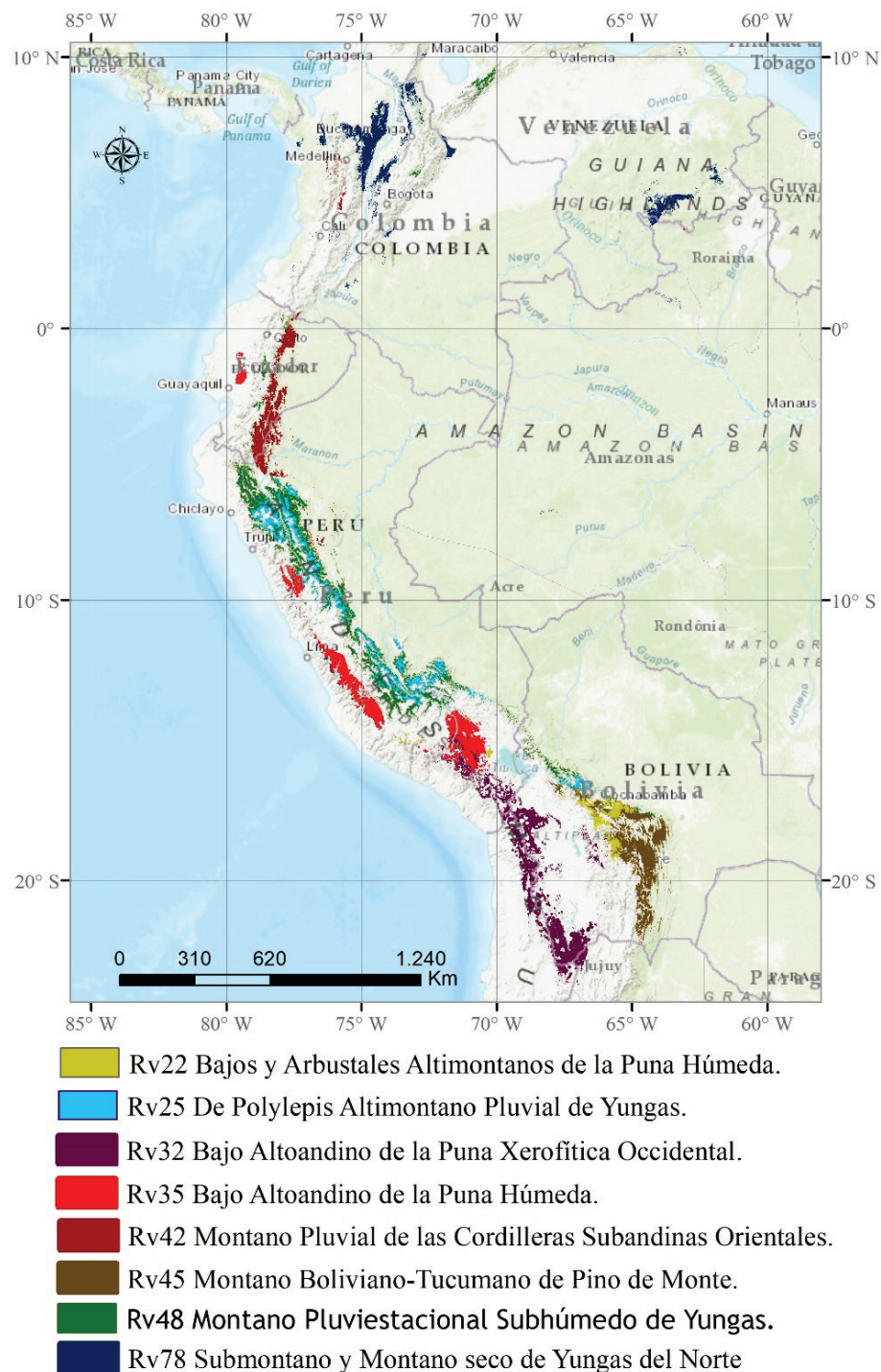


Figure 1. The forest of the Andes Mountain on this study.

## 2.2. Data

The selection of forests was carried out following distribution and seat representativeness judgements in different information sources (Josse *et al.*, 2009). The study modelled eight very characteristic forest formations of the Andes Cordillera (Fig. 1), selected because these eight formations are highly representative in the study area (Table 1).

Table 1. Type of forest formation selected with the distribution data and forest occurrence data.

Cod	Type of forest	Model	km <sup>2</sup>
CES409.074	Bajos y Arbustales Altimontanos de la Puna Húmeda	Rv22	4.368
CES409.045	De Polylepis Altimontano Pluvial de Yungas	Rv25	8.425
CES505.007	Bajo Altoandino de la Puna Xerofítica Occidental	Rv32	570
CES409.068	Bajo Altoandino de la Puna Húmeda	Rv35	173
CES409.913	Montano Pluvial de las Cordilleras Subandinas Orientales	Rv42	5.029
CES409.197	Montano Boliviano-Tucumano de Pino de Monte	Rv45	3.641
CES409.921	Montano Pluviestacional Subhúmedo de Yungas	Rv48	13.480
CES411.434	Submontano y Montano seco de Yungas del norte	Rv78	10.196

Source: information source Condesan Project (Cuesta, 2009).

The Bioclimatic Variables (Vb) used for the study were obtained from World Climate Monitor. This server allows the download of data from 19 Vb, as well as the insertion of data from climate stations from 1949 to 2069 excluding Antarctica (Hijmans *et al.*, 2005) with information on these variables in the past and future. For this purpose, the ANUCLIM software was used with the CCma.

The 19 bioclimatic variables (Vb) of Worldclim are organised into 11 temperature vb, from Vb1 to Vb11, annual mean temperature, maximum, minimum, monthly, four-monthly, four-monthly and seasonal, and into 8 precipitation vb from Vb12 to Vb 19 (Fick and Hijmans, 2017) (Table 2).

Table 2. Description of the nineteen Bioclimatic Variables.

Bioclimatic Variable (Bv)	Description	Unit
Bv 1	Annual Mean Temperature	°C
Bv 2	Mean Diurnal Range (Mean of monthly (max temp - min temp))	°C
Bv 3	Isothermality (Vb2/Vb7*100)	Variation
Bv 4	Temperature Seasonality (standard deviation *100)	%
Bv 5	Max Temperature of Warmest Month	°C
Bv 6	Min Temperature of Coldest Month	°C
Bv 7	Temperature Annual Range (Vb5-Vb6)	°C
Bv 8	Mean Temperature of Wettest Quarter	°C
Bv 9	Mean Temperature of Driest Quarter	°C
Bv 10	Mean Temperature of Warmest Quarter	°C
Bv 11	Mean Temperature of Coldest Quarter	°C
Bv 12	Annual Precipitation	mm
Bv 13	Precipitation of Wettest Month	mm
Bv 14	Precipitation of Driest Month	mm
Bv 15	Precipitation of Seasonality (Coefficient of Variation)	%
Bv 16	Precipitation of Wettest Quarter	mm
Bv 17	Precipitation of Driest Quarter	mm
Bv 18	Precipitation of Warmest Quarter	mm
Bv 19	Precipitation of Coldest Quarter	mm

Data: °C: degrees Celsius; Cv: coefficient of variation; mm: millimetres. Obtained from worldclim and Hijmans (Hijmans *et al.* 2005).

## 2.3. Methodology

In the development of the PDMs, data on the presence and absence of the species studied were used to create Generalised Linear Models, in which the MaxEnt v.3.3.3 software was used with 100% of the presence data. It provides a continuous range of probability across the geographical area with values

ranging from 0 to 1, and the closer they are to 1 the greater the probability of finding presence of the forest formations used, and the further away from 1 the lower the probability (Phillips and Dudík, 2008).

The area of potential distribution is the area where there are suitable environmental conditions for that species or plant formation to thrive. Its extent may be due to both abiotic (topography, geology, climate) and biotic factors (interspecific competition, barriers, dispersal capacity...) (Recalde-Coronel *et al.*, 2020). MDP are indicators of habitat suitability for the development of populations of a particular species or community estimated from observations of field occurrences and their relationships with a series of environmental variables that act as predictors (Elith *et al.*, 2006).

This software is based on a set of methodological (Fig. 2) principles in which the distribution of forests is subject to a binary logistic regression of probability ( $\rho$ ) of occurrence and non-occurrence ( $\gamma'$ ) on a set of potential distribution sites (Gutiérrez and Trejo, 2023). The likelihood function for  $\gamma$  environmental variables is expressed as follows:

$$\text{Absence} \quad \gamma' = \ln(\gamma/(1 - \gamma))$$

$$\text{Presence} \quad \rho = e^y / (1 + e^y)$$

The MDP ( $\rho$ ) is constructed through probability values thus obtained, by means of relative suitability values for the presence of forest formations, where ( $\gamma$ ) represents the vector of environmental variables, ( $e^y$ ) refers to Napier's constant, and is used to ensure that ( $\rho$ ) results in the disposition of the species (Saraiva, 2023).

The derived parameters of sensitivity (true/disposition) and specificity (true absences/inexistences) of the models are Area Under Curve and Receiver Operating Characteristic indicating the validity of the model. The Maximum Entropy distribution estimates the probability of presence-disposition of forests depending on environmental conditions (Phillips and Anderson, 2006). And for validation it indicates the Receiver Operating Characteristic behaviour which has an AUC value greater than 0.7, indicating that the models are acceptable and in this case the AUC values define the degree of fit of the data.

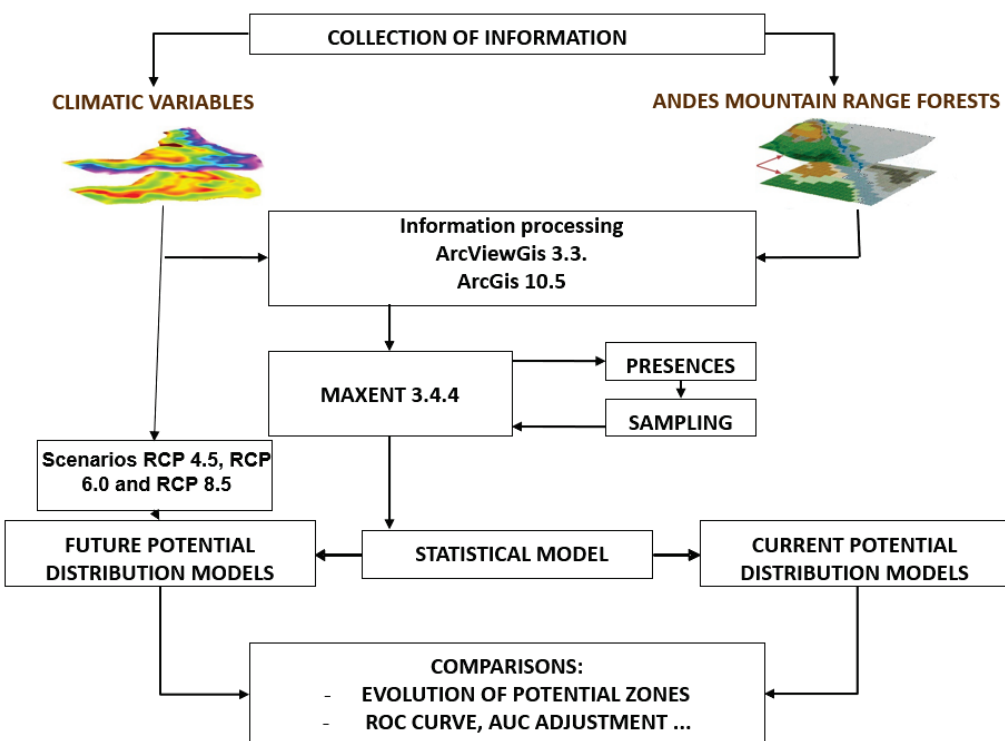


Figure 2. The overall methodological framework of this study.

For each model, 20% of the entries were used for cross-validation and estimation of the error of these parameters derived from the sensitivity and specificity of the models (Jain and Jana, 2023), so only those whose final test values were greater than 0.7 were included. An AUC of less than 0.6 indicates that the MDP is inaccurate, but a value greater than 0.7 indicates a highly accurate MDP (Alaggia *et al.*, 2022).

### 3. Results

The first results that were analysed were those used to evaluate the degree of adjustment of the models created. This is done through the ROC (Receiver Operating Characteristic) curve, for which Area Under the Curve AUC is used, a value that indicates the discrimination capacity of the model and defines its fit. The construction of the ROC curve is a process applied to each fitness threshold of the model; Maxent uses the presence records, and the area under the ROC curve indicates that for a presence point a random one is selected. The probability that the fitness value predicted by the model for the point of presence is greater than that predicted for the random point is determined by AUC. Therefore, the AUC statistic can take values between 0 and 1. A value of AUC between 0.5 and 0.7 corresponds to a low-precision model, while a value greater than 0.7 corresponds to a high-precision or high-discrimination model. In this case, all models were found to have a degree of fit to the data greater than 0.97, indicating that they are highly accurate (Table 3).

In the results obtained we can analyse the climatic variables that have had a greater influence on each forest typology in the model.

*Table 3. Percentage contribution of the variables used for each forest type after analysis and validation of the models. Source: Calculations base on bioclimatic variables used on the models. CPD: Current potencial distribution; FPD: Future potencial distribution.*

<b>Forest</b>	<b>Bioclimatic Variable (Bv)</b>	<b>(%) CPD</b>	<b>Bioclimatic Variable (Bv)</b>	<b>(%) FPD</b>	<b>AUC (TD)</b>
<b>Rv22</b>	Bv 2	25.8	Bv 2	26.7	
	Bv 15	13.4	Bv 15	13.4	0.991
	Bv 11	11.3	Bv 11	12	
<b>Rv25</b>	Bv 10	22.4	Bv 10	23	
	Bv 6	15	Bv 6	11	0.989
	Bv 2	12.2	Bv 2	12.2	
<b>Rv32</b>	Bv 11	37.8	Bv 11	38	
	Bv 19	26.4	Bv 19	27.3	0.988
	Bv 6	14.6	Bv 6	14	
<b>Rv35</b>	Bv 1	36.6	Bv 1	28	
	Bv 19	14.6	Bv 19	17.3	0.987
	Bv 18	11.2	Bv 18	13.6	
<b>Rv42</b>	Bv 8	35.1	Bv 8	37.3	
	Bv 15	34.7	Bv 15	34.7	0.990
	Bv 14	10.6	Bv 14	11.6	
<b>Rv45</b>	Bv 9	28.3	Bv 9	26	
	Bv 4	22.1	Bv 4	22	0.988
	Bv 1	11.9	Bv 1	14	
<b>Rv48</b>	Bv 8	43.7	Bv 8	37.7	
	Bv 14	12.1	Bv 14	12.1	0.972
	Bv 11	11.1	Bv 11	13	
<b>Rv78</b>	Bv 15	24.1	Bv 15	28.2	
	Bv 3	22.6	Bv 3	22	0.994
	Bv 13	15	Bv 13	14	

In the analysis of the results obtained for each type of forest formation, the three most representative Vb that influence each forest were selected. For all the forests studied, the same bioclimatic variables have influenced their current potential distribution (CPD) and future potential distribution (FPD), but with different influences. For the forest Rv22 Bajos y Arbustales Altimontanos de la Puna Húmeda (Table 3), the same Vb 2, Vb 15 and Vb 11, related to mean temperatures 25.8% and 13.4% and seasonal precipitation 11.3%, increasing significantly in the FPD, it is a forest characteristic of a supratropical pluvial-pluvial bioclimatic floor with sub-humid and humid ombrotypes.

The mean temperature of the coldest quarter Bv11 influences about 40% in the CPD of the forest (Rv32) of the Bajo Altoandino de Puna Xerofítica Occidental, the precipitation of the coldest quarter Bv11 influences 26.4 and the minimum temperature Bv6 14.6%, of the three variables only the minimum temperature of the coldest month (Bv6) decreases in its FPD (Fig. 3). It is located at an altitude of 3600 m to 4000 m on the Altiplano, the characteristic and dominant species is *Polylepis*. It develops on substrates of predominantly volcanic lithology (rhyodacites and andesites), and still maintains remarkably extensive forest patches, especially in western Bolivia. The forest Rv22 Bajos y Arbustales Altimontanos de la Puna Húmeda (Fig. 4), it is a forest characteristic of a supratropical pluvial-pluvial bioclimatic floor with sub-humid and humid ombrotypes.

The mapping of potential suitable areas may shed some more light on the expected variations in the area of distribution in some of the cases mentioned. Table 3 shows the CPD and FPD for the different forest formations. In this case the current distribution is only a fraction of the CPD, so that high percentages of suitability indicate good conservation, as in the case of the *Rv35 Bajo Altoandino de la Puna Húmeda* with 20.4% of its surface and the *Rv48 Montano Pluvial Subhúmedo de Yungas* with 36.8% of its Surface.

There is an increase in WTP in the different forests as shown in Table 3, values that indicate the suitability conditions of each forest formation.

In the three scenarios there are notable differences in the potential area of distribution, there is a predominance of generalised loss in all forest types in the CPD and in the FPD, the *Rv32 Bajo Altoandino de Puna Xerofítica Occidental*, suffers a FPD of more than 80% in the RCP 8.5 scenario (Fig. 5), and the *Rv78 Submontano y Montano Seco de Yungas del Norte* ha 81.6% (Fig. 6), and the *Rv48 Montano Pluvial Subhúmedo de Yungas* with 36.8% of its Surface (Fig. 7).

The pattern of potential site decline was most pronounced in climate scenario RCP 4.5 (2040-2069) for forest *Rv35 Bajo Altoandino de la Puna Húmeda*, reducing its potential area by 78.5%. The layout of each forest and its potential site is shown in Table 4.

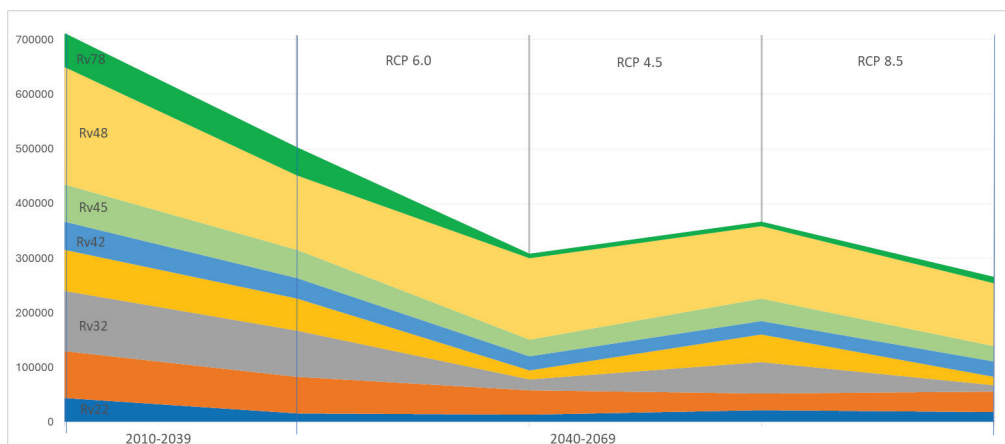


Figure 3. Potential current and future distribution of forests under three emission scenarios RCP 6.0, RCP 4.5 and RCP 8.5.

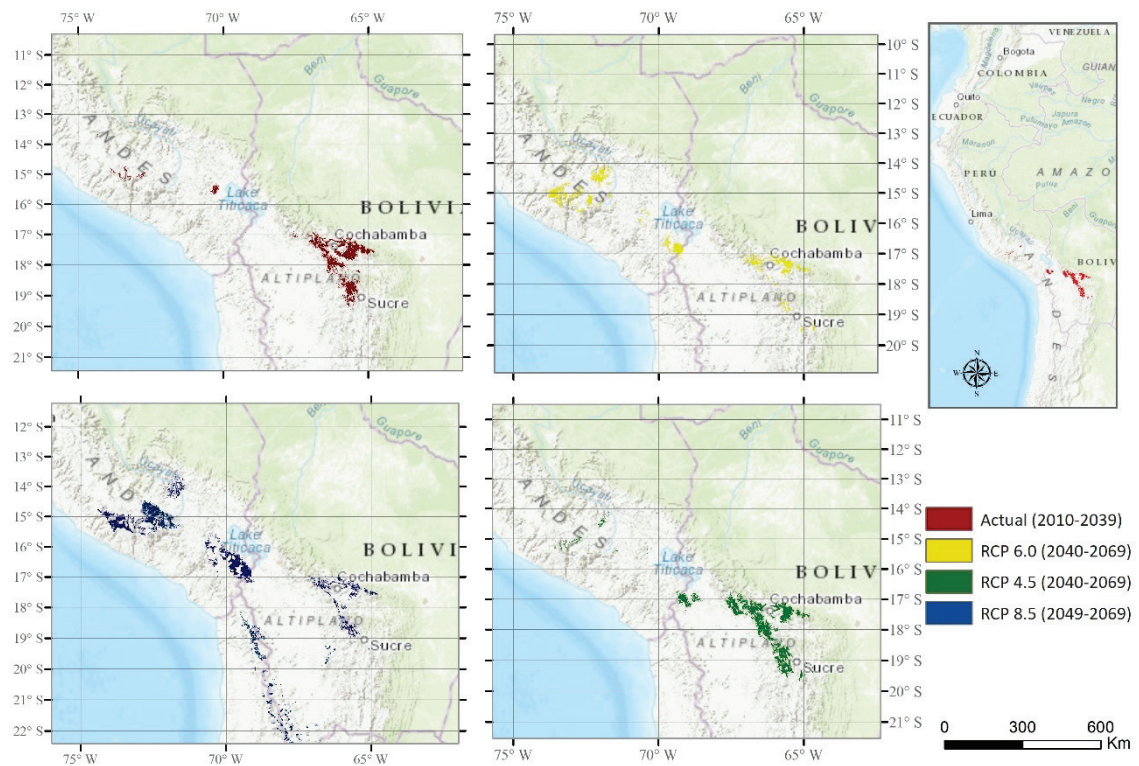


Figure 4. The potential site of forest Rv22 Bajos y Arbustales Altimontanos de la Puna Húmeda in different scenarios. Source: ArcGis 10.3 implementation. WGS84 datum system. Universal Transverse Mercator Datum.

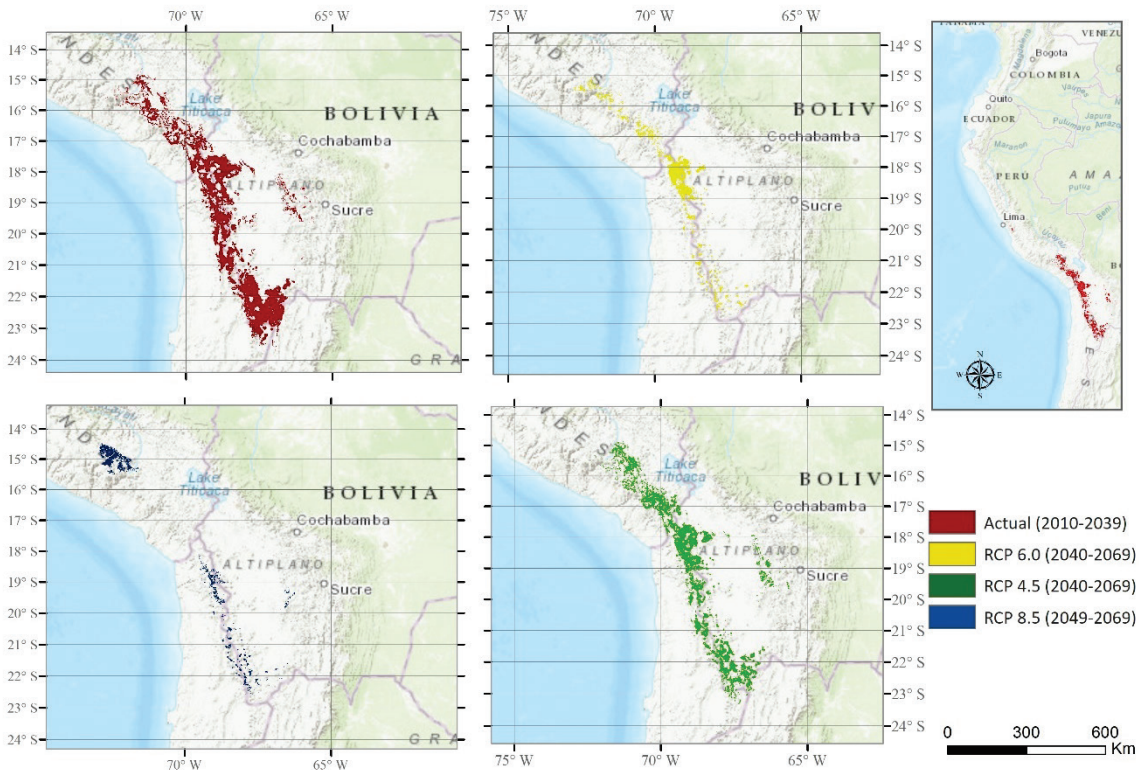
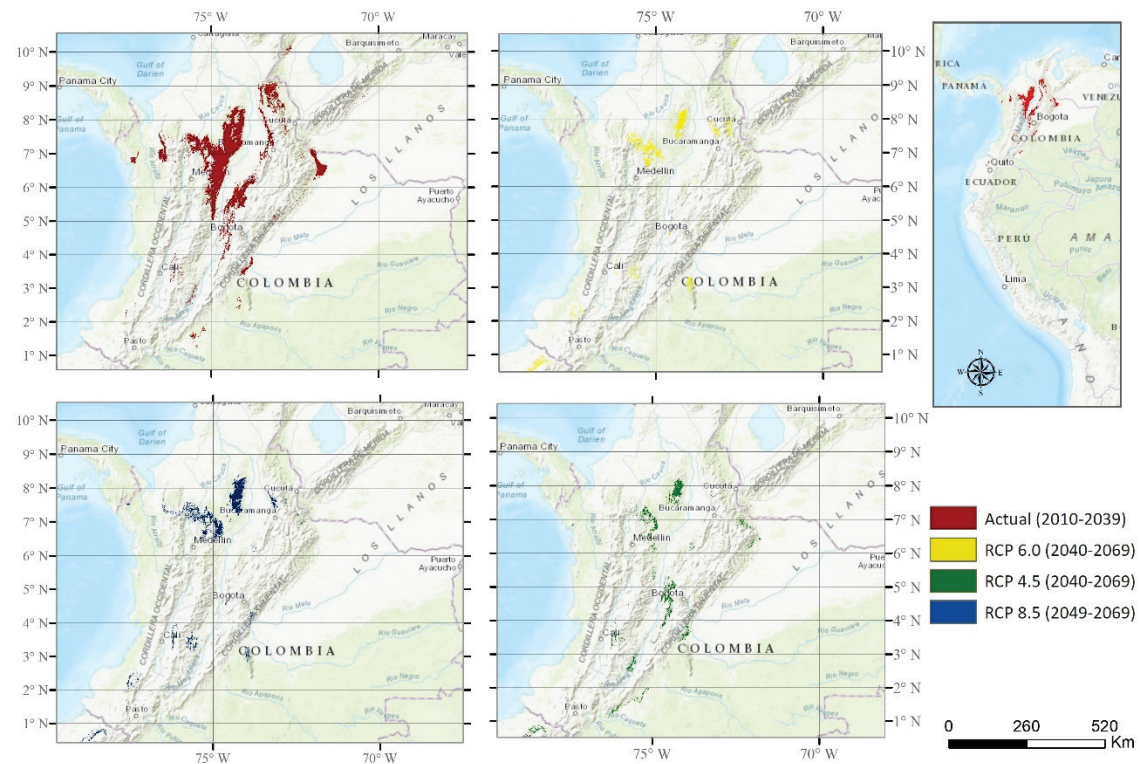
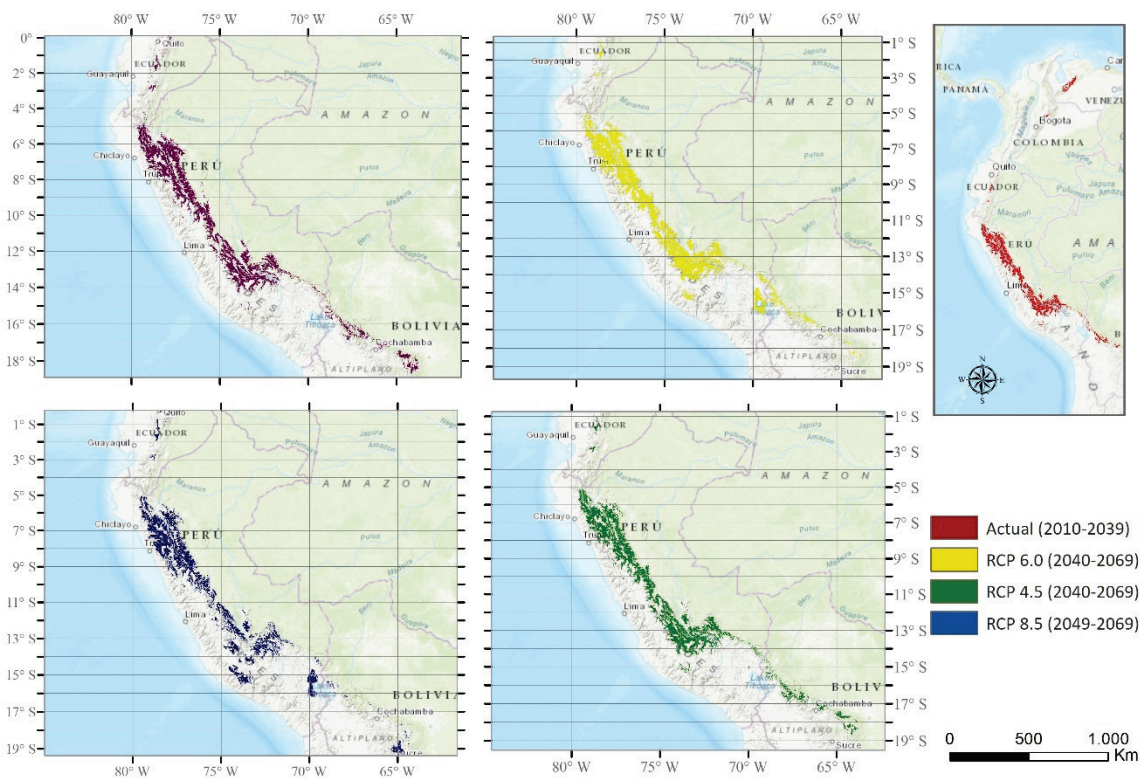


Figure 5. Potential site forest Rv32 Bajo Altoandino de Puna Xerofitica Occidental. Source: ArcGis 10.3 implementation. WGS84 datum system. Universal Transverse Mercator Datum.



*Figure 6. Potential site forest Rv78 Submontano y Montano seco de Yungas del Norte in different scenarios.*  
Source: ArcGis 10.3 implementation. WGS84 datum system. Universal Transverse Mercator Datum.



*Figure 7. Potential site forest Rv48 Montano Pluviesacional Subhúmedo de Yungas in different scenarios.*  
Source: ArcGis 10.3 implementation. WGS84 datum system. Universal Transverse Mercator Datum.

*Table 4. Evolution of the current and future potential distribution of forests in the Andes Mountain under three emissions scenarios RCP.6.0, RCP4.5 and RCP 8.5.*

	<b>Forest</b>	<b>2010-2039</b>		<b>2040-2069</b>			
		<b>Current</b>	<b>RCP 6.0</b>	<b>Future %</b>	<b>RCP 4.5</b>	<b>Future %</b>	<b>RCP 8.5</b>
<b>Rv22</b>	Bajos y Arbustales						
	Altimontanos de la Puna Húmeda	15.693	64.6	14.179	68.3	21.710	51.5
<b>Rv25</b>	De Polylepis						
	Altimontano Pluvial de Yungas	67.029	21.8	44.723	47.8	30.728	64.2
<b>Rv32</b>	Bajo Altoandino de Puna Xerofítica Occidental	84.948	23.3	19.541	82.3	57.147	48.4
<b>Rv35</b>	Bajo Altoandino de la Puna Húmeda	58.947	20.4	16.061	78.3	50.518	31.7
<b>Rv42</b>	Montano Pluvial de las Cordilleras Subandinas Orientales	36.650	29.2	26.545	48.7	25.136	51.4
<b>Rv45</b>	Montano Boliviano-Tucumano de Pino de Monte	52.517	23.2	30.161	55.8	40.460	40.8
<b>Rv48</b>	Montano Pluviestacional Subhúmedo de Yungas	135.884	36.8	148.773	30.8	133.213	38.0
<b>Rv78</b>	Submontano y Montano Seco de Yungas del Norte	51.519	15.9	8.445	86.2	8.281	86.5

Source: Percentage results of potential distribution models for each forest through the Maxent Software.

The forest Rv42 Montano Pluvial de las Cordilleras Subandinas Orientales decreases its potential site by 48.7% and 51.4% in scenarios RCP 6.0 and RCP 4.5. In contrast, Rv25 De Polylepis Altimontano Pluvial de Yungas decreases its potential site by 51% for the period 2040-2069, characterised by conserved forests with tree ferns and woody vines in northern Peru.

Forests Rv45 Montano Boliviano-Tucumano de Pino de Monte and Rv48 Submontano y Montano Seco de Yungas del Norte, decrease 57.3% and 46.6% of their future distribution in the FPD in the RCP 8.5 scenario, where mean temperatures influence (Bv9) 28.3% and (Bv8) 43.7%; and precipitation Bv 14 12.1%.

#### 4. Discussion

The analysis of the forest formations used in the study shows the complexity and heterogeneity of the natural forest (Mateo *et al.*, 2011). The use of models is based on the ecological interpretation they receive from different authors. Some consider that we are working with ‘suitability models’ that represent the potential distribution of the species, understanding as such the space where the species under study could be present according to its environmental characteristics (Felicísimo and Muñoz, 2011), others define it as ‘potential habitat models’, where the concept of habitat can be applied to the description of the association between organisms and environmental factors, understood as descriptive habitat modelling exercises for a given species (Kessler, 2006), but most of these models, regardless of their ecological interpretation, reflect the distribution of species in a defined temporal space.

From the analysis of the effects of climate change on forest formations we have obtained information on the potential distribution models for each forest formation. In general, very different results are observed for each scenario, taking into account that the RCP 4.5 and RCP 8.5 scenarios on average may be more unfavourable than the RCP 6.0 scenario (Alberdi, 2021).

In order to analyse the effects of climate change on forest formations, information on bioclimatic variables can be considered. The temperature variations in the future could mark the seasonality and precipitation in these forest habitats, it can be considered that the bioclimatic variables related to temperature have influenced 80% of the expected changes in the medium term in the near future are the reduction of the potential site of the forest formations studied, the Bv 8 which refers to the average temperature of the wettest month influences the forest Rv 48 *Montano Pluvial Subhúmedo de Yungas* 43.7%, decreasing in the future to 37%, on the other hand the variable Vb 15 which is characterized by the seasonality of precipitation has an influence of 28.2% in the Rv78 *Submontano y Montano seco de Yungas del Norte* forest for its future distribution, so it is observed that the probability of presence increases in a higher humidity regime (Hernández-Silva and Juárez-García, 2019; Acosta *et al.*, 2022). This increase in average temperature could shift these forests to higher latitudes, as also indicated by Anderson *et al.* (2003) in their work, where an increase in temperature of 3°C could cause a displacement of 600 m upwards with the consequent loss of habitat area. There are several studies linking displacements of forest formations caused by temperature increases (Duque *et al.*, 2015; Fadrique *et al.*, 2018).

The Rv35 Bajo Altoandino de la Puna Húmeda forest, are structurally low shrubs forests with, semi-open to open, with a canopy of 3-10 m and a variable understory depending on the degree of conservation, where grasses and other herbaceous plants are frequent, as well as some shrubs and ferns (Navarro and Maldonado, 2002). In most of its potential area, these climax forests have been replaced by a complex of seral plant communities, mainly grasslands and scrublands. It develops between 3200 m altitude and 4,100 m.

Temperature variations show that seasonality may increase in forest formations where Bv15, related to rainfall variability, has an important influence of 34%, as in the case of Rv42 Montano Pluvial de las Cordilleras Subandinas Orientales where a 47.4% decrease in its DPF is observed. In the Rv32 Lower High Andean forest of the Western Xerophytic Puna, Bv19 influences precipitation of the coldest quarter, with 26.4% and Bv11 with 37.8% of average temperature where a strong decrease in forest formation of 89.7% in its DPF and in all scenarios because the area meets the climatic suitability but does not take into account other factors related to land uses (Hernández-Silva and Juárez-García, 2019), deforestation or human intervention (Alberdi, 2021).

The problem of potential areas disconnected from the current range is the difficulty for seeds to get from the current area to the new, potentially suitable area (Poblete and Albeiro 2021). The actual management of these areas must take into account this circumstance, which can nullify the real potential of emerging areas and which conditions the expansion processes of forest stands which (García-Romero *et al.*, 2010), in turn, are governed by a series of ecological elements, mechanisms and processes such as competition, fragmentation, stability, disturbance, fragment shape and connectivity (Storch *et al.*, 2012).

On the other hand, we can conclude that there is a reduction of the potential future range by more than 50% compared to the current potential range of the seven forest types.

In all three climate scenarios there is a pattern of decrease in potential area, most marked in the RCP 8.5 scenario where there is a clear pattern for the period 2040-2069, with three forests decreasing by half and one by almost 80%.

## 5. Conclusion

Most projections of future scenarios foresee a reduction in the potential area of the most representative forests in the Andes. Of the scenarios considered, the most benign is RCP 6.0 and the most restrictive RCP 8.5. These projections should be taken only as a guideline or warning and there are several considerations to be made in their interpretation.

The first is that the actual scenario that will occur in the coming decades is unknown. The range is wide and the available models predict values of change consistent in their general trends but with significant differences. The possibility of harsher scenarios than those shown here cannot be ruled out in view of the scant success in complying with the Kyoto agreements in their first and second periods of validity.

Even so, there are factors that may profoundly modify the response of vegetation to climate change compared to what is predicted in these models.

One such factor is the plasticity of forest formations to change. It is possible that some species or forests as a whole may respond more flexibly to environmental change than models estimate. For example, a rise in temperature could be supported if it occurs simultaneously with a rise in precipitation in the warmer season. Unfortunately, we do not have the information to assess these responses, so it is more prudent to assume the situation that the models predict. The vulnerability of species to climate change has sometimes been discussed, but the scarcity of data is always a limiting factor in the effectiveness of models (Arribas and Abellán, 2012).

It should also be considered that this type of model does not consider biotic interactions or other factors that can influence such a complex spatio-temporal process as species distribution (Cuesta and Becerra, 2012). Nature is complex and models are simplifications that allow us to manage it, but the uncertainties are great.

## References

- Acosta, F., Aguilera, X., Campero, M., Prado, P., Fernández, C.E. 2022. Estructura del ensamblaje de microcrustáceos en tres distritos biogeográficos de los Andes de Bolivia. *Ciencia y Tecnología* 14, 35-45. <https://revistas.umss.edu.bo/index.php/cienciaytecnologia/index>
- Alberdi Nieves, V. 2021. Modelado de distribución de especies en los bosques de los andes meridionales. *Papeles de Geografía*, 66. <https://doi.org/10.6018/geografia.409051>
- Alaggia, F.G., Torres, R.C., Nori, J. 2022. Efecto hipotético del cambio climático sobre la distribución de dos especies leñosas dominantes del Chaco Serrano. *Ecología Austral*, 32(2), 319-330. <https://doi.org/10.25260/EA.22.32.2.0.1828>
- Anderson, R.P., Lew, D., Townsend, A.P. 2003. Evaluating predictive models of species' distributions: criteria for selecting optimal models. *Ecological Modelling* 162, 211-232. [https://doi.org/10.1016/S0304-3800\(02\)00349-6](https://doi.org/10.1016/S0304-3800(02)00349-6)
- Arribas, P., Abellán, P. 2012. La vulnerabilidad de las especies frente al cambio climático, un reto urgente para la conservación de la biodiversidad. *Ecosistemas* 21(3), 79-84. <https://doi.org/10.7818/ECOS.2012.21-3.10>
- Araújo, M., Peterson, A. 2012. Uses and misuses of bioclimatic envelope modelling. *Ecology*, 93(7), 1527-1539. <https://doi.org/10.1890/11-1930.1>
- Ávila-Núñez, J.L., Otero LD. 2019. Entomofauna asociada a especies de helechos Pteridium (Pteridopsida: Dennstaedtiaceae) en el Cerro La Bandera de Los Andes venezolanos. *Ecotrópicos* 31, e0006 <https://doi.org/10.53157/ecotropicos.31e0006>
- Báez, S., Jaramillo, L., Cuesta, F., Donoso, D.A. 2016 Effects of climate change on Andean biodiversity: a synthesis of studies published until 2015, *Neotropical Biodiversity*, 2(1), 181-194.
- Barrera Sánchez, C.F., Félix, C., Ruiz-Corral, J.A., Zarazúa Villaseñor, P., Lépez Ildefonso, R., González Eguiarte, D.R. 2020. Cambio climático Y distribución Potencial De Frijol Lima En Mesoamérica y Aridoamérica. *Revista Mexicana de Ciencias Agrícolas* 11 (6), 1361-1375. <https://doi.org/10.29312/remexca.v11i6.2412>
- Beaumont, L.J., Pitman, A., Perkins, S. 2011. Impacts of climate change on the world's most exceptional ecoregions. *Proceeding of the National Academy of Sciences* 108(6), 2306-2311. <https://doi.org/10.1073/pnas.1007217108>

- Buytaert, W., Bievre B., 2012. Water for cities: The impact of climate change and demographic growth in the tropical Andes. *Water Resources Research* 48. <https://doi.org/10.1029/2011WR011755>
- Cuentas Romero, M.A. 2022. Análisis de la incidencia del cambio climático en especies de aves amenazadas en los Andes peruanos: modelos de distribución y propuestas de conectividad. *Pirineos* 177, e071. <https://doi.org/10.3989/pirineos.2022.177004>
- Cuesta, F. 2009. *Los Bosques Montaños de los Andes Tropicales. Una evaluación regional de su estado de conservación y de su vulnerabilidad a efectos del cambio climático.* La Paz (Quito), Programa Regional Ecobona-Intercooperation. <https://www.bivica.org/files/bosques-montanos.pdf>
- Cuesta, F., Becerra, M. T. 2012. *Panorama andino de cambio climático: Vulnerabilidad y adaptación en los Andes Tropicales.* M. Bustamente, F. Cuesta, M. T. Becerra, J. Postigo and J. Peralvo. Lima, CONDESAN, Secretaría General de la Comunidad Andina. <https://redbosques.condesan.org/wp-content/uploads/2017/10/Panorama-andino-de-cambio-clim%C3%A1tico-min.pdf>
- De la Torre, L., Navarrete, H., Muriel, M. 2008. *Enciclopedia de las Plantas Útiles del Ecuador.* Quito: Herbario QCA de la Escuela de Biología, Pontificia Universidad Católica del Ecuador. [https://bibdigital.rjb.csic.es/medias/63/42/27/85/63422785-1490-4c78-9c97-a4a75a66cc63/files/TOR\\_En\\_Pl\\_Ut\\_Ecuador.pdf](https://bibdigital.rjb.csic.es/medias/63/42/27/85/63422785-1490-4c78-9c97-a4a75a66cc63/files/TOR_En_Pl_Ut_Ecuador.pdf)
- Djoghlaf, A. 2007. Climate Change and Biodiversity in Polar Region. Sustainable PNUMA. <https://digitalcommons.wcl.american.edu/cgi/viewcontent.cgi?article=1059&context=sdlp>
- Duque, A., Stevenson, P.R., Feeley, K.J. 2015. Thermophilization of adult and juvenile tree communities in the northern tropical Andes. *Proceedings of the National Academy of Sciences* 112,10744-10749. <https://doi.org/10.1073/pnas.1506570112>
- Elith, J., Graham C., Anderson R., Zimmermann N. 2006. Novel methods improve prediction of species distribution from occurrence data. *Ecography* 29, 129-151. <http://doi.org/10.1111/j.2006.0906-7590.04596.x>
- Fadrique, B., Báez, S., Duque, Á., Malizia, A., Blundo, C., Carilla, J., ... Feeley, K. J. 2018. Widespread but heterogeneous responses of Andean forests to climate change. *Nature* 564(7735), 207-212. <https://doi.org/10.1038/s41586-018-0715-9>
- FAO, Organización de las Naciones Unidas para la Alimentación y la Agricultura. 2014. *Cordillera de Los Andes, una oportunidad para la integración y desarrollo de América del Sur.* Santiago de Chile. ISBN 978-92-5-308431-9. <https://openknowledge.fao.org/handle/20.500.14283/i3854s>
- Felicísimo, A., Muñoz, J. 2011. *Bosques y cambio global.* España -México.Madrid, CYTED. [https://www.rjb.csic.es/jardinbotanico/ficheros/documentos/pdf/pubinv/JMF/Felicisimoetal%202011\\_FORCLIM3CYTEDEspañaMexico.pdf](https://www.rjb.csic.es/jardinbotanico/ficheros/documentos/pdf/pubinv/JMF/Felicisimoetal%202011_FORCLIM3CYTEDEspañaMexico.pdf)
- Fick, S.E., Hijmans R.J. 2017. WorldClim 2: New 1-km spatial resolution climate surfaces for global land areas. *International Journal of Climatology* 37(12), 4302-4315. <https://doi.org/10.1002/joc.5086>
- García-Romero, A., Muñoz, J., Andrés, N. 2010. Relationship between climate change and vegetation distribution in the Mediterranean mountains: Manzanares Head valley, Sierra De Guadarrama (Central Spain). *Climatic Change* 100. <https://doi.org/10.1007/s10584-009-9727-7>
- Gonzalez, P., Neilson, R.P. 2010. Global patterns in the vulnerability of ecosystems to vegetation shifts due to climate change. *Global Ecology and Biogeography* 19, 755-768. <https://doi.org/10.1111/j.1466-8238.2010.00558.x>
- Gutiérrez, E., Trejo, I. 2023. Aplicación de diferentes tipos de datos en el modelado de la distribución de especies arbóreas en México. *Colombia Forestal* 26(1), 48-63. <https://doi.org/10.14483/2256201X.19392>
- Hernández-Silva, N., Suárez-García, R.A 2019. Variables bioclimáticas que determinan la distribución de la hormiga myrmecocystus mexicanus en México. *Revista Ciencia e Innovación Agroalimentaria* 1, 1. <https://doi.org/10.15174/cia.v1i1.6>
- Herzog, S.K., Martínez, R., Jorgensen, P.M., Tiessen, H. 2012. *Cambio Climático y Biodiversidad en los Andes Tropicales.* Instituto Interamericano para la investigación del Cambio Global y Comité Científico sobre problemas del Medioambiente. París. 426 pp. ISBN: 978-85-99875-06-3. [https://www.iai.int/admin/site/sites/default/files/libro\\_completo.pdf](https://www.iai.int/admin/site/sites/default/files/libro_completo.pdf)

- Hijmans, R.J. 2012. Cross-validation of species distribution models: removing spatial sorting bias and calibration with a null model". *Ecology*, 93, 679-688. <https://doi.org/10.1890/11-0826.1>
- Hijmans, R., Cameron, S., Parra, J.L., Jones, P.G., Jarvis, A. 2005. Very high resolution interpolated climate surfaces for global land areas. *International Journal of Climatology* 25, 1965-1978. <https://doi.org/10.1002/joc.1276>
- Jain, N., Jana, P. K. 2023. LRF: A logically randomized forest algorithm for classification and regression problems. *Expert Systems with Applications* 213, 119225. <https://doi.org/10.1016/j.eswa.2022.119225>
- Josse, C., Cuesta, F., Navarro, G., Barrena, V., Cabrera, E., Chacón-Moreno, E., Ferreira, W., Peralvo, M., Saito, J., Tovar, A. 2009. *Ecosistemas de los Andes del Norte y Centro*. Secretaría General de la Comunidad Andina, Programa BioAndes, EcoCiencia, NatureServe, <https://www.natureserve.org/sites/default/files/publications/files/josseetal2009.pdf>
- Kessler, M. (2006). Bosques de Polylepis. En Moraes, M., Øllgaard, B., Kvist, L.P., Borchsenius, F., Balslev, H. (Eds.) *Botánica Económica de los Andes Centrales*. Universidad Mayor de San Andrés, La Paz. pp: 110-120.
- Malcolm, R.J., Liu, C., Neilson, R., Hansen, L., Hannah, L. 2006. Global warming and extinctions of endemic species from Biodiversity Hotspots. *Conservation Biology* 20 (2), 538-548. <https://doi.org/10.1111/j.1523-1739.2006.00364.x>
- Mateo, R.G., Felicísimo, A., Muñoz, J. 2011. Modelos de distribución de especies y su potencialidad como recurso educativo. *Revista Chilena de Historia Natural* 84(2), 217-240. [http://rchn.biologiachile.cl/pdfs/2011/2/Mateo\\_et\\_al\\_2011.pdf](http://rchn.biologiachile.cl/pdfs/2011/2/Mateo_et_al_2011.pdf)
- Mujica, B.E., Holle, M. 2002. Los Andes y la transformación cultural del paisaje. *Paisajes Culturales en los Andes. Revista de Arqueología Americana* 33, 67-79. <https://doi.org/10.35424/rearam332015>
- NatureServe. 2009. *Sistemas Ecológicos de los Andes del Norte y Centro*. International Ecological Classification Standard: Terrestrial Ecological Classifications, NatureServe Central Database: 70. [https://sinia.minam.gob.pe/sites/default/files/siar-puno/archivos/public/docs/ecosistemasandesnorteycentro\\_pesado.pdf](https://sinia.minam.gob.pe/sites/default/files/siar-puno/archivos/public/docs/ecosistemasandesnorteycentro_pesado.pdf)
- Navarro, I. 2014. Estudio arqueológico sobre los guancas y taramas. Un nuevo análisis sobre el desarrollo económico y social de estas culturas en los Andes Centrales. *Arqueología y Sociedad*. 26, 153-192. <http://doi.org/10.15381/arqueolsoc.2014n27.e12200>
- Navarro, G., Maldonado, M. 2002. *Geografía Ecológica de Bolivia: Vegetación y ambientes acuáticos*. Centro de Ecología Simón I. Patiño. [https://www.researchgate.net/publication/312134030\\_Geografia\\_Ecológica\\_de\\_Bolivia\\_Vegetacion\\_y\\_Ambientes\\_Acuáticos](https://www.researchgate.net/publication/312134030_Geografia_Ecológica_de_Bolivia_Vegetacion_y_Ambientes_Acuáticos)
- Pitman, N., Widmer, J., Jenkins, C.N. 2011. Volume and geographical distribution of ecological research in the Andes and the Amazon, 1995-2008. *Tropical Conservation Science* 4(1), 64-81 <http://doi.org/10.1177/194008291100400107>
- Poblete, A.G., Albeiro Castro, M.A. 2021. Influencia del ENSO en los factores y agentes climáticos que inciden en las precipitaciones níveas de los Andes Áridos. *Estudios Socioterritoriales*". *Revista de Geografía*, (29), 078. <https://doi.org/10.37838/unicen/est.29-209>
- Phillips, S.J., Dudik, M. 2008. Modeling of species distributions with Maxent: new extensions and a comprehensive evaluation. *Ecography* 31, 161-175. <http://doi.org/10.1111/j.0906-7590.2008.5203.x>
- Phillips, S. J., Anderson, R.P. 2006. A maximum entropy modelling of species geographic distributions. *Ecological Modelling* 190, 231-259. <https://doi.org/10.1016/j.ecolmodel.2005.03.026>
- Recalde-Coronel, G.C., Zaitchik, B., Pan, W.K. 2020. Madden-Julian Oscillation Influence on Sub-Seasonal Rainfall Variability on the West of South America. *Clim. Dyn.* 54, 2167-2185. <https://doi.org/10.1007/s00382-019-05107-2>
- Rey Benayas, J.M., Fraile Real, L., de la Torre Cejas, R., Fernández, N. 2020. Idoneidad del hábitat para el Oso pardo (*Ursus arctos*) en el sureste del Sistema Ibérico. *Ecosistemas* 29(2), 1972. <https://doi.org/10.7818/ECOS.1972>

- Reyes, M., Di Maio, L., Dominguez, L., Frischknecht, C., Biass, S., Freitas, L., Nieto, A., Elisondo, M., Figueroa, M., Amigo, A., García, S., Bonadonna, C. 2023. Mapa regional y ranking de riesgos volcánicos de la zona volcánica Central de los Andes. En: Masías, P., Ortega, M., eds., Libro de Resúmenes IX Foro Internacional de Peligros Volcánicos – IX FIPVO. Lima: Instituto Geológico Minero y Metalúrgico, pp. 176-181. <https://hdl.handle.net/20.500.12544/4511>
- Saupe, E., Barve, V., Myers, C., Soberón, J., Barve, N., Hensz, C., Peterson, A., Owen, H., Lira-Noriega, A. 2012. Variation in niche and distribution model performance: The need for a priori assessment of key causal factors. *Ecological Modelling* 237, 11-22. <https://doi.org/10.1016/j.ecolmodel.2012.04.001>
- Saraiva de Menezes, J.F. 2023. Comparando las estimaciones de selección de hábitat mediante modelos de distribución de especies y step selection functions. *Ecosistemas* 32(2), 2455. <https://doi.org/10.7818/ECOS.2455>
- Storch, D., Keil, P., Jetz, W. 2012. Universal species-area and endemics area relationships at continental scales. *Nature* 488(7409), 78-83. <https://doi.org/10.1038/nature11226>
- Terán-Valdez, A., Cuesta, F., Pinto, E., Peralvo, M. 2019. Los Bosques del Noroccidente de Pichincha: una mirada profunda a los pulmones de Quito. Proyecto EcoAndes, CONDESAN. Quito, Ecuador <https://condesan.org/recursos/los-bosques-del-noroccidente-pichincha-una-mirada-profunda-los-pulmones-quito/>
- Thuiller, W., Albert, C., Araújo, M.B., Berry, P.M., Cabeza, M., Guisan, A., Hickler, T., Midgley, G., Paterson, J., Schurr, F.M., Sykes, M., Zimmermann, N. 2008. Predicting global change impacts on plant species distributions: Future challenges. *Perspectives in Plant Ecology Evolution and Systematics* 9, 137-152. <https://doi.org/10.1016/j.ppees.2007.09.004>
- Villarreal-Veloz, J., Zapata-Ríos, X., Uvidia-Zambrano, K., Borja-Escobar, C. 2023. Spatio-Temporal Description of the NDVI (MODIS) of the Ecuadorian Tussock Grasses and Its Link with the Hydrometeorological Variables and Global Climatic Indices. *Sustainability*, 15, 11562. <https://doi.org/10.3390/su151511562>
- Vistín, D.A., Salas, E.M., Balseca, J.E., Lara, N.X. 2022. Distribución potencial de Polylepis incana en los Andes ecuatorianos para estudios de fisiología vegetal y planes de rehabilitación forestal. *Ecología Austral*, 33(1), 001-012. <https://doi.org/10.25260/EA.23.33.1.0.1991>



## VARIABILIDAD ESPACIAL Y TEMPORAL DE LAS PRECIPITACIONES EXTRAORDINARIAS EN ESPAÑA (1916-2022)

DHAIS PEÑA-ANGULO<sup>1,2,3</sup> , SANTIAGO BEGUERÍA<sup>2,4</sup> ,  
VÍCTOR TRULLENQUE-BLANCO<sup>2,4</sup> ,  
JOSÉ CARLOS GONZÁLEZ-HIDALGO<sup>1,2,3\*</sup>

<sup>1</sup> Departamento de Geografía, Universidad de Zaragoza, España.

<sup>2</sup> Laboratorio de Climatología y Servicios Climáticos (CSIC-UNIZAR), España.

<sup>3</sup> Instituto Universitario Ciencias Ambientales (IUCA) Universidad Zaragoza, España.

<sup>4</sup> Estación Experimental de Aula Dei (EEAD-CSIC), Zaragoza, España

**RESUMEN.** La combinación de los fondos documentales de AEMET y los Libros Resúmenes de Observaciones Anuales nos ha permitido elaborar un catálogo de lluvias extraordinarias en el territorio peninsular español durante el periodo 1916-2022. Este catálogo incluye 19.184 observaciones diarias de máximas mensuales de precipitación que superaron 100 mm, procedentes de 4.325 observatorios y producidas en 4.814 días distintos. Con cantidades superiores a 200 mm /día se han contabilizado 1.130 registros, agrupados en 530 días procedentes de 664 observatorios. La distribución espacial de estas precipitaciones pone de manifiesto que estos eventos se pueden producir en cualquier punto del territorio, si bien se detecta una concentración tanto de registros como de fechas en las costas, especialmente en las del mar Mediterráneo en el caso de cantidades superiores a 200 mm. En general, las precipitaciones extraordinarias se producen con mayor frecuencia en otoño. En el extremo opuesto, los meses de verano son los que menos registros acumulan, así como un menor número de eventos diarios. Estos sucesos están muy ligados a situaciones sinópticas determinadas, y su estudio por Divisiones Hidrológicas permite diferenciar aquellas afectadas por advecciones atlánticas del oeste (Cantábrico, Duero, Guadiana, Guadalquivir, parcialmente Andalucía Oriental) de las advecciones mediterráneas del este (Pirineos orientales, Júcar, Segura, parcialmente Andalucía oriental), mientras la División del Ebro por su extensión y posición recibe influencias diversas. La disposición del relieve parece ser uno de los factores que determinan la extensión en el espacio de los episodios de lluvias extraordinarias. La frecuencia de estos sucesos extraordinarios no muestra señales de variación en el tiempo.

### *Spatial and Temporal Variability of Extraordinary Precipitations in Spain (1916-2022)*

**ABSTRACT.** The use of AEMET's documentary archives and the Annual Summary Books has allowed us to create a catalog of extraordinary rainfall events in mainland Spain from 1916 to 2022. During this period, at least 19,184 daily observations of monthly maximum rainfall exceeding 100 mm were recorded, from 4,325 observatories, spread across 4,814 days. Records with more than 200 mm/day amounted to 1,130, spread over 530 days and 664 observatories. The spatial distribution shows that these events can occur anywhere, but there is a clear concentration of both records and dates along the coasts, particularly on the Mediterranean coast for rainfall over 200 mm. In general, extraordinary rainfalls are more frequent in autumn, while summer months have the fewest records and daily events. These events are strongly linked to specific weather patterns. Analyzing them by Hydrological Divisions allows us to differentiate areas influenced by Atlantic advections from those affected by Mediterranean advections. The Ebro Division, due to its size and location, experiences various influences. The region's topography seems to play a role in determining the spatial extent of extraordinary rainfall events. Overall, the frequency of these events shows no clear trend over time.

**Palabras Clave.** Precipitación, extremos diarios, España, tipos de tiempo.

**Keywords:** Precipitation, extreme events, Spain weather Type.

\*Correspondencia: José Carlos González-Hidalgo, Departamento de Geografía, Universidad de Zaragoza, España. E-mail: jcgh@unizar.es

## 1. Introducción

La cuenca mediterránea es un área conocida por la recurrencia de precipitaciones intensas, como demuestra la ya clásica revisión de Poesen y Hooke (1997) en la que se compilaron registros de precipitaciones observadas en 24 horas durante el siglo 20, con máximos absolutos que superan 900 mm/día y que en España se completa con las compilaciones publicadas entre otros por Pérez-Cueva (1983), Llasat (1987), Olcina (1994a, p. 82; Olcina 1994b, p. 45, 46, 55, 92), Martín-Vide (1994), López Bermúdez y Romero (1993), Martín-Vide *et al.* (2021), Sánchez-Almodóvar *et al.* (2022) y Beneto y Khodayar (2023), en los que abundan las precipitaciones varias veces centenarias.

Estos eventos son fuente de pérdidas de vidas y bienes. Solamente en el periodo 2006-2020 las pérdidas medias ocasionadas en los diez municipios más afectados fueron de 2.522.306 euros (Consorcio Compensación de Seguros, 2021 y 2023). Entre 1981 y 2022, en torno al 70% de las indemnizaciones por desastres naturales se debieron a inundaciones provocadas por riadas a consecuencia de lluvias extraordinarias, y el coste de los daños causados por estos fenómenos en las últimas tres décadas se estima en 7.000 millones de euros. Por estas razones, el interés de estudiar las precipitaciones extraordinarias es muy elevado, especialmente ante su eventual aumento como consecuencia del calentamiento global, como se señala con frecuencia.

No obstante, la señal de la tendencia de las precipitaciones extraordinarias no es clara, al menos en el ámbito Mediterráneo. Siguiendo la revisión que hemos publicado recientemente (González-Hidalgo *et al.*, 2025), el aumento generalizado de los extremos sugerido por Alpert *et al.* (2002) no ha sido confirmado posteriormente ni en el conjunto de la cuenca (Norrant y Douguedroit, 2006; Karagiannidis *et al.*, 2012; Marani y Parisi, 2014), ni en diversos sectores del Norte de África y Oriente Próximo (Zhang *et al.*, 2005; Zittis, 2018), sector centro oriental (Kostopoulou Jones, 2005; Mathboub *et al.*, 2017), costa norte (Toreti *et al.*, 2010, 2016), Maghreb (Tramblay *et al.*, 2013 a; Salhi *et al.*, 2022), o norte de África desde Marruecos a Egipto (Donat *et al.*, 2014), si bien Benabdellouahab *et al.* (2020) identifican tendencias positivas en el sector occidental de la Cuenca, y algunos autores han sugerido el aumento de determinados eventos extraordinarios en sectores costeros del occidente de la misma (Ribes *et al.*, 2019; Miró *et al.*, 2022; Nouaceur *et al.*, 2022, véase discusión final).

En el análisis de las precipitaciones extraordinarias de la España peninsular destacan dos textos clásicos, el de Elías-Castaño y Ruíz-Beltrán (1979) sobre precipitaciones máximas, y el de Font-Tullot (1983) sobre el clima de España y Portugal, ambos elaborados con datos de las décadas entre 1940-1980. Los dos textos muestran que los eventos extraordinarios se concentran con preferencia a lo largo del margen costero peninsular. Desde entonces, y que sepamos, solamente Queralt *et al.* (2009) y Merino *et al.* (2016) han vuelto a analizar las precipitaciones extraordinarias en el conjunto del territorio peninsular español si bien con un número más reducido de observaciones, mientras los estudios con información detallada se concentran en la margen mediterránea peninsular (González-Hidalgo *et al.*, 2025).

Las razones apuntadas nos indican dos hechos. En primer lugar, que carecemos de un análisis de los eventos extraordinarios de precipitaciones diarias con la suficiente densidad de observaciones y con datos actualizados; y, en segundo lugar, que desconocemos el contexto secular de las precipitaciones extraordinarias actuales, hecho de máximo interés ante la reiterada insistencia en que la frecuencia de estos fenómenos debe incrementarse a consecuencia del aumento de las temperaturas.

En lógica consecuencia, el objetivo del presente trabajo es analizar, con la mayor densidad de información disponible, las lluvias extraordinarias en la España peninsular durante el periodo 1916-2022, incluyendo su variabilidad espacial y temporal, e identificar las condiciones sinópticas en las que tienden a producirse dichos eventos. Este texto es la continuación del que describe el catálogo de precipitaciones extraordinarias en el territorio peninsular español del periodo 1866-2022 (González-Hidalgo *et al.*, 2025), cuya base de datos está disponible en González-Hidalgo *et al.* (2024).

## **2. Datos y métodos**

### *2.1. Fuentes documentales*

Las fuentes documentales que hemos analizado combinan, por un lado, los fondos del Banco Nacional de Datos Climáticos (BNDC) de la Agencia Estatal de Meteorología (AEMET), y por otro las series de máximos diarios mensuales publicadas en los Libros Resúmenes Anuales de Observaciones (LRA). La información suministrada por los LRA se refiere al periodo 1866-1950, e incluye la cantidad y la fecha del máximo evento mensual de las estaciones, no especificándose si ha habido lagunas de observación en el mes, o si en otros días del mismo se han producido precipitaciones cuantiosas de menor magnitud que la del máximo, excepto si la precipitación coincide en cantidad en dos o más días en el mes, en cuyo caso se incluye esta información. Numerosos análisis emplean el acrónimo Rx1day para referirse al dato que analizaremos, como se recoge en el *Expert Team on Climate Change Detection and Indices* (de Lima *et al.*, 2015).

Por razones de densidad de observaciones, y dado el escaso número de observatorios con información en fechas anteriores a 1916, el presente estudio cubre el periodo 1916-2022. La relevancia del rescate de los datos procedentes de los LRA es grande, pues entre 1916-1950 suponen un 40% del total de los datos finales una vez combinados con los procedentes del BNDC. A partir de 1951, la única fuente de información es el BNDC.

### *2.2. Umbrales de identificación, máximos extremos y extraordinarios*

Un evento extremo por definición es un suceso raro, pero precisar exactamente el umbral que define un evento extremo no es tarea fácil. Estos se suelen elegir por estimaciones de sucesos previos, por períodos de retorno, desviaciones de la media, o por distancias intercuartílicas (véase Insua-Costa *et al.*, 2021). Por ejemplo, en la vertiente mediterránea española Pino *et al.* (2016) emplearon las condiciones sinópticas, mientras Sillero *et al.* (2022), Beneto y Khodayar (2023), Lázaro *et al.* (2001), Lemús-Canovas *et al.* (2021) y Claro *et al.* (2023), entre otros, aplicaron diversas magnitudes directamente como umbrales de identificación de eventos extremos.

Por la longitud del periodo analizado, la densidad de información, y el deseo de buscar las situaciones extraordinarias, hemos optado por analizar las precipitaciones máximas mensuales diarias con dos umbrales: el primero de 100 mm/día o más, que denominaremos por conveniencia precipitaciones extremas; y el segundo de 200 mm/día o más, que llamaremos extraordinarias. Las razones de esta elección se basan simplemente en ser cantidades muy elevadas, en teoría muy poco probables en latitudes medias, evidentemente distintas en su probabilidad y con seguridad origen de situaciones potencialmente peligrosas. A ello se suma que han sido umbrales seleccionados en numerosos estudios previos (Tabla 1), lo que permitirá su comparación y haber sido los umbrales seleccionados para elaborar el catálogo de lluvias extraordinarias de España (González-Hidalgo *et al.* 2024 y 2025).

*Tabla 1. Estudios de precipitaciones extraordinarias en España. En González-Hidalgo et al. (2025), con modificaciones.*

Autor	Área analizada	Periodo	Eventos analizados	Umbral mm/día
Peñarrocha <i>et al.</i> (2002)	Valencia	1971-1995	57	>250
	Valencia	1971-1995	19	>350
Martín-Vide <i>et al.</i> (2008)	Cataluña	1950-2006	304	>100
Llop-Garau y Alomar-Garau (2012a)	Cataluña	1950-2005	304	>100
	Mallorca	1950-2005	387	
Llop-Garau y Alomar-Garau (2012b)	Mallorca	1931-2001	49	>200
Gilabert y Llasat (2018)	Cataluña	1900-2010	261	>100
Meseguer <i>et al.</i> (2018)	Júcar y Segura	1950-2016	239	>200
López-Bustins <i>et al.</i> (2020)	Cataluña	1956-2016	50	>200
Martín-Vide <i>et al.</i> (2021)	Murcia y Alicante	1941-2017	68	>200
Sánchez-Almodóvar <i>et al.</i> (2022)	Alicante	1981-2020	129	>100
González-Hidalgo <i>et al.</i> (2025)	España Peninsular	1916-2022	4814	>100

Para poder combinar las dos fuentes documentales hay que tener presente que los datos analizados siempre son el máximo diario de precipitación mensual del periodo 1916-2022 de cada estación, pues esta es la información que suministran los LRA, con independencia que desde 1951 en adelante el segundo máximo, o el enésimo máximo mensual, pudiese superar también los umbrales elegidos y el dato estuviera disponible en el BNDC. Como es obvio este procedimiento puede dar lugar a que registros de más de 100 mm e incluso 200 mm que ocasionalmente no fuesen el máximo mensual no aparezcan en el estudio; no obstante, cabe pensar que por su magnitud y su baja probabilidad (implicaría que en el mismo observatorio se registrase precipitación superior a 100 mm o 200 mm en más de un día en el mismo mes) su frecuencia debe ser muy escasa. Por ello, consideramos que dicho catálogo constituye una buena aproximación a la ocurrencia de eventos de precipitación extraordinaria.

La identificación de los eventos diarios con precipitaciones superiores a 100 y 200 mm se realizó del siguiente modo: en cada día del año desde 1916 a 2022 se identificó el máximo absoluto de la base de datos; si superaba uno de los dos umbrales la fecha se identificó como evento extremo o extraordinario; a continuación, se identificaron todos los observatorios que registraron su máximo diario mensual en dicho día, con independencia de la magnitud de la precipitación. Los observatorios que superaron 100 mm o 200 mm se anotaron como frecuencias de lluvias extremas o extraordinarias en ese evento. Por último, con la información recopilada se elaboró el mapa de cada evento diario; este mapa no es exactamente la precipitación de la fecha, dado que los observatorios que hayan registrado su máximo mensual en otra no aparecerán, pero ello no obsta para que el documento muestre la distribución de precipitaciones máximas mensuales en ese día, y sea también una aproximación razonable a la distribución espacial del evento analizado.

### 2.3. Análisis espacial

Los eventos fueron asignados por su máximo a las diferentes Divisiones Hidrológicas que son la base de las unidades territoriales de la red meteorológica, así como las unidades de planificación hidrológica de España. Su disposición y código se muestran en la Figura 1. El análisis de la distribución espacial de los eventos de precipitaciones extraordinarias por Divisiones Hidrológicas tiene una lógica a priori, puesto que la disposición del relieve aparece como uno de los factores que determinan la penetración de las masas de aire oceánicas causantes de las precipitaciones extraordinarias.

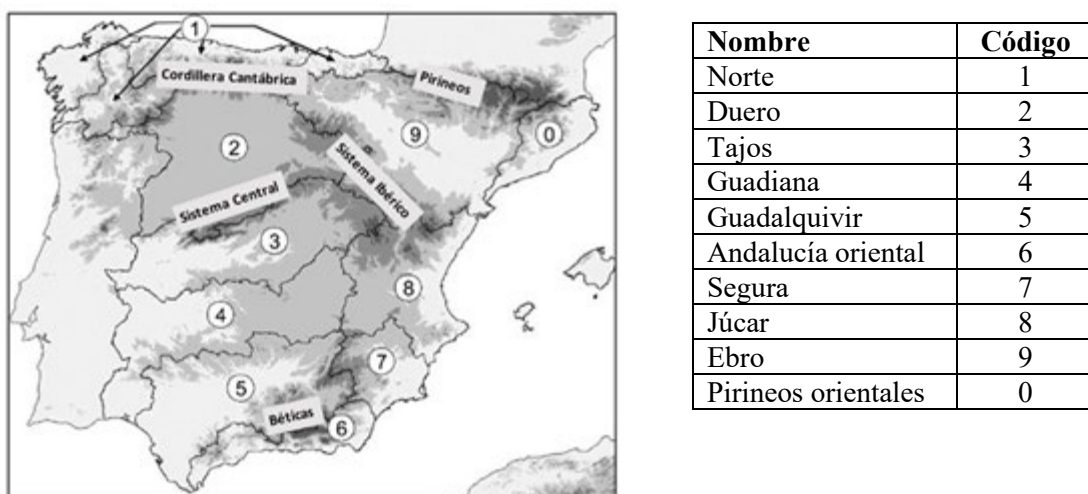


Figura 1. Divisiones Hidrológicas de España.

En cada División se identificaron el número de registros observados, así como el número de eventos (fechas diferentes) en que se habían producido.

#### 2.4. Las condiciones sinópticas de los eventos

Las condiciones atmosféricas en las que se produjeron las precipitaciones extraordinarias se analizaron por medio de la clasificación de tipos de tiempo de Jenkinson y Collison (1977), que automatiza la clasificación manual de Lamb, según el procesamiento de Trigo y DaCamara (2000). Dicha clasificación ha sido aplicada a valores diarios ligados a eventos extremos en la vertiente mediterránea peninsular con resultados óptimos por Llop-Garau y Alomar-Garau (2012), Gilabert y Llasat (2018), Cordobilla y Martín Vide (2018) y Sánchez-Almodóvar *et al.* (2022), y al conjunto peninsular por Meseguer-Ruiz *et al.* (2018). Básicamente esta clasificación permite identificar la dirección diaria de los vientos dominantes y las condiciones de estabilidad o inestabilidad en la atmósfera. Por otro lado, para aprovechar al máximo las posibilidades que la base de datos proporcionada hemos empleado como fuente documental la malla de presiones de superficie del reanálisis del siglo 20 cuya información abarca el periodo 1835-2015 (Slivinski *et al.*, 2019), recientemente validada para este fin (Fernández-Granja *et al.*, 2023). El nodo de clasificación escogido fue el más central de la malla en la Península Ibérica ( $40^{\circ}\text{N}$ ,  $3^{\circ}\text{W}$ ) y el periodo analizado se restringe al del re-análisis: 1916-2015. Los valores de la clasificación se encuentran disponibles en Cortesi y Peña-Angulo (2024) quienes emplearon el ya citado reanálisis del siglo 20.

Por último, una vez clasificados los eventos diarios por su tipo de tiempo se analizaron sus frecuencias temporales y su distribución espacial y mensual en las diversas Divisiones Hidrológicas.

### 3. Resultados

#### 3.1. Frecuencia de observaciones y eventos diarios

En el catálogo que hemos publicado recientemente (González-Hidalgo *et al.*, 2024 y 2025) se condensan los principales resultados descriptivos del análisis en las siguientes magnitudes: en el periodo analizado se han contabilizado 19.184 observaciones de precipitaciones máximas diarias mensuales con más de 100 mm, registradas en 4.325 observatorios y a lo largo de 4.814 días (Tabla 2). Por lo que se refiere a los sucesos de precipitaciones diarias máximas mensuales superiores 200 mm, se han identificado 1.130 registros, agrupados en 530 días procedentes de 664 observatorios.

*Tabla 2. Precipitaciones superiores a 100 y 200 mm /día. Distribución mensual de los eventos de precipitación, su porcentaje, frecuencia de observaciones (Registros) y ratios de eventos y observaciones. Modificado a partir de González-Hidalgo et al. (2025).*

	>100 mm			200 mm			Ratio Eventos	Ratio Registros
	Evento	Evento %	Registros	Evento	Evento %	Registros		
Enero	477	9,9%	1616	32	6,0%	51	7%	3%
Febrero	398	8,3%	1354	34	6,4%	51	9%	4%
Marzo	375	7,8%	1092	31	5,8%	43	8%	4%
Abril	273	5,7%	789	29	5,5%	41	11%	5%
Mayo	239	5,0%	615	18	3,4%	28	8%	5%
Junio	212	4,4%	523	13	2,5%	20	6%	4%
Julio	132	2,7%	294	14	2,6%	18	11%	6%
Agosto	242	5,0%	577	13	2,5%	18	5%	3%
Septiembre	522	10,8%	2427	62	11,7%	196	12%	8%
Octubre	659	13,7%	3820	138	26,0%	349	21%	9%
Noviembre	687	14,3%	3354	87	16,4%	231	13%	7%
Diciembre	598	12,4%	2723	59	11,1%	84	10%	3%
	4814		19184	530		1130		

La localización de estos eventos extraordinarios muestra un patrón espacial claro. En la Figura 2 se muestra la distribución de los eventos a partir de la frecuencia con que en los observatorios de la red se alcanzó el máximo mensual superando 100 o 200 mm/día. Como se puede observar, la localización de estos eventos muestra una preferencia litoral en la costa del Cantábrico y Mediterráneo, más algunos eventos en sectores del interior ligados a condiciones locales del relieve.

Los meses con mayor número de observaciones superiores a 100 mm son Octubre y Noviembre (más de 3.000), seguidos por Septiembre y Diciembre (más de 2.000). Por encima de 1.000 registros se encuentran Enero, Febrero y Marzo. En el extremo opuesto, Julio es el mes con menos registros (294). Las observaciones superiores a 200 mm son evidentemente menos frecuentes, siendo los meses con mayor frecuencia Octubre (349), Noviembre (231) y Septiembre (196), todos con más de 100 registros. Si bien ningún mes está libre de estos eventos, los valores menos frecuentes del periodo Mayo-Agosto arrojan cantidades de 20 eventos para todo el periodo analizado.

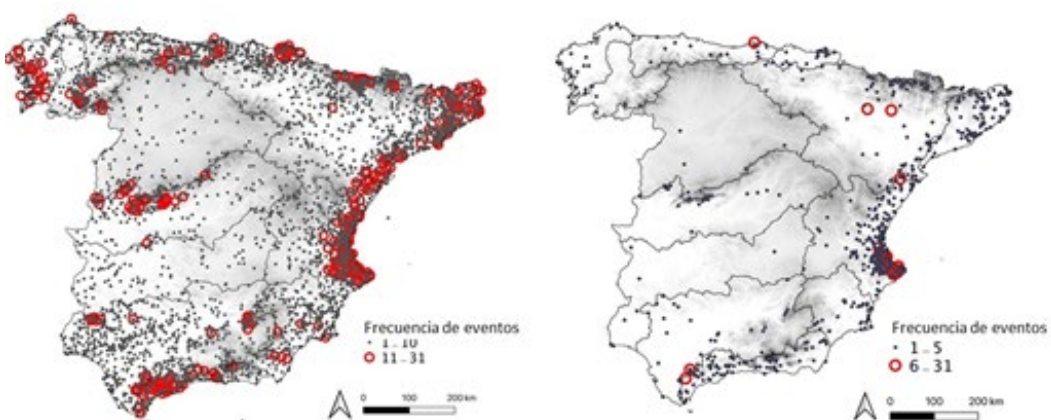


*Figura 2. Distribución espacial de los eventos diarios máximos mensuales de precipitación superiores a 100 (izquierda) y 200 (derecha) mm/día. Frecuencia (número de días) en que el observatorio registró el máximo absoluto de la red.*

Entre los meses de Septiembre y Diciembre al menos un observatorio superó el umbral de 100 mm en 500 ocasiones (con máximo en Noviembre, 687), mientras que los meses con menor número de eventos diarios son Julio (132) y Junio (212). Salvo Octubre (138), ningún mes pasa de 200 mm/día, y valores elevados también se encuentran en Noviembre (87), Septiembre (62) y Diciembre (59). Los resultados sugieren que, en el periodo 1916-2022, se han registrado precipitaciones diarias superiores a 100 mm en todos los meses del año, con una media de al menos 2 días en cada mes, no siendo extraño que en la misma fecha las precipitaciones superen 100 mm en varios observatorios simultáneamente. En Octubre, el 9% de las observaciones superiores a 100 mm registraron valores superiores a 200 mm, y en Septiembre y Noviembre el 8% y 7% respectivamente. Por el contrario, los valores más bajos se encuentran en los meses más fríos, con porcentajes entre 3% y 5%.

Las ratios de observaciones de registros de 100 y 200 mm/día muestran que no es extraño que en un mismo día varios observatorios pueden superar los umbrales establecidos, y que estos umbrales son más fáciles de superar en unos meses que en otros.

Los eventos más extremos en cuanto a la frecuencia de registros se produjeron los días 6/11/1982, 4/9/1989, 17/12/1997 y 23/10/2000. En cada uno de ellos más de 100 observatorios registraron precipitaciones superiores a 100 mm/día, lo que supone el 3% de la red operativa en esas fechas. Además, en el primer caso 12 observatorios registraron cantidades superiores a 200 mm/día, en el segundo 16, y en el cuarto 14. En observaciones superiores a 200 mm el caso más extremo es el evento de 4/11/1987, cuando 67 observatorios registraron más de 100 mm, y de ellos 24 más de 200 mm.

Merece la pena comentar los casos de algunas localidades en las que la frecuencia de estas precipitaciones ha sido más elevada. Hay cinco observatorios en los que hemos contabilizado más de 75 registros de 100 mm/día, y 24 en los que superan 40 veces. El máximo se localiza en el observatorio de Grazalema (código 5911) con 223 días, seguido de Artikutza con 95 (código 1024) y Pego Convento con 90 (código 8057A). En general estos registros se localizan en la vertiente mediterránea, con las excepciones de Guisando el Risquillo, Navalguijo y Serranillos, en Ávila, La Alberca, en Salamanca, y Artikutza, en el Pirineo Navarro, todos ellos, salvo este último, localidades ligadas al Sistema Central (Sierra de Gredos, Peña de Francia), en un núcleo conocido por su peculiar pluviometría asociada a factores topográficos en el interior central peninsular (Tabla 3). Finalmente, dos notas curiosas son las siguientes: el día del año con mayor número de observaciones superiores a 100 mm es el 5 de noviembre (262 registros), seguido del día 6 del mismo mes (248 registros); el día en que mayor número de veces se registraron más de 200 mm es el 19 de octubre (34 ocasiones), seguido del 11 de septiembre (31).

*Tabla 3. Observatorios con mayor número de registros diarios máximos mensuales > 100 mm.*

Nº	Id	Observatorio	Provincia	Nº	Id	Observatorio	Provincia
223	5911	Grazalema	Cádiz	45	1477	Dodro (a poza)	Coruña
95	1021	Artikutza	Navarra	45	6035	Benaojan (Cueva de la Pileta)	Málaga
90	8057A	Pego Convento	Alicante	45	8056	El Verger Racons	Alicante
82	3407	Guisando el Risquillo	Ávila	45	9984	Godall	Tarragona
74	3319	Serranillos	Ávila	44	3487	La Alberca	Salamanca
68	8054	Vall de Laguard Fontilles	Alicante	44	8296	Xativa (el Realengo)	Valencia
63	8039A	Tarbena CH Júcar	Alicante	43	2818e	Navalguijo	Ávila
59	8286	Beniatjar les Planises	Valencia	43	6039	Cortes de la Frontera (Bañuelos)	Málaga
53	8072	Barx	Valencia	42	6182	Alcaucín	Málaga
50	5911B	Grazalema (ama)	Cádiz	42	8063	Gorga	Alicante
50	8076	Benifairó de la Valldigna	Valencia	41	6006	Algeciras	Cadiz
49	8066	Almudaina	Alicante	41	8040	Bolulla	Alicante

### 3.2. Variaciones espaciales

Las variaciones espaciales de las precipitaciones superiores a 100 mm/día por Divisiones Hidrológicas ofrece un valioso punto de partida para conocer la distribución de las precipitaciones extraordinarias, pues son las unidades de gestión del agua en España y, además, porque sus límites coinciden con las principales alineaciones montañosas de la península Ibérica (Figura 1). En la Tabla 4 se incluye información relativa a su superficie, el número de observatorios de la red nacional que han registrado en algún momento eventos diarios y están incluidos en la base de datos, y el número de registros máximos diarios mensuales superiores a 100 y 200 mm.

*Tabla 4. Divisiones Hidrológicas, y características generales. Distribución del número de registros máximos mensuales diarios superiores a 100 y 200 mm (1916-2022).*

División Hidrológica	Código	Superficie		Observatorios		Observaciones	
		Km	%	Total	%	100 mm	200 mm
Norte	1	53.804	10,9	1.495	14,2	2.988	69
Duero	2	78.972	16,0	13.49	12,8	755	11
Tajo	3	54.769	11,1	800	7,6	1.125	29
Guadiana	4	59.873	12,2	967	9,2	488	12
Guadalquivir	5	63.085	12,8	1.297	12,3	1.567	66
Andalucía Oriental	6	18.391	3,7	497	4,7	2.009	133
Segura	7	18.254	3,7	425	4,0	650	42
Júcar	8	42.904	8,7	1.080	10,2	4.939	539
Ebro	9	86.098	17,5	1.925	18,2	1.954	102
Pirineos Orientales	0	16.493	3,3	730	6,9	2.709	127
Total		492.643	100,0	10.565	100,0	19.184	1.130

En general los registros de las precipitaciones diarias extremas y extraordinarias se han producido de manera abrumadoramente concentradas a lo largo de la costa mediterránea en las Divisiones de Andalucía Oriental (10,5%), Júcar (25,7%) y Pirineos orientales (14,1%). En conjunto, estas observaciones suponen más del 50% del total, habiendo sido registradas en el 19,4% del territorio y en el 21,8% de observatorios de la red (Tabla 4). La División del Segura, también orientada al Mediterráneo, aporta un bajo porcentaje, pero hay que tener en cuenta que su extensión es muy pequeña. La división del Ebro y la División del Segura aportan en torno al 14% de los registros. Por el contrario, las extensas divisiones del Duero, Tajo, Guadiana e incluso Guadalquivir, todas ellas orientadas al oeste, contribuyen al total de los registros máximos diarios superiores a 100 mm/día con porcentajes individuales que no superan nunca el 10% del total, a pesar de representar más del 50% del territorio peninsular e incluir el 41,9% de observatorios de la red. La excepción es la división del Norte, donde se ha registrado un 15,6% de eventos con el 14,2% de observatorios en el 10,9% del territorio.

Si el umbral se eleva a registros superiores a 200 mm/día, la División del Norte pierde claramente posiciones, y la División del Júcar aumenta su contribución hasta representar el 47,7% del total, manteniendo un valor por encima del 10 % las divisiones de Andalucía Oriental y Pirineos Orientales, de manera que las divisiones mediterráneas aglutinan más del 70% de los registros de esta magnitud.

La distribución mensual del número de eventos diarios de precipitaciones extremas y extraordinarias de cada cuenca se muestran en las Tablas 5 y 6. Recordemos que este valor indica que en esa fecha el máximo registro de la red se localiza en dicha cuenca y superó uno de los dos umbrales. Sorprendentemente, la División Hidrológica en la que se ha registrado el mayor número de episodios con máximo diario mensual superior a 100 mm/día es la cuenca Norte (1.018 eventos, el 21,1% del total de eventos), seguida de la del Júcar (834 eventos, 17,3%) y Pirineos Orientales (712 eventos, 14,8%).

Las proporciones varían en caso de considerar el umbral de 200 mm, donde el mayor número de eventos corresponde a la del Júcar (176 casos, 33,2% del total), seguida de Pirineos Orientales (66 eventos, 12,5 %), Andalucía Oriental (64 eventos, 12,1 %), Ebro (63 eventos, 11,9%) y Guadalquivir (57 eventos, 10,8 %) y Norte (54 eventos, 10,2 %) (Tabla 7) todas ellas con más del 10% de eventos sobre el total.

En los eventos superiores a 100 mm/día los meses de Enero y de Septiembre a Diciembre contribuyen con más de 400 eventos diarios (es decir más del 10 % del total). Particularmente entre los meses de Septiembre a Diciembre en las Divisiones Norte, Guadalquivir, Júcar y Pirineos Orientales se han superado los 100 eventos en al menos un mes, e igualmente en Enero en la División Norte. Valores ligeramente inferiores con 93 eventos en Noviembre aparecen en Andalucía Oriental, Febrero en la División Norte, 98 en el Júcar en Diciembre, y 84 eventos en Septiembre en la División del Ebro.

*Tabla 5. Frecuencia de eventos diarios con máximo mensual >100 mm/día por Divisiones Hidrológicas.*

Divisiones	Ene	Feb	Mar	Abr	May	Jun	Jul	Ago	Sep	Oct	Nov	Dic	Total
Norte	<b>125</b>	93	72	69	54	37	35	44	85	<b>121</b>	<b>142</b>	<b>141</b>	1018
Duero	24	22	17	12	12	9	9	8	16	24	30	23	206
Tajo	52	30	30	22	8	8	3	4	16	35	50	42	300
Guadiana	11	6	13	10	9	3	3	0	13	19	20	20	127
Guadalquivir	72	60	51	36	19	14	0	6	27	46	58	<b>101</b>	490
Andalucía Or	61	58	39	24	11	10	2	5	34	59	93	73	469
Segura	7	5	4	12	4	5	1	8	12	15	15	10	98
Júcar	54	60	65	38	38	35	9	43	<b>109</b>	<b>148</b>	<b>137</b>	98	834
Ebro	29	22	35	25	39	57	43	60	84	67	66	33	560
Pirineo Or	42	42	49	25	45	34	27	64	<b>126</b>	<b>125</b>	76	57	712
	<b>477</b>	398	375	273	239	212	132	242	522	659	687	598	4.814

En el caso de eventos superiores a 200 mm/día la frecuencia de los mismos disminuye notablemente en todas las divisiones y meses en un orden de magnitud (Tabla 6). Estos eventos se concentran de modo abrumador en el mes de Octubre (26% del total, 138 eventos), seguido de Noviembre (87 eventos) y Septiembre y Diciembre con más de 50 eventos. En cuanto a las variaciones espaciales domina la División del Júcar con 176 eventos, lo que supone más del 30% del total, destacando los meses de Octubre (57 casos) y Noviembre (34) sobre el conjunto; solamente la División de Pirineos Orientales con 30 eventos en octubre presenta valores parecidos. Con más de 10 eventos mensuales de precipitación superior a 200 mm/día en el periodo analizado solamente hemos identificado los meses de Octubre y Noviembre en la División de Andalucía Oriental, Diciembre en la del Guadalquivir, Septiembre en Pirineos Orientales, Ebro en Octubre y Noviembre y de nuevo finalmente Júcar en Febrero y Marzo.

Estas variaciones internas en cada División son importantes. Entre Septiembre y Diciembre, por lo general, se producen el 40% de los eventos con precipitaciones diarias máximas superiores a 100 mm/día de cada División. La concentración oscila en el binomio Septiembre-Octubre en las Divisiones mediterráneas y Noviembre-Diciembre en las atlánticas. El descenso en Septiembre en las cuencas de orientación atlántica se compensa relativamente en los meses de Enero a Marzo y en conjunto los tres meses iniciales del año superan el 25% de los eventos. Lo mismo ocurre en el caso de los eventos superiores a 200 mm, si bien se observa una mayor concentración en octubre en las divisiones Pirineos Orientales, Andalucía oriental, Júcar y Segura con más del 30% de los eventos anuales producidos en dicho mes.

*Tabla 6. Frecuencia de eventos diarios con máximo mensual >200 por Divisiones Hidrológicas. Se señalan valores superiores a 10.*

Divisiones	Ene	Feb	Mar	Abr	May	Jun	Jul	Ago	Sep	Oct	Nov	Dic	Total
Norte	3	3	2	4	4	2	4	5	3	9	7	8	54
Duero	3	0	0	0	1	0	1	0	0	1	1	1	8
Tajo	1	3	2	1	0	0	1	1	1	4	4	4	22
Guadiana	0	2	1	2	0	0	0	0	0	0	4	2	11
Guadalquivir	9	6	7	2	2	0	0	1	3	4	6	17	57
Andalucía Or	5	3	4	1	1	2	1	1	7	18	14	7	64
Segura	0	1	0	2	0	0	0	0	3	3	0	0	9
Júcar	5	11	11	9	4	5	0	1	25	57	34	14	176
Ebro	2	2	2	5	6	3	6	4	6	12	11	4	63
Pirineo Or	4	3	2	3	0	1	1	0	14	30	6	2	66
	32	34	31	29	18	13	14	13	62	138	87	59	530

Los resultados muestran que la frecuencia con que se producen estos eventos de precipitaciones tiene calendarios mensuales distintos en el espacio. En las cuencas orientadas al Atlántico las lluvias superiores a 100 mm se producen en los meses fríos tanto de invierno como otoño. En las divisiones mediterráneas los días de precipitación extrema y extraordinaria se concentran preferentemente entre Septiembre y Noviembre. Llama la atención la ocurrencia de eventos superiores a 100 mm/día en la cuenca del Duero en los meses de verano, si bien su número es escaso, que podrían vincularse a fenómenos convectivos por su posición interior.

### 3.3. Patrones espaciales y situaciones sinópticas asociadas

La Tabla 7 presenta el porcentaje de los eventos producidos en cada División, en función del tipo de tiempo. Las precipitaciones extremas y extraordinarias se han producido en todos los tipos de tiempo analizados, si bien cuatro situaciones aportan cada una más del 10% del total en el caso de 100 mm/día: C, E, SW y W por este orden.

*Tabla 7. Porcentaje de eventos superiores a 100 mm en cada División Hidrológica según los tipos de tiempo (periodo 1916-2015).*

Cuenca	A	C	N	NE	E	SE	S	SW	W	NW	Total
Norte	96	96	141	86	30	11	17	112	208	155	952
Duero	8	26	13	3	11	14	24	64	38	3	204
Tajo	7	28	2	2	8	15	29	115	65	11	282
Guadiana	6	21	5	3	12	17	20	20	11	5	120
Guadalquivir	16	67	18	11	37	26	21	58	155	58	467
Andalucía Oriental	12	94	5	15	88	82	37	54	52	11	450
Segura	1	7		11	49	13	4	1	3	1	90
Júcar	29	98	28	122	304	138	28	3	10	12	772
Ebro	34	104	69	79	68	23	21	33	42	63	536
Pirineos Orientales	38	203	69	101	111	49	26	37	33	26	693
Total registros	247	744	350	433	718	388	227	497	617	345	4.566
Porcentaje	5,4	16,3	7,7	9,5	15,7	8,5	5,0	10,9	13,5	7,6	100

El estudio por cuencas permite identificar en cada caso los tipos de tiempo más “eficaces”: en la División Norte cuatro situaciones aportan cada una más del 10% al total (N, SW, W y NW), en la División del Tajo las precipitaciones superiores a 100 mm se producen en el 40,8 % de los casos con el tipo SW, mientras en la División del Guadalquivir es el tipo W el dominante (más del 30%) pero con importante contribución del SW y NW; hacia el este en el Segura el tipo E es origen del 54,4 % de estos eventos, en Pirineos Orientales los tipos NE y E aportan el 30 % del total de eventos; en otros casos la concentración mensual es menor y se reparte en un mayor número de meses. La División de Andalucía Oriental aparece como un espacio de transición con importantes contribuciones de los tipos E y SE así como SW y W (pero no NW). Igualmente, en la División del Ebro se combina la contribución de tipos atlánticos (NW) y mediterráneos (NE y E). Su distribución se muestra en la Figura 3.

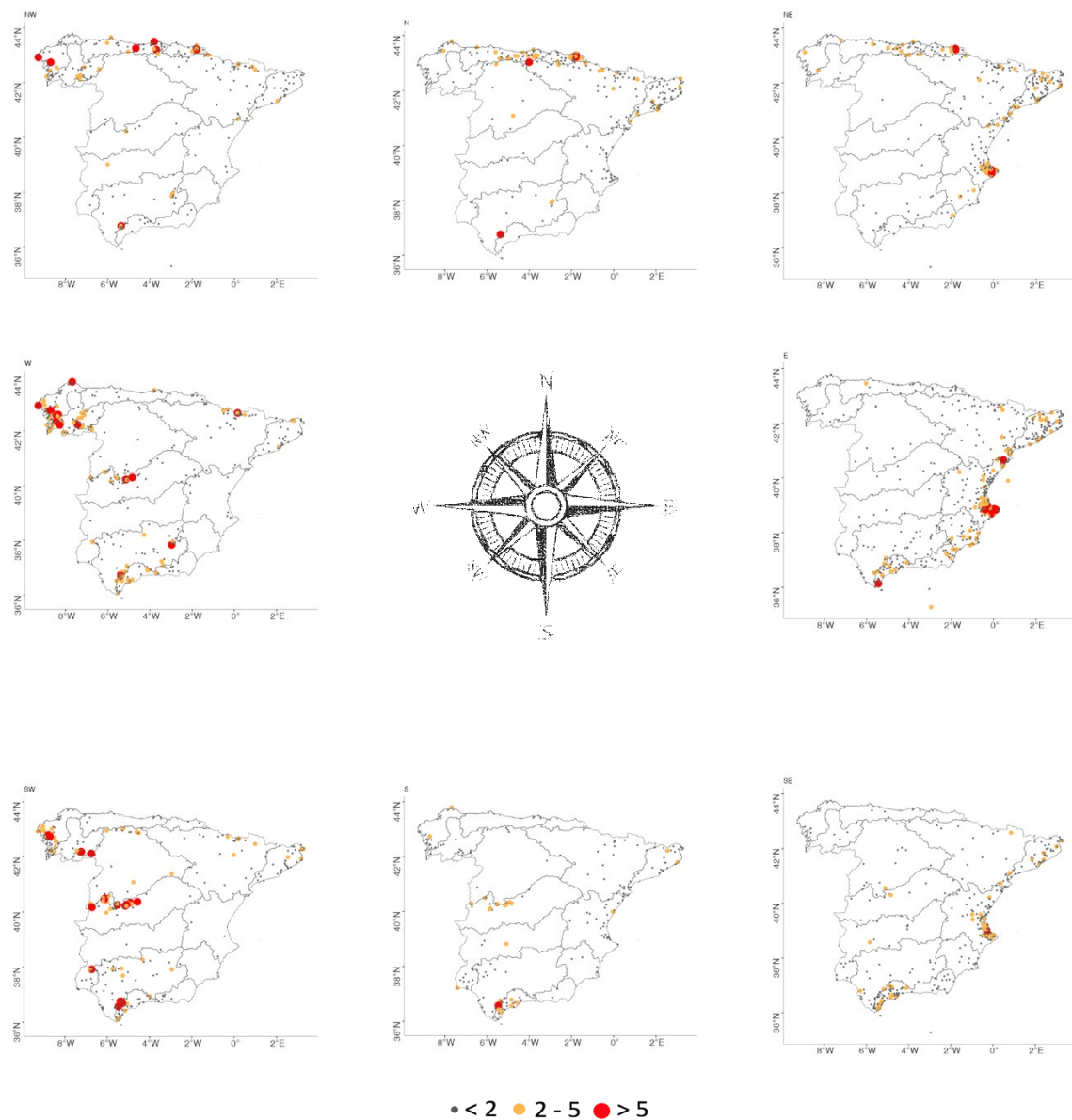
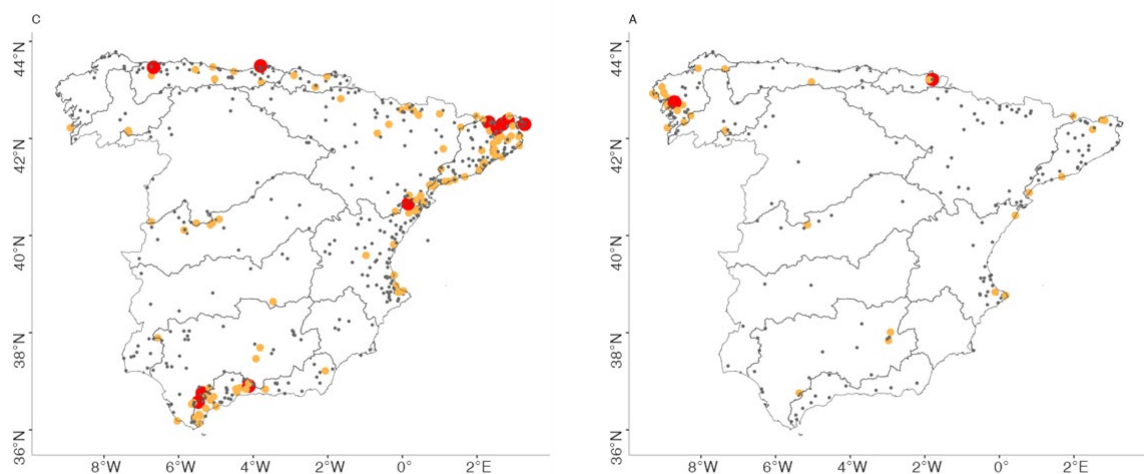


Figura 3. Distribución (frecuencia de días) del máximo mensual diario (mm) y tipos de tiempo. Número de eventos diarios en los que el observatorio fue máximo diario mensual de la red de observaciones en la fecha “n”.

La diversidad de las direcciones del viento en superficie resultante de estas situaciones sugiere que las áreas afectadas deberían ser diferentes al combinarse con las alineaciones principales de las cadenas montañosas en la península, y por ello también el reparto espacial de los eventos extremos y extraordinarios. Unido a ello, su calendario mensual es distinto, porque los tipos C y E ocurren preferentemente en los meses finales de verano y otoño, mientras que SW y W tienden a concentrarse desde mediados de otoño hasta Febrero. Algunos tipos de tiempo (E, N y NE) presentan elevadas frecuencias en primavera e incluso verano. La diferencia entre las dos vertientes peninsulares es muy clara, y así los tipos SW, W y NW afectan principalmente a las cuencas orientadas al Atlántico (Duero, Tajo, Guadiana, Guadalquivir), mientras en las divisiones mediterráneas (Segura, Júcar, Pirineos Orientales) son las advecciones del este las que predominan (Figura 3). En la división Norte los flujos de componente norte se combinan con los de procedencia oeste, y en la división Ebro, por su posición espacial, no predomina claramente ningún tipo de flujo dominante salvo el ciclónico. En la División de Andalucía Oriental por su posición de transición las advecciones Atlánticas (SW y W), y Mediterráneas (E y SE) presentan porcentajes superiores al 10 %. Finalmente, en las condiciones del tipo de tiempo Ciclónico (C) los máximos diarios producidos se distribuyen por todo el litoral norte, sur y este-sureste mientras en las condiciones Anticiclónicas (A) estos eventos son escasos y preferentemente se localizan en el litoral cantábrico (Figura 4).

En el caso de las precipitaciones superiores a 200 mm/día (Tabla 8), los eventos se concentran en tres situaciones sinópticas (E, C y SE), si bien en cada División el tipo de advección (atlántica o mediterránea) se diferencia con claridad. Así, por ejemplo, en la División del Duero y Segura se contabilizan 8 eventos, de los que 7 en el primer caso se produjeron en condiciones de flujos SW y W, y en el segundo otros siete con flujo E. En el conjunto destaca la División del Júcar con 71 eventos con flujos E, 37 en condiciones SE y finalmente 21 eventos con flujos del NE (total 81,6 % del total de la División), así como Andalucía Oriental con 16 eventos E y 13 SE (50,0 %), mientras el Guadalquivir registró 19 eventos en condiciones W (34,5 %), en condiciones NW y SW acumuló 14 (25,5 %) pero también los flujos del SE aportaron 6 eventos



*Figura 4. Distribución (frecuencia de días) del máximo mensual diario (mm) y tipos de tiempo Ciclónico y (izquierda) y Anticiclónico (derecha). Número de eventos diarios en los que el observatorio fue máximo diario mensual en la fecha “n” en la red.*

Tabla 8. Porcentaje de eventos >200 mm en cada División Hidrológica según Tipo de Tiempo (periodo 1916-2015).

Cuenca	A	C	N	NE	E	SE	S	SW	W	NW	Total
Norte	4	9	7	8	2		2	3	8	9	52
Duero						1		3	4		8
Tajo		1		1		2		<b>10</b>	3	1	18
Guadiana		4	1				2	2	1	1	11
Guadalquivir	1	5	2		4	6	4	7	<b>19</b>	7	55
Andalucía Oriental		9	3	1	<b>16</b>	<b>13</b>	4	9	2	1	58
Segura					7		1				8
Júcar	3	<b>14</b>	6	<b>21</b>	<b>71</b>	<b>37</b>	4	1		1	158
Ebro	4	<b>18</b>	6	9	3	4	3	6	5	5	53
Pirineos Orientales	3	<b>27</b>	5	4	4	6	8	1	1	2	61
Total registros	15	87	30	44	107	69	28	42	43	27	492
Porcentaje	3,0	17,7	6,1	8,9	21,7	14,0	5,7	8,5	8,7	5,5	100

### 3.4. Tendencia temporal

La evolución en el tiempo de los eventos superiores a 100 mm/día se muestra en la Figura 5. La figura incluye, de arriba abajo, el número de observatorios totales y agrupados por cuencas de vergencia oeste y este (A), el total de eventos identificados anualmente y la ratio entre el número de eventos diarios y de observatorios operativos en el total (B), ídem en las cuencas de vergencia atlántica Norte, Duero, Tajo, Guadiana y Guadalquivir, ídem en las cuencas de vergencia mediterránea de Andalucía Oriental, Segura, Júcar y Pirineos Orientales (D).

La figura permite apreciar que el número de eventos diarios máximos mensuales superiores a 100 mm no ha aumentado en el conjunto peninsular en ninguna de las dos vertientes, y que su evolución temporal está más bien ligada a la de la densidad de la red de observación. La figura muestra que cuando mayor fue número de eventos registrados, entre las décadas de los años 1960 y 1970, mayor era el número de observatorios operativos, fecha desde la que comenzaron a disminuir. Sin embargo, el número de eventos respecto al de observatorios se mantiene estable en un porcentaje en torno al 1% en la vertiente atlántica, y más variable y en torno al 2% en la mediterránea. Dado que el número de observatorios operativos desde 1950 hasta el presente supera los 2.500 en el conjunto peninsular, cabe pensar que en las décadas recientes la detección de un evento con más de 100 mm se realiza con precisión y por tanto la ausencia de tendencias observadas representa la realidad.

El promedio anual de 30/40 eventos en los que la precipitación supera 100 mm/día en algún observatorio es una prueba evidente de la elevada frecuencia de estos eventos en la Península. Este dato supone que anualmente se produce un evento con precipitación superior a 100 mm/día en un 10% de los días, y en el caso de más de 200 mm/día su media de 10 eventos sugiere un valor en torno al 3% de los días.

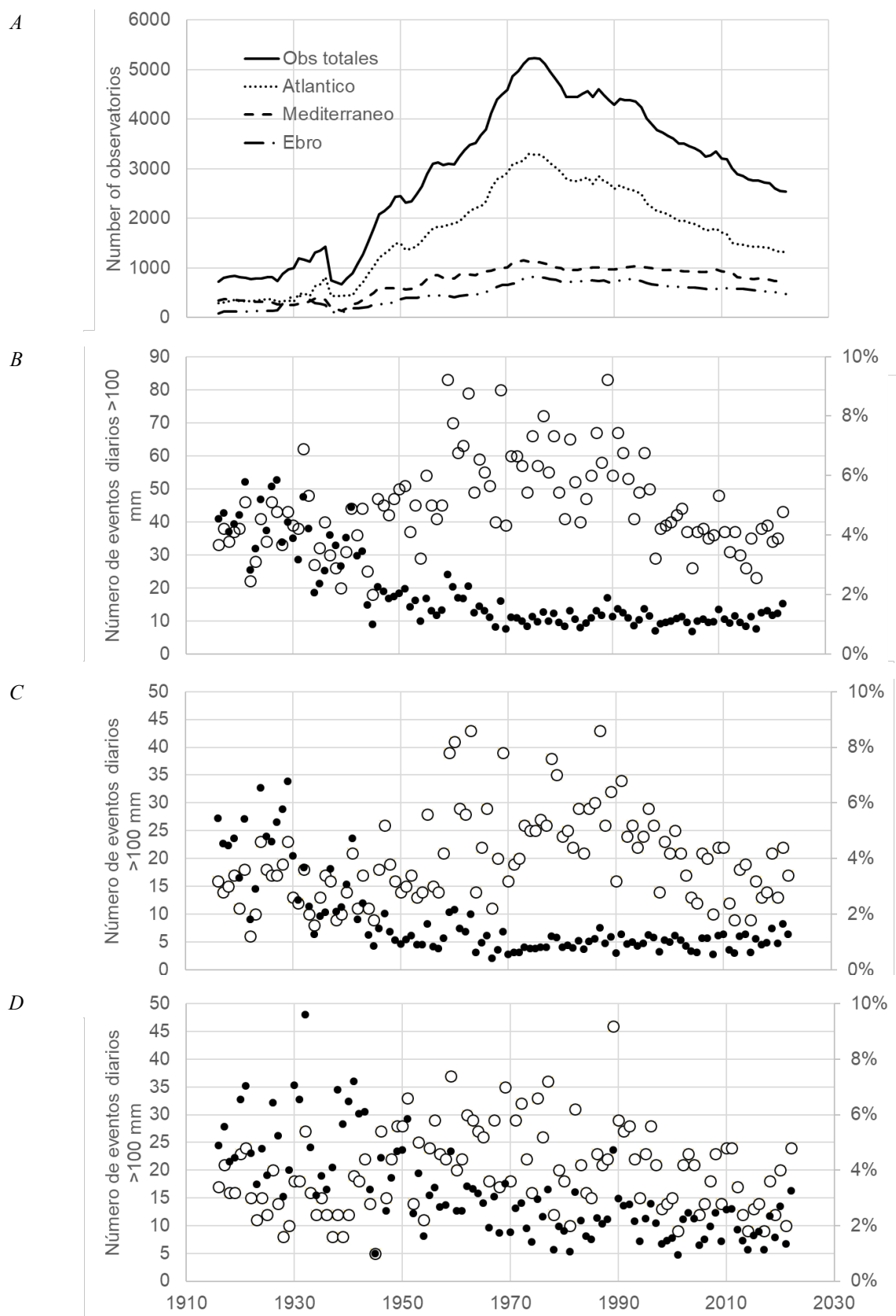


Figura 5. Número de eventos superiores a 100 mm/día. De arriba abajo (A) evolución del número de observatorios de la red nacional y cuencas Atlánticas, Mediterráneas y Ebro; (B) eventos totales >100 mm/día eventos diarios (o) y su proporción respecto a los observatorios operativos (•); (C) ídem en las cuencas Atlánticas (1, 2, 3, 4, 5), y (D) ídem cuencas mediterráneas (6, 7, 8, 0)

#### 4. Discusión

El análisis de las precipitaciones extraordinarias en el territorio de España peninsular muestra que los registros superiores a 100 mm/día son un fenómeno recurrente que ha quedado registrado desde el inicio de la red meteorológica con una elevada frecuencia. Estas precipitaciones generalmente se producen en los meses de otoño e invierno y tienen patrones espaciales reconocibles ligados a situaciones meteorológicas claramente definidas y diferentes según las áreas afectadas, con clara preferencia a una localización de costa.

Por su posición latitudinal entre dos masas de agua contrastadas (el Atlántico y el Mediterráneo), la Península Ibérica recibe en sus márgenes occidental y oriental diferentes influencias que originan una gran variedad de regímenes pluviales cuyo reparto espacial está afectado por la distribución del relieve (de Luis *et al.*, 2010; Gonzalez-Hidalgo *et al.*, 2022). Estas direcciones dominantes del relieve condicionan la penetración o no de los flujos y la extensión de sus efectos durante las distintas situaciones atmosféricas. De este modo, las advecciones atlánticas desde el oeste son capaces de producir eventos de precipitaciones cuantiosas superiores a 100 mm/día en el interior peninsular, sobre todo si se combinan localmente con estribaciones montañosas como ocurre en el Sistema Central, lo que explica la elevada frecuencia de registros centenarios de algunos observatorios de las provincias de Ávila y Salamanca. Por el contrario, los eventos vinculados a las advecciones mediterráneas del este producen sus máximos siempre en la franja costera, porque en este caso la alineación del relieve es paralela a la línea de costa e impide que sus efectos penetren hacia el interior. La misma situación ocurre en la fachada norte, donde las advecciones atlánticas, sobre todo de componente NW y N, limitan su área de influencia a la línea de costa por el efecto de barrera de las montañas cantábricas. Un hecho notable es que las precipitaciones superiores a 200 mm/día no llegan a producirse en las áreas del interior y siempre se localizan en las cercanías de la costa ligadas a las barreras transversales de advecciones marítimas principalmente de condiciones E, en la costa mediterránea, y SW en el extremo suroccidental peninsular.

El diferente origen de las advecciones explica también las variaciones mensuales y espaciales de estos sucesos. En general, las precipitaciones extremas y extraordinarias se concentran en los meses finales del verano y en el otoño, pero también son frecuentes los eventos invernales, cuyas variaciones espaciales parecen responder a las situaciones sinópticas generales y su relación con el relieve. Durante los meses fríos en invierno y primavera estos eventos de lluvias extraordinarias aparecen vinculados al paso de frentes fríos procedentes del Atlántico, en el caso de las componentes norte y oeste, y a advecciones meridionales atlánticas, con componentes SW y aire frío en altura que son determinantes especialmente en el cuadrante suroccidental. En todas ellas la distribución del relieve explica el reparto desigual en el espacio, pudiéndose identificar un patrón que podríamos denominar norte que produce eventos que no penetran al interior al ser obstaculizados por la barrera montañosa paralela a la costa. Las advecciones del oeste por su parte pueden penetrar profundamente hacia el interior, en donde el efecto del relieve puede producir situaciones de máxima frecuencia de eventos superiores a 100 mm. Finalmente, las advecciones del suroeste son canalizadas hacia el interior por el valle del Guadalquivir o penetran en el Mediterráneo atravesando el estrecho de Gibraltar, en donde el relieve alineado en paralelo a la costa de nuevo sirve de mecanismo de disparo a lo largo de la División Andalucía Oriental, mientras el relieve limita la penetración al interior de las advecciones este o noreste en la costa mediterránea (Segura, Júcar, Pirineos Orientales).

Los mecanismos que se han sugerido como origen de estas lluvias tan copiosas han sido explicados entre otros autores por Llasat (1987), Martín-Vide (1989), y Castillo-Requena (1978) y aparecen ligadas a una inestabilidad favorecida por aire frío en altura, siendo particularmente “eficaces” en la vertiente mediterránea las situaciones clasificadas como ciclónicas y advecciones del este combinadas con el relieve (Peñarrocha *et al.* 2002; Llop-Garau y Alomar-Garau 2012; Gilabert y Llasat 2018; Martín-Vide *et al.*, (2021)).

En definitiva, los eventos de precipitaciones extremas en la vertiente mediterránea española se asocian a situaciones en las que predomina la inestabilidad de condiciones ciclónicas, los flujos del este

y su combinación con el relieve que ejerce un claro efecto en los mecanismos de disparo. Por el contrario, los eventos de lluvias copiosas en la vertiente atlántica se deben más al paso de frentes o a los ramales de entrada o salida de vaguadas. El resultado final es un reparto espacial de las lluvias extraordinarias sugerido en sus líneas generales en los estudios globales de Font-Tullot (1983) y Elías-Castillo y Ruíz-Beltrán (1979), que el nuevo catálogo permite ampliar al periodo 1916-2022.

Por lo que respecta a su evolución en el tiempo, debemos recordar que en la Península Ibérica no se han detectado señales generalizadas de eventos extremos (Rodrigo and Trigo 2007), ni tampoco en el territorio portugués (Costa and Soares, 2009; Espírito Santo *et al.*, 2014; De Lima *et al.*, 2013, 2015; Santos *et al.*, 2019) ni en el territorio peninsular español (Gallego *et al.*, 2006; García *et al.*, 2007; Rodrigo, 2010; Gallego *et al.*, 2011; Merino *et al.*, 2016; Serrano-Notivoli *et al.*, 2018), si bien Espinosa *et al.* (2022) informa de un aumento de los extremos en Portugal. Los estudios más locales tampoco arrojan conclusiones definitivas, ni detectan señales (tendencias) significativas en el noreste español (Burgueño *et al.*, 2005; López-Moreno *et al.*, 2009; Beguería *et al.*, 2011; Valencia *et al.*, 2012; Vicente-Serrano *et al.*, 2017), sureste peninsular (Sánchez-Almodóvar, 2022), áreas meridionales (Hidalgo-Muñoz *et al.*, 2011; Valdés-Abellán *et al.*, 2017), y suroeste (García *et al.*, 2018), que coinciden con los resultados del presente análisis en el periodo considerado, lo que no obsta para que se puedan haber registrado en observatorios o sectores concretos. Así, se ha señalado su incremento en sectores costeros en el sur de Francia (Tramblay *et al.*, 2013; Ribes *et al.*, 2019; Blanchet *et al.*, 2021; Nouaceur *et al.*, 2022; Blanchet y Creutin, 2022), costa este de España (Romero *et al.*, 1999; Goodess y Jones, 2002; Acero *et al.*, 2011; Fernández-Montes *et al.*, 2012; Miró *et al.*, 2018, 2022), sur de Portugal (Durao *et al.*, 2010) y sectores de Marruecos (Khomssi *et al.*, 2015; Ouatiki *et al.*, 2019; Hadria *et al.*, 2019).

En todo caso, la ausencia de una señal en el tiempo de aumento o descenso de los eventos superiores a 100 o 200 mm/día no implica que otras magnitudes inferiores hayan podido variar, a la vez que debemos tener presente que muchas situaciones que terminan en catástrofes derivan de precipitaciones inferiores a los umbrales analizados en el presente estudio.

## 5. Conclusiones

- En el territorio peninsular español, entre 1916 y 2022 en el 12,4% de días se ha registrado en algún observatorio de la red meteorológica cantidades superiores a 100 mm, y en el 1,4% del tiempo se ha registrado una precipitación superior a 200 mm/día.
- El análisis de la frecuencia de observaciones y eventos diarios en las Divisiones Hidrológicas indica que es la División Norte la que ha registrado un mayor número de eventos superiores a 100 mm/día, y la del Júcar en el caso de los superiores a 200 mm/día.
- Las precipitaciones superiores a 100 mm/día se pueden producir en cualquier punto del territorio, si bien preferentemente se localizan en la orla costera. En el caso de cantidades diarias superiores a 200 mm, estas se concentran preferentemente en las provincias de Murcia-Alicante-Valencia.
- En la distribución espacial de los eventos de lluvias cuantiosas el relieve juega un papel determinante, sirviendo de barrera en la orla norte y mediterránea a las entradas de advecciones marítimas y canalizando su penetración hacia el interior desde el oeste, razón que explica registros centenarios asociados a condiciones locales siempre ligadas de nuevo al relieve. La escasez de eventos de estas magnitudes en el interior sugiere que los eventos convectivos están muy controlados por las fuentes de evaporación y por tanto no alcanzan los umbrales analizados
- En general las precipitaciones extraordinarias se producen en cuatro situaciones sinópticas bien definidas por los tipos de tiempo de la clasificación de Jenkinson y Collison, que son Ciclónico (C), Este (E), Suroeste (SW) y Oeste (W) en los eventos superiores a 100 mm/día y E, C y SE (Sureste) en los de más de 200 mm/día.

- Se detectan dos grandes áreas diferenciadas. Por un lado, las Divisiones orientadas al oeste, receptoras de influencias atlánticas (Norte, Duero, Tajo, Guadiana, Guadalquivir) y por otro las de orientación mediterránea (Segura, Júcar, Pirineos Orientales). La División Andalucía Oriental parece ser un punto de encuentro de ambas influencias, y la División del Ebro por su extensión y distribución espacial es un caso diferenciado.
- El calendario de eventos extremos y extraordinarios difiere entre ambas áreas, de manera que en las de influencia atlántica los eventos se concentran en los meses de invierno, mientras en las de influencia mediterránea tienden a concentrarse en el final de verano y otoño.

## Agradecimientos

AEMET por el acceso al BNDC y el uso del repositorio ARCIMIS. Gobierno de Aragón “E02-23R: Grupo de Investigación Geoambiente y Cambio Global”.

## Referencias

- Acero, F.J., García, J.A., Gallego, M.C. 2011. Peaks-over-. Threshold Study of Trends in Extreme Rainfall over the Iberian Peninsula. *Journal of Climate* 24, 1089-1105. <https://doi.org/10.1175/2010JCLI3627.1>
- Alpert, P., Ben-Gai, T., Baharad, A., Benjamini, Y., Yekutieli, D., Colacino, M., Diodato, L., Ramis, C., Homar, V., Romero, R., Michaelides, S., Manes, A. 2002. The paradoxical increase of Mediterranean extreme daily rainfall in spite of decrease in total values. *Geophysical Research Letters* 29 (11). <https://doi.org/10.1029/2001GL013554>
- Beguería, S., Angulo-Martínez, M., Vicente-Serrano, S.M., López-Moreno, J.I., El-Kenawy, A. 2011. Assessing trends in extreme precipitation events intensity and magnitude using non-stationary peaks-over-threshold analysis: a case study in northeast Spain from 1930 to 2006. *International Journal of Climatology* 31, 2102-2114. <https://doi.org/10.1002/joc.2218>
- Benabdoulahab, T., Gadouali, F., Boudhar, A., Lebrini, Y., Hadria, R., Salhi, A. 2020. Analysis. and trends of rainfall amounts and extreme events in the Western Mediterranean region. *Theoretical and Applied Climatology* 141, 309-320. <https://doi.org/10.1007/s00704-020-03205-4>
- Beneto, P., Khodayar, S. 2023. On. the need for improved knowledge on the regional-to-local precipitation variability in eastern Spain under climate change. *Atmospheric Research* 290, 106795. <https://doi.org/10.1016/j.atmosres.2023.106795>
- Blanchet, J., Blanc, A., Creutin, J.D. 2021. Explaining. recent trends in extreme precipitation in the Southwestern Alps by changes in atmospheric influences. *Weather and Climate Extremes* 33, 100356. <https://doi.org/10.1016/j.wace.2021.100356>
- Blanchet, J., Creutin, J.D. 2022. Instrumental. agreement and retrospective analysis of trends in precipitation extremes in the French Mediterranean Region. *Environmental Research Letters* 17, 17 074011. <https://doi.org/10.1088/1748-9326/ac7734>
- Burgueño, A., Martínez, M.D., Lana, X., Serra, C. 2005. Statistical distributions of the daily rainfall regime in Catalonia (Northeastern Spain) for the years 1950-2000. *International Journal of Climatology* 25, 1381-1403. <https://doi.org/10.1002/joc.1197>
- Castillo-Requena, C.S. 1978. Estudio. sobre el comportamiento de la gota de aire frío y la distribución de sus consecuencias pluviométricas en la España Peninsular. *Rev. Paralelo* 37, 57-80. <https://dialnet.unirioja.es/descarga/articulo/1381076.pdf>
- Claro, A.M., Fonseca, A., Fraga, H., Santos, A.S. 2023. Susceptibility. of Iberia to Extreme Precipitation and Aridity: A New High-Resolution Analysis over an Extended Historical Period. *Water* 15, 3840. <https://doi.org/10.3390/w15213840>
- Consorcio de Seguros. 2021 y 2023. *Revista digital*, 14. <https://www.consorsegurosdigital.com/es/numero-14/portada/analisis-de-los-danos-por-inundacion-en-espana-a-nivel-municipal>

- Cordobilla, M.J., Martín Vide, J. 2018. Patrones. sinópticos de precipitaciones torrenciales en la cuenca del río Muga (NE de España) en el área del Mediterráneo occidental y su evolución temporal. En Montávez Gómez, J.P. *et al.* (eds.). *El clima: aire, agua, tierra y fuego*, 199-208. Madrid: Asociación Española de Climatología; Agencia Estatal de Meteorología. <https://aeclim.org/wp-content/uploads/2019/07/199-CORDOBILLA.pdf>
- Cortesi, N., Peña-Angulo, D. 2024. *WETYDAS: Weather Types Dataset in Spanish mainland, v.2.0.0*. [Dataset]. <https://doi.org/10.20350/digitalCSIC/16333>
- Costa, A. C., Soares, A. 2009. Trends. in extreme precipitation indices derived from a daily rainfall database for the South of Portugal. *International Journal of Climatology* 29, 1956-1975. <https://doi.org/10.1002/joc.1834>
- de Lima, M.I., Santo, F.E., Ramos, A.M., Trigo, R.M. 2015. Trends. and correlations in annual extreme precipitation indices for mainland Portugal, 1941-2007. *Theoretical and Applied Climatology* 119, 55-75. <https://doi.org/10.1007/s00704-013-1079-6>
- de Lima, M.I., Santo, F.E., Ramos, A., de Lima, J.L.M.P. 2013. Recent changes in daily precipitation and surface air temperature extremes in mainland Portugal, in the period 1941-2007. *Atmospheric Research* 127, 195-209. <http://doi.org/10.1016/j.atmosres.2012.10.001>
- de Luis, M., Brunetti, M., González-Hidalgo, J.C., Longares, L.A., Martín-Vide, J. 2010. Changes. in seasonal precipitation in the Iberian Peninsula during 1946-2005. *Global Planetary Changes* 74, 27-33. <https://doi.org/10.1016/j.gloplacha.2010.06.006>
- Donat, M.G., Peterson, T.C., Brunet, M., King, A.D., Almazroui, M., Kolli, R.K., Boucherf, D., Al-Mulla, A.Y., Nour, A.Y., Aly, A.A., Nada, T.A.A., Semawi, M.M., Al Dashti, H.A., Salhab, T.G., El Fadli, K.I., Muftah, M.K., Dah Eida, S., Badi, W., Driouech, F., ..., Al Shekaili, M.N. 2014. Changes. in extreme temperature and precipitation in the Arab region: long-term trends and variability related to ENSO and NAO. *International Journal of Climatology* 34, 581-592. <https://doi.org/10.1002/joc.3707>
- Durão, R.M., Pereira, M.J., Costa, A.C., Delgado, J., del Barrio, G., Soares, A. 2010. Spatial-temporal. dynamics of precipitation extremes in southern Portugal: a geostatistical assessment study. *International Journal of Climatology* 30, 1526-1537. <https://doi.org/10.1002/joc.1999>
- Elías-Castillo, F., Ruiz-Beltrán, L. 1979. *Precipitaciones máximas en España*. Servicio de Publicaciones Agrarias, Ministerio de Agricultura, Madrid, 545 p.
- Espinosa, L.A., Portela, M.M., Mato, J.P., Gharbia, S. 2022. Climate. Change Trends in a European Coastal Metropolitan Area: Rainfall, Temperature, and Extreme Events (1864-2021). *Atmosphere* 13 (12), 1995. <https://doi.org/10.3390/atmos13121995>
- Espírito Santo, F., Ramos, A.M., de Lima, M.I.P., Trigo, R.M. 2014. Seasonal. changes in daily precipitation extremes in mainland Portugal from 1941 to 2007. *Regional Environmental Change* 14, 1765-1788. <https://doi.org/10.1007/s10113-013-0515-6>
- Fernández-Granja, J.A., Brands, S., Bedia, J., Casanueva, A., Fernández, J. 2023. Exploring. the limits of the Jenkinson-Collison weather types classification scheme: a global assessment based on various reanalyses. *Climate Dynamics* 61, 1829-1845. <https://doi.org/10.1007/s00382-022-06658-7>
- Fernández-Montes, S., Subert, S., Rodigo, F.S., Hertig, E. 2012. Wintertime. circulation types over the Iberian Peninsula: long-term variability and relationships with weather extremes. *Climate Research* 53, 205-227. <https://doi.org/10.3354/cr01095>
- Font-Tullot, I. 1983. *Climatología de España y Portugal*. Servicio de publicaciones del Instituto Nacional de Meteorología, 422 p. ISBN: 978-84-5009-467-4. New edition in 2000.
- Gallego, M.C., García, J.A., Vaquero, J. M., Mateos, V.L. 2006. Changes. in frequency and intensity of daily precipitation over the Iberian Peninsula. *Journal of Geophysical Research* 111, D24105. <https://doi.org/10.1029/2006JD007280>
- Gallego, M. C., Trigo, R.M., Vaquero, J. M., Brunet, M., García, J. A., Sigró, J., Valente, M.A. 2011. Trends. in frequency indices of daily precipitation over the Iberian Peninsula during the last century. *Journal Geophysical Research* 116, D02109. <https://doi.org/10.1029/2010JD014255>

- García, J., Gallego, M.C., Serrano, A., Vaquero, J.M. 2007. Trends. in block-seasonal extreme rainfall over the Iberian Peninsula in the second half of the twentieth century. *Journal of Climate* 20, 113-130. <https://doi.org/10.1175/JCLI3995.1>
- García, J.A., Acero, F.J., Portero, J.A. 2018. Bayesian. hierarchical spatio-temporal model for extreme temperatures in Extremadura (Spain) simulated by a Regional Climate Model. *Climate Dynamics* 61, 1489-1503. <https://doi.org/10.1007/s00382-022-06638-x>
- Gilabert, J., Llasat, M.C. 2018. Circulation. weather types associated with extreme flood events in Northwestern Mediterranean. *International Journal Climatology* 38, 1864-1876. <https://doi.org/10.1002/joc.5301>
- Gonzalez-Hidalgo, J.C., Beguería, S., Peña-Angulo, D., Trullenque, V. 2025. Catalogue and analysis of extraordinary precipitation events in the Spanish mainland, 1916-2022. *International Journal of Climatology*, e8785. <https://doi.org/10.1002/joc.8785>
- González-Hidalgo, J.C., Beguería, S., Peña-Angulo, D., Trullenque-Blanco, V. 2022. MOPREDAS\_Century. database and precipitation trends in mainland Spain, 1916-2020. *International Journal of Climatology* 43, 3828-3840. <https://doi.org/10.1002/joc.8060>
- González-Hidalgo, J.C., Peña-Angulo, D., Beguería, S., Trullenque Blanco, V. 2024. *Summaries of meteorological observations from the Spanish Meteorological Service, v.2.0.0.* [Dataset]. <https://doi.org/10.20350/digitalCSIC/16516>
- Goodess, C.M., Jones, P.D. 2002. Links. between circulation and changes in the characteristics of Iberian rainfall. *International Journal of Climatology* 22, 1593-1615. <https://doi.org/10.1002/joc.810>
- Hadria, R., Boudhar, A., Ouatiki, H., Lebrini, Y., Elmansouri, L., Gadouali, F., Lionbou H.L.H., Benabdellahab, T. 2019. Combining. use of TRMMand ground observationsof annual precipitations for meteorological drought trends monitoring in Morocco. *American Journal of Remote Sensing* 7, 25-34. <https://doi.org/10.11648/j.ajrs.20190702.11>
- Hidalgo-Muñoz, J.M., Argüeso, D., Gámiz-Fortis, S.R., Esteban-Parra, M.J., Castro-Díez, Y. 2011. Trends of extreme precipitation and associated synoptic patterns over the southern Iberian Peninsula. *Journal of Hydrology* 409, 497-511. <https://doi.org/10.1016/j.jhydrol.2011.08.049>
- Insua-Costa, D., Lemus-Cánovas, M., Miguez-Macho, G., Llasat, M.C. 2021. Climatology. and ranking of hazardous precipitation events in the western Mediterranean area. *Atmospheric Research* 255, 105521. <https://doi.org/10.1016/j.atmosres.2021.105521>
- Jenkinson, A.F., Collison, F.P. 1977. *An. initial climatology of gales over the North Sea*, Synoptic Climatology Branch Memorandum, No. 62. Meteorological Office, Bracknell.
- Karagiannidis, A.F., Karacostas, T., Maher, P., Makrogiannis, T. 2012. Climatological. aspects of extreme precipitation in Europe, related to mid-latitude cyclonic systems. *Theoretical and Applied Climatology* 107, 165-174. <https://doi.org/10.1007/s00704-011-0474-0>
- Khomsi, K., Mahe, G., Tramblay, Y., Sinan, M., Snoussi, M. 2015. Trends. in rainfall and temperature extremes in Morocco. *Natural Hazards Earth System Sciences* 16, 1079-1090. <https://doi.org/10.5194/nhess-16-1079-2016>
- Kostopoulou, E., Jones, P. 2005. Assessment. of climate extremes in the Eastern Mediterranean. *Meteorology and Atmospheric Physics* 89, 69-85. <https://doi.org/10.1007/s00703-005-0122-2>
- Lemus-Canovas, M., Lopez-Bustins, J.A., Martín-Vide, J., Halifa-Marin, A., Insua-Costa, D., Martinez-Artigas, J., Traper, L., Serrano-Notivoli, R., Cuadrat, J.M. 2021. Characterisation. of Extreme Precipitation Events in the Pyrenees: From the Local to the Synoptic Scale. *Atmosphere* 12, 665. <https://doi.org/10.3390/atmos12060665>
- Llasat, M.C. 1987. *Episodios de lluvias copiosas en Catalunya: génesis, evolución y factores coadyuvantes*. PhD, Universidad de Barcelona. <http://www.tdx.cat/TDX-0426110-132107>
- Llop-Garau, J.L., Alomar-Garau, G.A. 2012a. Clasificación sinóptica automática de Jenkinson y Collison para los días de precipitación mayor o igual a 200 mm en la isla de Mallorca. *Territoris* 8, 143-152. <https://raco.cat/index.php/Territoris/article/view/259933/347140>

- Llop-Garau, J.L., Alomar-Garau, G.A. 2012b. Clasificación sinóptica automática de Jenkinson y Collison para los días de precipitación mayor o igual a 100 mm en la franja litoral catalana e islas baleares. En Rodríguez Puebla, C. *et al.* (Coords.) *Cambio climático. Extremos e impactos*, 449-458. ISBN 978-84-695-4331-3. <https://dialnet.unirioja.es/servlet/articulo?codigo=7336466>
- Lázaro, R., Rodrigo, F.S., Gutiérrez, L., Domingo, F., Puigdefábregas, J. 2001. Analysis. of a 30-year rainfall record (1967-1997) in semi-arid SE Spain for implications on vegetation. *Journal of Arid Environments* 48, 373-395. <https://doi.org/10.1006/jare.2000.0755>
- López-Bermúdez, F., Romero, M.A. 1993. Génesis. y consecuencias erosivas de las lluvias de alta intensidad en la región mediterránea. *Cuadernos de Investigación Geográfica* 18-19. 7-28. <https://doi.org/10.18172/cig.1000>
- López-Bustins, J.A., Arbiol-Roca, L., Martin-Vide, J., Barrera-Escoda, A., Prohom, M. 2020. Intra-annual variability of the Western Mediterranean Oscillation (WeMO) and occurrence of extreme torrential precipitation in Catalonia (NE Iberia). *Natural Hazards Earth Systems Science* 20, 2483-2501. <https://doi.org/10.5194/nhess-20-2483-2020>
- López-Moreno, J.I., Vicente-Serrano, S.M., Angulo-Martínez, M., Beguería, S., Kenawy, A. 2009. Trends. in daily precipitation on the northeastern Iberian Peninsula. *International Journal of Climatology* 30, 1026-1041. <https://doi.org/10.1002/joc.1945>
- Marani, L., Parisi, S.G. 2014. Extreme. rainfall in the Mediterranean Basn. En N. Diodato and G. Bellochi (Eds). Storminess and environmental change. *Advances in Natural and Technological Hazards Research* 39, 17-36. [https://doi.org/10.1007/978-94-007-7948-8\\_2](https://doi.org/10.1007/978-94-007-7948-8_2)
- Martín-Vide, J., Moreno-García, M.C., Lopez-Bustins, J.A. 2021. Synoptic. causes of torrential rainfall in south-eastern Spain (1941-2017). *Cuadernos de Investigación Geográfica* 47, 143-162. <https://doi.org/10.18172/cig.4696>
- Martín-Vide, J. 1989. Precipitaciones. torrenciales en España. *Rev. Norba de Geografía* 6, 63-70. <https://dialnet.unirioja.es/descarga/articulo/109702.pdf>
- Martín-Vide, J. 1994. Precipitacions:. maxims diaris probables i irregularitat. En Pérez Cueva, A. (ed.) *Atlas climàtic de la Comunitat Valenciana (1961-1990)*, 94-96. Generalitat Valenciana, Conselleria d'Obres Públiques, Urbanisme i Transports.
- Martín-Vide, J., Sánchez-Lorenzo, A., Raso-Nadal, J.M., López-Bustins, J.A., Cordobilla, M.J., Peña, J.C., Peña, J.C., Soler, X., Prohom, M., García Manuel, A., Cernocky, T. 2008. Catálogo de patrones sinópticos asociados a precipitaciones torrenciales en Cataluña. En Estrella, M. J. (Coord), *Riesgos climáticos y cambio global en el Mediterráneo español*, 39-56. ISBN 978-84-95484-88-8.
- Mathbou, S., Lopez-Bustins, J. A., Royé, D., Martin-Vide, J., Bech, J., Rodrigo, F.S. 2017. Observed. changes in daily precipitation extremes at annual timescale over the Eastern Mediterranean during 1961-2012. *Pure Applied Geophysics* 175, 3875-3890. <https://doi.org/10.1007/s00024-017-1695-7>
- Merino, A., Fernández-Vaquero, M., Lopez, L., Fernández-González, S., Hermida, L., Sánchez, J.L., García-Ortega, E., Gascón, E. 2016. Large-scale. patterns of daily precipitation extremes on the Iberian Peninsula. *International Journal of Climatology* 36, 3873-3891. <https://doi.org/10.1002/joc.4601>
- Meseguer-Ruiz, O., Osborn, T.J., Sarricolea, P., Jones, P.D., Olcina Cantos, J., Serrano-Notivoli, R., Martin-Vide, J. 2018. Definition. of a temporal distribution index for high temporal resolution precipitation data over Peninsular Spain and the Balearic Islands: the fractal dimension; and its synoptic implications. *Climate Dynamics* 52, 439-456. <https://doi.org/10.1007/s00382-018-4159-6>
- Miró, J.J., Estrela, M.J., Caselles, V., Gómez, I. 2018. Spatial. and temporal rainfall changes in the Júcar and Segura basins (1955-2016): Fine-scale trends. *International Journal of Climatology* 38, 4699-4722. <https://doi.org/10.1002/joc.5689>
- Miró, J.J., Lemus-Canovas, M., Serrano-Notivoli, S., Olcina Cantos, J., Estrela, M.J., Martin-Vide, J., Sarricolea, P., Meseguer-Ruiz, O. 2022. A. component-based approximation for trend detection of intense rainfall in the Spanish Mediterranean coast. *Weather and Climate Extremes* 38, 100513. <https://doi.org/10.1016/j.wace.2022.100513>

- Norrant, C., Douguedroit, A. 2006. Monthly and daily precipitation trends in the Mediterranean (1950-2000). *Theoretical and Applied Climatology* 83, 89-106. <https://doi.org/10.1007/s00704-005-0163-y>
- Nouaceur, Z., Murarescu, O., Muratoreanu, G. 2022. Statistical Analysis of Heavy Rains and Floods around the French Mediterranean Basin over One Half a Century of Observations. *Geosciences* 12, 447. <https://doi.org/10.3390/geosciences12120447>
- Olcina, J. 1994a. *Tormentas y granizadas en las tierras alicantinas*. Alicante, Editorial Universidad de Alicante, 317 p. <http://hdl.handle.net/10045/22610>
- Olcina, J. 1994b. *Riesgos climáticos en la Península Ibérica*. Madrid: Penthalon, 440 p.
- Ouatiki, H., Boudhar, A., Ouhinou, A., Arioua, A., Hssaisoune, M., Bouamri, H., Benabdellahab, T. 2019. Trend analysis of rainfall and drought over the Oum Er-Rbia River Basin in Morocco during 1970-2010. *Arabian Journal of Geosciences* 12, 128. <https://doi.org/10.1007/s12517-019-4300-9>
- Peñarrocha, D., Estrela, M.J., Millán, M. 2002. Classification of daily rainfall patterns in a Mediterranean area with extreme intensity levels: The Valencia region. *International Journal of Climatology* 22, 677-695. <https://doi.org/10.1002/joc.747>
- Pino, D., Ruiz-Bellet, J.L., Balasch, J. C., Romero-León, L., Tusset, J., Barriendos, M., Mazon, J., Castelltort, X. 2016. Meteorological and hydrological analysis of major floods in NE Iberian Peninsula. *Journal of Hydrology* 541 Part A, 63-89. <https://doi.org/10.1016/j.jhydrol.2016.02.008>
- Poesen, J., Hooke, J. 1997. Erosion flooding and channel management in Mediterranean environments of southern Europe. *Progress in Physical Geography* 21, 157-199. <https://doi.org/10.1177/03091339702100201>
- Pérez-Cueva, A. 1983. Precipitaciones extraordinarias en España peninsular. *Agricultura y Sociedad* 28, 189-203. <http://hdl.handle.net/10045/22610>
- Queralt, S., Hernández, E., Barriopedro, D., Gallego, D., Ribera, P., Casanova, C. 2009. North Atlantic Oscillation influence and weather types associated with winter total and extreme precipitation events in Spain. *Atmospheric Research* 94, 675-683. <https://doi.org/10.1016/j.atmosres.2009.09.005>
- Ribes, A., Thao, S., Vautard, R., Dubuisson, B., Somot, S., Colin, J., Planton, S., Soubeyroux, J.-M. 2019. Observed increase in extreme daily rainfall in the French Mediterranean. *Climate Dynamics* 52, 1095-1114. <https://doi.org/10.1007/s00382-018-4179-2>
- Rodrigo, F. S., Trigo, R. M. 2007. Trends in daily rainfall in the Iberian Peninsula from 1951-2002. *International Journal of Climatology* 27, 513-529. <https://doi.org/10.1002/joc.1409>
- Rodrigo, F.S. 2010. Changes in the probability of extreme daily precipitation observed from 1951 to 2002 in the Iberian Peninsula. *Int. J. Climatol.* 30(10), 1512-1525. <https://doi.org/10.1002/joc.1987>
- Romero, R., Sumner, G., Ramis, C., Genovés, A. 1999. A classification of the atmospheric circulation patterns producing significant daily rainfall in the Spanish Mediterranean area. *International Journal of Climatology* 19, 765-785. [https://doi.org/10.1002/\(SICI\)1097-0088\(19990615\)19:7<765::AID-JOC388>3.0.CO;2-T](https://doi.org/10.1002/(SICI)1097-0088(19990615)19:7<765::AID-JOC388>3.0.CO;2-T)
- Salhi, A., Benabdellahab, S., Martin-Vide, J. 2022. Statistical analysis of long-term precipitation in the Maghreb reveals significant changes in timing and intensity. *Theoretical and Applied Climatology* 150, 1369-1384. <https://doi.org/10.1007/s00704-022-04236-9>
- Santos, M., Fonseca, A., Fragoso, M., Santos, J.A. 2019. Recent and future changes of precipitation extremes in mainland Portugal. *Theoretical and Applied Climatology* 137, 1305-1319. <https://doi.org/10.1007/s00704-018-2667-2>
- Serrano-Notivoli, R., Beguería, S., Saz, M. A., de Luis, M. 2018. Recent trends reveal decreasing intensity of daily precipitation in Spain. *International Journal of Climatology* 38, 4211-4224. <https://doi.org/10.1002/joc.5562>
- Sillero-Medina, J.A., Molina-Luque, J., Ruiz-Sinoga, J.D. 2022. Dinámica de la precipitación torrencial en el sur de España. In Martí-Espeleta, A. et al. (Eds.). Retos del cambio climático: impactos, mitigación y adaptación, 643-652. Asociación Española de Climatología. <http://hdl.handle.net/20.500.11765/14110>
- Slivinski, L.C., Compo, Gilbert P., Whitaker, J.S., Sardeshmukh, P.D., Giese, B.S., McColl, C., Allan, R., Yin, X., Vose, R., Titchner, H., Kennedy, J., Spencer, L.J., Ashcroft, L., Brönnimann, S., Brunet, M., Camuffo,

- D., Cornes, R., Cram, T. A., Crouthamel, R., ..., Wyszyński, P. 2019. Towards. a more reliable historical reanalysis: improvements for version 3 of the Twentieth Century Reanalysis system. *Quarterly Journal of the Royal Meteorological Society*, 145, 2876-2908. <https://doi.org/10.1002/qj.3598>
- Sánchez-Almodóvar, E., Martín-Vide, J., Olcina-Cantos, J., Lemus-Canovas, M. 2022. Are atmospheric situations now more favourable for heavy rainfall in the Spanish Mediterranean? Analysis of episodes in the Alicante Province (1981-2020). *Atmosphere* 13, 1410. <https://doi.org/10.3390/atmos13091410>
- Toreti, A., Giannakaki, P., Martius, O. 2016. Precipitation extremes in the Mediterranean region and associated upper-level synoptic-scale flow structures. *Climate Dynamics* 47, 1925-1941. <https://doi.org/10.1007/s00382-015-2942-1>
- Toreti, A., Xoplaki, E., Maraun, D., Kuglitsch, F.G., Wanner, H., Luterbacher, J. 2010. Characterisation. of extreme winter precipitation in Mediterranean coastal sites and associated anomalous atmospheric circulation patterns. *Natural Hazards Earth Systems Science* 10, 1037-1050. <https://doi.org/10.5194/nhess-10-1037-2010>
- Tramblay, Y., El Adlouni, S., Servat, E. 2013a. Trends and variability in extreme precipitation indices over Maghreb countries. *Natural Hazards Earth Systems Science* 13, 3235-3248. <https://doi.org/10.5194/nhess-13-3235-2013>
- Tramblay, Y., Neppel, L., Carreau, J., Najib, K. 2013b. Non-stationary frequency analysis of heavy rainfall events in southern France. *Hydrological Sciences Journal*, 58, 280-294. <https://doi.org/10.1080/02626667.2012.754988>
- Trigo, R.M., DaCamara, C. 2000. Circulation. weather types and their influence on the precipitation regime in Portugal. *International Journal Climatology* 20, 1559-1581. [https://doi.org/10.1002/1097-0088\(20001115\)20:13<1559::aid-joc.4984>3.0.co;2-1](https://doi.org/10.1002/1097-0088(20001115)20:13<1559::aid-joc.4984>3.0.co;2-1)
- Valdés-Abellán, J., Pardo, M., Tenza-Abril, A. 2017. Observed. precipitation trend changes in the western Mediterranean region. *International Journal of Climatology* 37, 1285-1296. <https://doi.org/10.1002/joc.4984>
- Valencia, J.L., Tarquis, A. M., Saá-Requejo, A., Gascó, J.M. 2012. Change. of extreme rainfall indexes at Ebro River Basin, *Natural Hazards Earth Systems Science*, 12, 2127-2137. <https://doi.org/10.5194/nhess-12-2127-2012>
- Vicente-Serrano, S.M., Zabalza, J., Borràs, G., López-Moreno, J.I., Pla, E., Pascual, D., Savé, R., Biel, C., Funes, I., Azorin-Molina, C., Sanchez-Lorenzo, A., Martín-Hernández, N., Peña-Gallardo, M., Alonso-González, E., Tomas-Burguera, M., El Kenawy. A. 2017. Extreme. hydrological events and the influence of reservoirs in a highly regulated river basin of northeastern Spain. *Journal of Hydrological Regional Studies* 12, 13-32. <https://doi.org/10.1016/j.ejrh.2017.01.004>
- Zhang, X., Aguilar, E., Sensoy, S., Melkonyan, H., Tagiyeva, U., Ahmed, N., Kutaladze, N., Rahimzadeh, F., Taghipour, A., Hantosh, T. H., Albert, P., Semawi, M., Ali, M. K., Al-Shabibi, M. H. S., Al-Oulan, Z., Zatari, T., Khelet, I. D., Hamoud, S., Sagir, R., ..., Wallis, T. 2005. Trends in Middle East climate extreme indices from 1950. to. 2003. *Journal Geophysical Research* 110, D22104. <https://doi:10.1029/2005JD006181>
- Zittis, G. 2018. Observed. rainfall trends and precipitation uncertainty in the vicinity of the Mediterranean, Middle East and North Africa. *Theoretical Applied Climatology* 134, 1207-1230. <https://doi.org/10.1007/s00704-017-2333-0>



# ANÁLISIS ESPECTRAL ESPACIO-TEMPORAL DE HUMEDALES DE ALTA MONTAÑA Y SU RELACIÓN CON LA VARIABILIDAD CLIMÁTICA

CAROLINA CALVI<sup>1\*</sup>, EDOARDO MELENDI<sup>2</sup>, ELEONORA CAROL<sup>2</sup>

<sup>1</sup>*Instituto de Geocronología y Geología Isotópica (INGEIS-UBA-CONICET), Intendente Guiraldes 2160, Ciudad Universitaria, Pabellón INGEIS, C1428EGA, Ciudad Autónoma de Buenos Aires, Argentina.*

<sup>2</sup>*Centro de Investigaciones Geológicas (CIG-UNLP-CONICET), Diagonal 113 y 64, B1900 La Plata, Provincia de Buenos Aires, Argentina.*

**RESUMEN.** Los humedales de alta montaña de los Andes de Sudamérica son ecosistemas únicos, caracterizados por su hiperhumedad y su estrecha conexión con descargas de agua subterránea o deshielo. Estos ambientes presentan aguas relativamente estancadas o con poca circulación, favoreciendo la proliferación de vegetación que puede ser monitoreada a través de imágenes satelitales. El objetivo de este trabajo es analizar, mediante el uso de sensores remotos, la variación espacio-temporal asociada a los ciclos climáticos en dos humedales altoandinos de ambientes áridos, cuyas condiciones de acceso y de trabajo son limitadas. Para lograrlo, se tomaron dos casos de estudio, uno vinculado a humedales asociado a la descarga de agua subterránea, y otro, sustentado también por cursos fluviales con aportes de la lluvia y del deshielo. La variación espacial se la vinculó con los ciclos climáticos, para lo cual se calcularon los índices espectrales Índice de Vegetación de Diferencia Normalizada (NDVI) e Índice de Agua de Diferencia Normalizada (NDWI) en años representativos, seleccionados según los índices climáticos Índice de Precipitación Evapotranspiración Estandarizado (SPEI) para periodo secos y húmedos e Índice Niño Oceánico (ONI), y datos de estaciones meteorológicas disponibles para el periodo 1980-2022. Los resultados evidenciaron que existe una variación en la extensión de los humedales entre períodos El Niño y La Niña. En los períodos húmedos (El Niño) los humedales presentan las mayores extensiones, mientras que en los secos (La Niña) se ha cuantificado una reducción del área de humedal cercana al 30%. Esto muestra una rápida respuesta hidrológica del ambiente a los cambios climáticos, asociada a aportes de flujo subterráneo de corto recorrido. En consecuencia, es probable que, en un futuro, el impacto de los ciclos atmosféricos, intensificados por el cambio climático, genere una disminución crítica en la superficie de estos humedales. Monitorear la evolución de los humedales altoandinos en condiciones áridas es esencial para caracterizar su respuesta ante los ciclos climáticos. Extrapolar estos análisis a otros humedales en entornos similares permitirá futuras investigaciones a escalas regionales más amplias, facilitando un enfoque integral sobre su comportamiento frente a las variaciones climáticas. Comprender estos ecosistemas frágiles es clave para implementar medidas de conservación y gestión efectivas, especialmente ante la creciente presión del cambio climático global.

***Spatio-Temporal Spectral Analysis of High Mountains Wetlands and Their Relationship to Climate Variability***

**ABSTRACT.** The high-altitude wetlands of the Andes in South America are unique ecosystems, characterized by their hyper-humidity and close connection with groundwater discharge or snowmelt. These environments exhibit relatively stagnant waters or low circulation, which favors the proliferation of vegetation that can be monitored through satellite imagery. The objective of this study is to analyze, through the use of remote sensors, the spatiotemporal variation associated with climate cycles in two high-Andean wetlands located in arid environments, where access and working conditions are limited. To achieve this, two case studies were taken: one involving wetlands associated with groundwater discharge, and another supported by river courses with contributions from rainfall and snowmelt.

The areal variation was linked to climate cycles, for which the spectral indices Normalized Difference Vegetation Index (NDVI) and Normalized Difference Water Index (NDWI) were calculated for representative years, selected according to the climate indices Standardized Precipitation-Evapotranspiration Index (SPEI) for dry and wet periods, Oceanic Niño Index (ONI), and data from available meteorological stations for the period 1980-2022. The results showed a variation in the extent of the wetlands between El Niño and La Niña periods. During wet periods (El Niño), the wetlands reached their largest extents, while in dry periods (La Niña), a reduction in wetland area of approximately 30% was quantified. This indicates a rapid hydrological response of the environment to climate changes, associated with contributions from shallow groundwater flow. Consequently, it is likely that in the future, the impact of atmospheric cycles, intensified by climate change, will lead to a critical decrease in the surface area of these wetlands. Monitoring the evolution of high-Andean wetlands in arid conditions is essential to characterize their response to climate cycles. Extrapolating these analyses to other wetlands in similar environments will enable future research on a broader regional scale, facilitating a comprehensive approach to their behavior in the face of climate variations. Understanding these fragile ecosystems is key to implementing effective conservation and management measures, especially in the face of growing pressure from global climate change.

**Palabras clave:** Índice ONI, índice SPEI, índice NDVI, índice NDWI, humedales.

**Keywords:** ONI index, SPEI index, NDVI index, NDWI index, wetlands.

Recibido: 15 Octubre 2024

Aceptado: 11 Abril 2025

**\*Correspondencia:** Carolina Calvi, Instituto de Geocronología y Geología Isotópica (INGEIS-UBA-CONICET), Intendente Guiraldes 2160, Ciudad Universitaria, Pabellón INGEIS, C1428EGA, Ciudad Autónoma de Buenos Aires, Argentina. E-mail: calvi.ingeis@gmail.com

## 1. Introducción

Los humedales de alta montaña de los Andes de Sudamérica, situados en la diagonal árida, son ecosistemas únicos, caracterizados por su hiperhumedad y su estrecha conexión con descargas de agua subterránea o deshielo. Estos ambientes, caracterizados por aguas estancadas o de baja circulación, favorecen el crecimiento de vegetación densa, cuya presencia es detectable a través de imágenes satelitales. En este contexto, el sensor remoto se ha consolidado como una herramienta clave, eficiente y accesible para la identificación, evaluación y monitoreo de estos ecosistemas, siendo fundamental para comprender la dinámica de los humedales en relación con la disponibilidad hídrica y las fluctuaciones en las condiciones ambientales (Mallmann *et al.*, 2015; Gallant, 2015; Mahdavi *et al.*, 2018).

La dinámica hidrológica de los humedales de alta montaña está estrechamente vinculada a la variabilidad climática, lo que los convierte en ecosistemas altamente sensibles a los cambios en las precipitaciones, el deshielo y los eventos climáticos extremos, tales como sequías o lluvias intensas (Mejía *et al.*, 2022). Estos cambios afectan significativamente la extensión y la dinámica de los humedales, ya que modificaciones en los patrones de precipitación y deshielo pueden provocar expansiones o reducciones en su superficie, lo que influye directamente en su productividad y cobertura vegetal. En este contexto, el uso de índices climáticos, como el Índice de Precipitación Evapotranspiración Estandarizado (SPEI, por su sigla en inglés) para periodo secos y húmedos e Índice Niño Oceánico (ONI, por su sigla en inglés), junto con registros de precipitaciones locales, es esencial para identificar los patrones de variabilidad climática y comprender su influencia en estos ecosistemas. En la región de los Andes Centrales, las fases de El Niño se asocian con un aumento de las precipitaciones, incrementando los aportes hídricos subterráneos y superficiales, lo que favorece la expansión de los humedales. En contraste, las fases de La Niña tienden a generar condiciones más secas, reduciendo el aporte hídrico y disminuyendo la extensión y el vigor de la vegetación (Garreaud *et al.*,

2009; Rivera *et al.*, 2014; Peñalba y Rivera, 2016). Este enfoque integrado de la teledetección e índices climáticos proporciona un marco más preciso para el monitoreo a largo plazo de la respuesta de los humedales altoandinos ante la variabilidad climática (Meza Aliaga y Díaz Villalobos, 2020; Mejía *et al.*, 2022).

A pesar de la creciente cantidad de estudios sobre la variabilidad de estos ecosistemas, aún existe una falta de información detallada sobre la dinámica espacio-temporal de los humedales altoandinos en regiones menos exploradas. Estos humedales suelen encontrarse en zonas de difícil acceso, lo que dificulta su caracterización mediante métodos convencionales. En este sentido, la teledetección satelital se ha consolidado como una herramienta eficiente y de bajo costo para su estudio. A través del análisis de la respuesta espectral de estos ecosistemas en diferentes escalas temporales, es posible detectar cambios en su estructura y composición mediante metodologías avanzadas de clasificación y procesamiento de imágenes multiespectrales (Ozesmi y Bauer, 2002; Mahdavi *et al.*, 2018). En particular, los índices espectrales, como el Índice de Vegetación de Diferencia Normalizada (NDVI, por su sigla en inglés) e Índice de Agua de Diferencia Normalizada (NDWI, por su sigla en inglés), han demostrado ser particularmente efectivos para evaluar las condiciones de los humedales altoandinos (Otto *et al.*, 2011; Adauto y Bram, 2015; Mazzarino y Finn, 2016).

En este contexto, el presente estudio tiene como objetivo analizar la variación espacio-temporal de dos humedales altoandinos en ambientes áridos, ubicados en una zona poco explorada, mediante el uso de sensores remotos y su relación con los ciclos climáticos. La metodología aplicada se centra en el uso combinado de imágenes satelitales y datos climáticos para evaluar la dinámica de estos humedales en función de los cambios en las precipitaciones y de los eventos extremos asociados con el fenómeno El Niño-Oscilación Sur (ENSO). Se espera que los resultados obtenidos contribuyan a un monitoreo más preciso y a una mejor comprensión de la respuesta de los humedales altoandinos ante la variabilidad climática, además de ofrecer una metodología replicable para su estudio en otras regiones con condiciones similares. Así, este enfoque integrado podrá contribuir a la conservación y el manejo sostenible de estos ecosistemas vulnerables a escala meso y macroregional, en el contexto del cambio climático.

## 2. Área de estudio

La región de estudio se ubica en los Andes Centrales áridos entre los  $32^{\circ} 5'30.68''$  y  $32^{\circ}21'50.50''$  latitud sur y los  $70^{\circ}10'49.50''$  y  $69^{\circ}50'53.19''$  longitud oeste. La zona se caracteriza por un alto relieve (alturas que alcanzan 5000 m snm) cuyos cordones montañosos se encuentran separados entre sí por valles y bolsones intermontanos. Las condiciones climáticas son predominantemente áridas siendo la precipitación anual media cercana a 300 mm y la evapotranspiración potencial generalmente superior a 600 mm según el Sistema Nacional de Información Hídrica (<https://snih.hidricosargentina.gob.ar>), condición que refleja el marcado déficit hídrico del área. En esta zona montañosa se concentran campos de nieve y glaciares actuales, y los ríos son, en su mayoría, de carácter permanente, de origen nival-glacial-periglacial.

La selección de los dos sitios de estudio (Fig. 1a y b) se fundamentó en su relevancia como fuentes de abastecimiento de agua para los pobladores locales y como sustento del forraje para la ganadería, así como en la escasez de registros debido a las difíciles condiciones de trabajo de campo y los elevados costos. Asimismo, ambos sitios presentan diferentes características geológicas e hidrogeológicas cuyo estudio en conjunto ofrece la oportunidad de realizar un análisis comparativo más detallado de los factores que regulan su funcionamiento.

En el sitio de Pampa Manantial (Fig. 1c y d), se reconocen humedales a una altitud de 3166-3176 m snm, asociados con la descarga de agua subterránea en forma difusa que aflora en rocas sedimentarias de tipo silicoclásticas. Esta descarga es favorecida por controles estructurales de orientación N-S los cuales han sido parcialmente obliteradas por depósitos cuaternarios de facies fluviales y aluvionales, condicionando la dinámica del flujo y la distribución del agua en el sector.

Por otro lado, en el sitio de Valle Hermoso (Fig. 1c y e), se identifican una serie de humedales alimentados por manantiales situados entre los 2978 y 2986 m snm, cuya descarga se produce en rocas volcanoclásticas y evaporíticas. A diferencia de Pampa Manantial, aquí la descarga es de tipo puntual, emergiendo en sectores específicos favorecidos por lineamientos estructurales con orientación NE-SW, que controlan y canalizan el flujo subterráneo hacia la superficie correspondiente a la llanura fluvial del río Volcán.

En ambos sectores, el control estructural del área determina la dinámica del agua subterránea, favoreciendo flujos de corta trayectoria y tiempos de tránsito reducidos desde la zona de recarga hasta la descarga en forma de manantial. Esta rápida circulación, evidenciada en el área mediante trazadores hidroquímicos e isotópicos (Calvi *et al.*, 2024), propicia una rápida conexión entre el agua subterránea y superficial, que condiciona al sistema hidrológico.

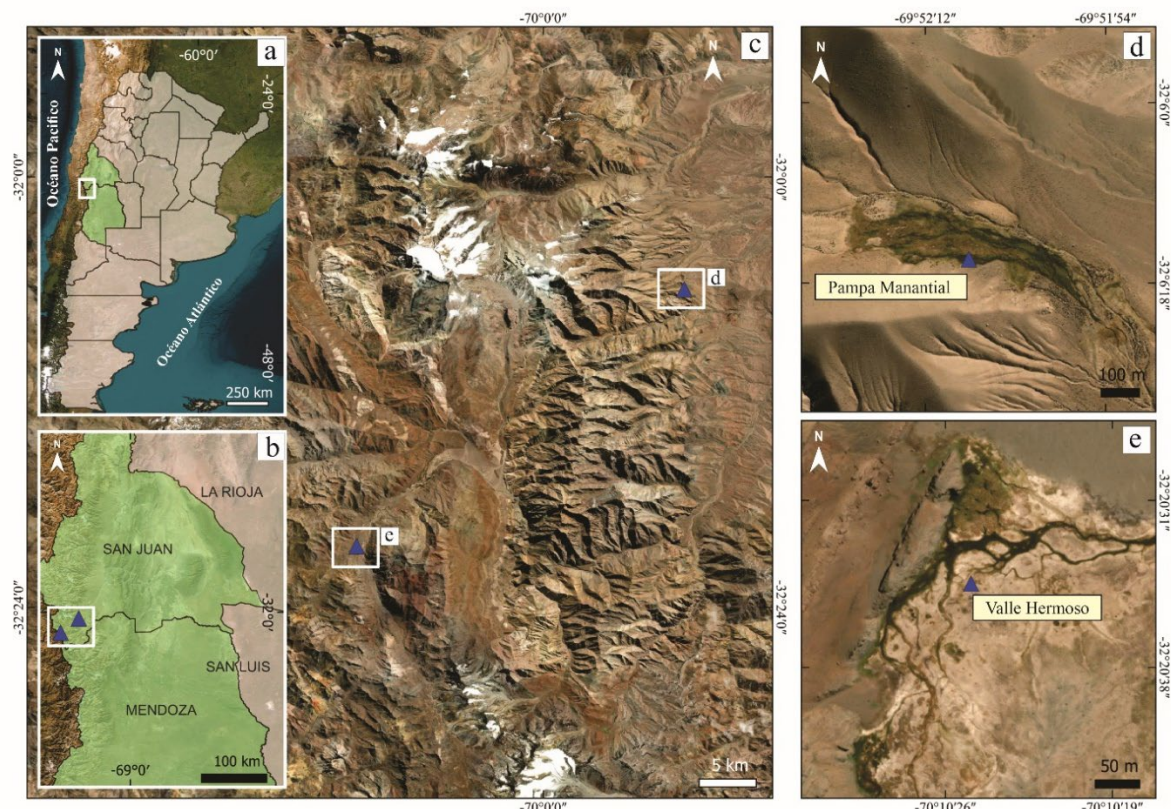


*Figura 1 a y b. Ubicación regional del área de estudio; c. Sector de humedales de altura en Pampa Manantial; d y e. Sector de humedales de altura en Valle Hermoso (Triángulos azules identifican el área de estudio).*

### 3. Metodología

Para la selección del período de imágenes a considerar, se realizó previamente un análisis de la variabilidad climática, integrando los registros hidrometeorológicos del área con el cálculo de los índices SPEI y ONI. Dado que el sitio de estudio no cuenta con registros pluviométricos específicos, se utilizaron datos de estaciones meteorológicas cercanas (Fig. 2).

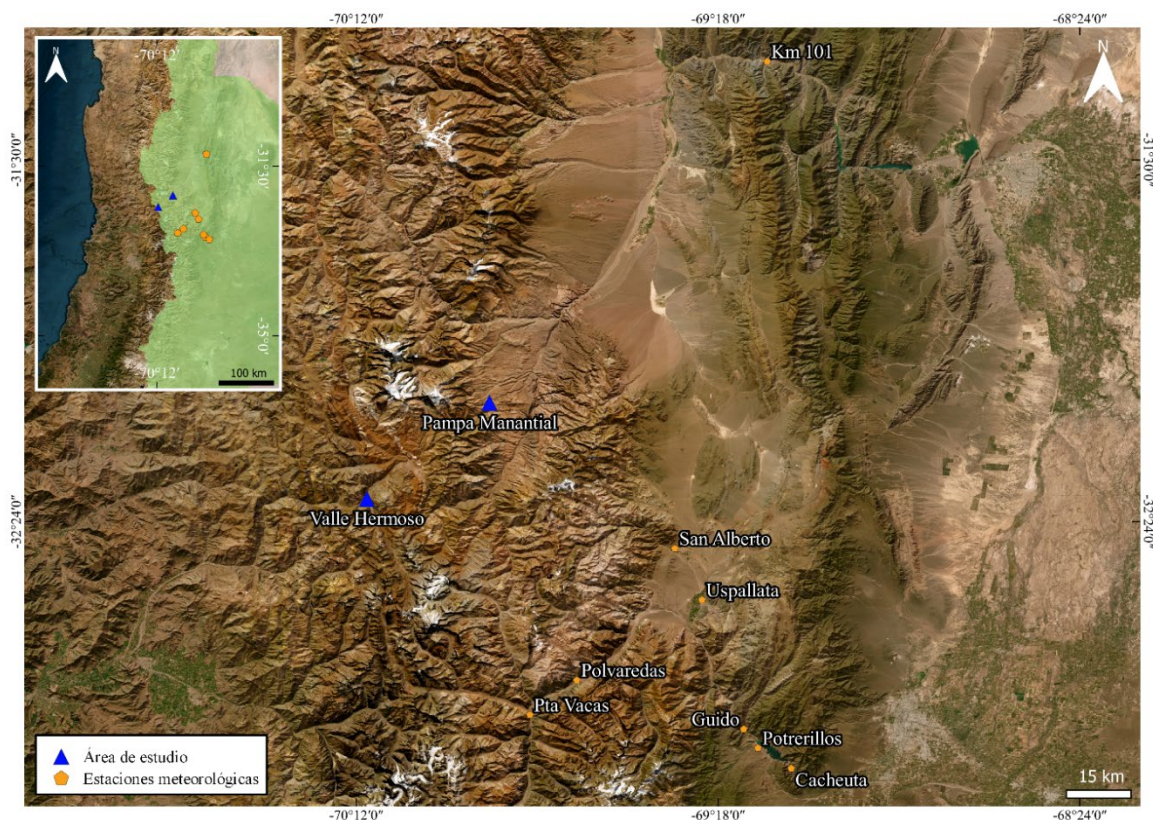


Figura 2. Ubicación de las estaciones meteorológicas en la zona de estudio.

Este análisis, basado en estadística descriptiva, incluyó el cálculo de promedios para caracterizar las fluctuaciones climáticas. Se evaluaron las series de precipitaciones anuales del período 1993-2019 correspondientes a las estaciones meteorológicas de San Alberto, Uspallata, Pta. de Vacas, Cacheuta, Polvaredas, Guido y Potrerillos (Fig. 2). Adicionalmente, se incorporaron datos de la estación Km 101 para el período 2010-2019 (Fig. 2). Los registros fueron obtenidos de la plataforma del Sistema Nacional de Información Hídrica ([snih.hidricosargentina.gob.ar](http://snih.hidricosargentina.gob.ar)). A partir de estos datos, se calcularon las precipitaciones anuales y se representaron gráficamente junto con el índice SPEI, permitiendo evaluar la relación entre las variaciones climáticas y la disponibilidad hídrica en la región.

La serie de datos para el cálculo del índice SPEI fue obtenida de la página web <http://spei.csic.es> y se calculó siguiendo la ecuación de Vicente-Serrano *et al.*, (2010):

$$\text{SPEI} = W - C_0 + C_1 + C_2 W^{21} + d_1 W + d_2 W^2 + d_3 W^3$$

donde  $W = -2 \ln(P)$ ,  $P$  es la probabilidad de exceder una  $D$  determinada,  $D$  es la diferencia entre la precipitación y la evaporación potencial,  $C$  y  $d$  son constantes:

$$C_0 = 2,515517, C_1 = 0,802853, C_2 = 0,010328,$$

$$d_1 = 1,432788, d_2 = 0,189269 \text{ y } d_3 = 0,001308$$

El mismo se aplicó en una escala temporal de 3 meses y permitió caracterizar los años según su clasificación por categorías en función del valor SPEI obtenido (Tabla 1).

Tabla 1. Categorías de SPEI (Fuente: Wang et al., 2015).

SPEI	Categorías
$\geq 2$	Extremadamente húmedo (EH)
(1,5 a 2,0]	Muy húmedo (MuH)
(1,0 a 1,5]	Moderadamente húmedo (MoH)
(0,5 a 1,0]	Humedad incipiente (HI)
[0,5 a -0,5]	Normal
(-0,5 a -1,0]	Sequía incipiente (SI)
(-1,0 a -1,5]	Moderadamente seco (MoS)
(-1,5 a -2,0]	Muy seco (MuS)
$\leq -2$	Extremadamente seco (ES)

Los datos anteriores se relacionaron con la ocurrencia e intensidad de los fenómenos El Niño y La Niña, según la información provista por el Centro de Predicción Climática de Estados Unidos (<http://www.cpc.ncep.noaa.gov/>), que los determina a partir del Índice ONI. Para evaluar la influencia de ENSO en la variabilidad climática regional, se agruparon los datos en tres fases del ONI de El Niño (ONI  $> 0,5$ ), La Niña (ONI  $< -0,5$ ) y Normales (ONI entre -0,5 y 0,5). En cada fase, se calcularon estadísticas descriptivas del SPEI y la precipitación, incluyendo medidas de tendencia central como la media, con el objetivo de caracterizar el comportamiento de ambas variables bajo distintos contextos climáticos. Adicionalmente, se analizaron las asociaciones entre eventos secos (según el SPEI a escala de 3 meses) y eventos fríos (La Niña), así como sus contrapartes: eventos normales o húmedos de SPEI y eventos cálidos (El Niño). La escala temporal de tres meses fue seleccionada debido a que el ONI se define como la media móvil trimestral de las anomalías de la Temperatura Superficial del Mar (TSM) en el Océano Pacífico ecuatorial. Además, se realizó un análisis de contingencia sobre datos climáticos estacionales para examinar la relación entre las categorías ONI y SPEI a escala de 3 meses. Este enfoque resulta más adecuado para evaluar la relación entre fenómenos climáticos, ya que se enfoca en la coocurrencia de estos, a diferencia del análisis de correlación, que puede no ser eficaz en el caso de fenómenos extremos (Davey *et al.*, 2014).

En base a los datos climáticos e índices ONI y SPEI se seleccionaron imágenes satelitales para el análisis de los índices NDVI y NDWI. Para el momento de captura de cada imagen seleccionadas se efectuó un análisis estadístico de las precipitaciones, y los índices ONI y SPEI mediante coeficientes de correlación de Pearson. Este análisis permitió medir tanto la fuerza como la dirección de las asociaciones entre las variables. Los valores cercanos a  $\pm 1$  indican una asociación perfecta, mientras que los valores cercanos a cero reflejan una relación más débil. El signo del coeficiente indica una relación positiva o negativa (Chen y Popovich, 2002). Para determinar el tamaño del efecto de la relación, se empleó la norma de Cohen *et al.* (2003) donde valores del coeficiente de correlación entre 0,10 y 0,29 indican una asociación pequeña, entre 0,30 y 0,49 una asociación media, y los coeficientes superiores a 0,50 sugieren una asociación fuerte.

Para la estimación de los índices espectrales NDVI y NDWI, se empleó EO Browser (<https://www.sentinel-hub.com/explore/eobrowser/>), una plataforma de acceso libre desarrollada por Sentinel Hub que permite la visualización, procesamiento y análisis de imágenes satelitales de las diferentes misiones que fueron utilizadas (Tabla 2).

*Tabla 2. Registros de las Imágenes Satelitales utilizadas, MSS: Multispectral Scanner (Landsat 1-5); TM: Thematic Mapper (Landsat 4-5); OLI/TIRS: Operational Land Imager / Thermal Infrared Sensor (Landsat 8-9); MSI: MultiSpectral Instrument (Sentinel-2); L1: Nivel 1 (datos sin corrección atmosférica); L2A: Nivel 2 (datos corregidos atmosféricamente)*

Fecha	Satélite	Sensor	Nivel de Procesamiento	Cobertura Nubosa (%)
1/11/1980	Landsat 1-5	MSS	L1	4
4/12/1994	Landsat 4-5	TM	L1	1
25/8/1998	Landsat 4-5	TM	L2	5
25/11/2005	Landsat 4-5	TM	L1	1
24/11/2008	Landsat 4-5	TM	L2	2
20/12/2014	Landsat 8-9	OLI/TIRS	L1	0,8
30/12/2015	Landsat 8-9	OLI/TIRS	L2	14
29/12/2021	Sentinel-2	MSI	L2A	0

Para garantizar la calidad y precisión de los datos, se aplicó un proceso de preprocesamiento adecuado a las imágenes satelitales, que incluyó corrección atmosférica, filtrado de nubes y sombras, y el uso de imágenes con reflectancia de superficie. En las imágenes de nivel L1, fue necesario aplicar una corrección atmosférica para minimizar los efectos de dispersión y absorción en la atmósfera. Esto permitió obtener valores más precisos de reflectancia y mejorar la comparabilidad de los datos. Para ello, se utilizó la herramienta Surface Reflectance de QGIS. La presencia de nubes y sus sombras puede introducir errores en la interpretación de los índices espectrales. Para mitigar este efecto, se enmascararon los píxeles afectados mediante el uso de bandas de calidad (QA) o clasificaciones de escena, asegurando un análisis más preciso.

Siempre que fue posible, se priorizó el uso de imágenes ya corregidas atmosféricamente y convertidas a reflectancia de superficie (niveles L2 o L2A), ya que estos datos permiten una mejor comparación temporal y espacial. En el caso de imágenes Landsat de nivel L1 (TM, MSS, OLI/TIRS), fue necesario convertir los valores digitales a reflectancia en la parte superior de la atmósfera (Top of Atmosphere: TOA) antes de su corrección atmosférica. Para este proceso, se utilizó el complemento Semi-Automatic Classification Plugin (SCP) de QGIS.

El cálculo del NDVI y NDWI varió según el satélite y el sensor empleado (Tabla 3 y 4). Las fórmulas fueron calculadas mediante el editor de scripts personalizados de EO Browser, donde se implementaron las fórmulas correspondientes en lenguaje JavaScript.

*Tabla 3. Fórmulas de cálculo de NDVI y NDWI para distintos sensores satelitales.*

Satélite / Sensor	Fórmula NDVI	Fórmula NDWI	Bandas y Longitud de Onda ( $\mu\text{m}$ )	Resolución Espacial
Sentinel-2 / MSI	$(B08 - B04) / (B08 + B04)$	$(B03 - B08) / (B03 + B08)$	<b>B03 (Green): 0,56</b>	10 m
			<b>B04 (Red): 0,665</b>	
			<b>B08 (NIR): 0,84</b>	
Landsat 1-5 / MSS	$(B04 - B02) / (B04 + B02)$	$(B01 - B04) / (B01 + B04)$	<b>B01 (Green): 0,50-0,60</b>	60 m
			<b>B02 (Red): 0,60-0,70</b>	
			<b>B04 (NIR): 0,70-0,80</b>	
Landsat 4-5 / TM	$(B04 - B03) / (B04 + B03)$	$(B03 - B05) / (B03 + B05)$	<b>B03 (Green): 0,52-0,60</b>	30 m
			<b>B04 (Red): 0,63-0,69</b>	
			<b>B05 (SWIR): 1,55-1,75</b>	
Landsat 8-9 / OLI-TIRS	$(B05 - B04) / (B05 + B04)$	$(B03 - B05) / (B03 + B05)$	<b>B03 (Green): 0,53-0,59</b>	30 m
			<b>B04 (Red): 0,64-0,67</b>	
			<b>B05 (NIR): 0,85-0,88</b>	

Tabla 4. Índices NDVI y NDWI: Descripción, Rango y Significado de los Valores.

Índice	Descripción	Rango	Interpretación de valores	Referencia
NDVI	Índice ampliamente utilizado para cuantificar la vegetación verde. Normaliza la dispersión de las hojas verdes en el infrarrojo cercano (NIR) con la absorción de clorofila en el rojo (RED).	-1 a 1	Valores negativos (~ -1): Corresponden a cuerpos de agua. Valores cercanos a 0 (-0,1 a 0,1): Representan áreas estériles como rocas, arena o nieve. Valores bajos y positivos (0,2 a 0,4): Indican la presencia de arbustos y pastizales. Valores altos (~1): Representan vegetación densa, como bosques templados y tropicales.	Jensen (2007).
NDWI	Utilizado para monitorear los cambios en el contenido de agua de los cuerpos de agua, resalta el agua debido a su fuerte absorción de luz en las bandas visibles e infrarrojas cercanas.	-1 a 1	Valores negativos (~ -1): Corresponden a cuerpos de agua. Valores cercanos a 0 (0 a 0,1): Representan áreas no acuáticas (suelo, vegetación). Valores positivos (~ 0,2 a 0,5): Indican áreas de agua poco profunda o cuerpos de agua parcialmente cubiertos por vegetación. Valores altos (~ 0,6 a 1): Representan cuerpos de agua más profundos y claros, especialmente lagos o ríos.	McFeeters (1996).

Los resultados se visualizaron en una escala de colores para facilitar la interpretación de las coberturas de vegetación y cuerpos de agua y se exportaron en formato raster para su análisis posterior en QGIS.

Para la cuantificación de las superficies de interés, se empleó la herramienta Calculadora Raster de QGIS, estableciendo expresiones condicionales para identificar los píxeles que cumplían con los criterios definidos. Se consideraron umbrales de  $NDVI > 0,2$  para la presencia de vegetación y  $NDWI < 0$  para la identificación de suelo húmedo o vegetación (Tabla 4). A partir de estos resultados, se utilizó la herramienta Contar píxeles para determinar el número total de píxeles correspondientes a cada categoría. Luego, este valor se multiplicó por el área de cada píxel, considerando la resolución espacial del raster, con el fin de calcular la superficie total ocupada por cada unidad de análisis. Este procedimiento aseguró un enfoque sistemático, reproducible y compatible con estudios geoespaciales similares, permitiendo la comparación de resultados en diferentes escenarios espaciales y temporales.

#### 4. Resultados

A continuación, se presentan los resultados del análisis espacio-temporal de los humedales de alta montaña, con un enfoque en el impacto de la variabilidad climática sobre su condición. En primer lugar, se examina la relación entre los índices ONI, SPEI y los registros de precipitación dentro del periodo 1980-2024, mientras que, en una segunda sección, se emplean indicadores espectrales para evaluar la variabilidad superficial de los humedales.

#### 4.1. Variabilidad climática

El análisis del SPEI a escala de 3 meses para el periodo 1980-2019 (Fig. 3) muestra que poco más de la mitad de los años (54%) se caracterizan por eventos de tipo normales con valores de SPEI comprendidos entre 0,99 y -0,99. Por su parte, los eventos húmedos (valores de SPEI mayores a 0,99) representan el 23%; éstos incluyen eventos moderadamente húmedos (valores de SPEI entre 1 y 1,49) en un 17%, muy húmedos (valores de SPEI entre 1,5 y 1,9) en un 5% y extremadamente húmedos (valores de SPEI mayores a 2) en un 1%. Por otro lado, en relación a los períodos secos, en conjunto los mismo representan el 23%, incluyendo éstos a eventos moderadamente secos (valores entre -1 y -1,49) en un 18%, muy secos (valores entre -1,5 y -1,9) en un 5% y extremadamente secos (valores menores a -2) en un 0% (Fig. 3).

Por otra parte, se analiza el índice SPEI a 3 meses, con la ocurrencia e intensidad de eventos cálidos (El Niño) y fríos (La Niña) utilizando el Índice ONI. La comparación de ambos índices muestra que existen en algunos períodos solapamientos en las áreas SPEI y ONI (Fig. 4). Cuando este solapamiento ocurre en valores positivos se asocian eventos normales - húmedos y a El Niño (flechas azules en Fig. 4), mientras que cuando los solapamientos ocurren en valores negativos se asocian a eventos secos y a La Niña (flechas rojas en la Fig. 4).

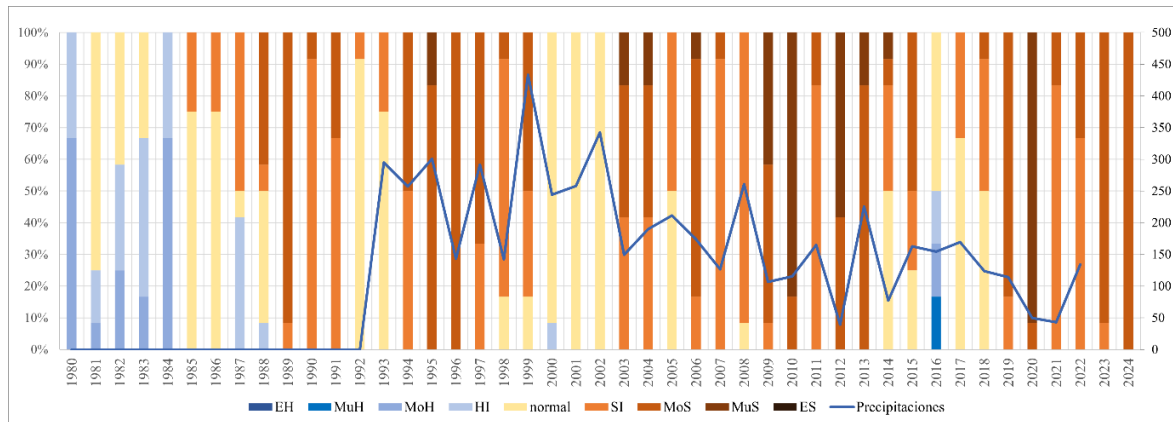


Figura 3. Porcentajes de meses con distintas categorías del SPEI para los años 1980-2024.

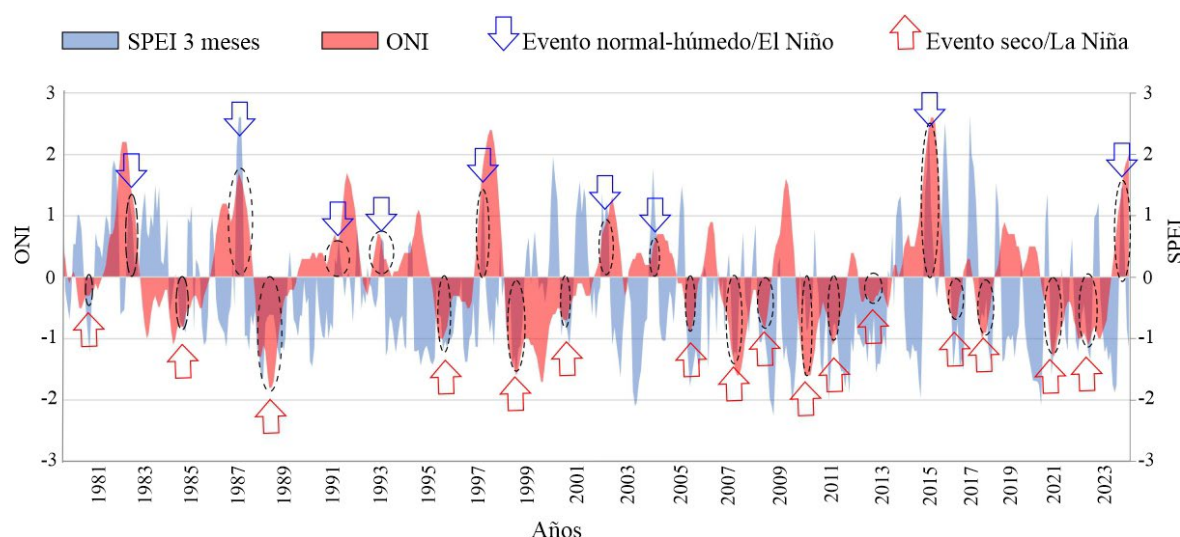
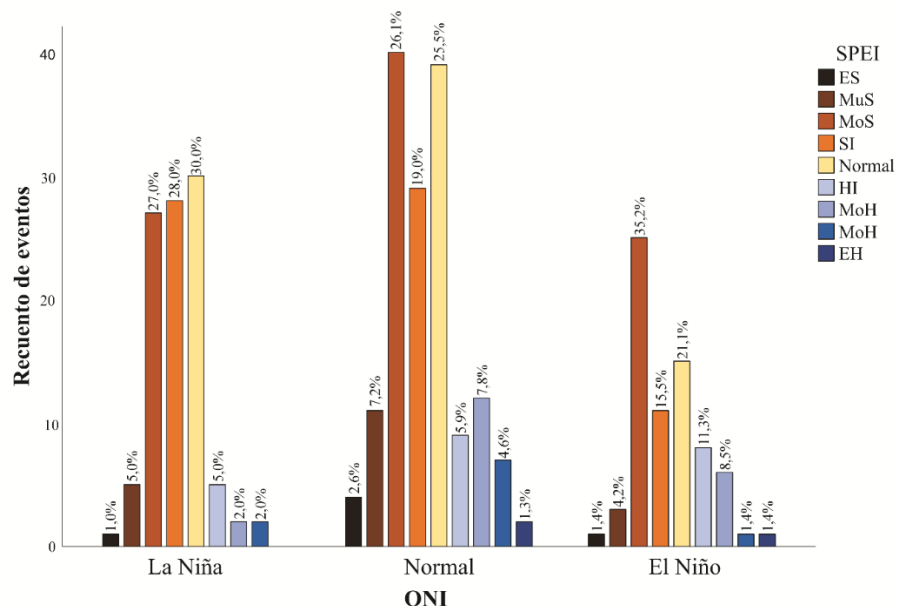


Figura 4. Relación SPEI (3 meses) - ONI.

Por otro lado, el análisis estadístico basado en el cálculo de tablas de contingencia en donde se agrupan las tres categorías del índice ONI (El Niño, La Niña y Normal), junto con las nueve categorías del índice SPEI (Tabla 1) muestra la distribución porcentual (valor de significancia < 0,05) entre dichas categorías (Fig. 5). Tal como se describió precedentemente, los eventos normales son los que presentan mayor frecuencia de ocurrencia, y en consecuencia dentro de ellos se encuentran los mayores valores porcentuales de las distintas categorías de SPEI. No obstante, si se comparan porcentualmente los eventos secos y húmedos dentro de los eventos El Niño y La Niña, pueden observarse claras diferencias. Los eventos de El Niño están asociados con una mayor frecuencia a períodos húmedos identificados por el SPEI los cuales totalizan un 22,6%, mientras que en La Niña los períodos húmedos sólo representan el 9%. Por otra parte, los eventos del tipo La Niña se caracterizan por presentar mayores porcentajes de períodos secos con un total de 61%, contra un total del 55,6% durante los eventos de tipo El Niño.



*Figura 5. Gráfico de barras obtenido a partir del análisis de contingencia donde se muestra el recuento de eventos y la tasa de ocurrencia (%) de las categorías del SPEI dentro de cada fase del Índice Oceánico de El Niño (ONI).*

#### 4.2. Variabilidad espacio -temporal de los humedales de altura

En base a los datos climáticos e índices ONI y SPEI se seleccionaron distintas imágenes satelitales para el análisis de los índices NDVI y NDWI. Las imágenes seleccionadas corresponden a momentos en donde el análisis estadístico mediante coeficientes de correlación de Pearson muestra que existe una correlación positiva entre los eventos asociados con el ENSO (índice ONI), los valores del índice SPEI y la precipitación media anual con valores de coeficientes que varían entre 0,394 y 0,585. Entre el SPEI y la precipitación se encontró una asociación media con un valor de correlación de 0,394. Por otro lado, el ONI con el SPEI y las precipitaciones mostraron una asociación fuerte con valores del coeficiente de correlación de 0,585 y 0,508 respectivamente. De esta manera, los resultados obtenidos apoyan la hipótesis que la alternancia de los eventos de tipo El Niño y La Niña del ONI tienen un impacto en la ocurrencia de los períodos secos y húmedos.

En las imágenes seleccionadas se calcularon los índices NDVI y NDWI para reconocer las variaciones espaciales que presentan temporalmente los humedales de altura en las dos áreas estudiadas. Para el área de Pampa Manantial (Fig. 1d) los valores obtenidos mediante el cálculo del índice NDVI,

permiten identificar y delimitar el área del humedal donde la vegetación se desarrolla sustentada por aportes de descarga de agua subterránea en forma de manantiales. En todos los años analizados se identificaron para el índice NDVI, valores positivos pero pequeños (entre +0,2 y +0,6) correspondientes a campos cubiertos de vegetación (Fig. 6 a-h). Las superficies máximas calculadas, de 0,40 y 0,45 km<sup>2</sup> según el índice NDVI, se registraron en los años 2014 y 2015, respectivamente (Fig. 6f y 6g; Tabla 5). En contraste, el valor mínimo de 0,17 km<sup>2</sup> corresponde a 1998 (Fig. 6c; Tabla 5). Por otro lado, superficies intermedias, en torno a los 0,30 km<sup>2</sup>, fueron observadas en 1980, 1994, 2005, 2008, 2014 y 2021 (Fig. 6a, 6b, 6d, 6e, 6h; Tabla 5).

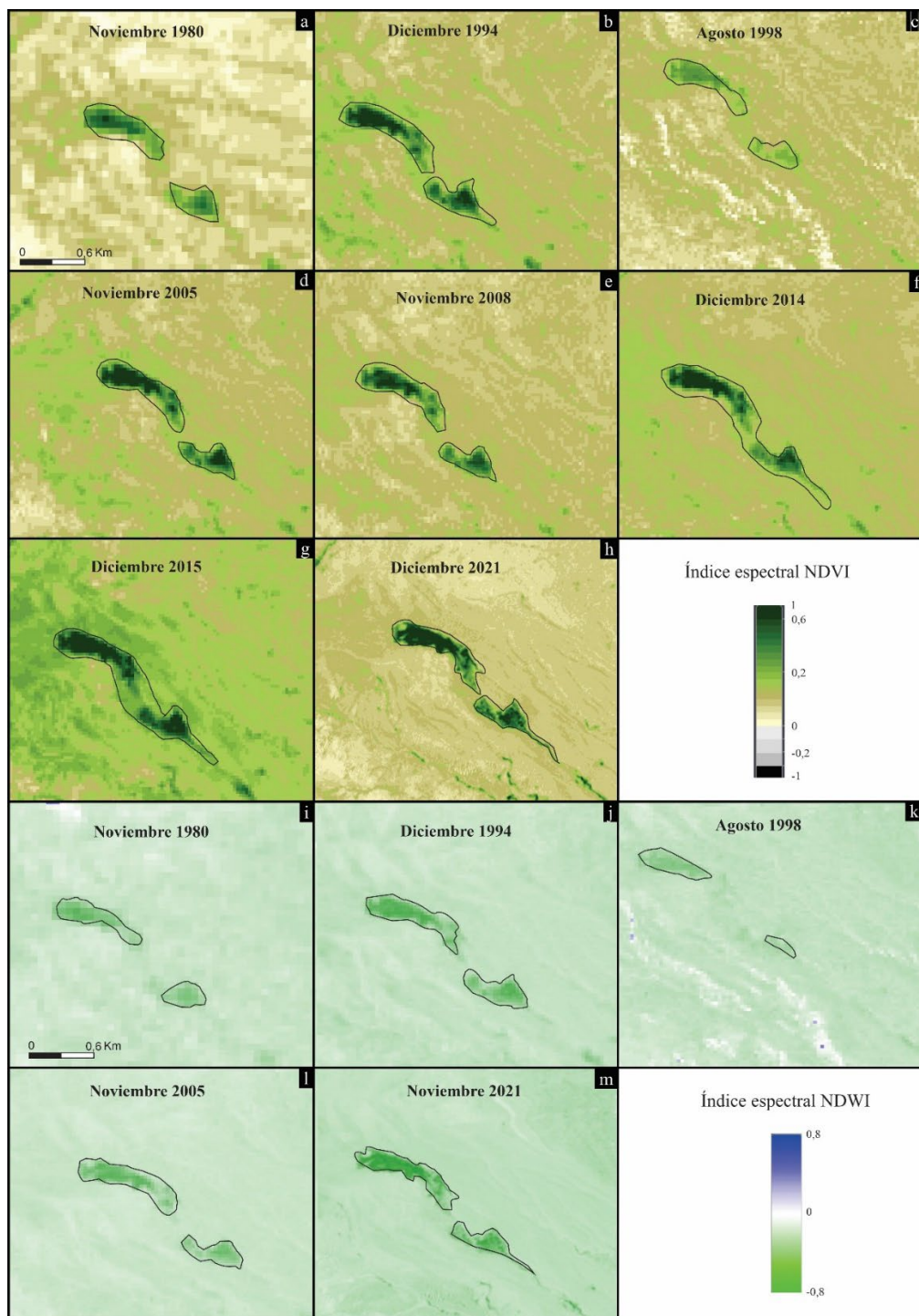


Figura 6. Análisis de índices espectrales en Pampa Manantial. a-h) NDVI; i-m) NDWI.

Tabla 5. Área calculada según los índices NDVI y NDWI para los años analizados.

Fecha	Pampa Manantial (Superficie km <sup>2</sup> )		Valle Hermoso (Superficie km <sup>2</sup> )	
	NDVI	NDWI	NDVI	NDWI
nov-80	0,27	0,25	0,30	0,22
dic-94	0,30	0,28	0,43	0,27
ago-98	0,17	0,10	0,30	0,22
nov-05	0,33	0,30	0,30	0,25
nov-08	0,33	s/d	0,42	0,28
dic-14	0,40	s/d	0,47	s/d
dic-15	0,45	s/d	0,47	s/d
dic-21	0,35	0,33	0,43	0,23

En cuanto al índice espectral NDWI, los valores obtenidos en el rango de -0,3 a -0,8 indican, en general, condiciones de estrés hídrico en la vegetación asociada al humedal a lo largo de todos los años analizados. Este índice permitió identificar, delimitar y cuantificar la superficie del humedal de Pampa Manantial mostrando una tendencia similar a la variación espacio-temporal observada con el NDVI, aunque con valores más bajos (Fig. 6 i-m, Tabla 5). La mayor diferencia se observó en 1998, cuando la superficie del humedal, medida con el NDWI, fue un 41% menor. En los demás años, la disminución fue de aproximadamente el 10%. En 2008, 2014 y 2015, no fue posible realizar el procesamiento de este índice debido a limitaciones en las imágenes.

Adicionalmente se identificó y delimitó la variación espacio-temporal mediante los índices NDVI y NDWI en una zona de humedales de altura ubicada en Valle Hermoso (Fig. 1e; 7 a-n). En este caso, estos humedales se encuentran dentro de la llanura aluvial del río Volcán, los cuales están alimentados por manantiales y por aguas de deshielo.

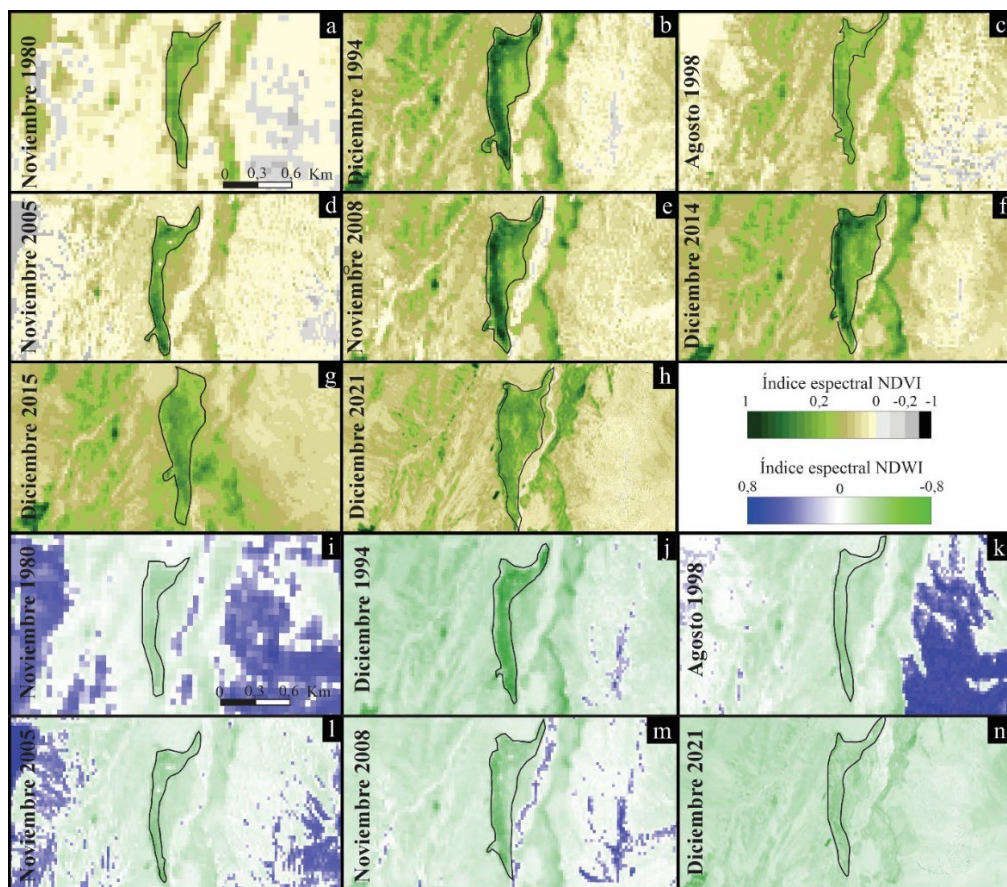


Figura 7. Análisis de índices espectrales en Valle Hermoso. a-h) NDVI; i-n) NDWI.

A lo largo de todos los años analizados, se observa que el índice NDVI en la zona de humedales de Valle Hermoso, varía en un rango de valores positivos entre +0,2 y +0,6 (Fig. 7 a-h). Las superficies máximas, calculadas en 0,47 km<sup>2</sup> según el índice NDVI, corresponden a los años 2014 y 2015 (Fig. 7 f-g; Tabla 5). Mientras que, en el resto de los años analizados, se registraron valores entre 0,30 y 0,43 km<sup>2</sup> (Fig. 8 a-e y 8 h; Tabla 5).

En cuanto al índice espectral NDWI, los valores obtenidos en el rango de -0,3 a -0,8 indican, de manera general para todos los años analizados, condiciones de estrés hídrico en la vegetación del sector (Fig. 7 i-n). Al igual que en PM, la superficie registrada con el NDWI es menor que la obtenida con el NDVI, aunque ambas siguen la misma tendencia de variación. El rango de superficie calculado con el NDWI varió entre 0,22 km<sup>2</sup> y 0,28 km<sup>2</sup> durante los años analizados (Fig. 7 i-n, Tabla 5). La mayor diferencia entre ambos índices se observó en 2021, con un 47%, mientras que la mínima, del 17%, se registró en 2005.

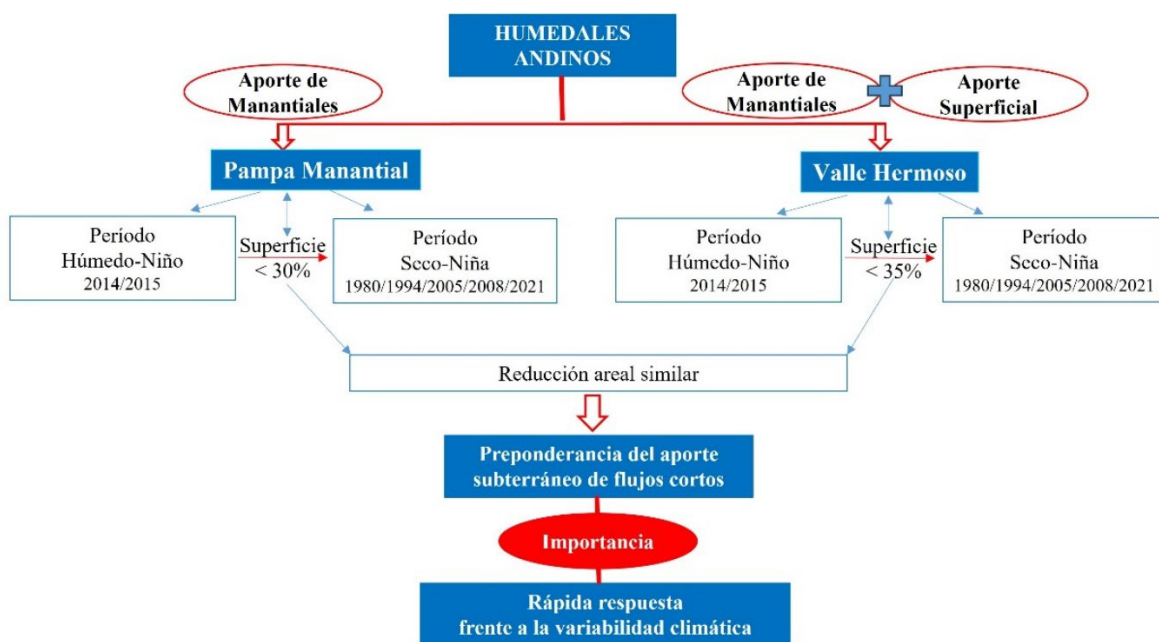


Figura 8. Esquema conceptual que relaciona tipos de humedales analizados, ciclos climáticos y variaciones areales.

## 5. Discusión

Los índices ONI y SPEI, debido a su naturaleza probabilística, se han convertido en los índices importantes para hacer análisis de riesgo de condiciones hídricas extremas a nivel mundial e informar la probable evolución futura de la situación hídrica (Cancelliere *et al.*, 2007; Llanes-Cárdenas *et al.*, 2018; Arana-Ruedas *et al.*, 2023; Ling *et al.*, 2023). En Argentina, el SPEI ha sido aplicado con éxito en la determinación de ciclos secos y húmedos en la Patagonia andina y extrandina (Scordo *et al.*, 2018; Gaiolini *et al.*, 2025) así como también en el estudio del efecto de la variabilidad climática sobre el estado de la vegetación y la cobertura de agua en cuencas de clima templado (Brendel *et al.*, 2017). Los resultados obtenidos en base al análisis de índices climáticos en conjunto con datos pluviométricos permitieron identificar en la zona andina estudiada la existencia de eventos secos, húmedos y normales, los cuales, en términos generales, mostraron concordancia con la ocurrencia de los fenómenos El Niño y La Niña (Fig. 4 y 5).

En Pampa de Manantial se observó un mayor desarrollo del área de los humedales asociado a El Niño, con valores de NDVI promedio de 0,43 km<sup>2</sup> en 2014 y 2015. En contraste, durante 1980, 1994, 1998, 2005, 2008 y 2021, los valores disminuyeron (NDVI~0,30 km<sup>2</sup>), asociados al ciclo climático de

La Niña. Este mismo comportamiento se observó en Valle Hermoso, donde las mayores superficies (NDVI~0,47 km<sup>2</sup>) también se registraron en 2014 y 2015, mientras que, en el resto de los años analizados, los valores fueron menores (NDVI~0,30 km<sup>2</sup>). Cabe destacar que, aunque las áreas obtenidas mediante el índice NDWI son menores tanto en Pampa Manantial como en Valle Hermoso, siguen la misma tendencia que el NDVI. Las diferencias calculadas entre el NDVI y el NDWI pueden atribuirse a las limitaciones individuales y las propiedades de cada índice. El primero, es comúnmente usado para evaluar el vigor de la vegetación, es decir, para diferenciar las coberturas de vegetación, según su densidad y salud (Wilson y Norman, 2018; Ashok et al 2021). Por lo tanto, detecta la variabilidad en que estas zonas concentran la humedad, asociado al contenido vegetal (Rouse *et al.*, 1973; Chen *et al.*, 2004; Xue y Su, 2017). La fotosíntesis en la vegetación está influenciada principalmente por el contenido de agua en las hojas, lo que genera diferencias en la reflectancia en el infrarrojo cercano y, por ende, en el NDVI. Las plantas más sanas presentan valores más altos en comparación con las menos saludables (Chuvieco, 1991; Zhu y Woodcock, 2014). Esta variabilidad proporciona información sobre la estabilidad y los cambios en los humedales analizados en la región cordillerana, vinculada al contenido de agua en la vegetación. No obstante, es posible que el NDVI sobreestime los valores de las áreas debido a la influencia del brillo del suelo, causado por una cobertura vegetal escasa o suelos desnudos. Para ajustar estos valores, se empleó el índice de diferencia normalizada de agua (NDWI), que es eficaz para evaluar cuerpos de agua abierta (McFeeters, 1996; Wilson y Norman, 2018). Al combinar las bandas espectrales GREEN-NIR (verde visible e infrarrojo cercano), el NDWI reduce considerablemente la reflectancia del suelo y la vegetación, permitiendo que las masas de agua destaqueen en la imagen. Esto facilitó la detección y cuantificación de pequeños cambios en la cantidad de agua en los humedales de Pampa Manantial y Valle Hermoso.

El análisis de la variabilidad superficial de los humedales de altura, junto con los cambios en los ciclos atmosféricos y datos de precipitaciones, revela que las dimensiones de los humedales en Pampa Manantial y Valle Hermoso muestran fluctuaciones relacionadas con los ciclos El Niño/La Niña (Fig. 8). En los ciclos El Niño las precipitaciones corresponden a eventos normales a húmedos y en estas condiciones los humedales presentan mayor desarrollo tanto aquellos asociados a la descarga de agua subterránea como los que son sustentados también por cursos fluviales con aportes de la lluvia y del deshielo. Esto evidencia una rápida respuesta del sistema hidrológico, la cual, si bien es de esperar en aquellas zonas de humedales dependientes de cursos fluviales, no siempre se observa en humedales dependientes de la descarga de agua subterránea. Las descargas de agua subterránea asociadas a flujos de trayectorias largas (desde la recarga hacia la descarga) pueden residir por mucho tiempo en el sistema acuífero, y su respuesta a la variabilidad climática está temporalmente desfasada. En consecuencia, los resultados obtenidos están evidenciando que los flujos subterráneos que sustentan a los humedales corresponden a trayectorias cortas de flujo, características que ya había sido apreciada en estudios hidroquímicos de este sistema hidrogeológico (Calvi *et al.*, 2024). Esto pone de manifiesto la fuerte dependencia que los humedales altoandinos estudiados tienen a los ciclos climáticos, ya que, durante los años asociados al fenómeno de La Niña, ambos tipos de humedales mostraron una reducción del 30 al 35%. En consecuencia, es probable que el impacto de los ciclos atmosféricos en el futuro, intensificados por el cambio climático, genere una disminución crítica en la superficie de estos humedales. Sin embargo, posiblemente, humedales del sector andino con un arreglo estructural diferente, sustentados con flujos subterráneos que tengan un tiempo de circulación mayor, podría retrasar su respuesta a la variabilidad climática afectando de un modo diferente su superficie.

Considerando la escasa extensión que los humedales de altura tienen dentro la región andina árida estudiada, es que su monitoreo resulta un tema prioritario en la evaluación de estos ambientes. En este sentido es importante resaltar que las imágenes satelitales ofrecen una herramienta poderosa para observar y analizar estos ambientes de manera remota, permitiendo la identificación de cambios en la cobertura vegetal y en la distribución del agua (Xiao *et al.*, 2002; Vicente-Serrano *et al.*, 2005; Riaño *et al.*, 2007; Alatorre *et al.*, 2010; Balbarini *et al.*, 2017; Tahsin *et al.*, 2018). Estudios previos han demostrado el éxito de las técnicas de análisis espectral en la caracterización de humedales altoandinos

(Buono *et al.*, 2010; Otto *et al.*, 2011; Mazzarino y Finn, 2016; Pauca-Tanco *et al.*, 2020; Marcosig y Liaudat, 2021; Gaitán *et al.*, 2021).

Los resultados obtenidos destacan la relevancia de estudiar el comportamiento de estos humedales de alta montaña desarrollados en condiciones áridas, ya que es crucial para comprender su respuesta ante los cambios climáticos y para implementar medidas de conservación y gestión eficaces en estos frágiles ecosistemas. La preservación y el manejo adecuado de estos entornos vulnerables son fundamentales en un contexto de creciente presión climática global.

## 6. Conclusión

En el intervalo temporal estudiado se observa una buena correlación entre el índice SPEI y el Índice Oceánico El Niño (ONI), donde los eventos secos tienden a coincidir con La Niña, mientras que los eventos húmedos se asocian a El Niño. Dichos ciclos climáticos, de diferentes intensidades, influyen en la cantidad de milímetros precipitados y, en consecuencia, en la recarga de acuíferos y flujos de agua superficial, repercutiendo en el aporte de agua que sustenta a los humedales de altura.

Los humedales estudiados, asociados a la descarga de agua subterránea como los que son sustentados también por cursos fluviales con aportes de la lluvia y del deshielo, evidenciaron una rápida respuesta del sistema hidrológico a los ciclos climáticos. Se observaron incrementos en las superficies de los humedales, según los índices NDVI y NDWI, durante El Niño, mientras que se registró una disminución de aproximadamente 30% durante La Niña. Este fenómeno se explica por el hecho de que, en ambos tipos de humedales, la principal fuente de agua proviene del aporte de aguas subterráneas, las cuales están asociadas a flujos cortos debido al control estructural del área. Sin embargo, es posible que este comportamiento varíe en áreas donde el tiempo de tránsito del agua subterránea sea más prolongado debido a diferencias en el arreglo estructural, lo que podría retrasar su respuesta frente a la variabilidad climática.

Resulta esencial monitorear la evolución de este tipo de humedales altoandinos en condiciones ardidas para caracterizar su comportamiento frente a los ciclos climáticos en un contexto de cambio climático global.

## Referencias

- Adauto, M., Bram, L.W. 2015. Identificación de humedales alto andinos integrando imágenes Landsat Aster GDEM con árbol de decisión sobre la cabecera de las cuencas de pisco y pampas en Huancavelica-Perú. *Anais XVII Simpósio Brasileiro de Sensoriamento Remoto - SBSR*, João Pessoa-PB, Brasil, 25 a 29 de abril de 2015, INPE.
- Alatorre, L.C., Beguería, S., Vicente-Serrano, S.M. 2010. Análisis de la evolución espacio-temporal del NDVI sobre áreas vegetadas y zonas de riesgo de erosión en el Pirineo Central. *Pirineos* 165, 7-27. <https://doi.org/10.3989/Pirineos.2010.165001>
- Arana-Ruedas, D.P.R., Moggiano, N. 2023. ENSO Influence on Agricultural Drought Identified by SPEI Assessment in the Peruvian Tropical Andes, Mantaro Valley. *Manglar* 20(2), 157-167.
- Ashok, A., Ponnamma Rani, H., Jayakumar K.V. 2021 Monitoring of dynamic wetland changes using NDVI and NDWI based landsat imagery, *Remote Sensing Applications: Society and Environment* V 23. <https://doi.org/10.1016/j.rsase.2021.100547>
- Balbarini, S., Comes, D., Langer, K. 2017. Estudio comparativo de índices de vegetación derivado de imágenes satelitales de mediana resolución y sensores terrestres: su aplicación en la viticultura de precisión. *Boletín de Estudios Geográficos* 108, 9-32. <https://bdigital.uncu.edu.ar/10249>
- Brendel, A., Bohn, V.Y., Piccolo, M.C. 2017. Variabilidad de la precipitación y su relación con los rendimientos agrícolas en una región semiárida de la llanura pampeana (Argentina). *Estudios Geográficos* 78, 282, 7-29. <https://doi.org/10.3989/estgeogr.201701>

- Buono, G., Oesterheld M., Nakamatsu V., Paruelo J.M. 2010. Spatial and temporal variation of primary production of Patagonian wet meadows. *Journal of Arid Environments* 74(10), 1257–1261. <https://doi.org/10.1016/j.jaridenv.2010.05.026>
- Cancelliere, A., Mauro, G.D., Bonaccorso, B., Rossi, G. 2007. Drought forecasting using the standardized precipitation index. *Water Resources Management* 21, 801-819. <https://doi.org/10.1007/s11269-006-9062-y>
- Calvi, C., Carol, E., Fennell, L., Naipauer, M. 2024. Assessment of hydrological systems associated with groundwater discharges in arid high mountain environments of the Argentine Andes. *Groundwater for Sustainable Development* 101218. <https://doi.org/10.1016/j.gsd.2024.101218>
- Chen, P.Y., Popovich, P.M., 2002. *Correlation: Parametric and Nonparametric Measures*, vol. 139. Sage.
- Chen, J., Jönsson, P., Tamura, M., Gu, Z., Matsushita, B., Eklundh, L. 2004. A simple method for reconstructing a high-quality NDVI time-series data set based on the Savitzky-Golay filter. *Remote Sensing of Environment* 91, 332-344. <https://doi.org/10.1016/j.rse.2004.03.014>
- Chuvieco, E. 1991. Fundamentos de teledetección espacial. *Estudios Geográficos* 52(203), 371.
- Cohen, J., Cohen, P., West, S.G., Aiken, L.S. 2003. *Applied Multiple Regression/correlation Analysis for the Behavioral Sciences*, third ed. Lawrence Erlbaum Associates, Mahwah, NJ. <https://doi.org/10.4324/9780203774441>
- Davey, M.K., Brookshaw, A., Ineson, S. 2014. The probability of the impact of ENSO on precipitation and near-surface temperature. *Climate Risk Management* 1, 5-24. <http://doi.org/10.1016/j.crm.2013.12.002>
- Gaiolini, M., Acosta, R., Carol, E., Colombani, N. 2025. Assessing the effects of ENSO-induced climate variability on shallow coastal groundwater reserves of north Patagonia, Argentina. *Groundwater for Sustainable Development*, 29. <https://doi.org/10.1016/j.gsd.2025.101427>
- Gaitán, J., Ciano, N., Oliva, G., Bran, D., Butti, L., Cariac, G., Caruso, C., Opazo, W., Ferrante, D., Echevarria, D., Buono, G., Fantozzi, A., Guirado, E., Maestre, F. 2021. La variación temporal del índice NDVI predice los cambios temporales de la cobertura vegetal en las tierras secas de la Patagonia argentina. *Ecosistemas* 30(3), 2229. <https://doi.org/10.7818/ECOS.2229>
- Gallant, A.L. 2015. The challenges of remote monitoring of wetlands. *Remote Sensing* 7(8), 10938-10950. <https://doi.org/10.3390/rs70810938>
- Garreaud, R., Vuille, M., Compagnucci, R., Marengo, J. 2009. Present-day South American climate. *Palaeogeography, Palaeoclimatology, Palaeoecology* 281(3-4), 180-195. <https://doi.org/10.1016/j.palaeo.2007.10.032>
- Jensen, J.R. 2007. *Remote Sensing of the Environment: An Earth Resource Perspective*. Pearson Prentice Hall.
- Ling, M., Han, H., Hu, X., Xia, Q., Guo, X. 2023. Drought characteristics and causes during summer maize growth period on Huang-Huai-Hai Plain based on daily scale SPEI. *Agricultural Water Management* 280, 108198. <https://doi.org/10.1016/j.agwat.2023.108198>
- Llanes-Cárdenas, O., Gaxiola-Hernández, A., Estrella-Gastelum, R.D., Norzagaray-Campos, M., Troyo-Diégo, E., Pérez-González, E., de J. Pellegrini Cervantes, M. 2018. Variability and factors of influence of extreme wet and dry events in Northern Mexico. *Atmosphere* 9(4), 122. <https://doi.org/10.3390/atmos9040122>
- Mahdavi, S., Salehi, B., Granger, J., Amani, M., Brisco, B., Huang, W. 2018. Remote sensing for wetland classification: A comprehensive review. *GIScience & Remote Sensing* 55(5), 623-658. <https://doi.org/10.1080/15481603.2017.1419602>
- Mallmann, C.L., Prado, D.D.A., Pereira Filho, W. 2015. Índice de vegetação por diferença normalizada para caracterização da dinâmica florestal no parque estadual Quarta Colônia, estado do Rio Grande do Sul-Brasil. *Revista Brasileira de Geografia Física, Recife* 8(5), 1454-1469. <https://doi.org/10.5935/1984-2295.20150080>
- Marcosig, I.P., Liaudat, D.T. 2021. Análisis de la dinámica de dos mallines de altura en Vallecitos, Cordón del Plata, Mendoza, Argentina en el periodo 2002-2019. *Acta Geológica Lilloana* 1-24. <http://doi.org/10.30550/j.agl/2021.33.1/2021-02-18>

- Mazzarino, M., Finn, J.T. 2016. An NDVI analysis of vegetation trends in an Andean watershed. *Wetlands Ecology and Management* 24, 623-640. <https://doi.org/10.1007/s11273-016-9492-0>
- McFeeters, S.K. 1996. The use of the Normalized Difference Water Index (NDWI) in the delineation of open water features. *International Journal of Remote Sensing* 17(7), 1425-1432. <https://doi.org/10.1080/01431169608948714>
- Mejía, J.F., González, J.D., Albarrán, A. 2022. Influencia de la variabilidad climática en los pantanos altoandinos de la microcuenca Miguaguó Andes venezolanos. *Revista de Ciencias Ambientales* 56 (2), 38-62. <https://doi.org/10.15359/rca.56/2.3>
- Meza Aliaga, M., Díaz Villalobos, Y. 2014. Efectos de la variabilidad climática sobre las fluctuaciones del nivel de las aguas y actividad ganadera en humedales altoandinos. *Interciencia* 39(9), 651-658.
- Otto, M., Scherer, D., Richters, J. 2011. Hydrological differentiation and spatial distribution of high-altitude wetlands in a semi-arid Andean region derived from satellite data. *Hydrology and Earth System Sciences* 15, 1713-1727. <https://doi.org/10.5194/hess-15-1713-2011>
- Ozesmi, S.L., Bauer, M.E. 2002. Satellite remote sensing of wetlands. *Wetlands ecology and management* 10, 381-402. <https://doi.org/10.1023/A:1020908432489>
- Pauca-Tanco, A., Ramos-Mamani, C., Luque-Fernández, C.R., Talavera-Delgado, C., Villasante-Benavides, J.F., Quispe-Turpo, J P., Villegas-Paredes, L. 2020. Análisis espacio temporal y climático del humedal altoandino de Chalhuanca (Perú) durante el periodo 1986-2016. *Revista de Teledetección* 55, 105-118. <https://doi.org/10.4995/raet.2020.13325>
- Peñalba, O.C., Rivera, J.A. 2016. Precipitation response to El Niño/La Niña events in Southern South America – emphasis in regional drought occurrences. *Advances in Geosciences* 42, 1-14. <https://doi.org/10.5194/adgeo-42-1-2016>
- Riaño, D., Moreno Ruiz, J.A., Isidoro, D., Ustin, S.L. 2007. Global spatial patterns and temporal trends of burned area between 1981 and 2000 using NOAA-NASA Pathfinder. *Global Change Biology* 13, 40-50. <https://doi.org/10.1111/j.1365-2486.2006.01268.x>
- Rivera, J.A., Peñalba, O.C., Villalba, R. 2014. ENSO-related precipitation variability in the Andes of subtropical Argentina: relationships with large-scale atmospheric circulation. *International Journal of Climatology* 34(12), 3476-3492.
- Rouse, J.W., Jr., Haas, R.H., Schell, J.A., Deering, D.W. 1973. *Monitoring the vernal advancement and retrogradation (green wave effect) of natural vegetation* (No. NASA-CR-132982). <https://ntrs.nasa.gov/citations/19750020419?utm>
- Scordo, F., Piccolo, M.C., Perillo, G.M.E. 2018. Aplicación del índice de precipitación evapotranspiración estandarizada (SPEI) para identificar períodos húmedos y secos en la Patagonia andina y extra andina argentina. *Geosciences = Geociências* 37(2), 423-436. <https://doi.org/10.5016/geociencias.v37i2.12241>
- Tahsin, S., Medeiros, S.C., Singh, A. 2018. Assessing the resilience of coastal wetlands to extreme hydrologic events using vegetation indices: A review. *Remote Sensing* 10(9), 1390. <https://doi.org/10.3390/rs10091390>
- Vicente-Serrano, S.M., Beguería, S., López-Moreno, J.I. 2010. A multiscalar drought index sensitive to global warming: the standardized precipitation evapotranspiration index. *Journal of Climate* 23(7), 1696-1718. <https://doi.org/10.1175/2009JCLI2909.1>
- Vicente-Serrano, S., Lasanta, T., Romo, A. 2005. Analysis of Spatial and Temporal Evolution of Vegetation Cover in the Spanish Central Pyrenees: Role of Human Management. *Environmental management* 34, 802-18. <https://doi.org/10.1007/s00267-003-0022-5>
- Wang, K., Li, Q., Yang, Y., Zeng M., Li, P., Zhang, J. 2015. Analysis of spatio-temporal evolution of droughts in Luanhe River Basin using different drought indices. *Water Science and Engineering* 8(4), 282-290. <https://doi.org/10.1016/j.wse.2015.11.004>
- Wilson, N.R., Norman, L.M, 2018. Analysis of vegetation recovery surrounding a restored wetland using the normalized difference infrared index (NDII) and normalized difference vegetation index (NDVI).

*International Journal of Remote Sensing* 39(10), 3243-3274. <https://doi.org/10.3989/estgeogr.20170110.1080/01431161.2018.1437297>

Xue, J., Su, B. 2017. Significant remote sensing vegetation indices: A review of developments and applications. *Journal of Sensors* 2017(1353691), 1-17. <https://doi.org/10.1155/2017/1353691>

Xiao, X., Boles, S., Frolking, S., Salas, W., Moore III, B., Li, C., He, L., Zhao, R. 2002. Observation of flooding and rice transplanting of paddy rice fields at the site to landscape scales in China using vegetation sensor data. *International Journal of Remote Sensing* 23(15), 3009-3022. <https://doi.org/10.1080/01431160110107734>

Zhu, Z., Woodcock, C.E. 2014. Automated mapping of land surface phenology using MODIS time series. *Remote Sensing of Environment* 152, 166-177. <https://doi.org/10.1016/j.rse.2014.06.013>



## ADVANCEMENTS IN HIGH-RESOLUTION LAND USE MAPPING: METHODOLOGIES AND INSIGHTS FROM THE RETHINKACTION H2020 PROJECT

CHRISTOPH CORREIA \*, JESÚS ORTUÑO CASTILLO\* ,  
MARTA TORO BERMEJO , PATRICIA PÉREZ RAMÍREZ\*

*Remote Sensing and Geospatial Analytics Division, GMV, Madrid, Spain.*

**ABSTRACT.** Land use and land cover (LULC) mapping is essential for land-based climate change adaptation and mitigation strategies. This study presents the development of 10-meter high-resolution (HR) land use maps within the RethinkAction H2020 project, aimed at enhancing spatial planning for climate mitigation and adaptation. The methodology integrates multi-source remote sensing data, machine learning classification techniques, and auxiliary datasets to generate accurate and transferable land use classifications across six European bioclimatic regions. The study employs Sentinel-2 and Landsat-8 imagery, using supervised classification with Random Forest (RF) and Geographic Object-Based Image Analysis (GEOBIA) to enhance accuracy and minimize spectral confusion. This approach resulted in the creation of twelve HR land use maps at two classification levels, covering six case study (CS) areas. A key contribution of this research is the generation of suitability maps, which assess the potential for implementing land-based mitigation and adaptation solutions (LAMS) such as reforestation, water harvesting, and photovoltaic energy development. This study highlights the importance of integrating remote sensing, machine learning, and spatial analysis to support evidence-based decision-making in land use planning, offering a scalable and replicable methodology for detailed LULC classification.

*Avances en la cartografía de alta resolución de usos del suelo: metodologías y aprendizajes del proyecto H2020 RethinkAction*

**RESUMEN.** La cartografía de uso y cobertura del suelo (LULC, por sus siglas en inglés) es fundamental para las estrategias de adaptación y mitigación del cambio climático basadas en el territorio. Este estudio presenta el desarrollo de mapas de uso del suelo de alta resolución (HR) a 10 metros en el marco del proyecto RethinkAction H2020, con el objetivo de mejorar la planificación espacial orientada a la mitigación y adaptación climática. La metodología integra datos de teledetección, técnicas de clasificación mediante aprendizaje automático y conjuntos de datos auxiliares para generar clasificaciones precisas y transferibles del uso del suelo en seis regiones bioclimáticas europeas. El estudio emplea imágenes de Sentinel-2 y Landsat-8, utilizando clasificación supervisada con Random Forest (RF) y análisis geográfico basado en objetos (GEOBIA) para mejorar la precisión y reducir la confusión espectral. Este enfoque dio lugar a la creación de doce mapas HR de uso del suelo en dos niveles de clasificación, abarcando seis áreas de estudio de caso (CS). Una contribución clave de esta investigación es la generación de mapas de idoneidad, que evalúan el potencial para implementar soluciones de mitigación y adaptación basadas en el suelo (LAMS), como la reforestación, la captación de agua y el desarrollo de energía fotovoltaica. Este estudio subraya la importancia de integrar teledetección, aprendizaje automático y análisis espacial para respaldar la toma de decisiones fundamentadas en la planificación del uso del suelo, ofreciendo una metodología escalable y replicable para la clasificación detallada de LULC.

**Keywords:** Land Use Maps, GEOBIA, Spatial Analysis Remote Sensing Techniques, High-Resolution Mapping.

**Palabras clave:** Usos del suelo, GEOBIA, Análisis espacial, Teledetección, Cartografía de alta resolución.

**\*Corresponding author:** Patricia Pérez Ramírez and Jesús Ortuno Castillo, Remote Sensing and Geospatial Analytics Division, GMV, Madrid, Spain. Email address: ppramirez@gmv.com; jortuno@gmv.com

## 1. Introduction

Land use mapping is an invaluable tool in the realm of climate change mitigation, serving as a foundational element for greenhouse gas inventories (ESA, 2024). It enables the identification of regions rich in carbon stocks, such as forests, peatlands, and wetlands. These areas are critical for devising strategies aimed at curtailing deforestation and degradation, thereby making significant contributions to climate change mitigation efforts. The precise delineation of land use through mapping is essential for pinpointing these carbon-dense areas, facilitating targeted conservation and management practices that help in reducing atmospheric carbon levels.

Furthermore, land use maps are essential tools in the siting of renewable energy projects, such as solar and wind farms, as they help identify suitable locations while considering environmental, social, and economic factors. Scientific studies have emphasized the importance of integrating land use considerations into renewable energy planning to minimize conflicts and promote sustainable development (Patankar, 2022). The selection of appropriate locations for these projects is crucial to ensure that they have minimal ecological impacts while maximizing energy production. Detailed land use information provided by mapping enables stakeholders to identify sites that are not only suitable for renewable energy generation but also are in harmony with the surrounding environment, thus balancing energy needs with ecological conservation.

LULC mapping is essential for environmental monitoring, urban planning, agriculture, and climate change mitigation. Advances in remote sensing and machine learning have significantly improved classification accuracy, enabling large-scale high-resolution mapping (Gong *et al.*, 2020). Studies have demonstrated its effectiveness in deforestation monitoring (Hansen *et al.*, 2013), urban expansion tracking (Zhao *et al.*, 2022), and land-use planning for renewable energy (Patankar *et al.*, 2022). The use of multi-temporal Sentinel-2 and Landsat-8 imagery has further enhanced spatial and temporal change detection (Holtgrave *et al.*, 2020).

LULC maps are widely used in agriculture and resource management to monitor crop phenology, irrigation, and soil degradation. Remote sensing has been applied to detect irrigated croplands (Wu *et al.*, 2011) and analyze crop phenology in China (You *et al.*, 2013), highlighting the value of HR land classification for precision agriculture and sustainable land-use planning. Additionally, spectral indices like NDVI, NDMI, and NDWI effectively distinguish vegetation types and water bodies in complex landscapes (Costa *et al.*, 2022).

Advancements in machine learning have improved LULC classification accuracy. Random Forest (RF), introduced by Breiman (Breiman, 2001), is widely used for its robust performance with large datasets and ability to reduce overfitting. Studies have shown its effectiveness in multi-temporal and multi-spectral land cover classification (Ramezan *et al.*, 2021; Tang *et al.*, 2021). The integration of GEOBIA with RF further enhances accuracy by reducing salt-and-pepper noise and improving object-based classification, making it a preferred method for HR land cover studies.

The aim of this paper is to detail the process followed in Rethink Action H2020 Project to develop 10-meter high resolution (HR) land use maps for six case study (CS) areas and highlights the significance of developing land use maps and spatial analyses for the strategic allocation of land uses in

different geographical areas. The objective of the selected methodology was to provide detailed land use maps which are aligned with the needs expressed by other project tasks (mainly regarding land use classes), are replicable in other potential CSs, and ensures the use of common inputs wherever feasible, considering the resources allocated for this activity within the project.

## **2. The RethinkAction project**

The RethinkAction project is a European initiative aimed at addressing climate change through innovative land use strategies. Funded by the Horizon 2020 program, it brings together thirteen partners from nine countries, integrating expertise from diverse fields such as social sciences, environmental sciences, and information technology.

Launched in October 2021, RethinkAction is developing a decision-making platform designed for policymakers, stakeholders, and citizens. This platform provides clear, actionable insights on climate change, emphasizing the crucial role of land use in sustaining life and achieving climate objectives. It also raises awareness about how individual and collective behavioral changes can shape land use patterns, thereby encouraging active participation in climate action.

A key component of the project is the creation of HR land use maps, which serve as the backbone for further analysis and decision-making. These HR land use maps are used in the project to create suitability maps through a multi-criteria spatial analysis. These maps support land use allocation modeling within the local System Dynamics (SD) models, whose goal is to define the adaptation and mitigation potential of each selected Land-based Adaptation and Mitigation Solution (LAMS).

### *2.1. Case Studies (CS)*

The HR land use maps have been created for the 6 CSs defined by RethinkAction (Figure 1). The CSs comprise relevant and representative examples of EU based territories with a variety of climate change impacts and land system pressures. The variety and representativeness of the CSs selected ensure a broad replicability of RethinkAction solutions across Europe. The spatial boundaries of the CSs have been defined following the Nomenclature of territorial units for statistics (NUTS) which is a geographical system, according to which the territory of the European Union is divided into hierarchical levels. The three hierarchical levels are known as NUTS -1, NUTS -2 and NUTS -3. RethinkAction uses NUTS-2 and NUTS-3 to define the CSs:

- Boreal CS (CS1): Gotland Region, Sweden (NUTS-3), 3142 km<sup>2</sup>.
- Atlantic CS (CS2): Tarn-et-Garonne, France (NUTS-3), 3730 km<sup>2</sup>.
- Continental CS (CS3): Southern Great Plain, Hungary (NUTS-2), 18332 km<sup>2</sup>.
- Alpine CS (CS4): Valle d'Aosta Region, Italy (NUTS-2), 3261 km<sup>2</sup>.
- Mediterranean CS (CS5): Almería province, Spain (NUTS 3), 8776 km<sup>2</sup>.
- Macaronesia CS (CS6): Azores archipelago, Portugal (NUTS 2), 2302 km<sup>2</sup>.

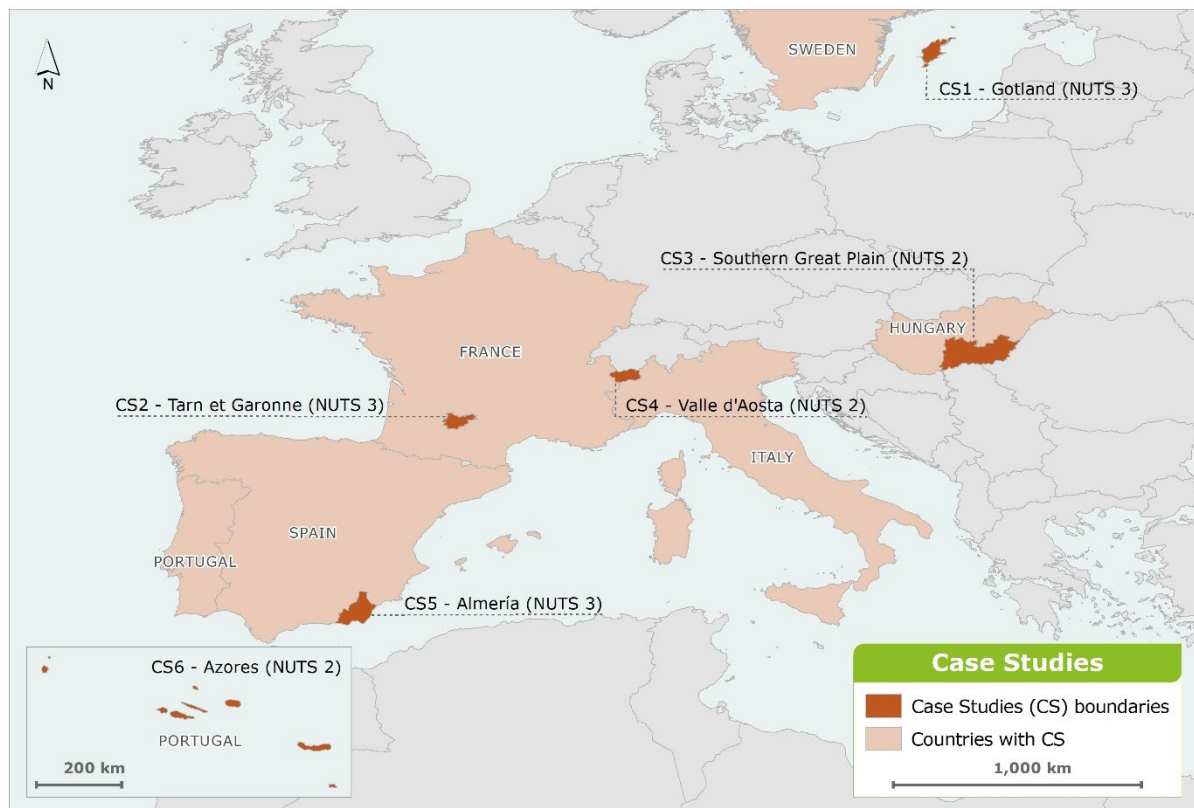


Figure 1.

### 3. Data and methodology

#### 3.1. Land use classes

The land use maps constitute the baseline for RethinkAction to study and assess relevant actions and solutions that are related to land use. The land use maps are the baseline for other RethinkAction tasks, mainly for the development of the local SD models. The design of the land use maps has taken into consideration the requirements provided by the SD models developers and other related project tasks. One of the main requirements was the request of specific land use classes which has resulted in the development of two different levels of land use maps: Level 1 (L1) and Level 2 (L2).

Land use maps L1 is the basic version of the land use maps which includes 12 land use classes. The definition of the L1 of the HR land use maps was based on the requirements mainly provided by the RethinkAction modellers that need the defined land use classes as inputs of the local SD models. Land use maps L2 is an extended version of the L1 land use maps including additional classes requested by the project that were considered for the development of the suitability maps generated for the project as well and based on the HR land use maps too. L2 provides 21 different classes: the ones included in L1 plus the disaggregation of Urban Land, Water and Other Land classes. The list of the classes of the HR land use maps L1 and L2 is included in Table 1.

Table 1. Land use classes of the HR land use maps L1 and L2.

Land use maps L1	Land use maps L2
Rainfed Cropland	Rainfed Cropland
Irrigated Cropland	Irrigated Cropland
Forest Managed	Forest Managed
Forest Primary	Forest Primary

Forest Plantation	Forest Plantation
Shrubland	Shrubland
Grassland	Grassland
Wetland	Wetland
Urban Land	Continuous Urban Land
	Discontinuous Urban Land
	Industrial/Commercial Units
	Roads
	Mining
Solar Land	Solar Land
Water	Water
	Water bodies
	Permanent Snow
Other Land	Bare Rock/Soil
	Sparsely Vegetated
	Beaches/Dunes/Sand

### 3.2. Input data

The input data for obtaining the required land use classifications consist of a combination of freely available satellite imagery and auxiliary data for automatic training site extraction. Specifically:

1. Sentinel-2 and Landsat-8 satellite imagery serve as the primary classification features.
2. A multi-temporal approach was adopted, using four trimestral Sentinel-2 composites (10 bands each) from 2021 and 2022 to represent an agricultural year.

In five of the six CS areas (excluding the Azores archipelago), the four trimestral 10-band Sentinel-2 composites (with 10 m spatial resolution) were processed in Google Earth Engine (GEE). Image compositing was applied to reduce outliers, shadows, and cloud cover, ensuring more accurate land cover classification (Beshir *et al.*, 2023).

Table 2 presents the technical specifications of the satellite data used.

Table 2. Satellite data specifications.

CS	Sensor	Bands	Central Wavelength ( $\mu\text{m}$ )	Spatial resolution (m)	Composite spatial resolution (m)	Time frame
CS1	Sentinel 2	Band 2 - Blue	0.49	10	10	1st trimester - 01/01/2022 - 31/03/2022 2nd trimester - 01/04/2022 - 30/06/2022 3rd trimester - 01/07/2021 - 31/08/2021 4th trimester - 01/09/2021 - 12/12/2021
CS2		Band 3 - Green	0.56	10		
CS3		Band 4 - Red	0.665	10		
CS4		Band 5 - Vegetation Red Edge	0.705	20		
CS5		Band 6 - Vegetation Red Edge	0.74	20		
		Band 7 - Vegetation Red Edge	0.783	20		
		Band 8 - NIR	0.842	10		
		Band 8A - Narrow NIR	0.865	20		
		Band 11 - SWIR I	1.61	20		
		Band 12 - SEIW II	2.19	20		

CS6o	Sentinel 2	Band 2 - Blue	0.49	10		1st trimester - 01/01/2022 - 31/03/2022
		Band 3 - Green	0.56	10		2nd trimester - 01/04/2022 - 30/06/2022
		Band 4 - Red	0.665	10		3rd trimester - 01/07/2021 - 31/08/2021
		Band 8 - NIR	0.842	10		4th trimester - 01/09/2021 - 12/12/2021
		Band 11 - SWIR I	1.61	20		
		Band 12 - SEIW II	2.19	20		
	Landsat 8	Band 2 - Blue	0.482	30		
		Band 3 - Green	0.561	30		
		Band 4 - Red	0.655	30		
		Band 5 - NIR	0.865	30		
		Band 6 - SWIR I	1.609	30		
		Band 7 - SWIR II	2.2	30		

In the Azores islands persistent cloud cover avoided cloud-free Sentinel-2 image composites. Therefore, Landsat 8 was also used in the Azores archipelago CS to cover this lack of cloud-free images. Sentinel 2 and Landsat 8 surface reflectance data were merged and downscaled to 10 meters. This resulted into four cloud-free median composites, one per trimester (2021 – 2022), each with 6 bands: Blue, Green, Red, Near InfraRed (NIR), Short-Wave InfraRed1 (SWIR1) and Short-Wave InfraRed2 (SWIR2).

To complete the set of classification features, the following spectral indices composites (using maximum values) were computed in GEE for each CS and each trimester: Normalized Difference Vegetation Index (NDVI), Bare Soil Index (BSI), Moisture Stress Index (MSI), Normalized Difference Moisture Index (NDMI), Normalized Difference Snow Index (NDSI), and Normalized Difference Water Index (NDWI).

For the extraction of training sites several datasets from the Copernicus Land Monitoring Service (CLMS) were used. The most recent datasets of the products were used, which are dated from 2018. To complement these datasets and to guarantee efficient training site extraction (see section Training site extraction), local land use/land cover data and different thematic land masks were requested and provided by the CS leaders. Other additional datasets such as the Solar Land feature from OpenStreetMap (OSM) as well as the 2015 Global Forest Management data (GFMD) were also used for training site extraction. Table 3 shows a summary of ancillary data used for this purpose.

Table 3. Ancillary data.

Data provider	Dataset	Date	CS	Source
CLMS	Corine Land Cover (CLC)	2018	All	<a href="https://land.copernicus.eu/pan-european/high-resolution-layers">https://land.copernicus.eu/pan-european/high-resolution-layers</a>
	Imperviousness Density (IMD)	2018	All	
	Impervious Built-up (IBU)	2018	All	
	Dominant Leaf Type (DLT)	2018	All	
	Tree Cover Density (TCD)	2018	All	
	Grassland (GRA)	2018	All	
	Water and Wetness (WAW)	2018	All	
	Urban Atlas (UAtlas)	2018	CS3 CS4 CS5 CS6	
National Geographic Information Center (CNIG) [Centro Nacional de Información Geográfica]	Natura 2000 (NK200)	2018	All	<a href="http://centrodedescargas.cnig.es/CentroDescargas/catalogo.do?Serie=SIOSE">http://centrodedescargas.cnig.es/CentroDescargas/catalogo.do?Serie=SIOSE</a>
	Sistema de Información sobre Ocupación del Suelo de España (SIOSE)	2018	CS5	
	Superficies de Secano (Rainfed)	2013		

Ministry of Agriculture of Hungary (AM) [Agrárminisztérium]	Ökoszisztemá-alaptérkép/ Ecosystem Map of Hungary (OSZ)	2015-2017	CS3	<a href="http://alapterkep.termeszetem.hu/">http://alapterkep.termeszetem.hu/</a>
Swedish Environmental Protection Agency [Naturvårdsverket]	Naturvårdsverket/National Land Cover Database (NMD)	2018	CS1	<a href="https://www.naturvardsverket.se/en/services-and-permits/maps-and-map-services/national-land-cover-database/">https://www.naturvardsverket.se/en/services-and-permits/maps-and-map-services/national-land-cover-database/</a>
National Institute of Geographic and Forest Information (IGN-F) [Institut national de l'information géographique et forestière]	Occupation du sol/Land cover map (LUF)	2013	CS2	<a href="https://www.data.gouv.fr/fr/datasets/occupation-du-sol-2013-tarn-et-garonne/">https://www.data.gouv.fr/fr/datasets/occupation-du-sol-2013-tarn-et-garonne/</a>
National Geographic Information System (SNIG) [Sistema Nacional de Informação Geográfica]	Carta de Ocupação do Solo Açores/Land Cover Map Azores (COS)	2018	CS6	<a href="http://ot.azores.gov.pt/CO SA-2018.aspx">http://ot.azores.gov.pt/CO SA-2018.aspx</a>
Institute for the Financing of Agriculture and Fisheries (IFAP) [Instituto de Financiamento da Agricultura e Pesca]	Sistemas de Identificação Parcelar/Agriculture Parcels Cultures (Parcels)	2015		<a href="https://publico-isip.ifap.pt/web/Index.aspx">https://publico-isip.ifap.pt/web/Index.aspx</a>
Copernicus Emergency Management Service (EMS)	Land use maps built under the framework of EMSN018 (EMS)	2015		<a href="https://emergency.copernicus.eu/mapping/list-of-components/EMSN018">https://emergency.copernicus.eu/mapping/list-of-components/EMSN018</a>
Department of Public Works, Territory and Environment. Autonomous Region of Aosta Valley [Assessorato opere pubbliche, territorio e ambiente. Région Autonome Vallée d'Aoste]	Copertura del Suolo della Valle d'Aosta/Land use VdA (VdA)	2020	CS4	<a href="https://mappe.partout.it/pub/GeoNavSCT/?repertorio=copertura_suolo">https://mappe.partout.it/pub/GeoNavSCT/?repertorio=copertura_suolo</a>
Lesiv, M., Schepaschenko, D., Buchhorn, M. <i>et al.</i>	GFMD	2015	All	<a href="https://zenodo.org/record/4541513#.Y6BDCXbMKUm">https://zenodo.org/record/4541513#.Y6BDCXbMKUm</a>
OpenStreetMap (OSM)	Solar Plants	Unknown	All	<a href="https://www.openstreetmap.org/">https://www.openstreetmap.org/</a>

### 3.3. Approach and Methods

LULC classification using Sentinel-2 and Landsat-8 imagery is a widely used remote sensing method. Sentinel-2's high spatial resolution enhances differentiation between vegetation, urban areas, and water bodies (Zhang *et al.*, 2022), while Landsat-8's long-term data supports time-series land cover analysis (Huang *et al.*, 2021).

Multi-temporal analysis improves LULC classification accuracy by capturing seasonal vegetation changes. Trimestral Sentinel-2 composites enhance crop and forest classification (García *et al.*, 2023). Additionally, spectral indices like NDVI and NDWI refine classification; NDVI quantifies vegetation health (Jones *et al.*, 2020), while NDWI enhances water detection by suppressing soil and vegetation reflectance (Gao, 1996).

These indices, when integrated into classification models, significantly improve the differentiation between various land cover types. As highlighted by other authors (Liu *et al.*, 2022), "combining NDVI and NDWI with Sentinel-2 and Landsat-8 imagery enhances the accuracy of LULC classifications by reducing spectral confusion among similar classes".

The HR land use maps were produced using a Geographic Object-Based Image Analysis (GEOBIA) approach, which simulates human visual perception by grouping pixels into objects/segments based on context and neighbourhood characteristics. Unlike pixel-based methods, where classification units are uniform pixels, GEOBIA uses image-objects, incorporating statistical, geometrical, and textural data for improved accuracy (Costa *et al.*, 2022). This method is particularly effective for high-resolution image classification and reduces the salt-and-pepper effect, minimizing classification noise. Figure 2 illustrates the workflow applied in the case studies. Figure 2 illustrates the workflow applied in the case studies. Figure 2 shows the workflow applied in the CSs.

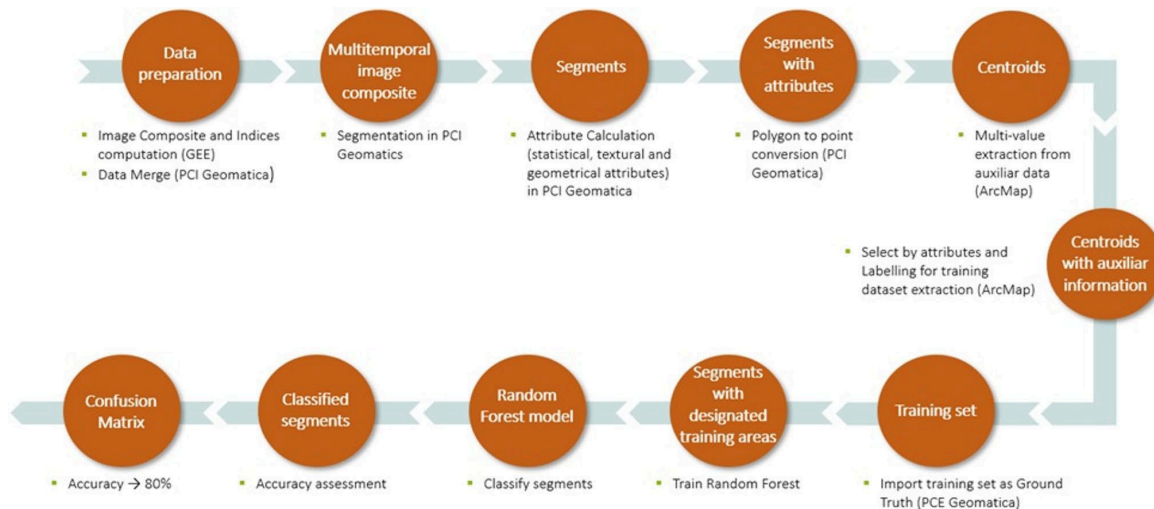


Figure 1. Classification process workflow.

As shown in the figure above, the processes were conducted using Google Earth Engine (GEE), PCI Catalyst Professional (PCI), and ArcMap. GEE was used for satellite imagery compositing (trimestral median values) and indices computation (trimestral maximum values), while PCI handled the GEOBIA process, including data merging, segmentation, attribute calculation, and Random Forest classification. Training sets were extracted and labelled using ArcMap.

Several studies confirm the effectiveness of Sentinel-2 and Landsat-8 for LULC classification. Sentinel-2 excels in urban mapping, while Landsat-8 is better suited for large-scale land cover assessments (Huang *et al.*, 2021). Combining both datasets enhances classification accuracy compared to using either alone (García *et al.*, 2023). The RethinkAction project's methodology, integrating Sentinel-2, Landsat-8, spectral indices, and multi-temporal compositing, aligns with these findings, ensuring high accuracy, particularly for vegetation and water body differentiation, which is essential for suitability mapping in land-based mitigation and adaptation solutions.

### 3.3.1. Segmentation and Attribute Calculation

The classification process incorporated a 64-layer raster dataset combining auxiliary data and spectral indices to enhance accuracy by capturing spectral, spatial, and temporal characteristics. However, this multi-layered approach introduces redundancy and correlation among variables, potentially causing computational inefficiencies and overfitting (Huang *et al.*, 2021).

To mitigate redundancy, dimensionality reduction techniques like Principal Component Analysis (PCA), Independent Component Analysis (ICA), and Feature Selection Algorithms are commonly used in remote sensing (Duro *et al.*, 2012). While no explicit reduction was applied, these methods were considered in structuring the workflow. Retaining all indices ensures no critical data loss,

though future iterations may explore automated feature selection to enhance efficiency and reduce correlation.

After computing median image composites and indices, they were merged into a 64-channel raster file and used for segmentation. The multiresolution segmentation algorithm in PCI (Ramezan *et al.*, 2021) was applied to generate a vector layer of statistically homogeneous objects, distinguishing them based on spectral and spatial characteristics. The segmentation parameters included:

- Scale: Controls object size; smaller values create more homogeneous, detailed segments, while larger values generate fewer, more heterogeneous objects.
- Shape (0.1–1.0): Adjusts the weight of spectral values, with lower values emphasizing pixel intensity.
- Compactness (0.1–1.0): Defines boundary smoothness, where higher values produce compact objects like crop fields or buildings.

The scale parameter, often the most critical, is typically selected through trial and error (Ramezan *et al.*, 2021). The goal was to create homogeneous segments, minimizing mixed objects to ensure accurate automatic training site extraction based on segment centroids. The chosen parameters were scale: 35, shape: 0.1, and compactness: 0.9.

GEOBIA's advantage over pixel-based classification is its ability to incorporate additional predictors beyond spectral data. PCI computes various spatial and statistical variables, allowing the classification model to determine their relevance. A total of 26 classification features were used:

- Spectral Parameters: Min, max, mean, and standard deviation (STD) were calculated for each band, totaling 256 spectral variables.
- Textural Features: Three co-occurrence-based metrics (mean, entropy, and contrast) were computed using VISIR bands (Red, Green, Blue, Infrared) across all trimesters, resulting in 48 variables. Due to high computational costs, only these key textural features were selected.
- Geometrical Attributes: Nine features (compactness, elongation, circularity, rectangularity, convexity, solidity, form factor, and major/minor axis length) were processed. These are shape-based and require less computational power than spectral or textural measures.
- Vegetation Indices: Ten indices, including NDVI, SAVI, GEMI, and LAI, were computed for the driest trimester, as PCI allowed only one trimester selection.

This approach optimizes classification accuracy while balancing computational efficiency. Overall, a high number of classification features were considered to provide enough information and allow the classification model to decide the relevance of each feature.

### 3.3.2. Training site extraction

After segmentation, the next step in GEOBIA is training sample collection. Unlike pixel-based approaches, where training areas are polygons delineating individual pixels, object-based image analysis (OBIA) assigns labels to image segments (Khan *et al.*, 2021). This method leverages segment homogeneity, reducing noise and enhancing classification accuracy compared to traditional pixel-based classification (Miranda *et al.*, 2018).

However, the manual extraction of training sites through photointerpretation was deemed unsuitable for this study due to the high number of segments and the large size of the CSs. As highlighted (Hussain *et al.*, 2013), "while manual interpretation remains a valuable tool for high-accuracy training data collection, it is often impractical for large-scale applications due to the high labor and time requirements". Similarly, Blaschke (Blaschke, 2010) emphasized that automated or semi-automated

training sample selection methods are increasingly necessary in large-scale GEOBIA studies to ensure feasibility and consistency in classification.

Given these constraints, alternative automated training site extraction methods have been explored in recent studies, such as machine learning-driven feature selection and rule-based classification strategies, which improve both efficiency and accuracy in LULC classification (Duro *et al.*, 2012).

This is mainly because manual training site extraction is very time consuming and human resource dependent. In addition, there is a lack of local terrain samples and a low spatial resolution of the input data which could not guarantee the quality of the training samples. Therefore, an automatic training site extraction methodology based on previous work of Costa was used (Costa *et al.* 2022).

The computed segments for each CS were converted into centroids and imported into ArcMap. Using the Extract Multi Values to Point tool, these points were assigned attributes from ancillary data for SQL-based labeling. This method requires homogeneous segments to ensure each point represents a single land use class. Labeling was performed through specific queries, e.g., points overlapping CLC Continuous Urban areas, matching local land use maps, and having >80% Imperviousness were classified as Continuous Urban Land. Table 4 illustrates an example of the ArcGIS queries build for the Southern Great Plain CS.

The Solar Land class from OSM was used as an input for training the Solar Land class of the RethinkAction land use maps. The polygons imported from the OSM data were subjected to a visual inspection for refinement before integrating them into the process

*Table 4. Queries in ArcGIS applied to the Southern Great Plain CS for point labelling.*

As que	Nomenclature_Level1	Code_Level2	Nomenclature_Level 2	Labelling rules
1; 2	Cropland (Rainfed and Irrigated)	1.1; 2.1	Annual	"CLC" in (12) and "OSZ" in(2100,2230) and "IMD" =0 and "WAW"=0 and "TCD" =0 and "GRASS" = 0 or "UAtlas" = 2 and "OSZ" in(2100,2230) and "IMD" =0 and "WAW"=0 and "TCD" =0 and "GRASS" = 0
		1.2; 2.2	Permanent	"CLC" in (15,16) and "OSZ" in (2210,2220) "IMD" =0 and "WAW"=0 and "IBU"=0 and "GRASS"=0 and "WAW"=0 or "UAtlas" = 18 and "OSZ" in (2210,2220) "IMD" =0 and "WAW"=0 and "IBU"=0 and "GRASS"=0 and "WAW"=0
		1.3; 2.3	Pastures	"CLC"=18 and "OSZ" in (3110,3120,3200) and "IBU"=0 and "TCD"=0 and "WAW"=0 and "GRASS"=1 or "UAtlas" =3 and "OSZ" in (3110,3120,3200) and "IBU"=0 and "TCD"=0 and "WAW"=0 and "GRASS"=1
3	Forest	3	Forest	"CLC" in (23,24,25) and "OSZ" in (4301,4302,4303,4304,4305,4306,4307,4308,4309,4401,4402,4403,4403) and "DLT" in (1,2) and "TCD" > 50 and "IMD"=0 and "WAW" = 0 or "UAtlas" =8 and "OSZ" in (4301,4302,4303,4304,4305,4306,4307,4308,4309,4401,4402,4403,4403) and "DLT" in (1,2) and "TCD" > 50 and "IMD"=0 and "WAW" = 0

6	Shrubland	6	Shrubland	"CLC"=29 and "OSZ" in (4502,4600,3500) and "TCD" < 30 and "WAW" =0 and "IMD"=0 or "UAtlas" = 19 and "OSZ" in (4502,4600,3500) and "GRASS"=0 and "TCD">> 30 and "WAW" =0 and "IMD"=0
7	Grassland	7	Grassland	"CLC" = 26 and "OSZ" in (3110,3120,3200,3400,3500) and "GRASS"=1 and "WAW"=0 and "TCD"<15 and "IMD"=0 or "UAtlas"= 19 and "OSZ" in (3110,3120,3200,3400,3500) and "GRASS"=1 and "WAW"=0 and "TCD"<15 and "IMD"=0
8	Wetland	8	Wetlands	"CLC" in (36,35) and "OSZ" in (5110,510,5200) and "WAW" in (3,4) and "IMD"=0 or "UAtlas" =21 and "OSZ" in (5110,510,5200) and "WAW" in (3,4) and "IMD"=0
9	Urban Land	9.1	Continuous	"CLC"=2 and "OSZ" in (1110,1120,1310) and "IMD" > 80 and "IBU"=1 and "TCD"=0 and "GRASS" =0 and "WAW" = 0 or "UAtlas" =1 and "OSZ" in (1110,1120,1310) and "IMD" > 80 and "IBU"=1 and "TCD"=0 and "GRASS" =0 and "WAW" = 0
		9.2	Discontinuous	"CLC"=2 and "OSZ" in (1110,1120,1310) and "IMD" < 80 and "IBU"=1 and "TCD"=0 and "GRASS" =0 and "WAW" = 0 or "UAtlas" in (5,9,11,14) and "OSZ" in (1110,1120,1310) and "IMD" < 80 and "IBU"=1 and "TCD"=0 and "GRASS" =0 and "WAW" = 0
		9.3	Industrial/commercial	"CLC"=3 and "OSZ" in (1110,1120,1310) and "IMD" >60 and "TCD"=0 and "GRASS" =0 and "WAW" = 0 or "UAtlas" = 4 and "OSZ" in (1110,1120,1310) and "IMD" >60 and "TCD"=0 and "GRASS" =0 and "WAW" = 0
		9.4	Mining	"CLC"=7 and "TCD"=0 and "GRASS"=0 and "WAW"=0 or "UAtlas" = 6 and "TCD"=0 and "GRASS"=0 and "WAW"=0
		9.5	Roads/Railways	"OSZ"= 1210 and "IMD">>60 and "GRASS"=0 and "TCD" = 0 and "WAW"=0 or "UAtlas" = 13 and "IMD">>60 and "GRASS"=0 and "TCD" = 0 and "WAW"=0
10	Solar land	10	Solar	Spatial Selection based on OSM data
11	Snow, ice, waterbodies	11	Water	"CLC" in (40,41) and "OSZ" in (6100,6200) and "WAW" in (3,4) and "IMD"=0 and "TCD"=0 and "GRASS"=0 or "UAtlas" = 10 and "OSZ" in (6100,6200) and "WAW" in (3,4) and "IMD"=0 and "TCD"=0 and "GRASS"=0
12	Other land	12	Bare rock/soil/Sparsely vegetated	"CLC" = 32 and "TCD">>15 and "GRASS"=1 and "WAW"=0 and "IMD"= 0 or "OSZ" = 4501 and "TCD">>15 and "WAW"=0 and "IMD"= 0

The training points are imported as “Ground truth” to PCI. The underlying segments of each labelled point were assigned as training segments and used to train the Random Forest model as explained in the next section.

### 3.3.3. Random Forest training and Object classification

The Random Forest algorithm is a supervised ensemble machine-learning classifier that constructs multiple decision trees (Breiman, 2001). Each decision tree is generated by randomly selecting a subset of the training data and variables. The effectiveness of the Random Forest approach has been demonstrated in various remote sensing applications, such as land surface temperature downscaling (Tang *et al.*, 2021), highlighting its robustness and supporting its suitability for LULC classification in this study. By introducing randomization into the learning process, the classifier generates multiple models from the same dataset and aggregates their predictions, improving accuracy and reducing overfitting. In other words, after training, each unknown sample is classified based on a majority vote from the ensemble of decision trees, enhancing classification reliability.

Random Forest has gained increasing popularity in remote sensed image classification due to very high accuracies compared to other commonly used classifiers, ease of parametrization, robustness in the presence of noise and its ability to handle high-dimensional datasets (important consideration for multi-spectral object-based analysis) (Costa *et al.*, 2022). The Random Forest classifier was chosen because of two main reasons: the high number of training areas (in theory, the higher the training set, the higher the randomness level, and thus a more efficient learning process is accomplished) and due to the less intensive computation of the classifier compared to other machine-learning classifiers (i.e., Support Vector Machine). Figure 3 shows a simplified schematization of the Random Forest algorithm.

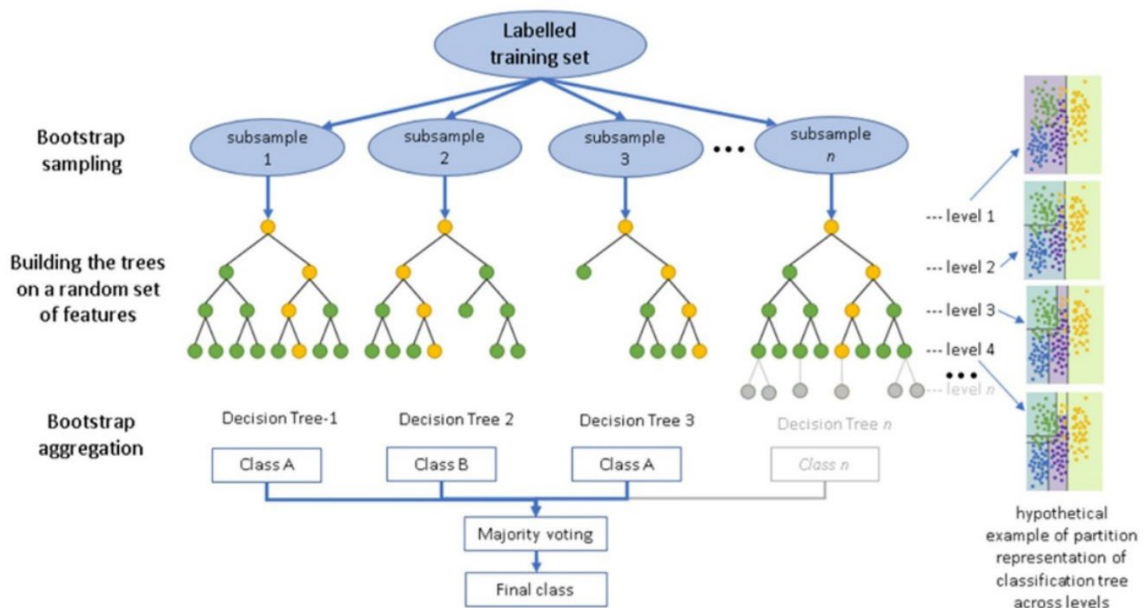


Figure 2: Simplified scheme of the Random Forest algorithm (image extracted from PCI Catalyst Help platform, 2021)

In PCI, the Random Forest classifier uses the OpenCV implementation and uses the following parameters:

- Maximum tree depth: maximum number of levels leaf nodes below the root node.
- Minimum number of samples: minimum number of samples at a leaf node to allow it to be further split into child nodes.
- Active variables: number of randomly selected subset of prediction variables (attributes).

- Tree accuracy (based on the Gini Impurity index): accuracy value used to stop a tree from growing.
- Maximum number of trees: number of trees to generate during the classification process.

The first three parameters determine the split point for a node on each decision tree, while the last two are used as stopping criteria in the Forest growth (both parameters can be used as stopping criteria individually or in a combination of both). The active variable parameter is, by default, set to 0 allowing the classifier to use the square root of the total number of input attributes. The tree accuracy and the maximum number of trees parameters can be used together as stopping criteria (when one is reached the forest stops growing) or can be used individually. Table 5 shows the values for each Random Forest parameter used in the classification of all CSs.

*Table 5. Random Forest parameter used in this study.*

Random Forest parameter	Parameter value
Max tree depth	20
Min samples count	35
Active variables	0
Max number of trees	500
Trees accuracy	0.05

Max number of trees was set as the stopping criteria and therefore the Trees accuracy was left by default and was not used as a stopping criterion in the Random Forest generation.

### 3.3.4. Post classification – Forest and Cropland classes

The previous classification method only enables the extraction of the forest class as one single class. Same applicable for cropland class. The lack of ancillary information, the low spatial resolution of the input data and limited resources disable the extraction of sub-classes during the classification process. For the differentiation of the forest area into the three requested forest classes (Forest Managed, Forest Primary, and Forest Plantation) and the cropland classes (Rainfed Cropland and Irrigated Cropland) a post-processing approach was implemented.

For the forest classes, the segments classified as Forest were intersected with the GFMD (see Table 3). In those segments where the auxiliary forest layer (GFMD) did not overlap with the forest mask from the classification, Copernicus Natura 2000 layer (see Table 3) was used to complement the information. Table 6 shows the correspondences between the classes of the global forest management layer, Natura 2000 forest classes and the RethinkAction HR land use classes. Most of the forest mask has been classified using the two referred ancillary datasets, but in some cases small and isolated segments could not be classified. For those segments, a spatial join operation was performed using the closest feature to guide the joining process.

*Table 6. Correspondence between ancillary forest layers and RethinkAction HR land use classes.*

Global Forest Management Data (GFMD)		
Global Forest Management Code	Global Forest Management classes	RethinkAction HR Land Use classes
11	Naturally, regenerating forest without any signs of human activities, e.g., primary forests	4 - Forest Primary
20	Naturally, regenerating forest with signs of human activities, e.g., logging, clear cuts etc.	3 - Forest Managed

31	Planted forest	3 - Forest Managed
32	Short rotation plantation for timber	5 - Forest Plantation
40	Oil palm plantations	Cropland (not considered)
53	Agroforestry	Cropland (not considered)
Natura 2000 (N2K 2018)		
Natura 2000 Code	Natura 2000 classes	Rethink HR Land Use Classes
4230	Agroforestry	Cropland (not considered)
3110	Natural, semi-natural broadleaved forest	4 - Forest Primary
3120	Highly artificial broadleaved plantations	5 - Forest Plantation
3210	Natural, semi-natural coniferous forest	4 - Forest Primary
3220	Highly artificial Coniferous plantations	5 - Forest Plantation
3310	Natural, semi-natural mixed forest	4 - Forest Primary
3320	Highly artificial mixed plantations	5 - Forest Plantation
3400	Transitional woodland and scrub	4 - Forest Primary
3500	Line of trees and scrub	4 - Forest Primary
3600	Damaged forest	4 - Forest Primary

Regarding cropland classes, the differentiation between rainfed and irrigated croplands was requested for the modelling needs. Several approaches were explored but finally it was decided to use a thresholding of vegetation indices. The selected vegetation indices are: NDVI, NDWI and NDMI. The NDVI is an index that indicates the greenness, density, and health of vegetation in each pixel. Thus, it is suitable for estimating the vegetation vigour throughout the crop cycle. The NDWI reflects moisture in plants and soil and therefore relates strongly with water content, while the NDMI detects moisture levels in vegetation. These indices are commonly used to assess the water stress of vegetation (Haralick, 1979; Wu *et al.*, 2011). The chosen approach is based on thresholding of the vegetation indices during the third trimester of the year as this is a period where the separation between irrigated and rainfed is possible, because of the crop's phenology cycle. Thresholding for rainfed and irrigated cropland differentiation is a well-documented process (Holtgrave *et al.*, 2020). In the Azores archipelago CS, no differentiation was possible due to high values of the indices in analysis and the assumption that no relevant irrigated cropland is present (based on the reference land cover and land use maps as well as the rainfall regime of the region) (You *et al.*, 2013; SNIG, 2018).

Thresholds were defined by trial and error to be adapted to the agroecological conditions of each CS, and the outputs were analysed and validated through visual inspection. Table 7 shows the final thresholds applied on the segments classified as Cropland. Segments with lower values than the indices thresholds shown in Table 7 were classified as rainfed and higher values as irrigated. NDVI was the main driver of the assignation supported by NDWI and NDMI.

Table 7. Thresholds used for Cropland differentiation.

CS	NDVI	NDWI	NDMI
CS1	0.5	0.5	0.3
CS2	0.6	0.55	0.3
CS3	0.45	0.35	0.25
CS4	0.6	0.64	0.2
CS5	0.2	0.25	1.7

### 3.4. Thematic accuracy assessment

A thematic accuracy assessment of all HR land use maps was conducted using a stratified random sampling approach to ensure an unbiased and representative validation process. The methodology followed these key steps:

- Stratified random sampling was applied to ensure that the sample was randomly distributed, reducing human bias.
- The sample was stratified per class to guarantee that all land use categories had a nonzero probability of inclusion.
- Validation points were generated randomly without classification information and labeled through visual photointerpretation by independent experts following a “four-eyes” review process.
- One hundred validation points per class were initially used, with a minimum of 20 points for smaller land cover classes to ensure statistical significance.
- Sample stratification was based on class area, meaning larger land cover types were assigned proportionally more validation points.
- Due to limited validation data, the three forest classes (Forest Managed, Forest Primary, and Forest Plantation) were validated as a single forest class to improve classification reliability.

#### 3.4.1. Accuracy Metrics and Confusion Matrix Analysis

The classification accuracy was assessed by comparing the mapped features against a reference database (ground truth), obtained through visual interpretation of satellite imagery. A confusion matrix was produced to calculate:

- Overall Accuracy (OA) – The proportion of correctly classified points across all land use classes.
- Producer Accuracy (PA) – The likelihood that a reference land cover type is correctly classified in the final map (indicating omission errors).
- User Accuracy (UA) – The probability that a classified land cover type matches the real-world category (indicating commission errors).

Table 8 presents the OA, PA, and UA values extracted from the confusion matrices for each CS at both classification levels L1 and L2.

*Table 8. OA, PA, UA confusion matrices summary table.*

Case Study (CS)	L1 OA (%)	L2 OA (%)	L1 PA Range (%)	L1 UA Range (%)	L2 PA Range (%)	L2 UA Range (%)
CS1	85	83	67 - 95	72 - 98	65 - 93	70 - 96
CS2	86	86	23 - 97	57 - 100	20 - 95	55 - 98
CS3	94	91	71 - 99	74 - 99	68 - 97	72 - 98
CS4	95	90	69 - 100	60 - 100	65 - 98	58 - 99
CS5	84	82	59 - 96	60 - 100	55 - 95	57 - 98
CS6	93	91	70 - 98	73 - 99	68 - 96	70 - 98

The accuracy results demonstrate strong classification performance, with Overall Accuracy (OA) ranging from 82% to 95% across different CSs.

- The highest accuracy was observed in CS4 at L1 (95%) and CS3 at L2 (91%), reflecting well-differentiated land cover types in these regions.
- Producer Accuracy (PA) indicates that certain land cover classes had higher omission errors, particularly in CS2 where PA values ranged from 23% to 97%.
- User Accuracy (UA) remained consistently high, with values exceeding 99% in some categories, particularly in CS6 and CS3, indicating strong classification reliability.

#### 4. Results and discussion

The created HR land use maps are in line with the requirements defined by the project in terms of spatial resolution, land use classes, spatial coverage and overall accuracy. The input data are as recent as possible to provide a full temporal and spatial coverage of the Areas of Interest (AOIs) dealing with unavailability of free cloud composites in part of the areas.

Figure 4 to 15 present the High Resolution (HR) land use maps for levels L1 and L2 across the six RethinkAction case studies (CS1–CS6). These case studies span diverse biogeographical regions in Europe and represent a wide range of land use dynamics and environmental conditions. The maps provide a detailed baseline for spatial analysis and scenario modelling.

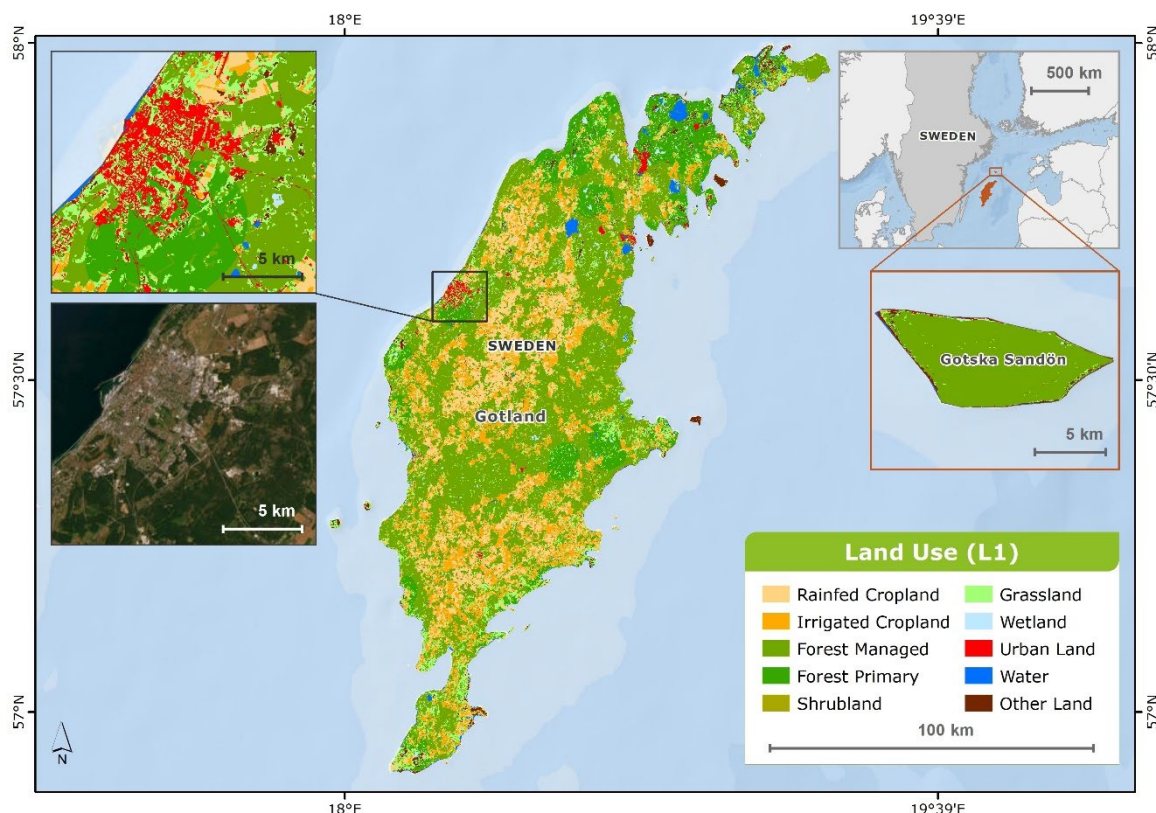


Figure 4: L1 HR land use map of CS1–Gotland Region.

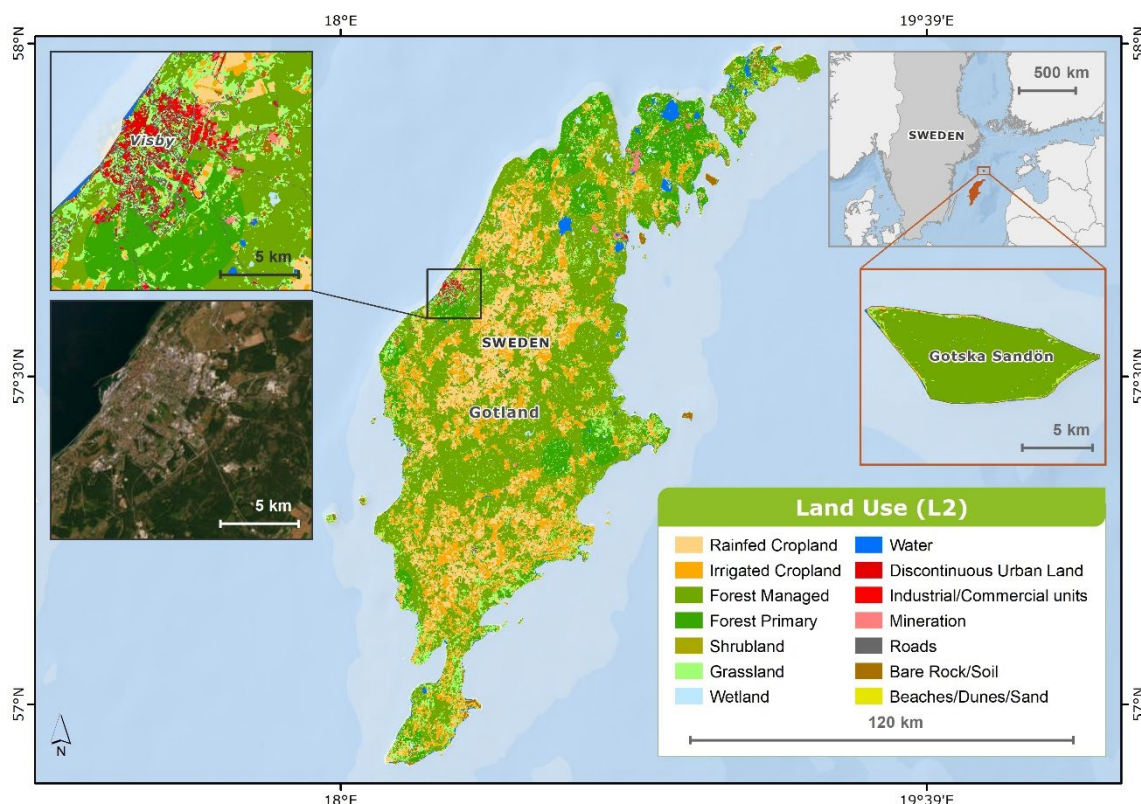


Figure 5: L2 HR land use map of CS1–Gotland Region.

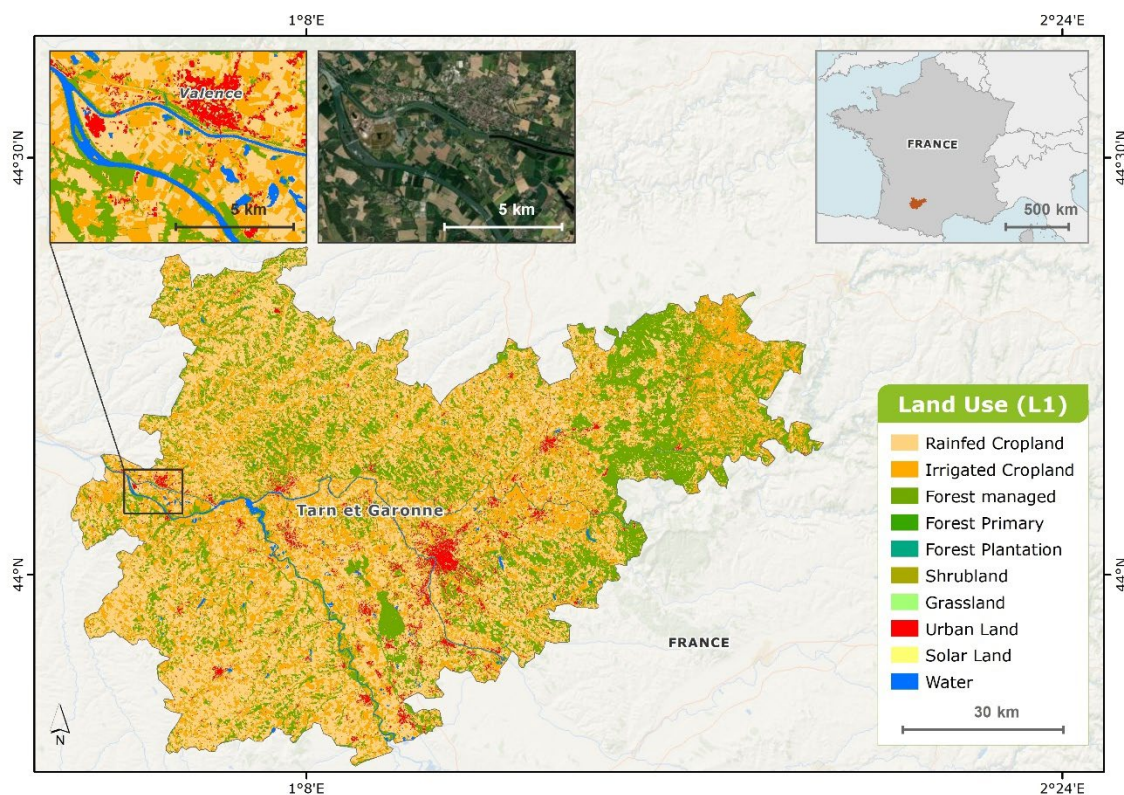


Figure 6: L1 HR land use map of CS2–Tarn-et-Garonne.

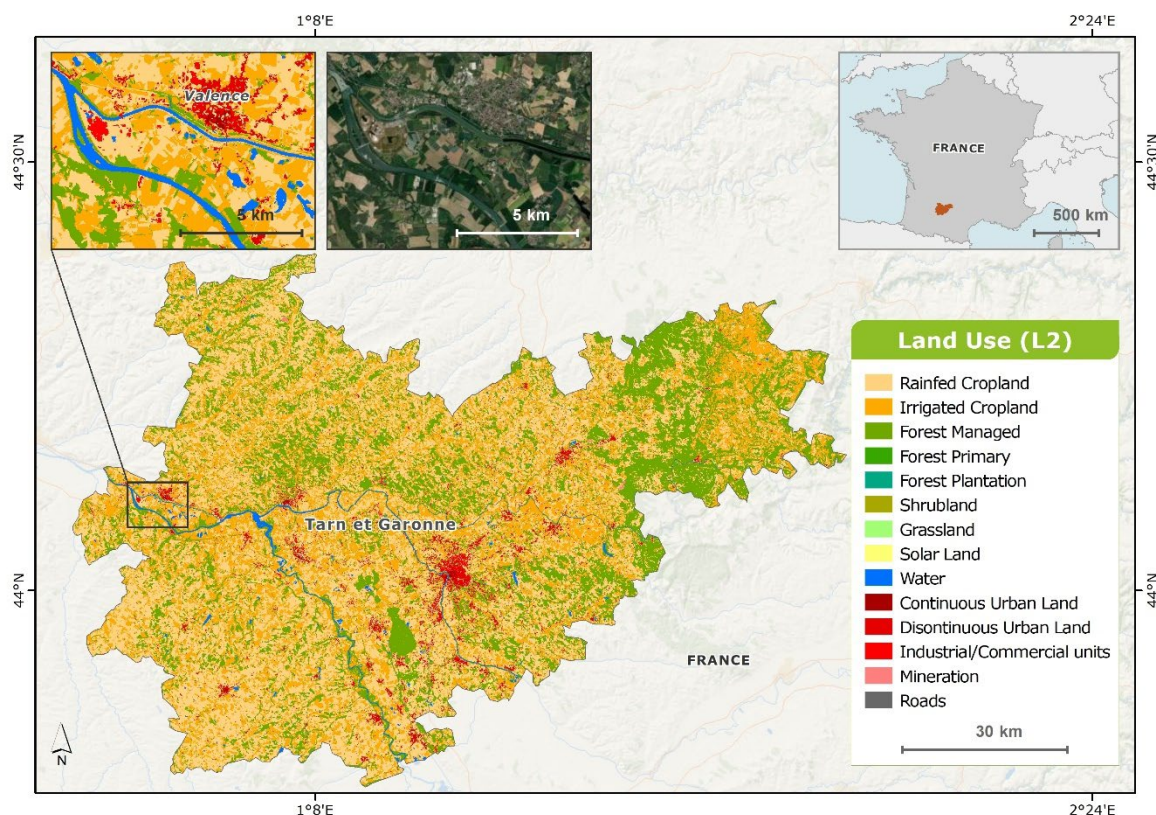


Figure 7: L2 HR land use map of CS2–Tarn-et-Garonne.

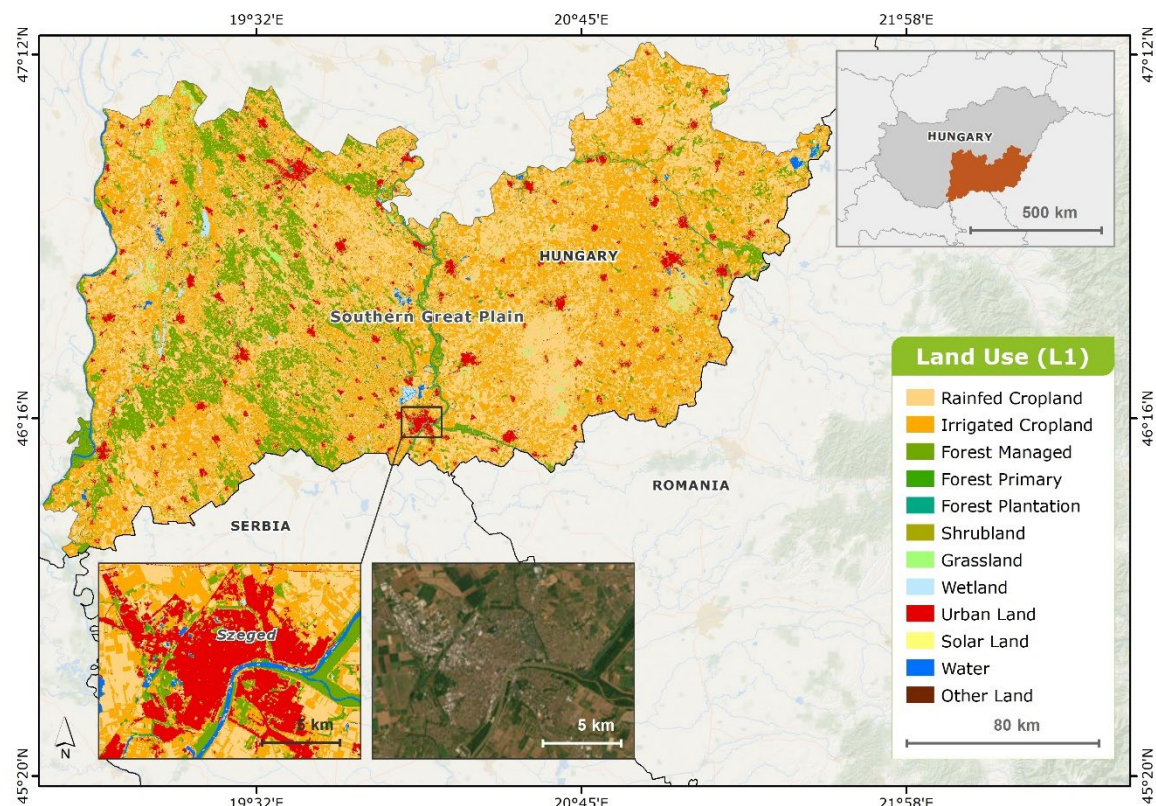


Figure 8: L1 HR land use map of CS3–Southern Great Plain.

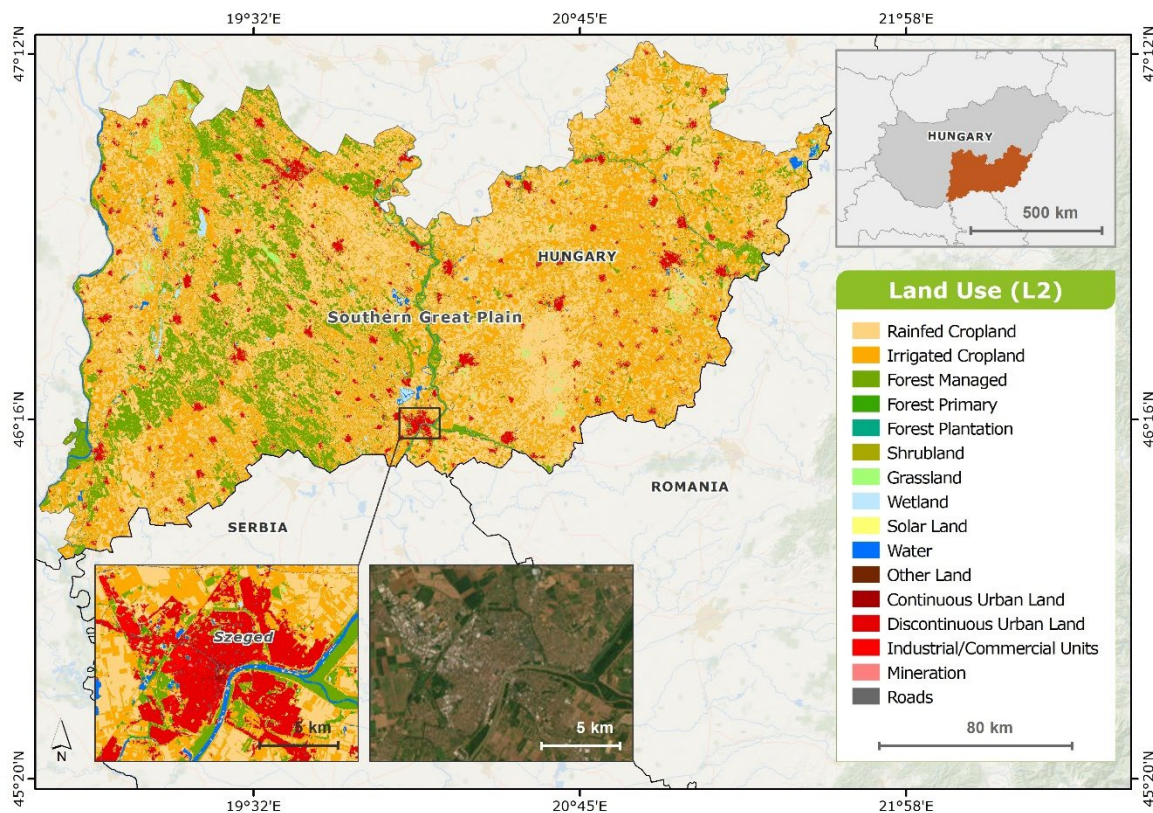


Figure 9: L2 HR land use map of CS3–Southern Great Plain.

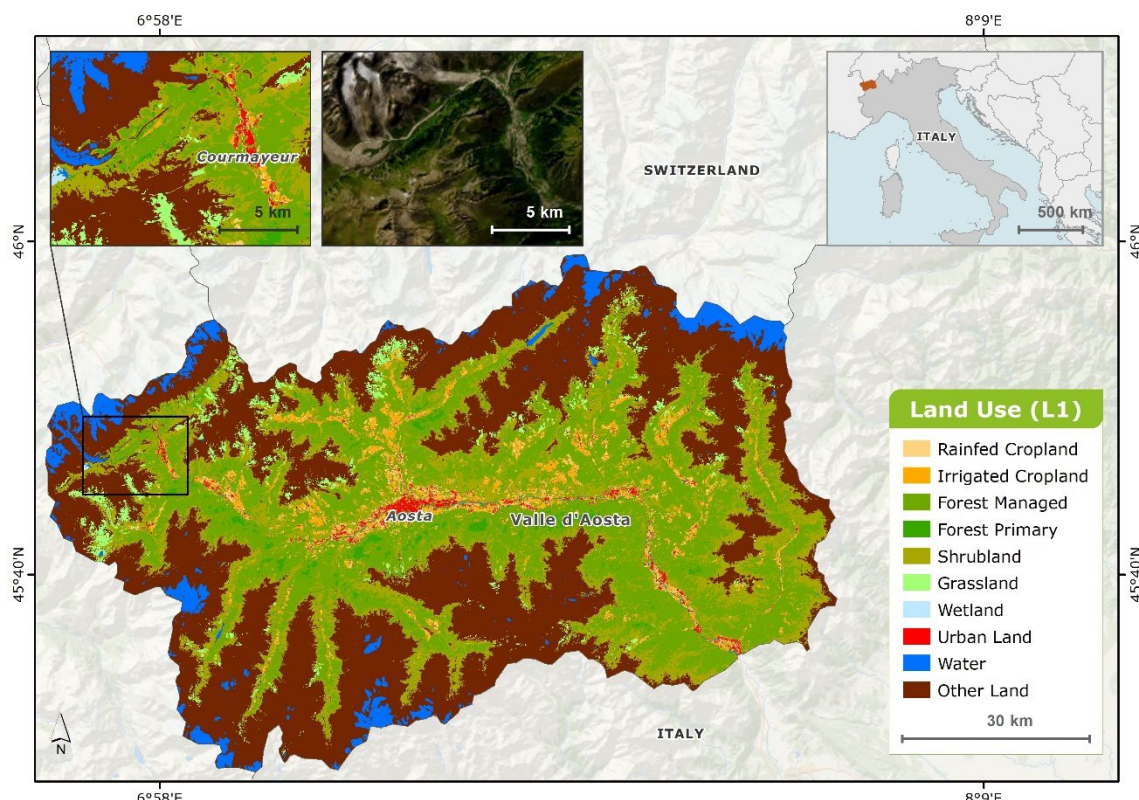


Figure 10: L1 HR land use map of CS4–Valle d'Aosta Region.

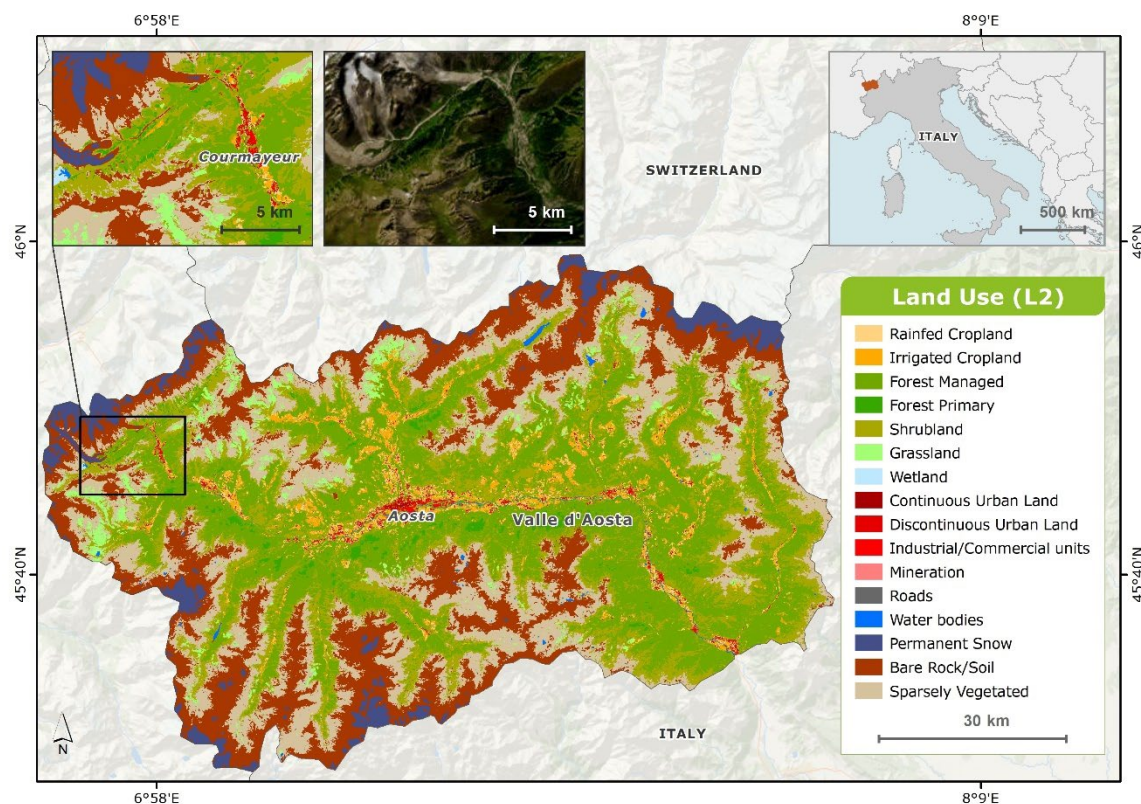


Figure 11: L2 HR land use map of CS4–Valle d'Aosta Region.

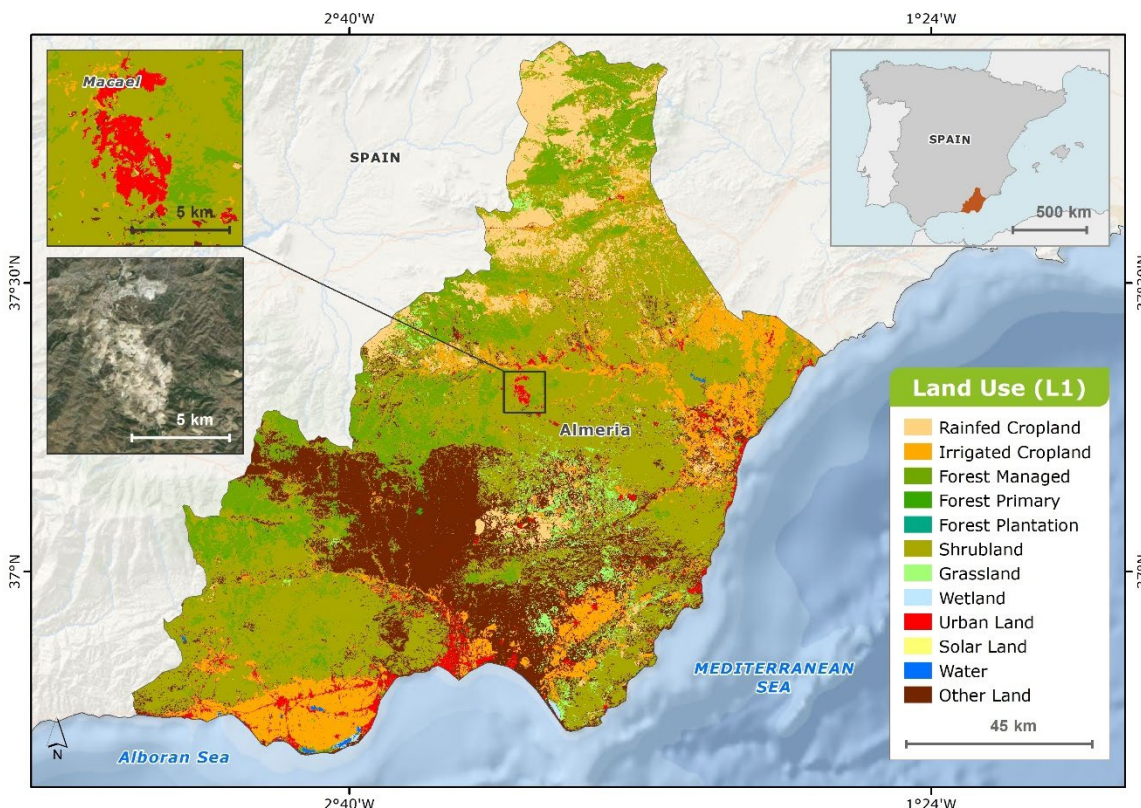


Figure 12: L1 HR land use map of CS5–Almería Province.

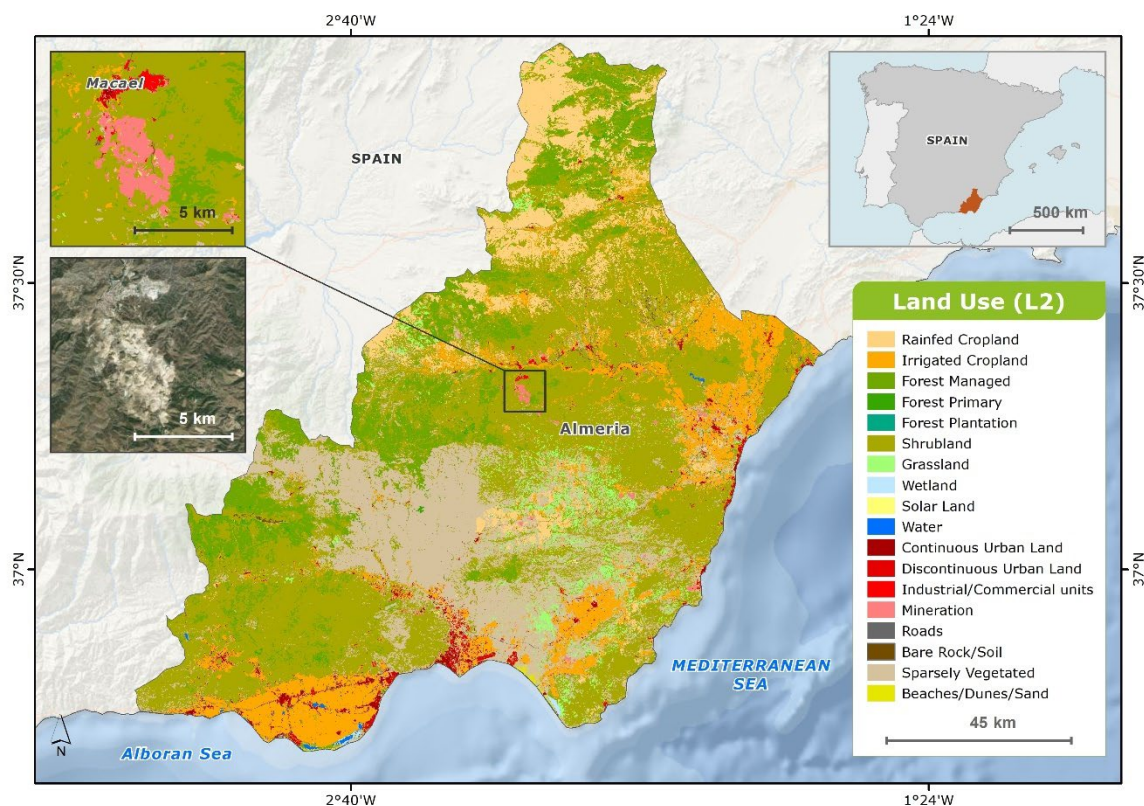


Figure 13: L2 HR land use map of CS5–Almería Province.

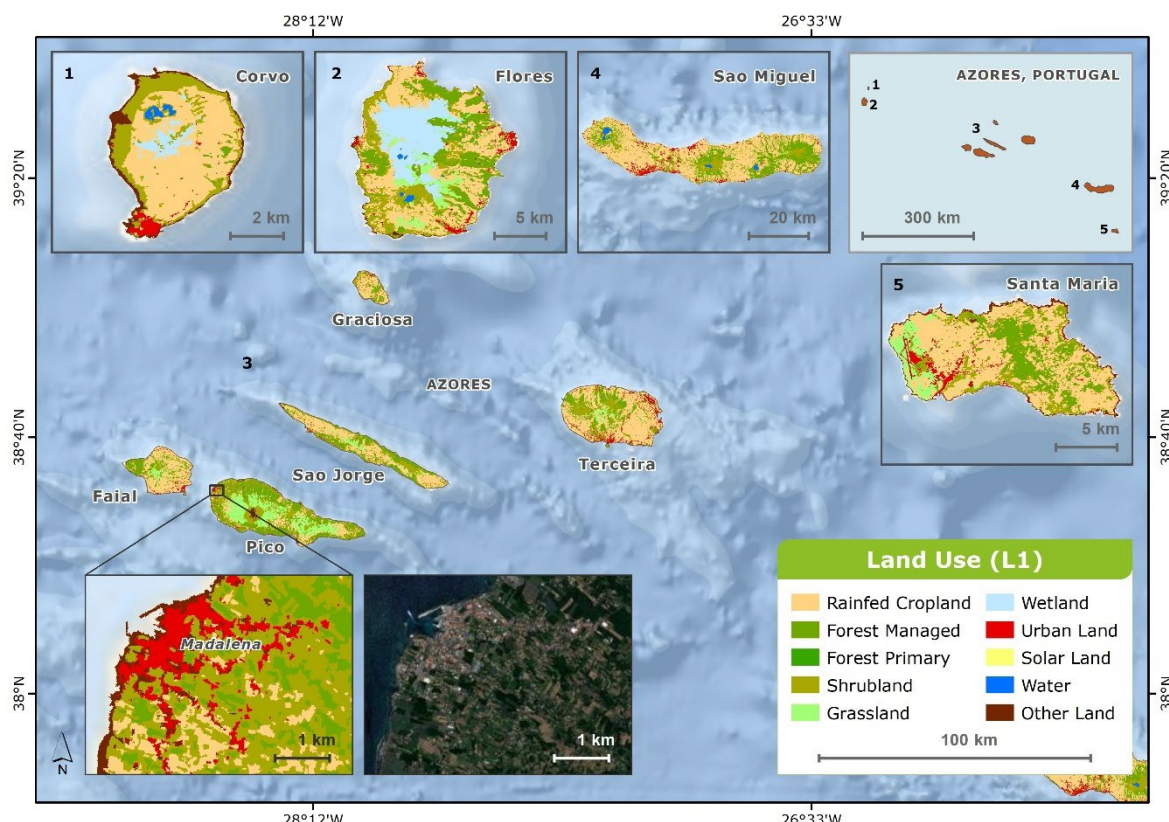


Figure 14: L1 HR land use map of CS6–Azores Archipelago.

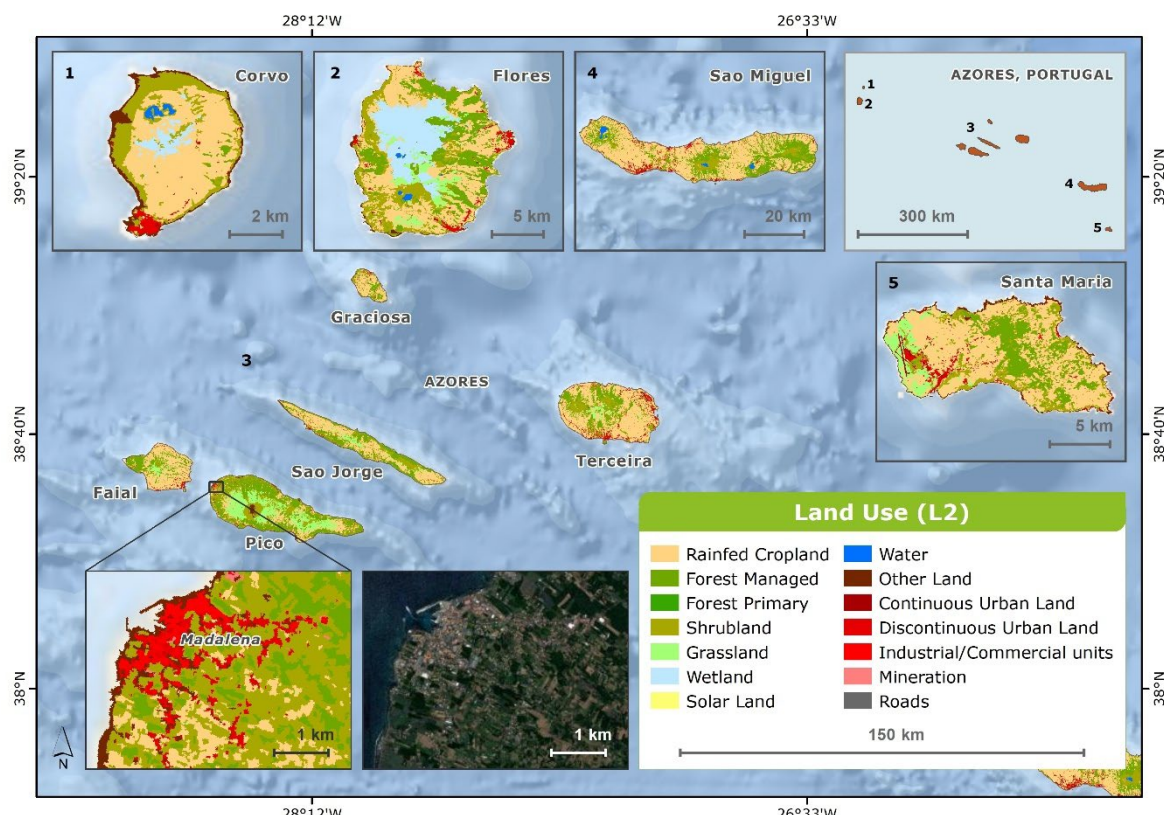


Figure 15: L2 HR land use map of CS6–Azores Archipelago.

All high-resolution land use maps are available in geospatial format for download from the project's Zenodo repository (RethinkAction Project, 2024)

Although relatively simple, the methodology seems robust and scientifically solid. However, the following improvements can be considered:

- Data used, especially in multitemporal approaches, are usually very large. A potential reduction of the number of bands could be explored to lighten the data size, making the process more efficient and avoiding data redundancy.
- For enhance computing and modelling efficiency, dimensionality reduction/classification feature selection techniques could be applied to feed the Random Forest model (a step that could be explored is exploratory data analysis (EDA) and Feature Engineering).
- An alternative classification based in a hierarchical logic could be considered to improve the results. Binary masks can be generated starting from water and non-water, then from non-water to extract vegetation and non-vegetation areas and so on.
- Training criteria could be reviewed and consequently refined as needed. To guarantee the quality of the training data, a random selection (10%) could be chosen and visually inspected.
- The possibility to distinguish additional classes such as pastures could be considered for future work if needed.

## 5. Conclusions

This study has detailed the creation and application of HR land use maps developed within the RethinkAction H2020 project. These maps serve as a fundamental baseline for analyzing land-based

adaptation and mitigation capacities, providing essential inputs for the project's scenario modeling and spatial assessments.

A key advancement in this study is the use of the RF machine-learning classifier, which has demonstrated its robustness, reliability, and superior accuracy in remote sensing applications (Breiman, 2001; Liu *et al.*, 2022). The ensemble learning nature of RF ensures better handling of high-dimensional datasets, a critical factor in object-based classification (Duro *et al.*, 2012). As highlighted by Costa *et al.* (2022), the integration of Random Forest with GEOBIA significantly reduces classification errors and salt-and-pepper noise, enhancing thematic accuracy and replicability of land use classifications.

The replicability of the proposed methodology is a notable outcome, as it allows for adaptation to different geographical areas with minimal modifications. The study demonstrates that the use of auxiliary data covering all or most CSs facilitates scalability and broader applicability. However, as identified in previous studies, local datasets with higher spatial resolution may be required in specific contexts to refine classification results (Duro *et al.*, 2012). Future applications of this methodology will need to identify and incorporate region-specific datasets to further enhance classification accuracy.

The RethinkAction HR land use maps provide a valuable resource for multiple applications. Beyond their immediate use in the project's scenario modeling, these maps are the cornerstone for the generation of suitability maps, which guide decision-making in land-based climate change adaptation and mitigation strategies. These suitability maps will enable stakeholders to assess which regions are most suitable for specific land use transitions, ensuring efficient resource allocation and sustainable development (ESA, 2024). Additional future analyses should focus on further refining the suitability mapping process by integrating multi-criteria decision analysis (MCDA) and machine learning-based spatial modeling approaches.

Further research should explore the integration of dimensionality reduction techniques, such as Principal Component Analysis (PCA) or Feature Selection Algorithms, to optimize the classification workflow and reduce redundancy in multi-layered datasets (Huang *et al.*, 2021). Additionally, future studies could investigate hierarchical classification approaches and alternative machine-learning models to further refine classification accuracy and processing efficiency.

In conclusion, the study provides the required HR land use maps, supporting the production of suitability maps and ensuring that the RethinkAction decision-making platform can provide data-driven insights for sustainable land management and climate adaptation. The established method provides a robust and replicable land use classification approach that can be implemented for further work. These findings contribute to the broader goal of sustainable land use planning and provide actionable insights for policymakers, researchers, and practitioners in the field of climate change mitigation and adaptation.

## **Acknowledgements**

This work was carried out within the framework of the project “RethinkAction”, that received funding from the European Union’s Horizon 2020 research and innovation programme under Grant Agreement No. 101037104.

## **References**

- Azores: National Geographic Information System (SNIG). Regional Secretariat for the Environment and Climate Change/Government of the Azores. 2018. *Carta de Ocupação do Solo de 2018 - Região Autónoma dos Açores (RAA)* [Cartography]. 1:25:000.
- Beshir, S., Moges, A., Donato, M. 2023. Trend analysis, past dynamics and future prediction of land use and land cover change in upper Wabe-Shebele river basin. *Heliyon*, 9. <https://doi.org/10.1016/j.heliyon.2023.e19128>

- Blaschke, T. 2010. Object based image analysis for remote sensing. *ISPRS Journal of Photogrammetry and Remote Sensing*, 65(1), 2-16. <https://doi.org/10.1016/j.isprsjprs.2009.06.004>
- Breiman, L. 2001. Random forests. *Machine Learning*, 45(1), 5–32. <https://doi.org/10.1023/A:1010933404324>
- Costa, H., Benevides, P., Moreira, F.D., Moraes, D., Caetano, M. 2022. Spatially stratified and multi-stage approach for national land cover mapping based on Sentinel-2 data and expert knowledge. *Remote Sensing*, 14, 1865. <https://doi.org/10.3390/rs14081865>
- Duro, D.C., Franklin, S.E., Dube, M.G. 2012. A comparison of pixel-based and object-based image analysis with selected machine learning algorithms for the classification of agricultural landscapes using SPOT-5 HRG imagery. *Remote Sensing of Environment*, 118, 259-272. <https://doi.org/10.1016/j.rse.2011.11.020>
- European Space Agency (ESA). 2024. Land use mapping is an invaluable tool in the realm of climate change mitigation, serving as a foundational element for greenhouse gas inventories. Retrieved from <https://climate.esa.int/de/neuigkeiten-und-veranstaltungen/high-resolution-maps-reveal-real-world-land-use-change/>
- Gao, B.C. 1996. NDWI—A normalized difference water index for remote sensing of vegetation liquid water from space. *Remote Sensing of Environment*, 58(3), 257-266. [https://doi.org/10.1016/S0034-4257\(96\)00067-3](https://doi.org/10.1016/S0034-4257(96)00067-3)
- García, M.L., Torres, R.J., Silva, D.P. 2023. Evaluating Sentinel-2 and Landsat-8 imagery for land cover classification in heterogeneous landscapes. *Remote Sensing Applications: Society and Environment*, 27, 100375. <https://doi.org/10.1016/j.rsase.2023.100375>
- Gong, P., Wang, J., Yu, L., Zhao, Y., Zhao, Y., Liang, L., ..., Chen, J. 2020. Finer resolution observation and monitoring of global land cover: First mapping results with Landsat TM and ETM+ data. *International Journal of Remote Sensing*, 41(6), 2000–2022. <https://doi.org/10.1080/01431161.2020.1724202>
- Hansen, M.C., Potapov, P.V., Moore, R., Hancher, M., Turubanova, S.A., Tyukavina, A., ..., Townshend, J.R. G. 2013. High-resolution global maps of 21st-century forest cover change. *Science*, 342(6160), 850–853. <https://doi.org/10.1126/science.1244693>
- Haralick, R.M. 1979. Statistical and structural approaches to texture. *Proceedings of the IEEE*, 67(5), 786-804.
- Holtgrave, A.K., Röder, N., Ackermann, A., Erasmi, S., Kleinschmit, B. 2020. Comparing Sentinel-1 and -2 data and indices for agricultural land use monitoring. *Remote Sensing*, 12(18), 2919. <https://doi.org/10.3390/rs12182919>
- Huang, X., Li, J., Zhang, J. 2021. A comparative assessment of Landsat-8 and Sentinel-2 for land cover classification in urban environments. *International Journal of Remote Sensing*, 42(18), 3576-3592. <https://doi.org/10.1080/01431161.2021.1911432>
- Hussain, M., Chen, D., Cheng, A., Wei, H., Stanley, D. 2013. Change detection from remotely sensed images: From pixel-based to object-based approaches. *ISPRS Journal of Photogrammetry and Remote Sensing*, 80, 91-106. <https://doi.org/10.1016/j.isprsjprs.2013.03.006>
- Jones, B., Kumar, S. 2020. The use of NDVI in land cover classification: A review of applications and challenges. *Journal of Remote Sensing & GIS*, 9(2), 29-41. <https://doi.org/10.1080/01431161.2020.1850203>
- Khan, H., Ali, I. 2021. Geographic Object-Based Image Analysis for Small Farmlands Using Sentinel-2 Imagery. *Pakistan Journal of Science*, 72(1), 1-10. [https://doi.org/10.53560/PPASA\(60-1\)795](https://doi.org/10.53560/PPASA(60-1)795)
- Liu, H., Wang, Z., Chen, Y. 2022. Integrating spectral indices and machine learning for accurate land cover classification: A case study using Sentinel-2 and Landsat-8. *ISPRS Journal of Photogrammetry and Remote Sensing*, 189, 12-28. <https://doi.org/10.1016/j.isprsjprs.2022.02.006>
- Miranda, H.D., Mutiara, A.B. 2018. Classification of land cover from Sentinel-2 imagery using supervised classification technique: Preliminary study. *Proceedings of the 2018 International Conference on Applied Engineering (ICAE)*, 1-5. <https://doi.org/10.1109/INCAE.2018.8579398>
- Patankar, N., Sarkela-Basset, X., Schivley, G., Leslie, E., Jenkins, J. 2022. *Land use trade-offs in decarbonization of electricity generation in the American West*. arXiv preprint.
- PCI Catalyst Help platform. 2021. Retrieved from <https://catalyst.earth/catalyst-system-files/help/>

- PCI Geomatics Enterprises, Inc. 2022. Retrieved from <https://catalyst.earth/catalyst-system-files/help/>
- Ramezan, C.A., Warner, T.A., Maxwell, A. E., Price, B.S. 2021. Effects of training set size on supervised machine learning land-cover classification of large-area high-resolution remotely sensed data. *Remote Sensing*, 13, 368. <https://doi.org/10.3390/rs13030368>
- RethinkAction Project (2024). RethinkAction project. CRoss-sEcToral planning decisIoN-maKing platform to foster climate Action. Retrieved from <https://zenodo.org/communities/rethinkaction/>
- Tang, K., Zhu, H., Ni, P. 2021. Spatial downscaling of land surface temperature over heterogeneous regions using random forest regression considering spatial features. *Remote Sensing*, 13, 3645. <https://doi.org/10.3390/rs13183645>
- Wu, W., De Pauw, E. 2011. A simple algorithm to identify irrigated croplands by remote sensing. *Proceedings of the 34th International Symposium on Remote Sensing of Environment (ISRSE)*, Sydney, Australia (pp. 10-15). Arinex.
- You, X., Meng, J., Zhang, M., Dong, T. 2013. Remote sensing-based detection of crop phenology for agricultural zones in China using a new threshold method. *Remote Sensing*, 5(7), 3190-3211. <https://doi.org/10.3390/rs5073190>
- Zhang, Q., Yu, X., Tang, W. 2022. Advances in remote sensing-based land cover classification: A review of Sentinel-2 and Landsat-8 applications. *Environmental Monitoring and Assessment*, 194, 123. <https://doi.org/10.1007/s10661-022-09879-7>
- Zhao, X., Tan, W., Guo, H., Wang, L., Wu, X. 2022. Urban expansion monitoring using Sentinel-2 imagery and deep learning methods. *Remote Sensing*, 14(2), 398. <https://doi.org/10.3390/rs14020398>



## **Administración / Administration**

Universidad de La Rioja  
Servicio de Publicaciones  
Piscinas, 1, 26006 LOGROÑO (España)  
Tel.: (+34) 941299187 Fax: (+34) 941299193  
Correo-e: [publicaciones@unirioja.es](mailto:publicaciones@unirioja.es)

## **Edición electrónica / E-Journal**

EISSN: 1697-9540  
<http://publicaciones.unirioja.es/revistas/cig> [cig@unirioja.es](mailto:cig@unirioja.es)

## **Indización y Calidad / Indexation and Quality Analysis**

Bases de Datos y Recursos para el análisis de la calidad de las revistas científicas / Databases and Resources for the analysis of the Scientific Journal's Quality:

CARHUS Plus+ 2018  
CIRC (EC3 Metrics)  
Dialnet Métricas (Fundación Dialnet)  
DOAJ (Directory of Open Access Journals)  
ERIH Plus (European Science Fundation)  
ESCI, Emerging Sources Citation Index (Web of Science™, Clarivate Analytics)  
Fuente Académica Plus (EBSCO)

Latindex (Catálogo)  
MIAR (Matriz de Información para el Análisis de Revistas)  
Periodicals Index Online (ProQuest)  
SCIMAGO Journal & Country Rank (SJR)  
Scopus (Elsevier)  
Sello de Calidad FECYT

## **Política del editor sobre copyright y autoarchivo**

- Sólo se puede archivar la versión final del editor/PDF.
- En el sitio web del autor o repositorio institucional o cualquier repositorio designado por los organismos financiadores a petición de dichos organismos o como resultado de una obligación legal desde el momento de su publicación.
- El uso debe ser no comercial, no permitiéndose obras derivadas.
- La fuente editorial debe reconocerse. Debe incluirse la declaración establecida por el editor: "Publicado originalmente en *Cuadernos de Investigación Geográfica / Geographical Research Letters* en [volumen y número, o año], por la Universidad de La Rioja (España)".
- Debe enlazar a la versión del editor con la inclusión del número DOI a partir de la siguiente frase: "La publicación original está disponible en *Cuadernos de Investigación Geográfica / Geographical Research Letters* a partir de [http://doi.org/\[DOI\]](http://doi.org/[DOI])".

## **Publisher copyright & self-archiving policies**

- Authors may self-archive publisher's version of the article (final PDF version) on their own websites.
- Authors may also deposit this version of the article in institutional or funder repositories, at the request of the funding organizations or as a result of legal obligation after publication.
- The final published version can only be used for non-commercial purposes. Derivative work is not allowed.
- Acknowledgement to the original source of publication must be given as follows: "First published in *Cuadernos de Investigación Geográfica / Geographical Research Letters* in [volume and number, or year] by Universidad de La Rioja (Spain)".
- A link must be inserted to the published article on the journal's website by including the DOI number of the article in the following sentence: "The final publication is available at *Cuadernos de Investigación Geográfica / Geographical Research Letters* via <http://doi.org/fDOI>".

---

**Cuadernos de Investigación Geográfica / Geographical Research Letters**  
A scientific Journal of Physical Geography

---



# CUADERNOS DE INVESTIGACIÓN GEOGRÁFICA

## *GEOGRAPHICAL RESEARCH LETTERS*

TOMO 51 (1), Año 2025

**José Arnáez, Noemí Lana-Renault, José María García-Ruiz, Isabel Terroba.**  
50 years of Cuadernos de Investigación Geográfica

**Adrián Melón-Nava, Amelia Gómez-Villar.** Snow Cover Variability in the Cantabrian Mountains (Spain): A Watershed-Level Study Using Satellite Records (2000-2024)

**Ana Casado, Federico Javier Berón De La Puente, Verónica Gil.** Effects of DEM Resolution and Area Thresholds on Automated Fluvial Morphometry, Arroyo del Oro (Argentina)

**Andrea S. Brendel, Federico Ferrelli, Maximiliano Garay, Agustina Gutierrez, Vanesa Perillo, Maria Cintia Piccolo.** The Role of Green Roofs in Climate Change Mitigation and Adaptation: Analyzing Performance During Extreme Rainfall Events

**Marco Navarro, Melina Paredes, Miguel Pezo, Eduardo Oyague.** Assessing the Design and Management of Protected Areas: Landscape Geography in Lomas and Tillandsiales of Southwestern Peru

**Virginia Alberdi Nieves.** Analysis of Climate Change Impacts on Andean Forests Using Potential Distribution Models (2010-2069)

**Dhais Peña-Angulo, Santiago Beguería, Víctor Trullenque-Blanco, José Carlos González-Hidalgo.** Variabilidad espacial y temporal de las precipitaciones extraordinarias en España (1916-2022)

**Carolina Calvi, Edoardo Melendi, Eleonora Carol.** Análisis espectral espacio-temporal de humedales de alta montaña y su relación con la variabilidad climática

**Christoph Correia, Jesús Ortuño Castillo, Marta Toro Bermejo, Patricia Pérez Ramírez.** Advancements in High-Resolution Land Use Mapping: Methodologies and Insights from the Rethinkaction H2020 Project



UNIVERSIDAD  
DE LA RIOJA